

**SEISMIC Q AND VELOCITY STRUCTURE FOR
THE MAGMA-HYDROTHERMAL SYSTEM OF THE
VALLES CALDERA, NEW MEXICO**

by

PETER MORSE ROBERTS

B.S., Massachusetts Institute of Technology

(1979)

**SUBMITTED TO THE DEPARTMENT OF EARTH,
ATMOSPHERIC, AND PLANETARY SCIENCES
IN PARTIAL FULFILLMENT OF
THE REQUIREMENTS FOR THE DEGREE OF
DOCTOR OF PHILOSOPHY**

at the

MASSACHUSETTS INSTITUTE OF TECHNOLOGY

April, 1989

© Peter Morse Roberts, 1989. All rights reserved.

The author hereby grants to MIT permission to reproduce and
to distribute copies of this thesis document in whole or in part.

Signature of Author _____

Department of Earth, Atmospheric, and Planetary Sciences

March, 1989

Certified by _____

Thesis Supervisor

Accepted by _____

Chairman, Department Committee

VOL 1
MASSACHUSETTS INSTITUTE
OF TECHNOLOGY

NOV 06 1989

1

LIBRARIES
Lindgren

**SEISMIC Q AND VELOCITY STRUCTURE FOR
THE MAGMA-HYDROTHERMAL SYSTEM OF THE
VALLES CALDERA, NEW MEXICO**

by

PETER MORSE ROBERTS

Submitted to the Department of Earth, Atmospheric,
and Planetary Sciences on March 10, 1989, in partial
fulfillment of the requirements for the degree of
Doctor of Philosophy

ABSTRACT

The Valles Caldera lies at the intersection of the Jemez Lineament and the western edge of the Rio Grande Rift in northern New Mexico. The caldera and its immediate surroundings comprise one of the world's largest and most complex volcanic centers, with a long history of eruptive activity extending up to geologically recent times. In this thesis we present the results of two different forward modeling methods used to determine the local 2-dimensional seismic structure directly beneath the caldera. In the first method we modeled observed P-wave delays by ray-tracing. In the second method we modeled spectral amplitude variations using the Aki-Larner discrete wavenumber spectral synthesis technique.

We used six portable seismic event recorders to collect teleseismic data at sites placed along a line bisecting the caldera. The azimuth of the array was approximately on-line to seismically active regions to the northwest and southeast, so that our observations would be for plane waves arriving nearly parallel to the plane used to specify a 2-D vertical cross-section of the caldera directly beneath the array line. This design minimized the effects of 3-D structure in the recorded data. Two separate deployments of the six instruments along the same line yielded 24 high quality

teleseismic signals for on-azimuth events recorded at most of the sites. The most useful data were obtained on the second array, which had 4 sites on the resurgent dome and 1 each on the northwest and southeast ring fractures.

Using spectral ratio techniques to characterize the amplitude variations for the vertical and radial components across the array, we found that the amplitudes for both components were much lower inside the caldera than at the ring fracture sites. This dominant behavior did not vary significantly with incidence angle or direction of the events. We modeled this dominant behavior using synthetic spectral displacement solutions for the P-SV scattering problem in irregularly layered models, solved using the Aki-Larner method. The model which best fit the data required a zone of strong attenuation and low velocity approximately 16 km wide, 4 km high and 1 km deep, centered beneath the caldera. We interpret this feature as a zone of highly fractured and partially water-saturated material created by the deformation which must have accompanied caldera collapse and dome resurgence, and by subsequent hydrothermal activity.

For each recorded event we also measured P-wave delays across the caldera, relative to the earliest site. The dominant behavior in these observations was that the delays are much stronger at the dome sites for southeastern events than for northwestern events. We used a standard ray-tracing method to model these observations and found that a large lens-shaped low velocity inclusion was required at significant depth beneath the caldera. We constrained the inclusion's width to be about 17 km and its average depth to be 10-13 km. We could not constrain its maximum height and velocity, but minimum values for these were found to be 8 km and 3.5 km/sec, respectively. We interpret this feature as a zone of partial melt related to the original Valles magma chamber, which has cooled considerably since the caldera and resurgent dome were created.

Thesis Supervisor: Prof. Keiiti Aki

Title: Professor of Geophysics

This thesis is dedicated to the memory of my father,
Victor Jamison Roberts,
and to the future of my son,
Alexander Collins Roberts.

ACKNOWLEDGEMENTS

During the course of my graduate studies I have received an immense amount of moral support and encouragement from family, mentors, friends and colleagues.

My mother, Martha Roberts, has shared in all of my excitement and disappointments with my thesis work. She was always helpful and encouraging even during those times when I was considering taking up the saxophone again. I can never thank her enough, although she will insist that no thanks are necessary.

I met my wife, Julie Collins, one week before I began graduate school. She has lived through the best and the worst with me, and her caring nature and wonderful sense of humor have made my life richer and my work easier. I thank her for her endurance and for her constant faith in me.

My brother, Hugh Roberts, has always been able to cheer me up with his humor and beautiful paintings. We had many pleasant and boisterous phone conversations which helped restore my perspective and gave me renewed confidence in my work.

It has been challenging and rewarding to work with Keiiti Aki. I will never fully comprehend the depth of Kei's knowledge and understanding, but I have learned to trust him implicitly because of his excellent guidance and his intuitive sense for what is or is not possible. Kei's patience, modesty, creativity and joyful commitment to scientific advance have helped instill in me the values and discipline which I believe are prerequisite for becoming a well-rounded scientist. He can also cook up a mean Peking duck.

Sean Solomon hired me as an undergraduate technician in his ocean-bottom-seismometer lab when I was still a Biology major. My first experiences with seismic instrumentation and the rudiments of my soon-to-be-growing interest in Seismology can be attributed to Sean. I have benefited greatly over the years from his professional guidance and support, and from his friendship.

Mike Fehler unwittingly became my on-site advisor when he set the stage for me to conduct my thesis work at Los Alamos. Mike has an uncanny natural ability for knowing whether or not proposed methods or theories are valid and useful. Because

of this, he has saved me from persuing fruitless approaches to solving problems many times. I have hounded him relentlessly for suggestions about nearly every aspect of my study, and he has always been cheerful, genuinely interested and, above all, extremely helpful. Mike put a great deal of effort into ensuring that I had everything I needed to conduct my research at Los Alamos. He also maintained my autonomy so that I could work efficiently and finish my thesis in a reasonable amount of time. This was all motivated by his sincere wish to see me succeed. Mike is a true friend.

Valerie Ferrazzini possesses unlimited energy that only a child of five could keep up with. I owe much to Valerie for her ability to make excitement contagious. She was always eager to help me with my field work, which involved lugging heavy equipment up and down steep talus slopes. Work which normally would take me most of a day to finish was done by noon when Valerie came along. She was also encouraging and supportive at times when my thesis work was not going so well. Thanks to her also for nicknaming my son "Little Dude".

My field work would have been impossible without the cooperation and assistance of the Baca Land and Cattle Company of Abilene, Texas, who own the land containing the Valles Caldera. They were always courteous and helpful and granted me complete freedom of movement on their property. I must express my deepest thanks to Tom Berry, Joe Harrell and Jim Wilson. It was a priviledge for me to have worked there.

The people who I hung out with at the Geological Engineering Group (ESS-4) at Los Alamos helped keep me in touch with the outside world of current research as well as provided comments and suggestions at various phases of my thesis work. Leigh House provided me with access to his vast knowledge of computers, without which I often would have just flailed around and eventually crashed a machine. Scott Phillips provided me with computer programs and lessons on how to use them and steered me to some great cross-country ski trails. Thanks also to Paul Johnson, who made several appreciated attempts at getting me back into rock climbing, and to Jim Rutledge, who made me feel like a jazz sage. I look forward to working with all of them in the future. I thank Hugh Murphy and Jim Albright, who allowed

me freedom with the facilities and equipment in ESS-4. Their cooperation reduced my work from insurmountable to straightforward. I must also thank Fraser Goff of ESS-1 for his crash-course on the geology and volcanic history of the Valles Caldera.

At MIT, George Blumberg, an office mate and more, made life bearable at ERL during Kendall Square construction. This was not often easy for him while I was working on my generals. Back in the Green Building, I shared company with the likes of Joao and Jose Rosa, Rafael Benites, Mark Murray, Kiyoshi Yomogida and Paul Huang, to name only a few. I could not have made it through my course work and initial research without their direct help. Nafi Toksoz, Ted Madden, Ari Ben-Menahem and Brian Evans served sentences on either my generals or thesis committees or both. I thank them for their careful appraisal of my work. I thank Ted also for making my defense more interesting than I had expected.

Unfortunately I cannot mention everyone that I would like to. I hope that those I have left out will understand.

This thesis research was funded primarily by DOE contract number DE-FG03-87ER-13807 to the University of Southern California. Additional support was provide by the Earth and Space Sciences Division, Geological Engineering Group, ESS-4, of the Los Alamos National Laboratory.

TABLE OF CONTENTS

	Page
TITLE PAGE	1
ABSTRACT	2
DEDICATION	4
ACKNOWLEDGEMENTS	5
TABLE OF CONTENTS	8
LIST OF FIGURES	10
LIST OF TABLES	16
Chapter	
1 Introduction and Review of the Valles Caldera	17
1.1 Introduction and Outline of Thesis	17
1.2 Overview and Tectonic Setting of the Valles Caldera	22
1.3 Formation and Evolution of the Valles Caldera	25
2 Data Collection and Processing	33
2.1 Field Experiments	33
2.2 Data Quality and Instrument Correction	44
2.3 Recorded Seismograms and Signal-to-Noise Estimation	54
2.4 Spectral Ratios	68
2.5 Measured P-Wave Arrival Time Delays	98
3 The Aki-Larner Discrete Wavenumber Method	109
3.1 Introduction and History	109
3.2 Formulation	114
3.3 Solution of the Integral Equations	125
3.4 Wavefield Damping and Complex Wavenumbers	134
3.5 Anelastic Attenuation and Parameterization of Q	146
4 Modeling of Arrival Time Delays	157
4.1 Introduction	157
4.2 Description of Ray Tracing Method	159
4.3 Delay Time Modeling Results	164

Chapter	Page
5 Modeling of Spectral Amplitude Ratios	198
5.1 Introduction	198
5.2 The Best Model	201
5.3 Parameter Perturbation Study and Uniqueness	233
5.4 Implications of 3-dimensional Structure	255
5.5 Resonance and Scattering Effects	260
6 Discussion and Conclusion	271
6.1 Comparison of the Two Caldera Fill Models	271
6.2 Interpretation and Discussion	277
6.3 Summary and Conclusion	289
6.4 Suggestions for Future Work	292
Appendices	
1 Detailed Formulas for Setting Up the Aki-Larner P-SV Problem	294
2 A Versatile Equalization Circuit for Increasing Seismometer Velocity Response Below the Natural Frequency	304
REFERENCES	326

LIST OF FIGURES

Figure	Abbreviated Caption	Page
1.1	Location and tectonic setting of the Valles Caldera	24
1.2	Schematic map of the Valles Caldera and vicinity	27
1.3	Schematic cross-section of the Valles hydrothermal system	30
1.4	Near-surface structure beneath the Valles Caldera	31
2.1a	Jemez seismic array 1 site locations	34
2.1b	Jemez seismic array 2 site locations	35
2.2	Measured and theoretical instrument response curves	42
2.3	Relative instrument amplitude response corrections	47
2.4	Relative instrument phase response corrections	48
2.5	Example of additive long-period noise removal	53
2.6	Seismograms for an Andreanof Islands event recorded on array 2	56
2.7	Seismograms for a Jujuy, Argentina event recorded on array 2	57
2.8	Seismograms for a Honshu, Japan event recorded on array 2	58
2.9	Seismograms for an Ecuador event recorded on array 2	59
2.10	Seismograms for a Kommandorsky Islands event recorded on array 2	60
2.11	Seismograms for a Central Chile event recorded on array 2	61
2.12	Signal and noise spectra for Jujuy, Argentina data	66
2.13	Signal and noise spectra for Fox Islands data	67
2.14	Spectral amplitude ratios for the data in Figure 2.6	73
2.15	Spectral amplitude ratios for the data in Figure 2.7	74
2.16	Spectral amplitude ratios for the data in Figure 2.8	75
2.17	Spectral amplitude ratios for the data in Figure 2.9	76
2.18	Spectral amplitude ratios for the data in Figure 2.10	77
2.19	Spectral amplitude ratios for the data in Figure 2.11	78
2.20	Vertical component spectral ratios vs. incidence angle for 8 array 2 events	82

Figure	Abbreviated Caption	Page
2.21	Radial component spectral ratios vs. incidence angle for 8 array 2 events	83
2.22	Transverse component spectral ratios vs. incidence angle for 8 array 2 events	84
2.23	Radial seismogram and spectrum for a Kuril islands event at SAM	86
2.24	Same as Figure 2.23, but for a different Kuril Islands event	87
2.25	Spectral amplitude ratios for Kuril Islands event A	89
2.26	Spectral amplitude ratios for Kuril Islands event B	90
2.27	Spectral amplitude ratios for Kuril Islands event C	91
2.28	Spectral amplitude ratios for Kuril Islands event D	92
2.29	Spectral amplitude ratios for averaged Kuril events A,B,C,D	94
2.30	Spectral amplitude ratios for 7 averaged northwestern events	95
2.31	Spectral amplitude ratios for 3 averaged southeastern events	96
2.32	Spectral amplitude ratios for all 10 events averaged	97
2.33	Observed arrival time delays for NW and SE events on array 2	102
2.34	Observed arrival time delays for NW and SE events on array 1	105
2.35	Observed ray paths for all data, categorized by delay strength	106
3.1	Aki-Larner problem configuration	119
3.2	k_n and ν_n summation paths for different incidence angles	140
3.3	Propagation, attenuation and difference angles for the summation paths in Figure 3.2	144
3.4	Velocity dispersion curves for Azimi attenuation law	151
3.5	Attenuated pulses calculated for different values of Q	153
3.6	Aki-Larner solutions for wave-damping and Q methods applied to the same model	155
4.1a	Caldera fill correction model for P-wave delays	166
4.1b	P-delays calculated for caldera fill model compared with observed delays for array 2 Kuril Islands data	167

Figure	Abbreviated Caption	Page
4.1c	P-delays calculated for caldera fill model compared with observed delays for array 2 Jujuy, Argentina data	168
4.2	Best LVZ model for P-wave delays	171
4.3	Typical calculated ray paths for the best LVZ model	172
4.4a	P-delays calculated for best LVZ model compared with observed delays for array 2 Kuril Islands data	174
4.4b	P-delays calculated for best LVZ model compared with observed delays for array 2 Jujuy, Argentina data	175
4.5a	P-delays calculated for best LVZ model compared with observed delays for array 1 Kommandorsky Islands data	178
4.5b	P-delays calculated for best LVZ model compared with observed delays for array 1 Central Chile data	179
4.6a	P-delays calculated for 9-km-depth LVZ model compared with observed delays for array 2 Kuril Islands data	183
4.6b	P-delays calculated for 9-km-depth LVZ model compared with observed delays for array 2 Jujuy, Argentina data	184
4.7a	P-delays calculated for 11-km-depth LVZ model compared with observed delays for array 2 Kuril Islands data	185
4.7b	P-delays calculated for 11-km-depth LVZ model compared with observed delays for array 2 Jujuy, Argentina data	186
4.8a	P-delays calculated for 12-km-depth LVZ model compared with observed delays for array 2 Kuril Islands data	187
4.8b	P-delays calculated for 12-km-depth LVZ model compared with observed delays for array 2 Jujuy, Argentina data	188
4.9	Best LVZ model with caldera fill layer 3 km thicker overall	194
4.10a	P-delays calculated for thick caldera LVZ model compared with observed delays for array 2 Kuril Islands data	195
4.10b	P-delays calculated for thick caldera LVZ model compared with observed delays for array 2 Jujuy, Argentina data	196

Figure	Abbreviated Caption	Page
5.1	Best Aki-Larner LQZ model for amplitude variations	202
5.2a	Vertical spectral ratios calculated for the best LQZ model compared with observed ratios for the averaged array 2 Kuril Islands data	205
5.2b	Horizontal spectral ratios calculated for the best LQZ model compared with observed ratios for the averaged array 2 Kuril Islands data	206
5.3a	Vertical spectral ratios calculated for the best LQZ model showing the P-wave and S-wave contributions to the combined solutions	208
5.3b	Horizontal spectral ratios calculated for the best LQZ model showing the P-wave and S-wave contributions to the combined solutions	209
5.4a	Boundary conditions and RMS errors for the 0.2 Hz Aki-Larner solution for the best LQZ model	213
5.4b	Boundary conditions and RMS errors for the 0.8 Hz Aki-Larner solution for the best LQZ model	214
5.5a	Potential wavenumber spectra for the 0.2 Hz Aki-Larner solution for the best LQZ model	217
5.5b	Potential wavenumber spectra for the 0.8 Hz Aki-Larner solution for the best LQZ model	218
5.6a	Vertical spectral ratios calculated for the best LQZ model compared with observed ratios for 7 averaged northwestern events	221
5.6b	Horizontal spectral ratios calculated for the best LQZ model compared with observed ratios for 7 averaged northwestern events	222
5.7a	Vertical spectral ratios calculated for the best LQZ model compared with observed ratios for 3 averaged southeastern events	223
5.7b	Horizontal spectral ratios calculated for the best LQZ model compared with observed ratios for 3 averaged southeastern events	224
5.8a	Vertical spectral ratios calculated for the best LQZ model compared with observed ratios for the average of all 10 events	226
5.8b	Horizontal spectral ratios calculated for the best LQZ model compared with observed ratios for the average all 10 events	227

Figure	Abbreviated Caption	Page
5.9a	Vertical spectral ratios calculated for the best LQZ model compared with observed ratios for the array 1 Kommandorsky Islands data	229
5.9b	Horizontal spectral ratios calculated for the best LQZ model compared with observed ratios for the array 1 Kommandorsky Islands data	230
5.10a	Vertical spectral ratios for the best model with LQZ $Q=2$ compared with observed ratios for the averaged array 2 Kuril Islands data	236
5.10b	Horizontal spectral ratios for the best model with LQZ $Q=2$ compared with observed ratios for the averaged array 2 Kuril Islands data	237
5.11a	Vertical spectral ratios for the best model with LQZ $Q=5$ compared with observed ratios for the averaged array 2 Kuril Islands data	238
5.11b	Horizontal spectral ratios for the best model with LQZ $Q=5$ compared with observed ratios for the averaged array 2 Kuril Islands data	239
5.12a	Vertical spectral ratios for the best model with LQZ $Q=10$ compared with observed ratios for the averaged array 2 Kuril Islands data	240
5.12b	Horizontal spectral ratios for the best model with LQZ $Q=10$ compared with observed ratios for the averaged array 2 Kuril Islands data	241
5.13a	Vertical spectral ratios for the best model with caldera $Q=5$ compared with observed ratios for the averaged array 2 Kuril Islands data	243
5.13b	Horizontal spectral ratios for the best model with caldera $Q=5$ compared with observed ratios for the averaged array 2 Kuril Islands data	244
5.14a	Vertical spectral ratios for the best model with caldera $Q=1$ compared with observed ratios for the averaged array 2 Kuril Islands data	245
5.14b	Horizontal spectral ratios for the best model with caldera $Q=1$ compared with observed ratios for the averaged array 2 Kuril Islands data	246
5.15a	Vertical spectral ratios for the best model minus caldera fill compared with observed ratios for the averaged array 2 Kuril Islands data	248
5.15b	Horizontal spectral ratios for the best model minus caldera fill compared with observed ratios for the averaged array 2 Kuril Islands data	249

Figure	Abbreviated Caption	Page
5.16a	Four of eight structural perturbations studied for the LQZ model	252
5.16b	Remaining four structural perturbations studied for the LQZ model	253
5.17a	Damped vertical spectral ratios for the best LQZ model compared with direct P-wave ratios for array 2 Kuril Islands data	258
5.17b	Damped vertical spectral ratios for the best LQZ model compared with direct P-wave ratios for array 1 Kommandorsky Islands data	259
5.18a	Test model for shallow non-attenuating low-velocity inclusion	263
5.18b	Vertical spectral ratios for the model in Figure 5.18a calculated for 5 different incidence angles	264
5.18c	Horizontal spectral ratios for the model in Figure 5.18a calculated for 5 different incidence angles	265
5.19a	Test model for deep non-attenuating low-velocity inclusion	266
5.19b	Vertical spectral ratios for the model in Figure 5.19a calculated for 5 different incidence angles	267
5.19c	Horizontal spectral ratios for the model in Figure 5.19a calculated for 5 different incidence angles	268
6.1	Comparison of the best P-delay and amplitude models	275
A2.1	Block diagram of instrument circuit components	307
A2.2	Theoretical amplitude and phase response curves for equalization circuit and seismometer	311
A2.3	Schematic circuit diagram for 1-pole equalization stage	314
A2.4	Typical vertical component P-wave seismogram recorded in 1987	317
A2.5	Recordings of equalized and unequalized calibration signals	320
A2.6	Measured and theoretical instrument amplitude response curves	321
A2.7	Measured and theoretical instrument phase response curves	322

LIST OF TABLES

Table	Heading	Page
2.1	Site Information for 1987 Jemez Field Experiments	37
2.2	Information for Teleseismic Events Recorded in 1987 in the Jemez Mountains	40
4.1	Residual Variance and Variance Reduction for Best Ray Model Compared with 21 Events	181
5.1	Boundary Condition % RMS Errors and Maximum Surface Traction for Best LQZ Model	215
5.2	Best LQZ Model Parameter Perturbations and Resulting Variance Reduction	251
A2.1	Circuit Component Values for 0.1 to 1.0 Hz Equalization Range	313

CHAPTER 1

Introduction and Review of the Valles Caldera

1.1 Introduction and Outline of Thesis

Seismological investigations into the processes and crustal structure associated with volcanic features at the earth's surface have been on the increase in recent years. Of particular interest to many earth scientists is the understanding of the mechanisms governing magma emplacement in the crust, transport to the surface and the resulting evolution of topographic surface features which are commonly identified with volcanic systems. The vast majority of scientific studies on volcanoes have been carried out using non-seismological methods and data. This is due largely to the complexity of volcanic structures and the unpredictable characteristics that seismic data display after interacting with the fine details of these structures. Typically the upper-crustal structure beneath volcanoes varies strongly in all three space dimensions, and to adequately constrain the parameters of this structure, using traditional seismic imaging methods, would require data from a very dense 2-D network of surface stations. Often the logistics of installing and maintaining such an array on volcanoes are prohibitive because of limited accessibility and extremely rugged terrain. This problem has been alleviated somewhat by the development of sophisticated waveform modeling methods which can be applied successfully to seismic data recorded on just a handful of instruments installed at key diagnostic locations on and around a volcano. This is the approach we have used in the present study for the Valles Caldera. Although accessibility was not a

problem in our case, we had only six portable event recorders to work with. So our field experiments were restricted to 1-D linear arrays, and our modeling efforts were concentrated on reproducing the observed variations in amplitude and P-wave delay, using 2-dimensional representations of the vertical structure beneath the array lines.

The Valles Caldera is one of the largest and most complex resurgent calderas in the world. Its topographic rim varies between 25 to 30 km in diameter, and from aerial photographs and topography and geology maps, it is seen very distinctly as a sub-circular depression in the Jemez volcanic highlands, containing a large, central resurgent dome and at least eight subsidiary volcanic domes which outline the approximate locations of the ring fracture. The topography of the region is so complex that there are few accessible vantage points on the ground where the bowl-like shape of the caldera can be clearly viewed. The caldera has frustrated all attempts to date at determining its detailed seismic crustal structure, for the simple reason that it lies entirely within the boundaries of a privately-owned ranch and, until recently, it has been difficult to obtain permission to install temporary seismic recorders there. The present study represents a major breakthrough in this respect, because the results we obtained would not have been possible without the generous cooperation and freedom of movement within the caldera that was granted to us by the owners, the supervisor and foreman of the ranch. We were allowed to place all six of our instruments entirely within the caldera and thus, the data we collected are by far the best obtained to date for the purposes of studying the seismic sub-structure.

In this thesis we give a detailed presentation of our seismic experiments in the Valles Caldera, carried out during the summer of 1987. We describe the types of data collected, the analysis methods used for data reduction and the major patterns observed which we used to infer the crustal structure. We give detailed descriptions of the modeling techniques used, as well as in-depth presentations and discussions of the best models we obtained which were capable of reproducing the majority of our observations. We then discuss possible interpretations of these results in terms of the known volcanic history and structural evolution of the caldera presented in numerous non-seismological studies of the region.

The remainder of the present chapter is devoted to a brief review of the volcanic history of the Valles Caldera and its geologic and tectonic setting. This is not intended as a comprehensive detailed review, since this has already been done by *Felch* [1987], among others. It is meant primarily to give enough background information on the region so that continuity can be maintained between the known history and geology of the caldera and possible interpretations of our results for seismic structure.

Chapter 2 is entirely devoted to the data. We discuss the design of the field experiments, describe the instruments used and the logistics of site reconnaissance, installation and maintenance. We discuss the types and quality of data recorded and describe the methods used to characterize and reduce or remove various forms of noise from the recorded seismograms. We then describe the data-reduction methods used to obtain information about the relative amplitude and P-wave delay variations across the caldera. Finally, we discuss the observed patterns in the data and the features of these patterns that we will attempt to model.

In Chapter 3 we present a detailed description of the Aki-Larner method used to synthesize spectral amplitudes for candidate structural models. The problem is formulated to solve for 2-D scattering and attenuation effects caused by plane P-SV wave interaction with layered models having irregularly shaped interfaces. The formulation and solution of the problem is presented in a generalized form which may be used to obtain solutions for models with an arbitrary number of irregular layers, although current computing capabilities limit the total number of interfaces to 4. Appendix 1 gives the detailed expressions needed to program the algorithm. We also present, in Chapter 3, the formulas needed to include anelastic attenuation in the models in terms of the seismic quality factor, Q .

In Chapter 4 the P-wave delays are modeled using a standard ray-tracing technique. We give a brief description of the method and how we used it for determining the major features of the P-velocity structure beneath the caldera. We then describe the forward modeling process which led to the best-fitting model and discuss the best model in terms of which parameters are or are not well constrained by the observed delays across the caldera. We show that a low velocity lens-shaped inclusion at depth, centered beneath the caldera, is required to explain the strong differences in observed delays between recorded events from the northwest and southeast.

Chapter 5 presents the major results obtained for the Aki-Larner modeling of the amplitude data for scattered waves. We find that the amplitudes are not sensitive to the deep low velocity inclusion found in Chapter 4, but they can be best reproduced by a large zone of very strong attenuation near the surface beneath the caldera. We discuss the internal reliability of the synthetic solutions for this model and demonstrate that the most important model parameters are reasonably

well constrained by the data. We also discuss possible implications of 3-D structure and demonstrate that our model is in fact a reasonable representation of the 2-D vertical structure for the caldera cross-section beneath our instrument array line. We conclude the chapter with a discussion of alternative mechanisms of wave interaction which might also be capable of reproducing the data. We eliminate these alternatives one-by-one, largely through counterexample, and conclude that our low Q effect is the only reasonable way to produce synthetic amplitudes that are consistent with the observations.

Finally, in Chapter 6 we discuss the differences between the two models obtained for the P-delay and amplitude data and conclude that these may be resolved in terms of the major differences between the ray-tracing and Aki-Larner methods and between the approaches we took for converging on the best models. We then discuss possible interpretations of the major features in each model by relating them to the known thermal and structural evolution of the Valles Caldera, based on previous non-seismological studies of the region. We conclude that the deep, low velocity inclusion is consistent with a zone of partial melt representing the remnant portion of the cooling magma chamber which was responsible for the formation of the caldera. The near-surface low Q zone is interpreted as a highly deformed and fractured portion of the caldera fill layer created by the process of dome resurgence. The extremely low value of Q that was obtained for this zone is a unique result. It is partially supported by the existence of a well-developed hydrothermal system, which, due to water-saturation of the fractured region, may be capable of producing strong attenuation effects for fairly low frequency waves.

1.2 Overview and Tectonic Setting of the Valles Caldera

The Valles Caldera and the surrounding Jemez Mountains volcanic field has long been the subject of diverse areas of scientific research. The earlier works of *Ross* [1938], *Smith et al.* [1961] and *Smith & Bailey* [1966, 1968] were aimed primarily at the geologic mapping of the region and studies of erupted volcanic material, eruption processes and ring fracture and resurgent dome formation [*Goff & Gardner*, 1988]. From the 1960's onward, increasing interest has been shown in the geothermal and hydrothermal properties of the region [*Dondanville*, 1971, 1978; *Goff & Grigsby*, 1982]. Almost 40 geothermal wells have been drilled in and around the caldera. Also, numerous wells have been drilled at Fenton Hill on the western flank of the caldera, to search for geothermal energy sources in hot dry rock (HDR) [*Heiken et al.*, 1981]. The combined stratigraphic information obtained from all of these wells has allowed the construction of detailed lithologic sections for a large portion of the caldera region [*Goff et al.*, 1986]. The result is that more is known about the near-surface structure of the Valles Caldera than any other resurgent caldera in the world. During the past decade or so there has been a noticeable increase in the publication rate for studies in and around the caldera. This in part has been due to the interest of the Continental Scientific Drilling Program (CSDP) in drilling exploration core holes in the caldera. The knowledge of the caldera's history and volcanism has increased remarkably during this current period of research. As stated in *Goff & Gardner* [1988]: "Only in the last 5 years has it been possible to view the region as a dynamic, integrated magma-hydrothermal system having a complex evolution lasting more than 13 m.y."

The caldera is located in a section of the southwestern United States where four major tectonic provinces nearly meet. These are the Basin and Range, the Colorado Plateau, the Southern Rocky Mountains and the Great Plains. *Felch* [1987] has reviewed the crustal structure in each of these provinces. Since the structure is different in all four tectonic provinces, it is in general useful to have some knowledge of how the regional structure may affect seismic data recorded near the caldera. We did not consider regional effects in our data because the instruments were confined mainly within the caldera itself, and the major variations among sites on this scale should be due primarily to local structure.

Superimposed on this provincial setting are two additional tectonic features which intersect each other at the location of the Valles Caldera. These are the Rio Grande Rift and the Jemez Lineament. Figure 1.1 is a schematic map showing the general tectonic setting of Valles Caldera. The wedge-shaped Basin and Range Transition zone corresponds to a region where the tectonics are a mixture of features characteristic of the Rio Grande Rift, the Colorado Plateau and the true Basin and Range to the west.

The Rio Grande Rift is a classic example of active continental crustal rifting. It is a nearly linear feature characterized by crustal thinning beneath its axis, active extensional tectonics, low gravity, high heat flow and recent volcanism along much of its length. The surface expression of the rift is a very clearly defined series of grabens extending from central Colorado into southern New Mexico with vertical offsets as large as 6 km [*Baldrige et al.*, 1984]. The locally thinned crust beneath the rift is underlain by upper mantle material with anomalously low P-wave velocity [*Davis et al.*, 1984]. The wavelength of this anomaly is about 150 km, however, so

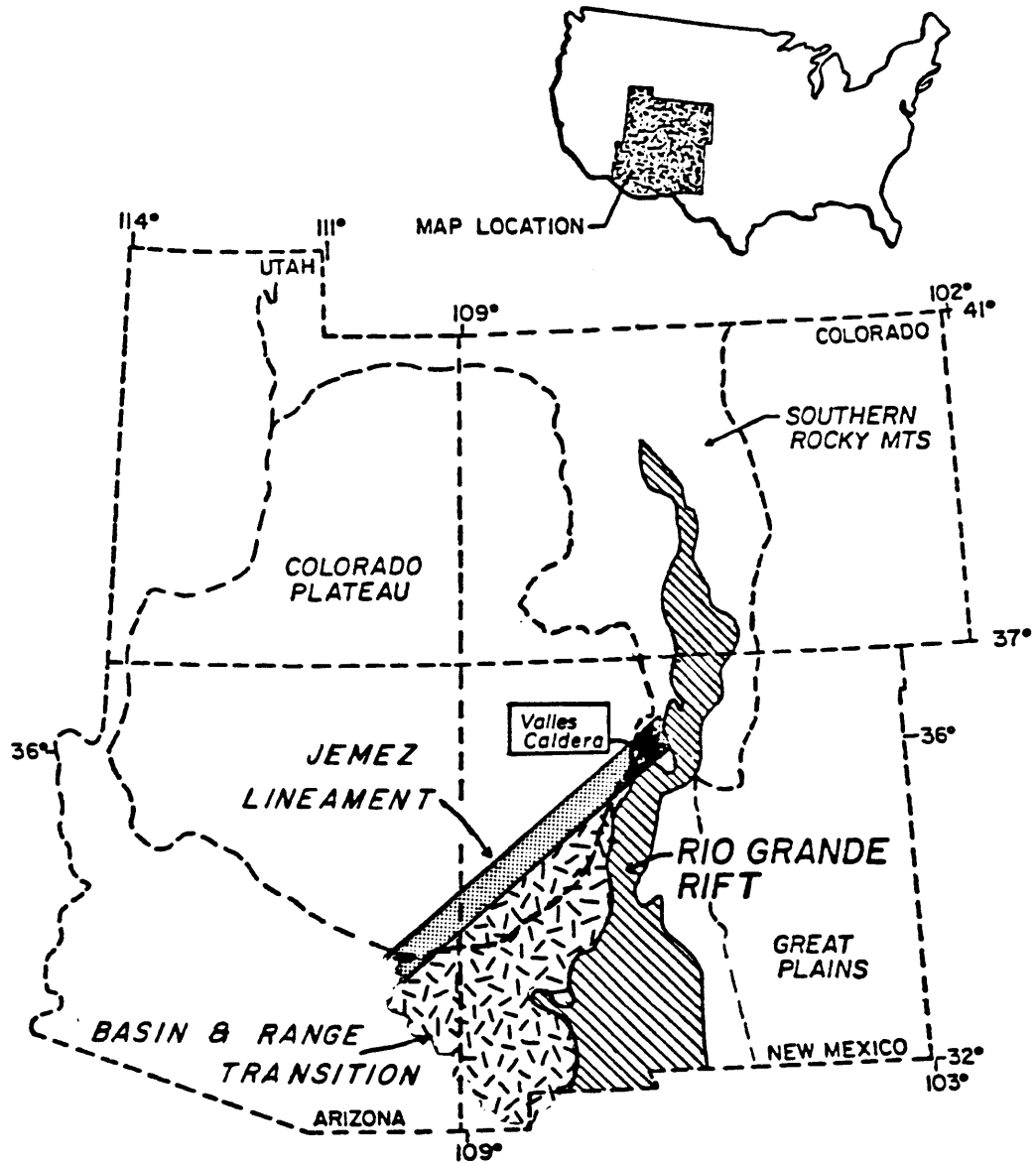


Figure 1.1 Map showing the tectonic setting of the Valles Caldera. The Basin and Range province is divided into the Rio Grande Rift and Basin and Range Transition sections. The Jemez Lineament continues eastward from the Valles Caldera. This figure is reproduced from *Felch* [1987] as modified from *Bridwell* [1976].

we should not see its effects on our seismic arrays, which had maximum apertures of 14 km and 32 km. The Valles Caldera lies on the western flank of the central portion of the rift, just north of the point where the rift takes a jog to the east.

The Jemez Lineament is a roughly northeast-trending tectonic feature passing through the southeastern Colorado Plateau and defined by a series of late Cenozoic volcanic fields. This trend extends from eastern Arizona to the Valles Caldera, where it then bends more eastward and tapers out after crossing the Rio Grande Rift. It appears to be linked to a region of weakness or a stress boundary in the Precambrian lithosphere [Aldrich & Laughlin, 1984; Aldrich, 1986], but the lineament cannot be attributed to a single fault or fracture zone or to some simple structural anomaly in the upper crust [Baldrige *et al.*, 1984]. In the vicinity of the Valles Caldera, the Jemez lineament is expressed clearly in the Jemez Fault Zone southeast of the caldera and in the apical graben slicing through the center of the resurgent dome. It is probably no coincidence that the Valles Caldera formed near the intersection of this feature with the Rio Grande Rift.

1.3 Formation and Evolution of the Valles Caldera

Caldera formation in the Jemez Volcanic Field occurred as two separate and distinct phases of Plinian ash and ignimbrite eruptions. The first occurred about 1.4 Ma, erupting about 200 km³ of material which formed the Guaje Pumice bed and the first, or Otowi, member of the Bandelier Tuff [Nielson & Hulen, 1984]. Rapid volumetric depletion of the silicic magma chamber caused collapse of the crustal block above it along pre-existing ring-fractures [Smith & Bailey, 1968], forming the Toledo Caldera. After a 300,000 year hiatus, renewed activation of the magma

chamber resulted in a repeat of the first cycle. The upper, or Tshirege, member of the Bandelier Tuff was erupted, preceded as before by a Plinian ash plume which deposited the Tsankawi Pumice at about 1.1 Ma. Subsequent collapse of the magma chamber formed the Valles Caldera (Figure 1.2). Until recently it was believed that the Toledo Caldera was a smaller feature located just northeast of the Valles Caldera. It is now known that the two calderas are approximately coincident [Goff *et al.*, 1984] and the obvious semi-circular depression to the northeast is now referred to as the Toledo Embayment.

After collapse of the Valles floor block and deposition of alluvial and volcanic caldera fill material, renewed magma rise caused the uplifting of the central caldera floor, creating the resurgent structure known as Redondo Dome. The dome is the dominant structural feature within the caldera, rising almost 1 km above the alluvial valleys surrounding it. It is riddled by a complex system of extensional fractures at its surface, which are dominated by a large longitudinal graben parallel to the Jemez Lineament. Following resurgent doming, volcanic activity continued in the caldera with the formation of a series of circumferential rhyolite domes beginning at about 1.04 Ma on the eastern ring fracture. Proceeding counterclockwise from this oldest post-resurgence dome, ages decrease steadily to about 0.5 Ma on the west and southwest ring fractures [Doell *et al.*, 1968]. The youngest erupted material, at 0.13 Ma, is the Banco Bonito Obsidian flow in the southeastern corner of the caldera [Self *et al.*, 1988].

The history of volcanic activity in the Jemez Volcanic Field, prior to the Toledo eruptions, dates back to earlier than 13 Ma [Gardner *et al.*, 1986]. The youngest eruptions which contributed to the major high peaks of the Jemez Mountains to

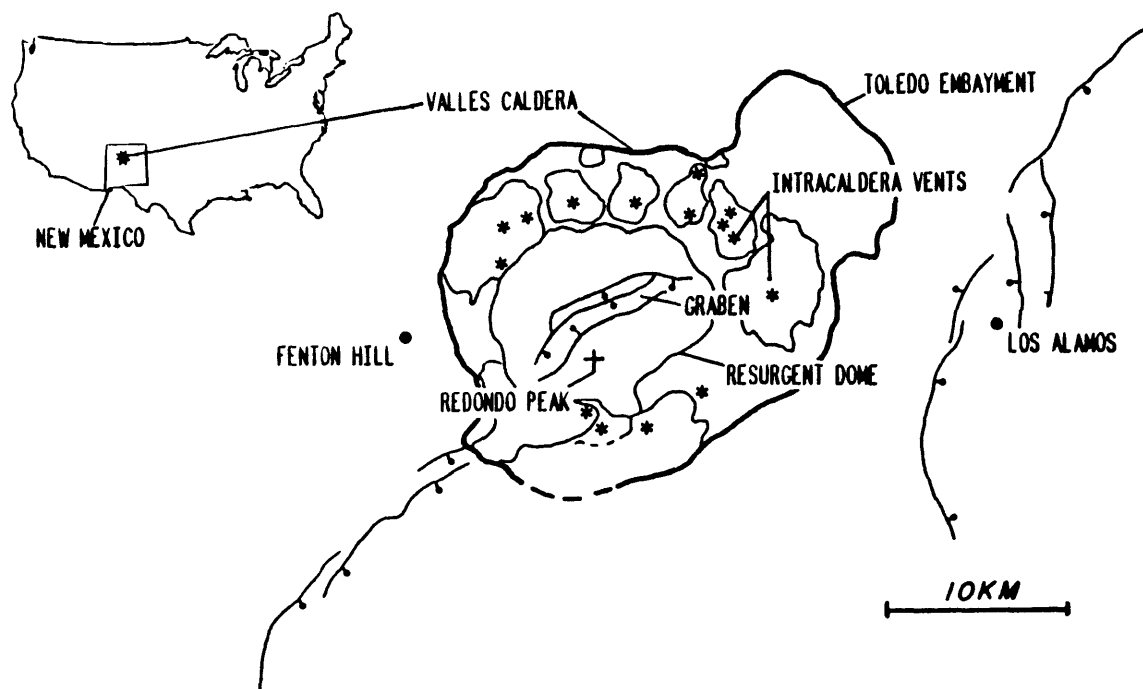


Figure 1.2 Schematic map showing location and major structural features of the Valles Caldera. The Jemez Fault Zone is shown to the southwest of the caldera, and the Pajarito Fault Zone is to the east, passing through Los Alamos. The Toledo Caldera is approximately coincident with the Valles Caldera. This figure is reproduced from *Felch* [1987].

the north and east of the caldera have ages of 7 to 2 Ma. The Toledo and Valles calderas were thus emplaced in the midst of an already well-developed and highly complex volcanic system. But, since our present study is entirely confined to the caldera vicinity, we will not be concerned with the surrounding volcanic setting in which it was formed. We will assume that the Bandelier events represent such major disruptions to the previous structure that, on the scale which we will be modeling, the features related solely to caldera formation should dominate.

Since the cessation of volcanic activity at about 0.13 Ma, the dominant behavior in the caldera has been hydrothermal activity and gradual cooling of the upper crust. However, there is evidence from temperature logs taken at the Fenton Hill drilling site that the age of heating at moderate depths within a few kilometers of the site is probably less than 40 ka [*Harrison et al.*, 1986]. The main implication here is that the second caldera-forming event of 1.1 Ma does not represent the most recent introduction of heat to the region. Any consideration of how long it would take for the Valles magma chamber to completely crystallize must take this into account. We will discuss this further in Chapter 6.

The complex hydrothermal system of the caldera and its immediate surroundings has been studied in detail by numerous investigators. *Goff & Grigsby* [1982] and *Truesdell & Janik* [1986] have suggested that hot fluid reservoirs may originate at depths in excess of 2 km near Redondo Dome. These studies were based primarily on deep exploration drilling near the dome and on the chemical compositions of fluid outflows. *Goff & Grigsby* [1982] estimated an average production depth, for a well near Redondo Dome, of about 1500 meters, with temperatures of 260° to 300° C, but they suggested that producing zones may also exist in the underlying

volcanics, sediments and Paleozoic formations. *Truesdell & Janik* [1986] have suggested that fluids may originate from parent sources in the Precambrian basement rocks. Figure 1.3 depicts a recent estimation for the size and configuration of the hydrothermal system along a SW-NE cross-section of the southwestern portion of the caldera and its surroundings. The presence of a large volume of fluid-saturated rock beneath Redondo Dome bears strong implications for the attenuation of seismic waves passing through this region. This will be discussed in Chapter 6.

We will see in Chapters 4 and 5 that the modeling of the caldera's sub-structure in terms of simple homogeneous components is a rather formidable undertaking, given the complex volcanic and tectonic history of the area. Fortunately we were able to reduce the number of free model parameters that we need to adjust by making use of existing detailed information concerning the near-surface structure beneath the central caldera locality. By combining stratigraphic information from a number of exploration wells with gravity profiles from *Segar* [1974] (reproduced in *Nielson & Hulen* [1984]), a cross-section of the near-surface structure down to the Precambrian granite basement was constructed by *Self et al.* [1986]. Figure 1.4 shows the cross-section they obtained. The drill hole data constrain the northwestern section extremely well, and this structure agrees with the gravity profile given in *Nielson & Hulen* [1984] for the same cross-section. The southeastern portion was constructed from the continuation of the same gravity profile, which indicates a significant low Bouguer anomaly in this area. There is thus a well-established trend of increasing depth to the Precambrian basement along this section.

In Chapter 2 we will see that the line we chose for our seismometer arrays was nearly coincident with the line A - B in Figure 1.4. In Chapters 4 and 5

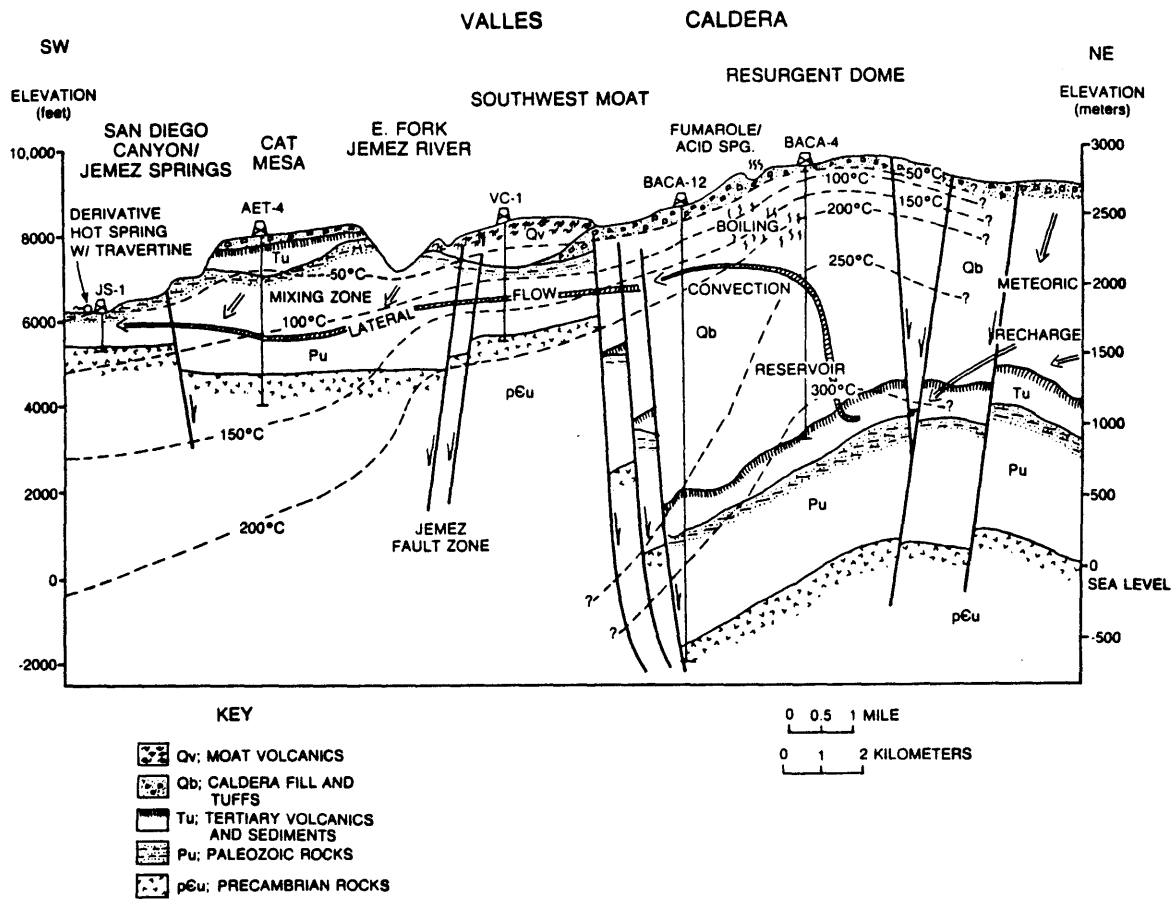


Figure 1.3 Cross-section through the southwestern portion of the Valles Caldera and surroundings, showing the estimated size and configuration of the Valles hydrothermal system. This figure is reproduced from *Goff et al.* [1989].

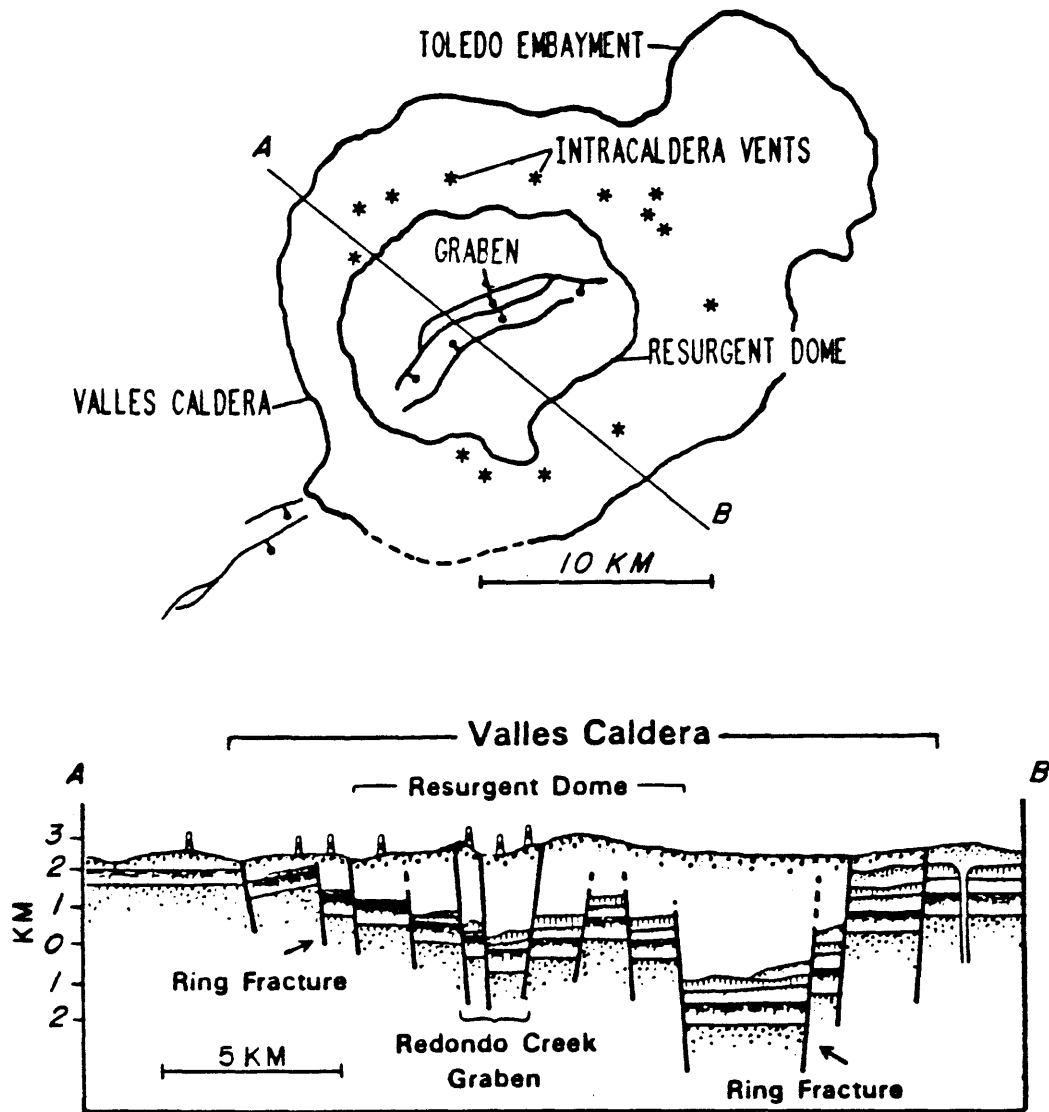


Figure 1.4 Cross-section through the central portion of the Valles Caldera (bottom) for section A-B shown in the top figure. The cross-section shows the complex shallow structure beneath the caldera, obtained from core hole data and gravity profiles. This figure is reproduced from *Felch* [1987], as modified from *Hulen & Nielson* [1986] (top) and *Self et al.* [1986] (bottom).

we will use this known structure to guide our initial modeling efforts. One of the few seismic surveys in the region, that of *Ankeny et al.* [1986], yielded average P-wave velocities for this surface layer in the range of 3.0 to 4.5 km/sec, and we will also use this a priori information in our initial models. We will see that the details of this a priori structural and velocity information is more important for removing predictable effects from observed P-wave delays across the caldera than for constraining model parameters based on the amplitude variations. This is because the cross-section in Figure 1.4 is more closely representative of the velocity structure than of the Q structure beneath the caldera. Thus, we will see that the two different types of data yield different types of best-fitting models. After presenting our models in Chapters 4 and 5, we will discuss their differences in some detail in Chapter 6.

CHAPTER 2

Data Collection and Processing

2.1 Field Experiments

The data used in this thesis were collected during the summer and fall of 1987. Six portable digital event recorders were used to record teleseismic earthquake signals along two array lines passing through the Valles Caldera. Both arrays used the same azimuth line but differed in the spacing of the six recorder sites. Figures 2.1a and 2.1b show both of these arrays on a schematic map view of the Jemez Mountains region with major topographic and structural features labelled. Figure 2.1a shows the site locations for array 1 and 2.1b shows array 2. A vertical cross-sectional view (looking northeast) of the surface topography across the array line (section A-A') is shown at the bottom of each array map with the six sites indicated. The topography profile was digitized from the USGS 7.5' quadrangle maps for the region, and elevations at each site were compared with altimeter readings taken in the field. The profile is referenced to an arbitrary zero-datum of 2290 meters elevation above sea-level. The vertical z -coordinates are given as depth (positive downward) relative to the zero-datum. The horizontal position axis shown will be used for the x -coordinates in the synthetic calculations in Chapter 5. This will require the definition of model structures over some fixed interval for the x -coordinate and, for reasons which will become clear in Chapter 3, we will use an interval of $x = 0$ to $x = 256$ km with x increasing from northwest to southeast. The caldera structure and free surface topography will be centered at $x = 128$ km and

SCHEMATIC MAP OF VALLES CALDERA AND SITE LOCATIONS FOR 1987 ARRAY 1

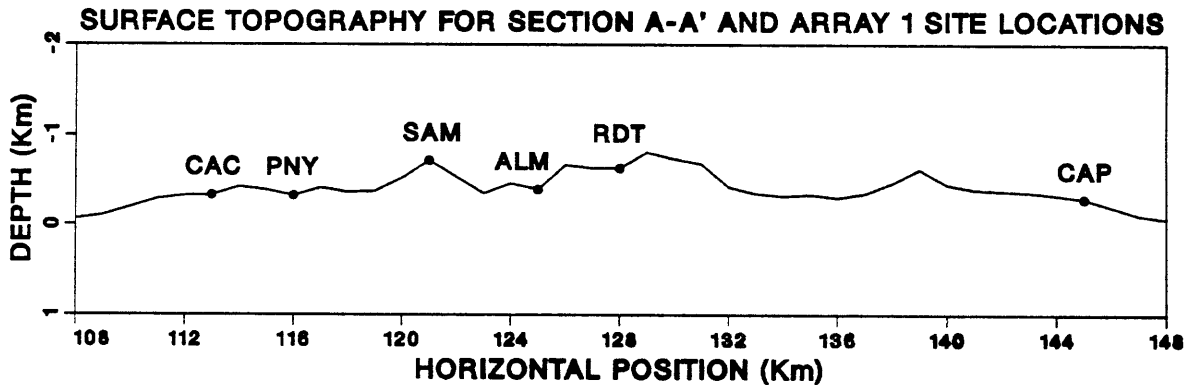
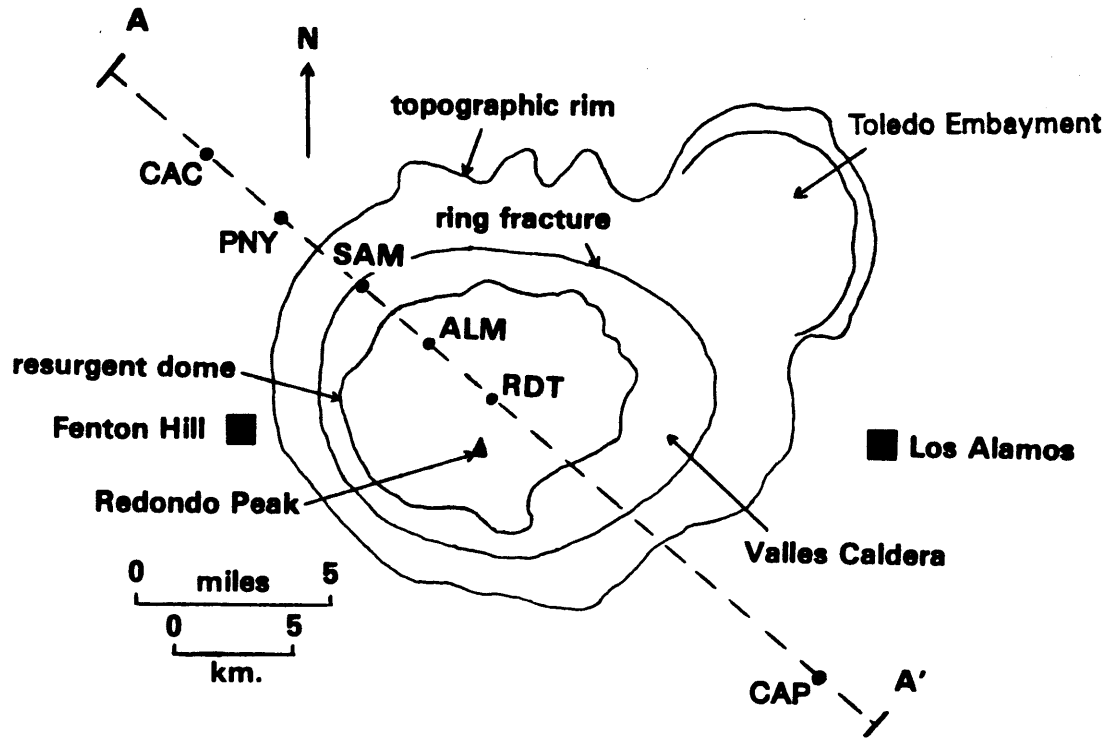


Figure 2.1a Schematic map (top), modified from *Nielson & Hulen* [1984], of Jemez Mountains study region in northern New Mexico showing major topographic and structural surface features of the Valles Caldera and seismometer deployment sites used in 1987 for array 1. Vertical cross-sectional view of digitized surface topography is shown at the bottom with the six sites indicated.

SCHEMATIC MAP OF VALLES CALDERA AND SITE LOCATIONS FOR 1987 ARRAY 2

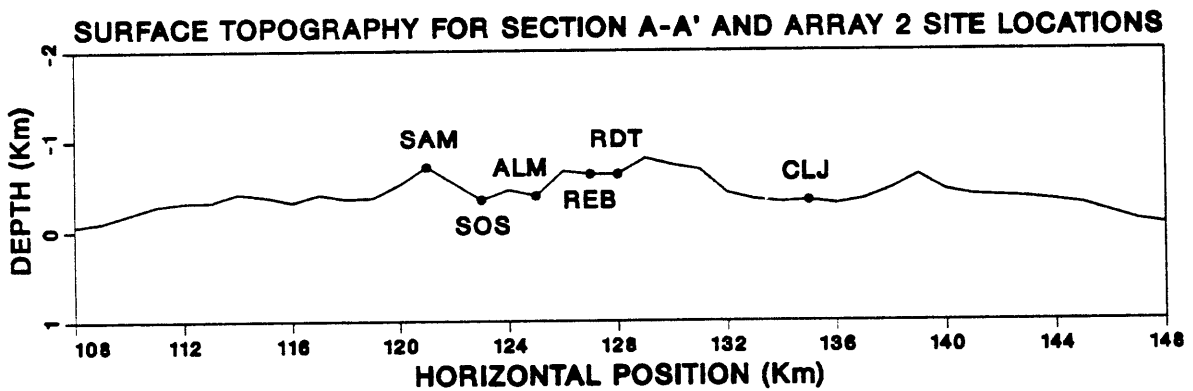
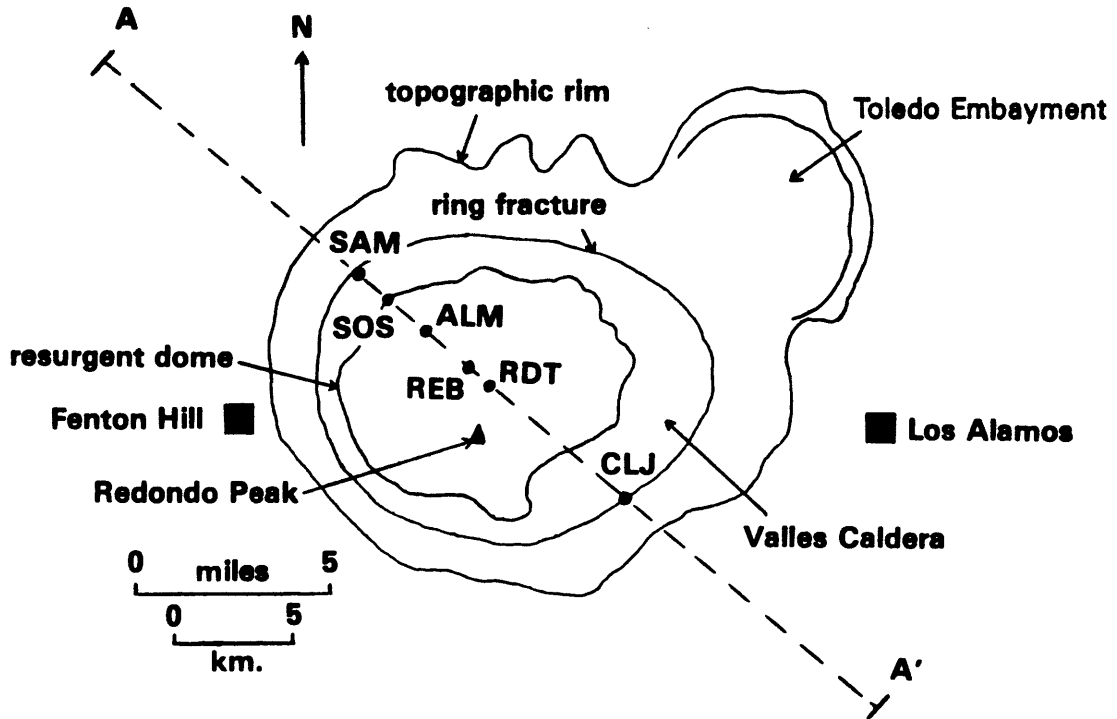


Figure 2.1b Same as Figure 2.1a except site locations shown are for array 2.

this will correspond to the site RDT. The aperture width for array 1, from CAC to CAP, was approximately 32 km and covers the range $x = 113$ to $x = 145$ km. For array 2 the aperture width, from SAM to CLJ, was approximately 14 km and covers the range $x = 121$ to $x = 135$ km, which spans the caldera's ring-fracture zone. Results of the synthetic modeling can be compared directly to the observed data by calculating the expected free-surface motion at x -coordinates corresponding to the site locations shown in Figures 2.1a and 2.1b.

Site coordinates, elevations and other information relevant to both arrays are listed in Table 2.1. The linear geometry was chosen with the intent of obtaining observations of amplitude and phase variations across the caldera which might be explained by anomalous upper crustal structure beneath the arrays. This choice of linear geometry was dictated primarily by the limited number of instruments available. It would be hopeless to attempt to characterize waveform variations due to 3-dimensional crustal structure with only six instruments. So our study here will be strictly limited to 2-dimensional models for the caldera structure within the vertical cross-section beneath the array lines. In order to minimize the effects of 3-dimensional structure in the data it is necessary to have the incident waves arriving along an azimuth nearly parallel to the trend of the array. For this reason the array azimuth was chosen to be approximately on line to seismically active regions to the northwest, such as Alaska, the Kuril Islands and Japan, and to South America to the southeast. We will consider only data from events that lie within $\sim \pm 20^\circ$ of the array azimuth. Rather than spacing the sites evenly across the aperture in each case, it was decided that it would be more useful to space them closely on one side of the caldera to obtain better spatial resolution. This is not unreasonable since

we expect to collect data for both positive and negative incidence angles and the caldera on a large scale may be assumed to be essentially axi-symmetric. The wide aperture array 1 was used to characterize variations on a regional scale with the hope that at least one of the two outer sites (CAC or CAP) would be relatively free of near-caldera effects. The narrow array 2 was used to observe the local variations within the ring-fracture zone of the caldera.

TABLE 2.1
Site Information for 1987 Jemez Field Experiments

Site Name	Instr #	Array #	Latitude (degrees)	Longitude (degrees)	Elevation (meters)	X-Position (km)
CAC	3	1	+35.987	-106.676	2617	113.0
PNY	6	1	+35.962	-106.651	2672	116.0
SAM	4	1 & 2	+35.932	-106.612	2965	121.0
SOS	3	2	+35.926	-106.596	2635	123.0
ALM	5	1 & 2	+35.915	-106.579	2678	125.0
REB	6	2	+35.901	-106.561	2916	127.0
RDT	2	1 & 2	+35.895	-106.552	2916	128.0
CLJ	1	2	+35.856	-106.493	2617	135.0
CAP	1	1	+35.799	-106.404	2562	145.0

There are two important reasons behind the need to use teleseismic data for this study. First, it is essential for the recorded waveforms to have sampled the deep structure beneath the caldera and this will be true only for steep incidence angles, θ_0 , which occur for teleseismic distances, i.e., $\Delta \gtrsim 20^\circ$. Secondly, we wish to restrict our attention here to only the large scale features, on the order of 1 km in scale-length or larger, and this requires the use of intermediate-period data which are very typical in large teleseismic events. The finer scale structure of the caldera is extremely complex, and it would be impossible to model higher frequency data with such limited instrument coverage. So we will only be concerned in this thesis

with steeply incident source waves, for which $|\theta_0| \lesssim 45^\circ$, and we will examine only the intermediate-period content of the data from 0.1 to 1.0 Hz.

The six instruments used for the field experiment were digital event-detecting recorders built nearly ten years ago at MIT. Since then, they have been used in numerous field studies, including a very successful experiment at Mount St. Helens in 1981. The equipment is described briefly in *Fehler & Chouet* [1982] and in *Fehler, Roberts & Fairbanks* [1988]. The instruments record 3-component seismic data, digitized at 240 samples per second, on 1/2 inch 9-track magnetic tape, with a maximum storage capacity of 3 hours. Analog voltage signals are recorded as 12-bit digital numbers, which gives a dynamic recording range of 72 db. The event detection circuit uses simple long-term and short-term averages. An event is detected when the short-term average of the rectified signal amplitude rises above the long-term average. Due to false triggering on spurious background noise, wind, thunder storms and wildlife disturbances, the tapes typically need to be changed every two weeks. Time is kept using a 5 MHz crystal oscillator as an internal frequency standard. The clocks typically will drift between 1.0 and 5.0 msec per day and, if checked regularly against an external time standard, the absolute timing of recorded signals can usually be obtained to within ± 10 msec, including the uncertainty due to the sampling interval. The instrument velocity amplitude response is flat up to ~ 50 Hz and decays sharply above this frequency due to the anti-aliasing filters. The flat portion of the response normally has a low-frequency cutoff at the natural frequency of the sensor and decays as ω^2 below this corner. The sensors used were 3-component geophones with a natural frequency of 1.0 Hz, and this makes the equipment ill-suited for recording intermediate-period signals. In fact,

an experiment similar to those described above was attempted with this instrument configuration in 1986 with very poor results. During three months of deployment in the caldera, only two teleseisms were recorded by all six instruments. This was due partly to the 1.0 Hz cutoff of the geophones and partly to the 3.0 to 5.0 Hz bandwidth setting used for the event detector circuitry, both of which made it very difficult to detect and trigger on small signals with dominant frequencies of 1.0 Hz and lower. To remedy this problem for the 1987 experiments, an equalization circuit was designed, built and installed in all six recorders in order to increase the signal level below 1.0 Hz. Also, the event detector bandwidth was shifted down in frequency to cover the range of 0.5 to 1.0 Hz. Briefly, the equalization circuit applies a gain boost to the geophone output signal. This boost is inversely proportional to the geophone rolloff below 1.0 Hz. The specific design used here successfully extended the flat portion of the instrument amplitude response curve down to 0.1 Hz. This circuit is described in detail in *Roberts* [1989, in press]. Since this paper is currently in press, it is included in this thesis as Appendix 2 for reference. As a result of these two instrument modifications, the 1987 experiment was much more successful than in 1986. During four months of operation, approximately 40 teleseisms were recorded on at least five instruments. From these, a total of 24 events were selected which fell close enough to the array line azimuth to be used here. Twelve of these were recorded on array 1 and the rest on array 2. Table 2.2 lists the locations, origin times and other relevant information for these 24 events. This information was obtained from the monthly NEIS listings (PDE) published by the U.S. Geological Survey.

TABLE 2.2
Information for Teleseismic Events Recorded in 1987 in the Jemez Mountains

Event Region	Origin Time (mo:dy:hr:mn:sec)	Latitude (degrees)	Longitude (degrees)	Depth (km)	m_b	# of Sites	Array #
Coast of Honshu	06:26:07:11:59.7	+37.086	+142.116	21	5.4	4	1
Coast of Oregon	06:27:06:01:36.7	+43.486	-127.094	10	5.2	6	1
Kuril Islands	07:08:22:56:02.7	+46.437	+149.558	152	5.4	5	1
Kommandorsky I.	07:10:18:49:53.9	+55.137	+165.525	33	6.1	6	1
Kuril Islands	07:11:05:13:15.1	+50.201	+156.278	75	5.4	5	1
Kommandorsky I.	07:11:14:52:27.5	+55.141	+165.496	33	5.3	6	1
Southern Peru	07:13:19:14:57.9	-15.332	-070.061	241	5.1	5	1
Sea of Okhotsk	07:14:23:46:03.5	+49.631	+147.828	576	5.7	5	1
South of Honshu	07:16:05:46:29.5	+33.059	+138.096	310	5.3	5	1
Kodiak Island	07:24:05:25:10.5	+56.231	-153.650	33	5.5	6	1
Coast of N. Calif.	07:31:23:56:58.0	+40.415	-124.407	16	5.6	6	1
Central Chile	08:04:15:04:40.0	-40.469	-073.189	38	5.9	6	1
Fox Islands	08:29:22:12:11.2	+52.840	-168.892	33	5.2	6	2
Jujuy, Argentina	09:01:04:26:07.4	-23.052	-066.529	199	6.0	6	2
Kuril Islands	09:04:04:27:08.8	+49.293	+156.410	33	5.9	6	2
Kuril Islands	09:06:15:27:22.4	+49.262	+156.266	43	5.7	6	2
Kuril Islands	09:08:13:35:16.1	+49.612	+156.360	83	5.6	6	2
Andreanof Islands	09:10:03:48:44.8	+51.931	-176.006	49	5.1	6	2
Northern Chile	09:11:00:34:52.1	-22.329	-068.384	130	5.4	5	2
Guatemala	09:13:11:20:52.2	+14.272	-089.979	123	5.1	6	2
Coast of Honshu	09:13:14:07:43.6	+39.429	+144.732	34	5.6	6	2
Chile-Argentina	09:13:20:08:51.6	-34.333	-069.971	10	5.8	5	2
Ecuador	09:22:13:43:37.6	-00.978	-078.050	10	6.1	6	2
Kuril Islands	09:23:07:15:43.2	+45.960	+149.519	131	5.9	6	2

Figure 2.2 shows the theoretical and measured response curves for the vertical channel of one of the six instruments with the equalization circuit installed. The theoretical curves were calculated using the transfer functions for all frequency-dependent circuits in the configuration. The top of this figure shows the voltage amplitude response one would observe at the instrument output, with the system gain set to unity, for an input ground velocity of $1/G$ (cm/sec), where G is the geophone sensitivity in volts/cm/sec. The bottom plots show the corresponding phase response. The measured curves were obtained from the Fourier transform of a recorded input step in acceleration to the geophone's calibration coil. Due to noise contamination the measured curves are plotted only up to 3.0 Hz, which is adequate for the low frequency study in this thesis. The measured amplitude response has been normalized to unity at $f = 0.2$ Hz for comparison with the theoretical curve. More details on this are given in *Roberts* [1989] (Appendix 2).

We will not be concerned with absolute measurements of ground velocity in this thesis because we only need to deal with spectral amplitude ratios throughout. So the normalized response shown in Figure 2.2 is adequate since we only need to know the relative differences in response among all six instruments up to ~ 1.0 Hz. In fact, we do not even need to know the shape of the individual response curves to accomplish this. Figure 2.2 is shown here only to demonstrate the extended bandwidth of the instruments down to 0.1 Hz and that the actual response of at least one instrument agrees well with the theoretical response. Similar measured curves were also obtained for the two horizontal channels. To obtain the relative instrument corrections a huddle test experiment was performed with all six instruments installed at a common site. This is described in detail in the next section.

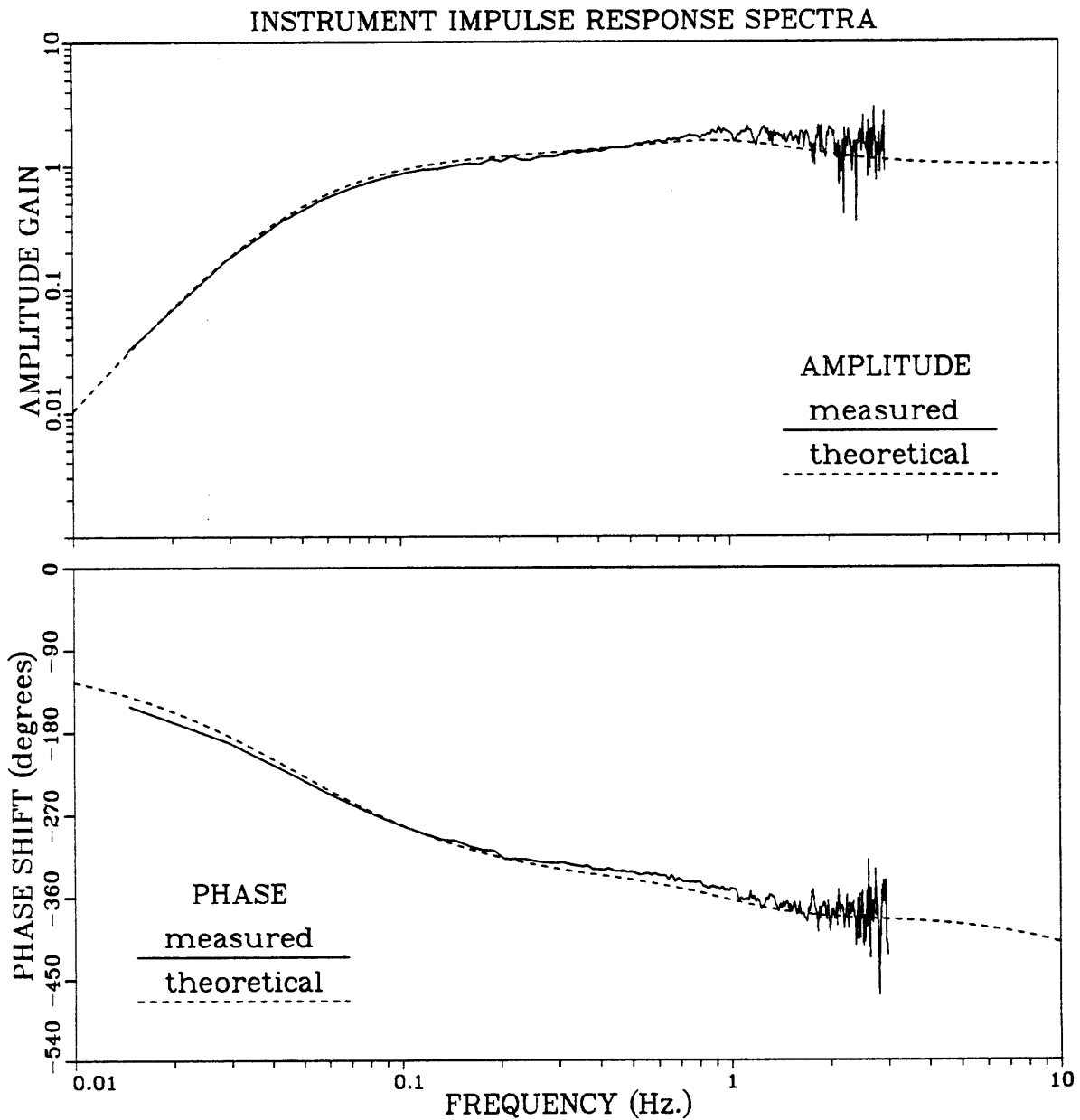


Figure 2.2 Measured and theoretical instrument response curves for the extended-bandwidth instruments used in 1987. Solid lines show the measured response obtained from a recorded step-acceleration input signal to the geophone calibration coil. Dashed lines show the theoretical response calculated from the relevant system component transfer functions. Top figure shows amplitude response and bottom shows phase response.

The nine sites used in 1987 were chosen carefully for their location and quality. The two most important criteria for site selection were, first, to keep all instruments lying as close as possible to the azimuth line and, secondly, to make sure that these sites were installed on hard rock to minimize the chances of anomalous site effects. This second criterion is less important than it would be for a higher frequency study in terms of site effects, but it is always desirable to obtain the best coupling possible between the ground and the geophones. So hard rock sites were considered to have higher priority over precise location. The spacing between successive instruments was considered less important because the method used here for modeling amplitude can be solved for any arbitrary location along the array line. Fortunately the caldera and its surroundings are well serviced by a system of dirt access roads, and suitable rock outcroppings are easily come by. Site reconnaissance and instrument installation for array 1 were completed in two days in mid-June. After two months of operation, the outer three sites, CAC, PNY and CAP, were moved inside the caldera to SOS, REB and CLJ for the remainder of the field season, which ended in mid-October. The remaining three sites, SAM, ALM and RDT were common to both arrays.

The two ring fracture sites, SAM and CLJ, were located on rhyolitic domes. The sites outside the caldera were on very densely welded Bandelier tuff. The remaining four sites were on the central resurgent dome on rock outcrops of similar hardness as the ring fracture sites. Since the quality of all nine site installations was similar and since we will be looking only at frequencies below 1.0 Hz, any observed amplitude variations across the caldera for a given event should be attributable

mainly to large-scale sub-surface structural anomalies rather than to small-scale near-surface site effects.

2.2 Data Quality and Instrument Correction

Before reducing the observed time series to a form which may be reliably interpreted in terms of modeling results, the data must be inspected and corrected for contaminating effects which are not relevant to the particular study at hand but which may influence the analysis results. The two most common forms of data contamination are caused by the instrument response and noise. In many types of seismic studies an accurate knowledge of the absolute instrument response is of paramount importance for avoiding erroneous interpretation of data. Because of this, there has been a steady increase over the years in the sophistication of instrument calibration methods [e.g., *Sauter & Dorman*, 1986]. Often, though, much simpler methods may be employed, depending on the type of experiment being performed and on the frequency band being considered. Most instrumentation experts flatly shun the step acceleration test used here to obtain the measured response curves in Figure 2.2. This is because the equivalent velocity input for this type of signal has an amplitude spectrum which decays as ω^{-2} and thus is a poor test signal for obtaining the response at higher frequencies in the presence of background noise. On the other hand, this method is clearly adequate for frequencies around 1.0 Hz or lower, as evidenced by Figure 2.2. We mentioned further in the last section that the absolute response of each instrument is not required when spectral ratios are being used. The differences in the responses of all instruments relative to one reference

instrument are all that are needed in this case. This allows all spectra to be corrected so that they will appear as if they were recorded by the reference instrument. The response of the reference instrument will then be removed by forming spectral ratios as described in Section 2.4.

The relative instrument response corrections were obtained by performing a so-called huddle test. This is a very simple and effective means for removing the instrument response from the observations and has been used successfully in the past by other investigators such as *Bard & Tucker* [1985]. The idea is to install all instruments at the same location with the geophones placed closely together and wait until all have recorded a seismic event having a frequency content in the range of interest. Then for each component of motion the Fourier spectra are computed and complex spectral ratios are calculated relative to one chosen reference instrument. These spectral ratios can then be used to correct the spectra of any other event recorded on the other instruments. Let us write the (complex) Fourier Transform of recorded data for a single component of motion as a combination of a source factor, receiver function, additive background noise and instrument response:

$$D_{jk}(\omega) = [S_j(\omega) \cdot R_k(\omega) + N_{jk}(\omega)] \cdot I_k(\omega), \quad (2.1)$$

where: j = source index, k = site and instrument index, D_{jk} = recorded data for event j at site k , S_j = source factor for event j , R_k = receiver function for site k , I_k = instrument response for site k and N_{jk} = additive background noise at site k at the time when event j was recorded.

Ultimately we wish to isolate R_k from the data by removing the source and instrument effects and reducing the noise through averaging. For the moment we

wish only to demonstrate how to remove the instrument response. Clearly, any data recorded by all six instruments in a huddle test will share the same source, receiver and background noise effects, $S(\omega)$, $R(\omega)$ and $N(\omega)$. The relative instrument corrections, $C_k(\omega)$, may be obtained simply by forming the ratios of the spectrum for one reference instrument divided by all of the rest. Using $k = 1$ as the reference instrument we can write:

$$C_k(\omega) = \frac{D_{j1}(\omega)}{D_{jk}(\omega)} = \frac{I_1(\omega)}{I_k(\omega)}. \quad (2.2)$$

Then, for the Jemez data, we can replace all instrument response functions with that of the reference instrument using the huddle test ratios above and then write the resulting corrected spectra as:

$$D'_{jk}(\omega) = D_{jk}(\omega) \cdot C_k(\omega) = [S_j(\omega) \cdot R_k(\omega) + N_{jk}(\omega)] \cdot I_1(\omega). \quad (2.3)$$

Now, all corrected spectra will share the same instrument response and this clearly will be removed in any spectral ratios formed using D'_{jk} for different sites or events.

Figure 2.3 shows the 3-component huddle test results for the instrument amplitude response corrections, $\|C_k\|$, that will be used throughout this thesis. Figure 2.4 shows the corresponding phase corrections, $\arg[C_k]$. The data used were for a magnitude $m_b = 6.2$ earthquake from California. The recorded time series were all windowed beginning at the same absolute time and the window width used was 34.133 secs. These plots show the corrections only for the 0.2 to 1.0 Hz frequency band that will be used in the modeling. Instrument # 1 was used as the reference and thus its amplitude correction is unity for all frequencies and its phase correction is zero. These plots show maximum variations in amplitude response, relative to

RELATIVE INSTRUMENT CORRECTIONS FROM HUDDLE TEST

REFERENCE INSTRUMENT: # 1

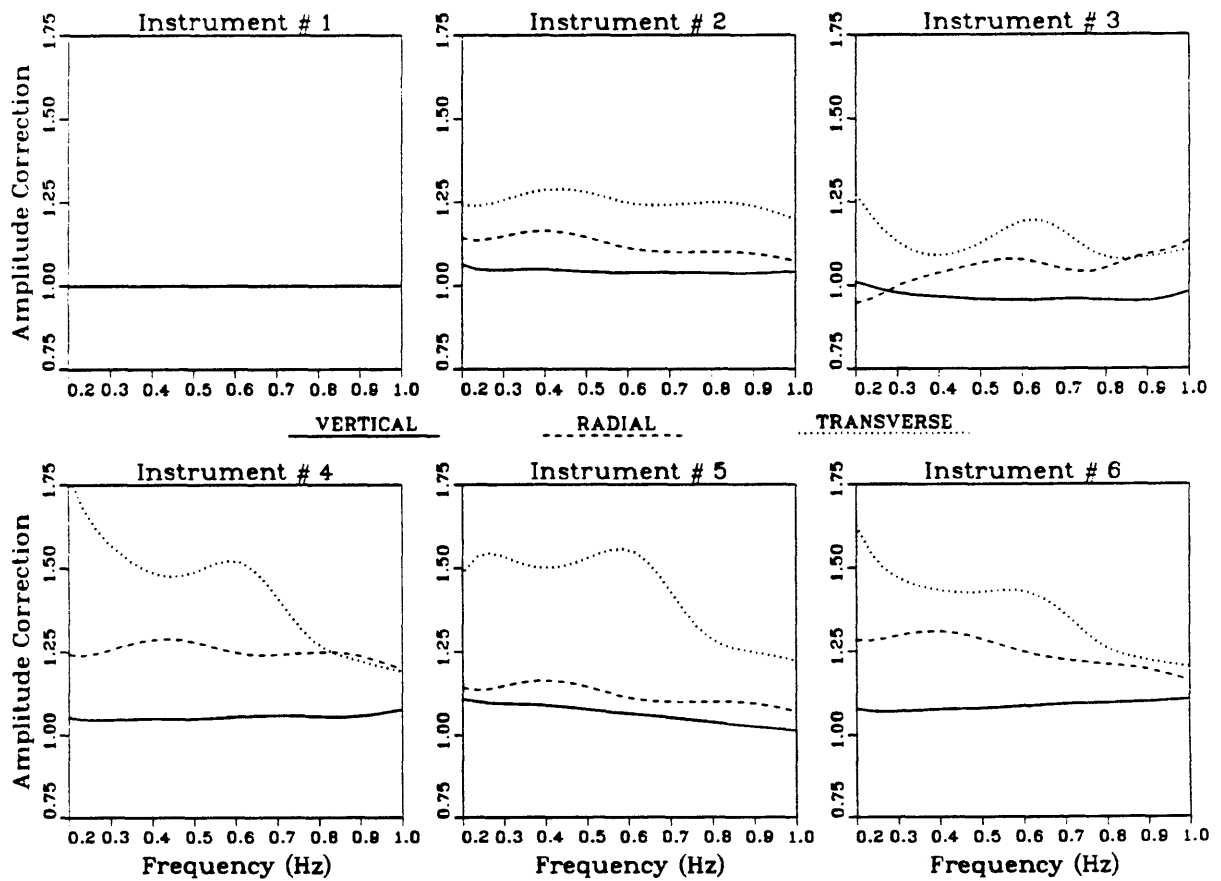


Figure 2.3 Relative instrument corrections for spectral amplitudes obtained from huddle test for 0.2 to 1.0 Hz. Instrument # 1 was used for the reference.

RELATIVE INSTRUMENT CORRECTIONS FROM HUDDLE TEST

REFERENCE INSTRUMENT: # 1

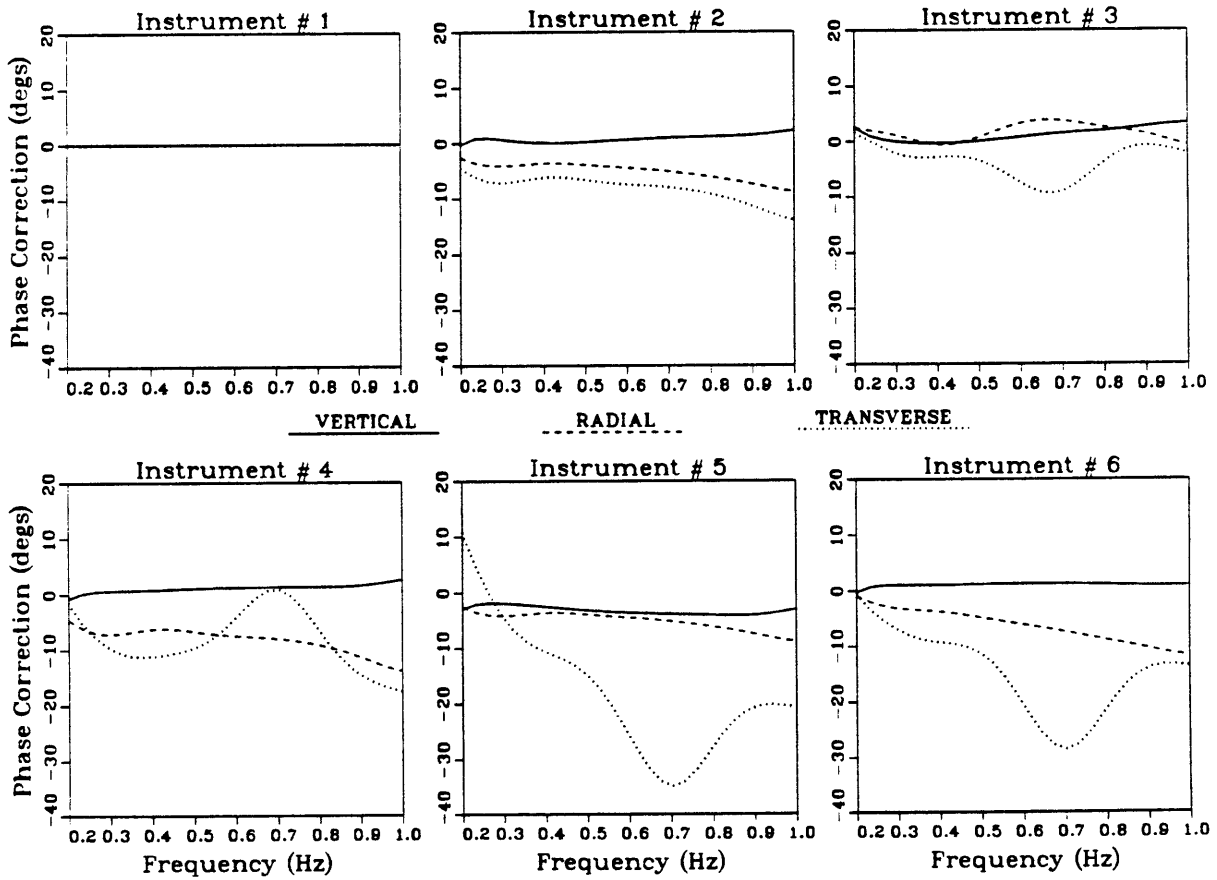


Figure 2.4 Relative instrument corrections for phase difference obtained from huddle test.

instrument # 1, of $\lesssim 10\%$ for the vertical component, $\sim 25\%$ for the radial, and $\sim 50\%$ for the transverse. The maximum phase correction for the vertical component is $\ll \pm 10^\circ$, $\sim -10^\circ$ for the radial, and $\sim -30^\circ$ for the transverse. Notice that the transverse components are significantly worse than the vertical or radial. Inspection of the seismograms and spectra for the transverse component revealed that the signal level was much smaller than for the vertical or radial components. This was due to the orientation of the geophones used for the huddle test, which happened to be aligned nearly on-azimuth for the event used. Thus the larger errors in the transverse component are probably due mainly to instrument noise in the equalization circuit, since the largest differences among the instruments occur at lower frequencies. Fortunately we will not be using the transverse components in the modeling, so we will not worry about these huddle test results here. The vertical and radial components are clearly more trustworthy. We will, however, be showing amplitude ratios for the transverse component to demonstrate that the observed pattern is similar for all three components. So we must bear in mind that the transverse ratios for data recorded on instruments 4, 5 and 6 are probably smaller, relative to instrument 1, than they will appear to be, since the signals recorded in the Valles Caldera for this component were at least as large as for the other two components, and the system noise was probably not as significant as it was for the huddle test.

Before the instrument corrections are applied, the raw data must be examined very carefully to ensure their suitability for analysis. First, one must make sure that all sites recorded the same signal. It is also preferable, but not critical, that the first motion is recorded clearly at all sites. Secondly, one must recognize and

deal with various forms of spurious noise. These types of transient noise include wildlife disturbances (most commonly elk stampedes and foraging bears in the Valles Caldera), logging trucks passing nearby, oceanic tremor or wind noise and electronic glitches or recording dropouts. For digital data, glitches and dropouts are usually the most prevalent form of noise, but there were several situations in 1987 where a teleseism was recorded while an elk herd or a log truck were also passing by. Fortunately, recording glitches can be removed rather easily since they usually occur as isolated samples in the signal. Animal noise is harder to remove because it usually persists through an entire recording and consists of a large number of closely spaced high-amplitude spikes, corresponding to hooves hitting the ground or paws hitting the instrument. In some cases the animal noise is of high enough frequency content not to have a devastating effect on the data spectra below 1.0 Hz. But usually it is not worth the risk of using such data, especially if enough other useful events have been recorded clearly. Log truck noise is by far the worst form of noise and renders any recording completely worthless. This is due mainly to the large amount of energy a fully loaded log truck on a bumpy, dirt road can put into the ground, as compared to a teleseismic signal. Even at distances up to 1 or 2 km a log truck can completely saturate the recording if the instrument gain is high enough. So these recordings are routinely discarded.

It is somewhat odd to note that such a mundane phenomenon as digital glitches continues to hound instrumentation and data analysis experts to this day. Over the years several clever methods have been developed which attempt to remove glitches from digital data automatically. One of the more successful methods is the running median filter technique of *Evans* [1981]. However, we know of no one

single automatic method which works perfectly under all circumstances. It is always necessary to re-inspect the data afterwards to see if any glitches were missed and, more importantly, if the data have been degraded in some way by the de-glitching process itself. Weighing all of these issues against the rather modest volume of data collected, we decided to avoid all automatic methods and remove glitches manually, using an interactive graphics program written explicitly for this purpose. This approach is clearly very tedious and time-consuming but in the end yields meticulously appraised data of the highest possible quality.

The final type of noise that we will address here occurs at the low end of the frequency band and is caused by two phenomena that can be attributed to weather conditions. These are oceanic tremor and long-period wind noise. Oceanic tremor should be familiar to readers of *Aki & Richards* [1980] and is manifested in seismic recordings as stationary sinusoidal oscillations at frequencies around 0.07 and 0.14 Hz. It is believed to be generated by ocean wave action and its amplitude as observed on continents correlates well with periods of calm or storms at sea and with distance from the recording site to the nearest ocean. Long-period wind noise, on the other hand, appears to be caused by cyclical wind interaction with large, tall trees and, at various sites used in 1987, had periods of about 10 to 20 secs. This appraisal is based on numerous personal observations made on-site while watching the instrument signal outputs on an oscilloscope. Good correlation was observed between the noise cycles in the signal, changes in wind strength and the motion of the largest trees. Typically this type of noise is less monotonic and more site-dependent than ocean tremor, so it is usually possible to discern the two in recorded signals.

Since we are interested in low frequencies in this thesis it is very important to either remove the long-period noise or at least use it to limit the low end of the usable frequency band for the teleseismic data. Long-period noise can be removed from a signal either by high-pass filtering or by subtracting a running amplitude average from the signal. The running average method is preferable in this case because, if used with care, it will only remove additive trends from the recorded signal. This is usually how ocean tremor and wind noise manifest themselves. The useful teleseismic signal will be seen superimposed on a clearly separate and distinguishable noise signal. If the noise signal is reasonably stationary and monotonic, then it is almost always possible to calculate a running average of the original signal which adequately represents only the smooth additive long-period noise component. This will be true, however, only if the width of the averaging window used is large enough not to affect higher frequency components of the teleseismic signal. Typically one should choose the window width to be at least half the period of the lowest frequency desired. The increment between successive windows should be narrow enough to produce a smooth average versus time. Throughout this thesis we will use a window width of 5 secs and an increment between windows of 1 sec. This will leave frequencies of 0.2 Hz and higher relatively unaffected and will adequately remove any additive signals with frequencies below 0.2 Hz.

Figure 2.5 shows one example of the running average procedure performed on a vertical component seismogram for an event from the Andreanof Islands, recorded at site SOS. The original seismogram at the top of the figure contains a large additive long-period wind noise signal. We believe this signal is not oceanic tremor because it was not present at any other site when this event was recorded. The seismogram

EXAMPLE OF LONG-PERIOD NOISE REMOVAL USING THE RUNNING-AVERAGE METHOD

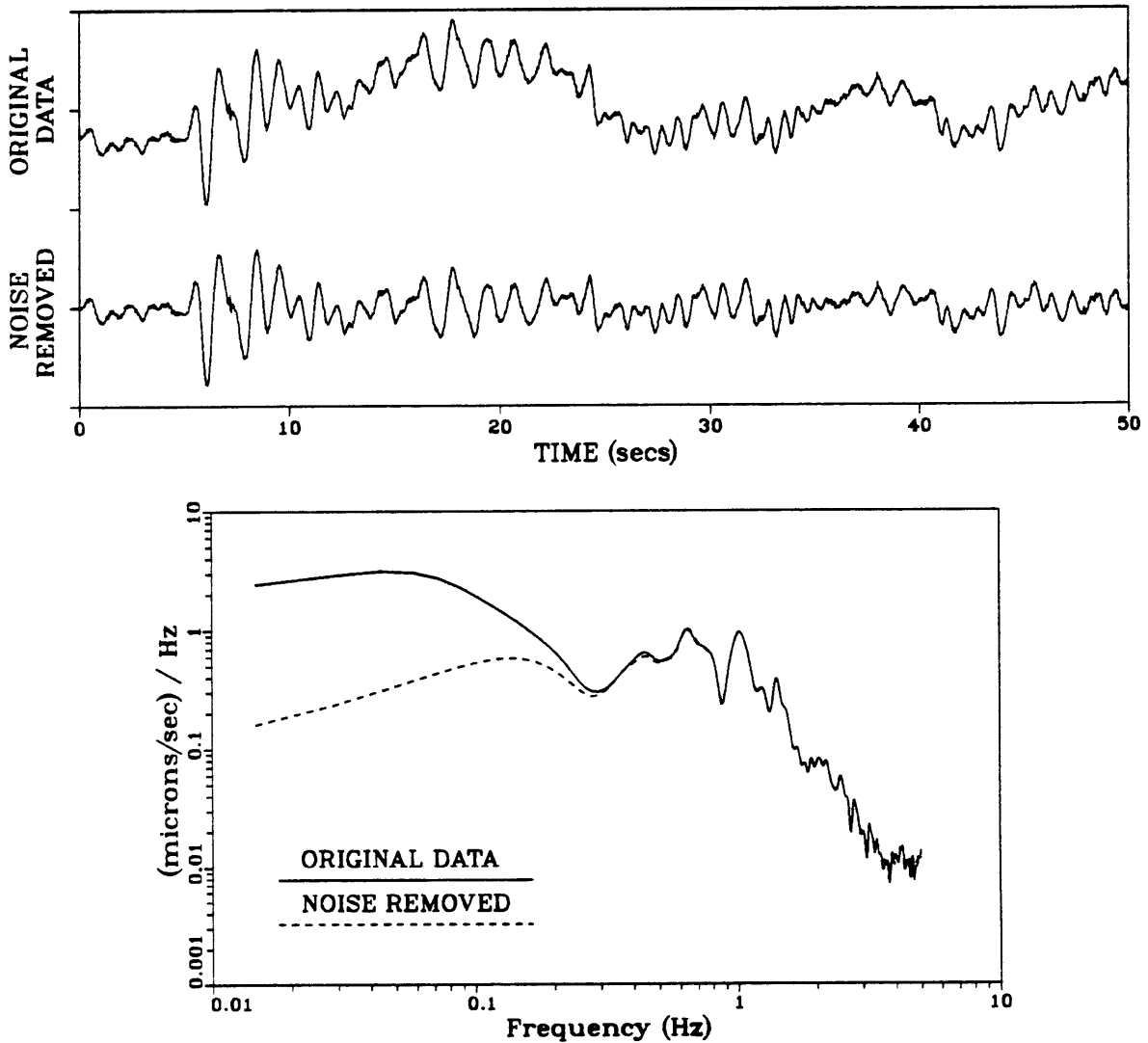


Figure 2.5 Example of long-period additive noise removed by the running-average method. Vertical component data are shown for an event from the Andreanof Islands recorded at site SOS. Top figure shows the original seismogram containing a large noise component caused by wind interaction with trees and the same signal after subtracting a 5.0 sec running average incremented by 1.0 sec intervals. The amplitude spectrum for each seismogram is plotted in the bottom of the figure. The major effect on the spectrum is a reduction in amplitude for frequencies below 0.2 Hz.

below this is the same signal after subtracting a running 5 sec average from it. The uncorrected velocity amplitude spectrum for each is plotted in the bottom of the figure to demonstrate that the only major changes in spectral content occur below 0.2 Hz.

The various types of noise discussed in this section can be easily recognized by visual inspection of the seismograms, primarily because they contain large frequency components well outside the dominant frequency band of the recorded teleseismic signal. All recorded data were examined for these noise types and treated accordingly before being used in the spectral analysis. However, it still remains to examine the ambient background noise within the dominant band of frequencies that we wish to use in the analysis. This is discussed in the next section.

2.3 Recorded Seismograms and Signal-to-Noise Estimation

Of the 12 events listed in Table 2.2 for array 1, only 6 were recorded at all six sites. Two of these 6 events had problems with either signal clipping or log truck noise at one site. The 4 remaining events were all from the northwest, so we have no complete 6-site amplitude observations for any southeastern events on array 1. On array 2, however, 10 of the 12 events listed were recorded on all 6 instruments and 3 of these were from the southeast. So the data from array 2 are much more complete than for array 1 in terms of site and azimuth coverage. Also, the closer spacing and more localized caldera coverage of array 2 is more desirable than the wider aperture of array 1 because this allows our modeling efforts to be confined to a smaller area around the caldera. For these two main reasons we will focus attention for modeling amplitudes much more on the data from array 2 than array

1. We will, however, consider as many data as possible from both arrays to see if any stable systematic patterns may exist as functions of incidence angle, azimuth and site location.

Figures 2.6 through 2.11 show some examples of 3-component seismograms recorded in 1987. Each figure shows one event recorded at all six sites for either array 2 (Figures 2.6 through 2.9) or array 1 (Figures 2.10 and 2.11). For each event the traces all begin at the same absolute time and are plotted on identical amplitude scales for comparison. The length of all plots is 34.133 secs and corresponds to the time window we will use to compute Fourier Transforms. Positive motion for the vertical components is upward. The horizontal components are rotated so that radial is parallel to the array line azimuth and positive motion is to the southeast for radial and to the northeast for transverse. In most cases the array azimuth is within $\pm 10^\circ$ of the true radial direction for northwestern events. Obviously the horizontal components for southeastern events are inverted relative to the true radial.

Figure 2.6 shows P-wave seismograms for a magnitude $m_b = 5.1$ event from the Andean Islands recorded on array 2. The epicentral distance is 5600 km, or $\Delta = 51^\circ$, and using tables from *Richter* [1958], the incidence angle is $\theta_0 \approx +24^\circ$. The convention for incidence angles used throughout this thesis is that positive angles correspond to waves arriving from the northwest and negative angles from the southeast. Figure 2.7 shows seismograms for a magnitude 6.0 event from Jujuy, Argentina with $\Delta = 70^\circ$ and $\theta_0 \approx -21^\circ$. Already, by comparing these first two events, two very clear patterns begin to emerge which are independent of the event direction. First, the horizontal components are very large for the long train of scattered waves following the first arrival and are often larger than the vertical.

EVENT REGION: ANDREANOF ISLANDS $M_b = 5.1$
 ORIGIN TIME: 1987/09/10 03:48:44.800 $\Delta = 51^\circ$
 START TIME: 1987/09/10 03:57:52.858 $V_{max} = 3.3880$ microns/sec
 UNFILTERED

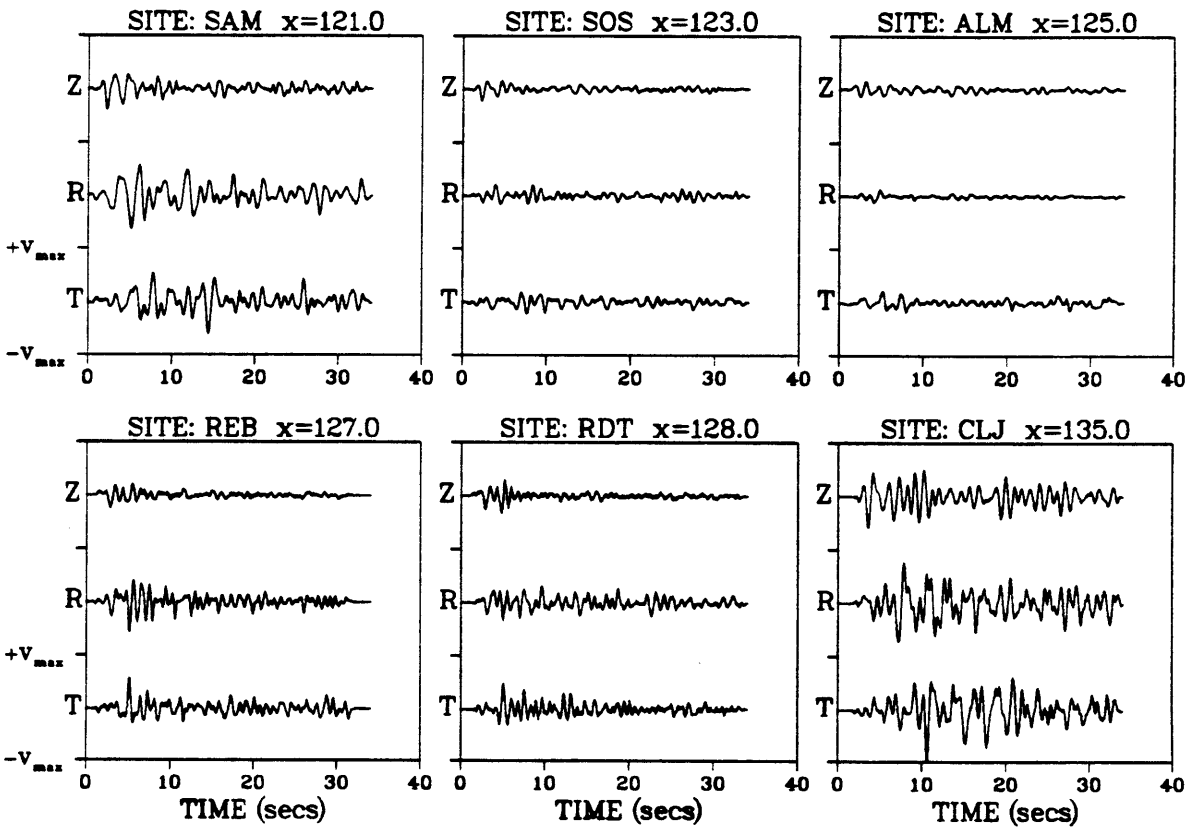


Figure 2.6 Seismograms for an Andreanof Islands event recorded on array 2. Distance and origin time of event are listed at the top. Also listed at top is the time at which all plots begin and the maximum velocity to which all plots are scaled. This amplitude scale is indicated on the two leftmost plots. Site codes and horizontal positions are indicated above each 3-component plot.

EVENT REGION: JUJUY, ARGENTINA $M_b = 6.0$
ORIGIN TIME: 1987/09/01 04:26:07.400 $\Delta = 70^\circ$
START TIME: 1987/09/01 04:36:56.448 $V_{max} = 26.6749$ microns/sec
UNFILTERED

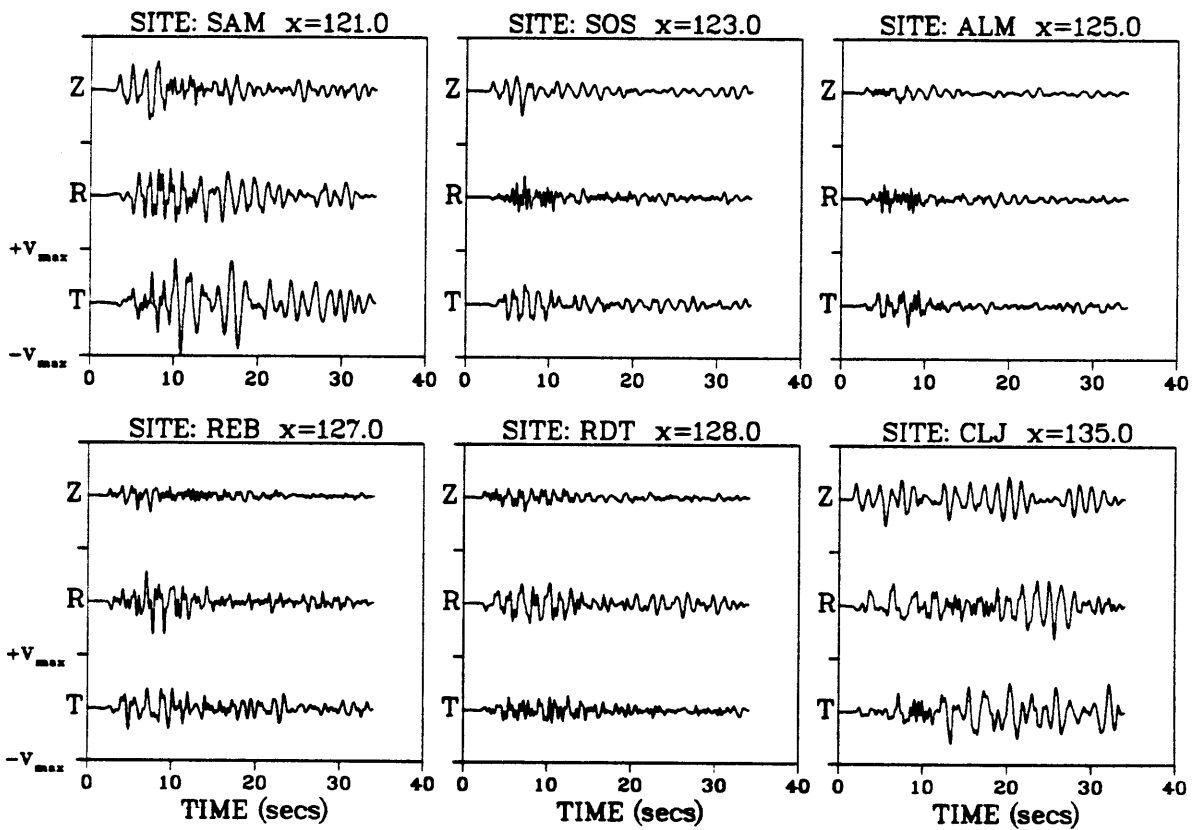


Figure 2.7 Seismograms for a Jujuy, Argentina event recorded on array 2.

EVENT REGION: HONSHU, JAPAN $M_b = 5.6$
ORIGIN TIME: 1987/09/13 14:07:43.600 $\Delta = 80^\circ$
START TIME: 1987/09/13 14:19:52.702 $V_{max} = 3.4534$ microns/sec
UNFILTERED

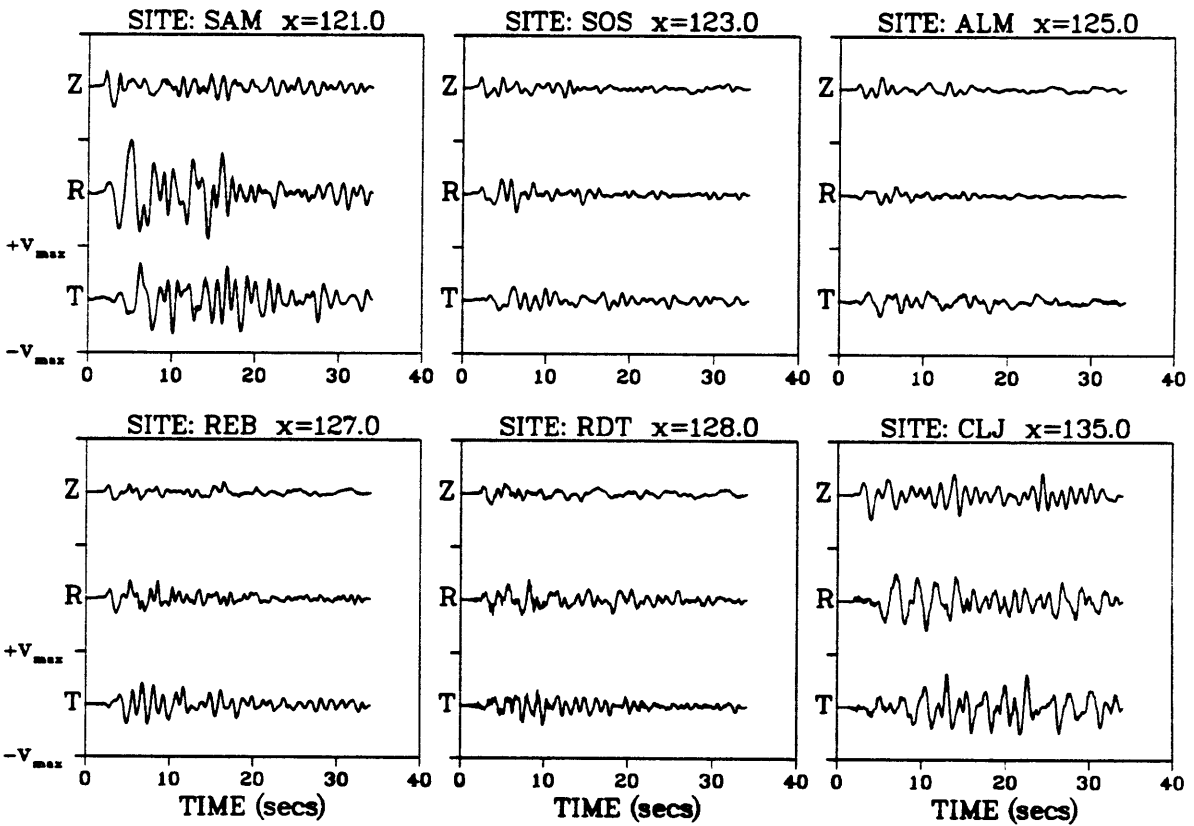


Figure 2.8 Seismograms for a Honshu, Japan event recorded on array 2.

EVENT REGION: ECUADOR $M_b = 6.1$
 ORIGIN TIME: 1987/09/22 13:43:37.600 $\Delta = 45^\circ$
 START TIME: 1987/09/22 13:51:56.528 $V_{max} = 13.0357$ microns/sec
 UNFILTERED

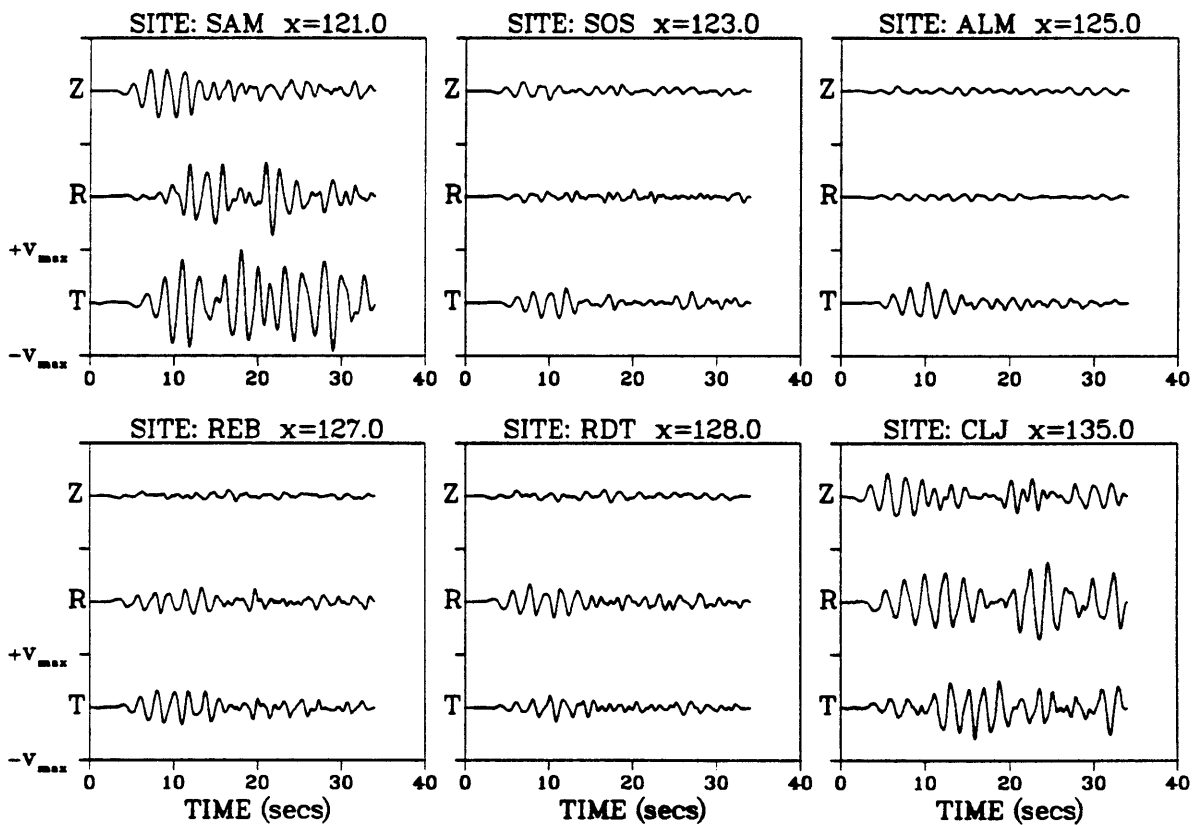


Figure 2.9 Seismograms for an Ecuador event recorded on array 2.

EVENT REGION: KOMMANDORSKY ISLANDS $M_b = 6.1$
ORIGIN TIME: 1987/07/10 18:49:53.900 $\Delta = 60^\circ$
START TIME: 1987/07/10 18:59:58.867 $V_{max} = 26.5440$ microns/sec
UNFILTERED

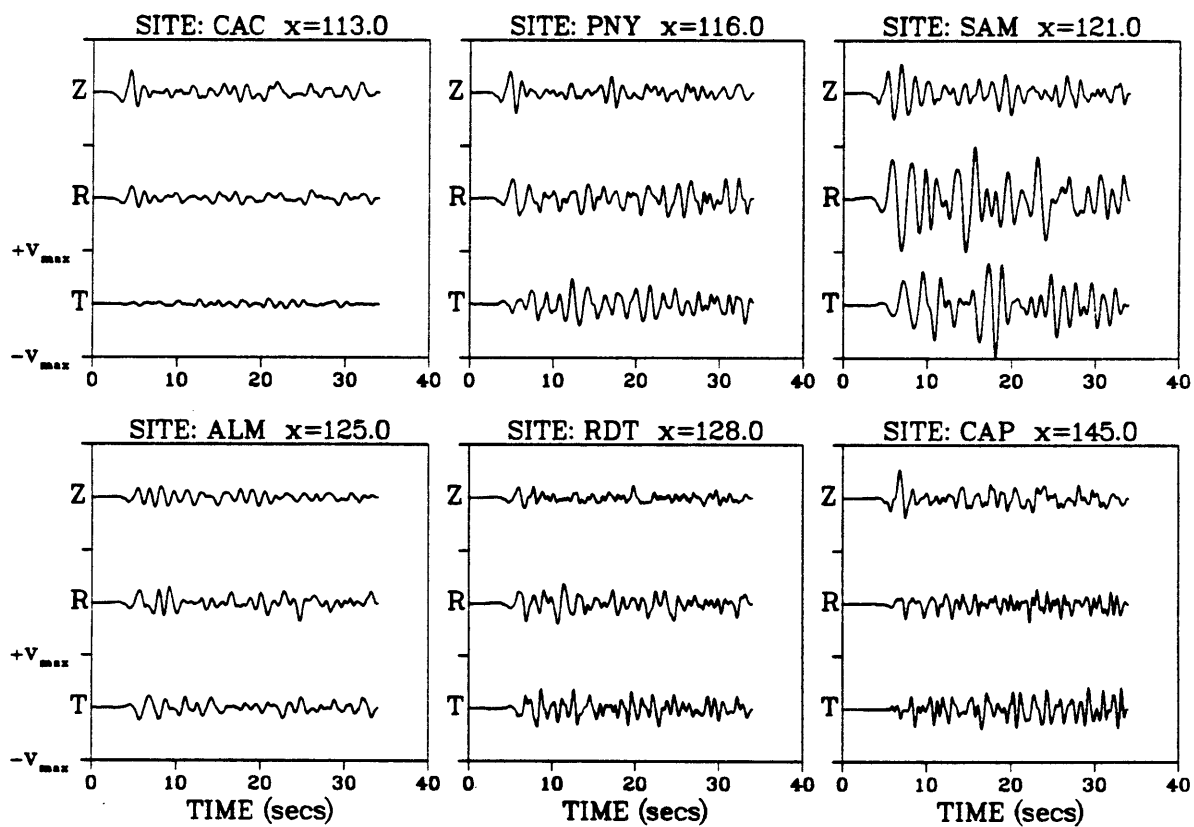


Figure 2.10 Seismograms for a Kommandorsky Islands event recorded on array 1.

EVENT REGION: CENTRAL CHILE $M_b = 5.9$
 ORIGIN TIME: 1987/08/04 15:04:40.000 $\Delta = 82^\circ$
 START TIME: 1987/08/04 15:16:55.000 $V_{max} = 5.6781$ microns/sec
 UNFILTERED

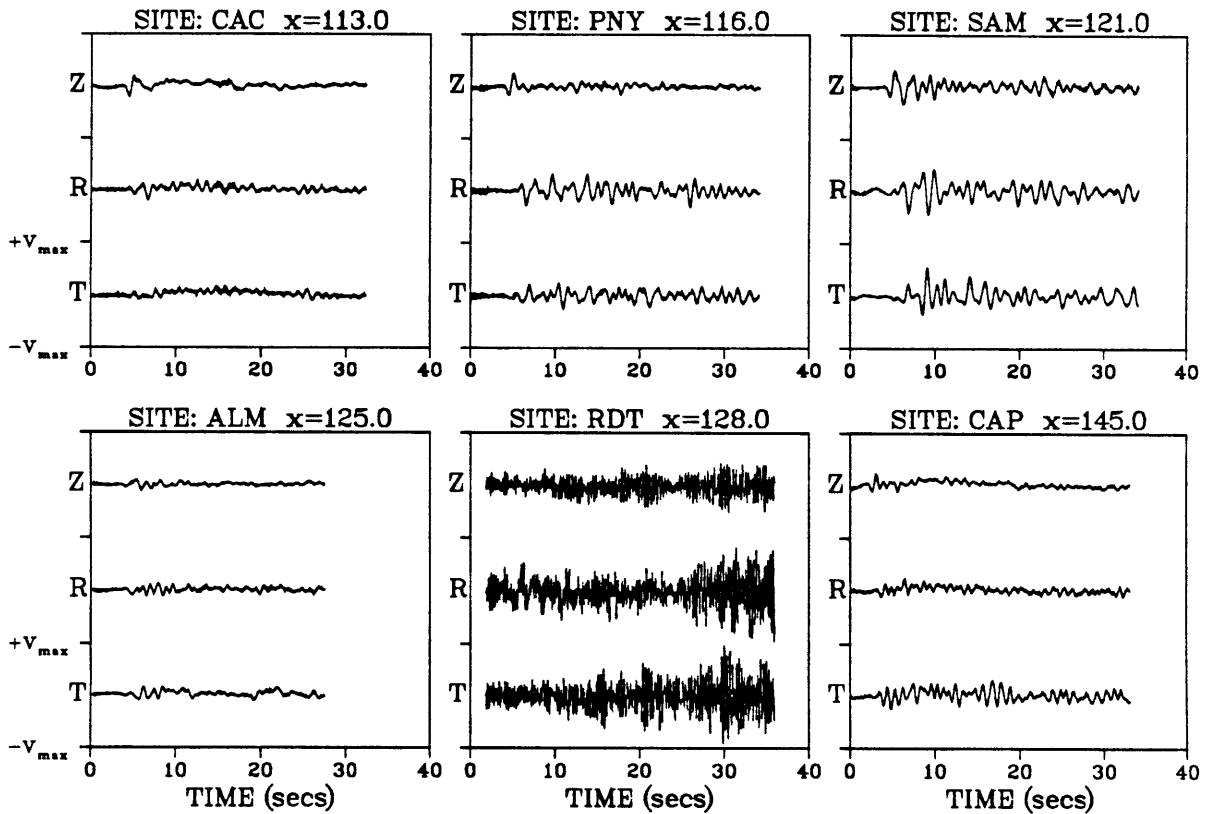


Figure 2.11 Seismograms for a central Chile event recorded on array 1. Note the logging-truck noise dominating the records at site RDT.

Second, the amplitudes of all components are significantly lower for sites inside the caldera (SOS, ALM, REB, RDT) than for the two ring-fracture sites (SAM, CLJ). We will see later that this second pattern is by far the most important observation concerning amplitudes, since it means that the low amplitudes in the caldera must be caused by a shallow structural anomaly. Figure 2.8 shows seismograms for a magnitude 5.6 event from Honshu, Japan with $\Delta = 80^\circ$ and $\theta_0 \approx +18^\circ$. Figure 2.9 is for a magnitude 6.1 event from Ecuador with $\Delta = 45^\circ$ and $\theta_0 \approx -26^\circ$. Once again the pattern of low amplitudes in the caldera is exhibited in both cases, and now the observed stability of this pattern is extended to both steeper and shallower incidence angles.

The data from array 1 show a similar pattern. Figure 2.10 shows seismograms for a magnitude 6.1 event from the Kommandorsky Islands with $\Delta = 60^\circ$ and $\theta_0 \approx +23^\circ$. Note that the amplitudes are still lower at ALM and RDT than at SAM. But on this larger scale we can see that SAM also has larger amplitudes than sites outside of the caldera (CAC, PNY, CAP). The smallest radial amplitudes actually occur at the two outermost sites, CAC and CAP. The modeling will show that this is reasonable in terms of a shallow, local anomaly beneath the caldera because the scattering effects on a nearly vertically incident P wave will diminish away from the caldera as the structural complexity decreases, and thus less energy is converted to horizontal motion. This, as mentioned, is one reason why it is more useful to concentrate attention on the array 2 data, since then we will be concerned less with the relative degree of scattering and more with what happens to the scattered waves after they have been generated. Finally, Figure 2.11 shows seismograms for a magnitude 5.9 event from central Chile with $\Delta = 82^\circ$ and $\theta_0 \approx -18^\circ$. Again, SAM

has the highest amplitude and ALM is much smaller. This is the event mentioned earlier which was recorded at all six sites, but recorded logging-truck noise at one site, RDT. The recordings at RDT are shown here only for reference since these data cannot be used.

At first glance, the array 1 data in Figures 2.10 and 2.11 might lead one to propose that the primary amplitude anomaly occurs at SAM rather than at the inner caldera sites. Perhaps we are observing mainly an amplification effect on the ring fracture rather than anomalously low amplitudes within the caldera. Although the scattered wave amplitudes at ALM and RDT are larger than at CAC, they are qualitatively similar in comparison to the large amplitudes at SAM. However, if one examines the first arrival for the vertical components in Figure 2.10, it is clear that the direct P-wave amplitude is much smaller at ALM and RDT than at the remaining sites. Also, there is the following evidence in the data that, as mentioned above, the strength of scattering and resonance effects increases toward the caldera. First, the near absence of a transverse component at CAC indicates that the scattering process is much simpler near this site than at the caldera sites, which have a strong transverse component. Secondly, there is a distinct trend of increasing scattered-wave amplitude from CAC to PNY to SAM for all three components of motion. Finally, at SAM, ALM and RDT the scattered-wave amplitudes are comparable to or larger than the direct P-wave amplitude at the same site, whereas at the three outer sites the P wave is significantly larger than the scattered waves. In light of the four qualitative observations discussed above, the waveforms observed inside the caldera have a much different character than those at the outer three sites. Although there may be some additional amplification at SAM, we still must view the

amplitudes within the ring fracture as being anomalously low, rather than “normal”. So in this thesis we will make the assumption that the strength of scattering and resonance effects is similar at all sites in array 2, and we will focus our attention on modeling the low relative amplitudes within the caldera. In Chapter 5 we will discuss the array 1 data further, in terms of their consistency with the modeling results.

In order to quantify the amplitude variations across each array we will make use of the spectral ratio, and this is discussed in the next section. Before we can do this with confidence, we first need to examine the spectral content of the data to determine the signal amplitude levels relative to the background noise level over the frequency band of interest. We have already seen one example of low frequency noise contamination in Figure 2.5, and we showed that by removing this noise the amplitude spectrum was affected significantly only below 0.2 Hz. This means that we can safely consider signals only for 0.2 Hz and above. We now need to justify the use of frequencies from this lower limit up to about 1.0 Hz in the presence of noise. The best way to do this is to compare the seismogram spectrum with the spectrum of a noise window taken just before the first arrival. However, to obtain reliable noise information down to 0.2 Hz we would need a noise window at least 15 secs wide and none of the recorded seismograms contained more than about 6 secs of noise at the beginning of the record. This window width is sufficient only for frequencies down to about 0.5 or 0.4 Hz. So first we examined the available noise signals down to the lowest reliable frequency for every seismogram to be used. Having established that in all cases the signal levels were considerably higher than the noise at about 0.4 Hz, we extrapolated the measured curves down to 0.2 Hz and

found that the resulting estimate was still much lower than the signal. We justified this extrapolation by comparison with the power spectra for ambient noise given in *Aki & Richards* [1980], which show that the noise power spectrum should vary logarithmically with frequency down to about 0.2 Hz, below which the large peaks for oceanic tremor begin to dominate. In all cases the noise spectra that we were able to obtain displayed a clear logarithmic dependence on frequency.

Figures 2.12 and 2.13 show two examples of the direct measurement of noise for a window preceding the first arrival. Figure 2.12 shows the displacement spectra for one of the larger events, $m_b = 6.0$, from Jujuy, Argentina. The seismograms for this event were shown in Figure 2.7. Figure 2.13 is for one of the smaller events, $m_b = 5.2$, from the Fox Islands. For the Jujuy event we were able to obtain a noise window approximately 7 secs wide, whereas for the Fox Islands events we only had about 5 secs of noise before the first arrival. We have plotted the noise spectra down to 0.3 Hz in both cases. Notice that the noise is significantly larger relative to the signal for the Fox Islands event than for the Jujuy event. However, the noise level below 1.0 Hz is about one order of magnitude or more lower than the signal, even for the Fox Islands event. The corners at about 0.5 Hz in most of the noise spectra in Figure 2.13 are due to the smaller window width used and indicate that the measured noise amplitude should not be trusted below about 0.5 Hz for the Fox Islands event. The larger 7 sec window used for the Jujuy event allows us to estimate the noise reliably down to at least 0.4 Hz. The measured signal and noise amplitudes for all other recorded events listed in Table 2.2 fell within the range of these two examples, which represent the best and worst cases for our data. Examination of the equivalent power spectra for the noise signals

DISPLACEMENT SPECTRA FOR EVENT FROM: JUJUY, ARGENTINA $M_b = 6.0$
 ORIGIN TIME: 1987/09/01 04:26:07.400 $\Delta = 70^\circ$
 FFT START TIME: 1987/09/01 04:36:56.448 LENGTH= 34.133 secs
 UPPER CURVES: SEISMIC DATA LOWER CURVES: PRE-EVENT NOISE

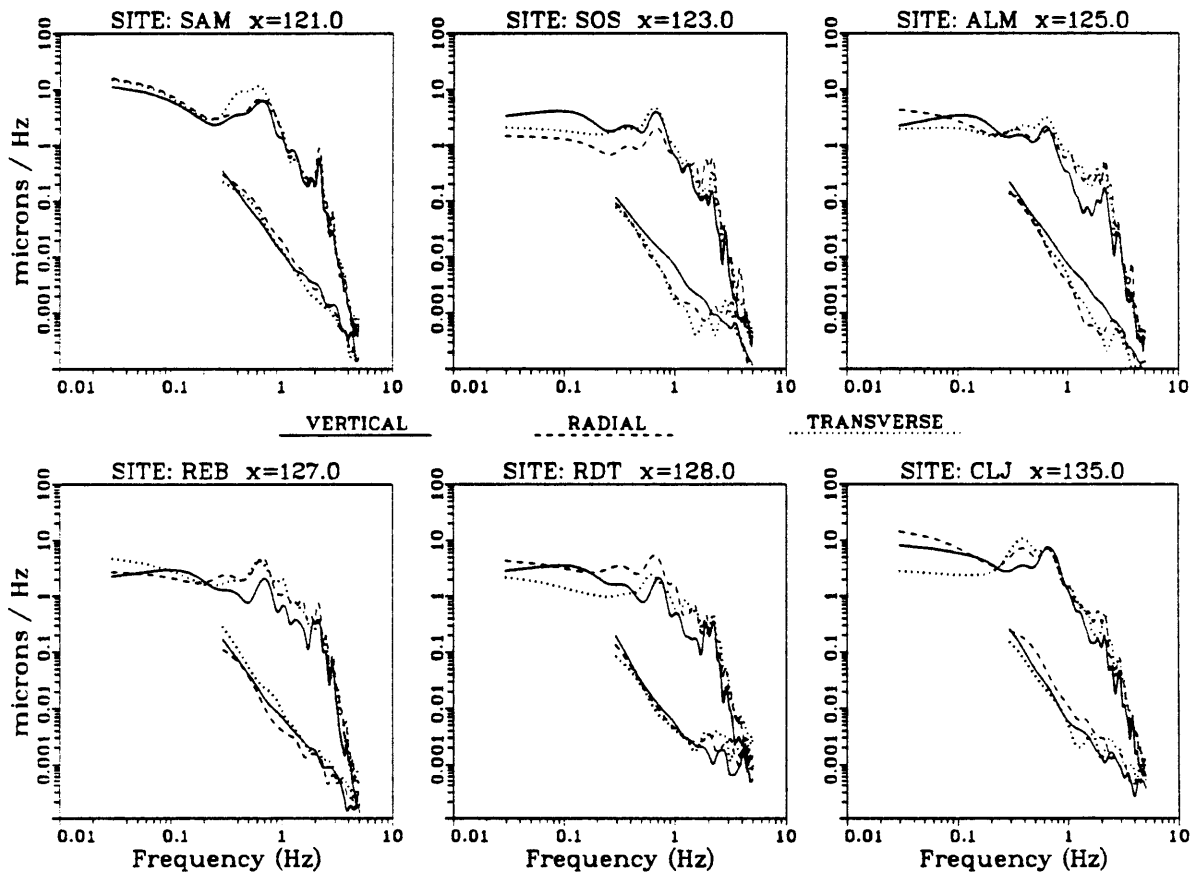


Figure 2.12 Displacement spectra for 3-component seismograms for the magnitude 6.0 Jujuy, Argentina event (see Figure 2.7 for seismograms) compared with the spectra for a 7 sec noise window taken prior to the first arrival. In each sub-plot the signal spectra are the upper three curves and the noise spectra are the lower curves. Solid lines are for the vertical component, dashed for the radial and dotted for the transverse.

DISPLACEMENT SPECTRA FOR EVENT FROM: FOX ISLANDS $M_b = 5.2$
 ORIGIN TIME: 1987/08/29 22:12:11.200 $\Delta = 46^\circ$
 FFT START TIME: 1987/08/29 22:20:33.088 LENGTH= 34.133 secs
 UPPER CURVES: SEISMIC DATA LOWER CURVES: PRE-EVENT NOISE

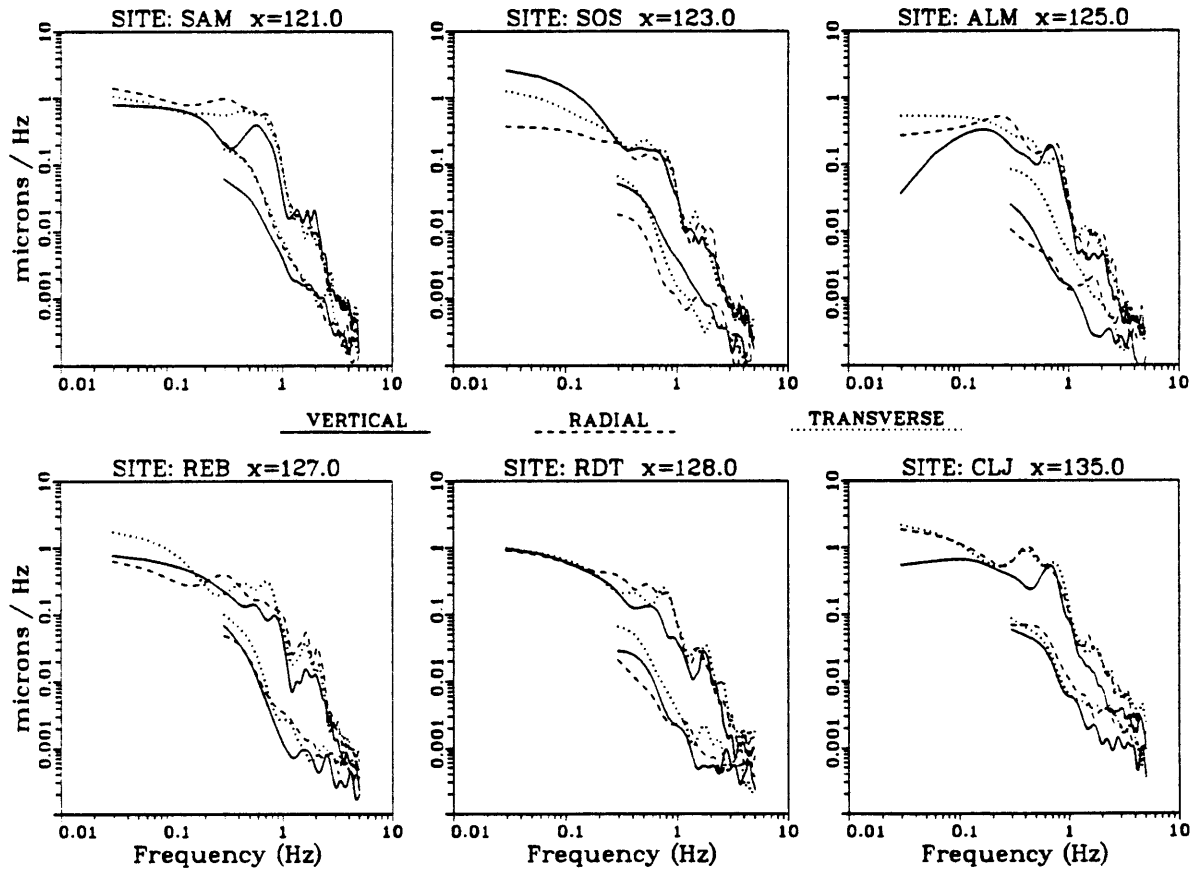


Figure 2.13 Same as Figure 2.12 except spectra are for a magnitude 5.2 event from the Fox Islands and the available noise window used was only 5 secs wide.

demonstrated that the behavior given in *Aki & Richards* [1980] was approximated well for frequencies of 0.5 Hz and higher. So the logarithmic dependence of the noise displacement spectra in Figures 2.12 and 2.13 should allow us to extrapolate their curves down to 0.2 Hz, where clearly the level will still be lower than for the signals. We will also see in the next section that the most significant variations in amplitude across the two instrument arrays occur at frequencies higher than about 0.3 Hz, where the noise level has been directly confirmed to be very low through the direct measurements discussed above.

2.4 Spectral Ratios

The spectral ratio is a very useful quantity for separating the various effects which compose recorded seismograms. In general the spectral ratio will remove any effects which are common to both the numerator and denominator spectra. For the present study we wish to isolate the receiver functions, $R_k(\omega)$, from spectral data represented by equation (2.1) and ideally this requires the complete removal of the source effect, instrument response and background noise from each spectrum. The instrument response has already been effectively removed from all data to yield the corrected observed spectra, $D'_{jk}(\omega)$, given by equation (2.3). If the background noise, $N_{jk}(\omega)$, is small enough to be neglected then the receiver response at one site, say $k = 1$, relative to that at another site, say $k = 2$, may be obtained simply by forming the ratio between the corrected spectra recorded at both sites for any common event, j :

$$\frac{D'_{j1}(\omega)}{D'_{j2}(\omega)} = \frac{R_1(\omega)}{R_2(\omega)}. \quad (2.4)$$

This is the approach taken by *Bard & Tucker* [1985], who successfully modeled local crustal structure using spectral ratios all computed relative to a common reference site.

This approach causes any information about spectral variations versus frequency at the reference site to be mixed in with that of the remaining sites. Also, if the data at the reference site contain varying amounts of noise from event to event, which is usually the case, this effect will also be mixed in with the actual site effects at all other locations. Thus it is safer to compute the spectral ratio at each site relative to the average over all sites for each event so that a particularly noisy record from a reference site will not contaminate all of the ratios. We will see soon that this approach is also beneficial for reducing the noise contribution in the denominator. For now though, let us continue to assume that the noise is much smaller than the signal. We will also show, later in this section, that we cannot hope to model the observed spectral phase variations for our data because the phase spectra are extremely unstable for similar events recorded at the same site. Our entire analysis will be based solely on spectral amplitude ratios. So in all following equations we will drop the convention that spectral quantities are complex, and all variables are assumed to represent amplitude spectral density. Then the spectral amplitude ratio for event j at site k relative to the average over all sites may be written for one component as:

$$\frac{D'_{jk}(\omega)}{\langle D'_{jk}(\omega) \rangle_k} = \frac{R_k(\omega)}{\langle R_k(\omega) \rangle_k}, \quad (2.5)$$

$$\text{where: } \langle \rangle_k \equiv \frac{1}{K} \sum_{k=1}^K,$$

and for the present study the total number of sites averaged will be $K \leq 6$. The quantity on the left-hand side, $D'_{jk}/\langle D'_{jk} \rangle_k$, is what we will calculate for single events at each site. The assumption that $N_{jk}(\omega) \ll S_j(\omega) \cdot R_k(\omega)$ is crucial for equation (2.5) to hold. This is why we were so concerned about quantifying the signal-to-noise ratio in the previous section.

When the noise is not negligible it may be reduced if numerous events from the same source region have been recorded at each site. If we collect enough signals for similar events at a particular site, the noise contribution to the average of all of these signals should decrease as the number of sample events increases, assuming that the same signal is repeated in each event. In this sense the process of averaging has the opposite effect of taking spectral ratios, since now the differences are reduced and the similarities are enhanced. This should hold then for any suite of events recorded at one site. The requirement that all of these events be from the same source region must be observed in our case because the 2-dimensional receiver functions that we will be modeling are dependent on the source incidence angle and azimuth. The spectral ratio in equation (2.5) can then be re-written as:

$$\frac{\langle D'_{jk}(\omega) \rangle_j}{\langle D'_{jk}(\omega) \rangle_{jk}} = \frac{\langle S_j(\omega) \rangle_j \cdot R_k(\omega) + \langle N_{jk}(\omega) \rangle_j}{\langle S_j(\omega) \rangle_j \cdot \langle R_k(\omega) \rangle_k + \langle N_{jk}(\omega) \rangle_{jk}} \approx \frac{R_k(\omega)}{\langle R_k(\omega) \rangle_k}, \quad (2.6)$$

$$\text{where: } \langle \rangle_{jk} \equiv \frac{1}{K} \sum_{k=1}^K \left[\frac{1}{J} \sum_{j=1}^J \right],$$

and now the event index j must be restricted to events from similar source regions.

We have assumed throughout this discussion that we are dealing only with one component of motion in the data and that the receiver functions are valid only for

one particular source direction. We will see in Chapter 5 that this is in keeping with the way in which the modeling results will be presented since the synthetic spectral ratios will be obtained for a specific incidence angle and for separate components of motion. We have mentioned also that our modeling efforts must be restricted to two dimensions, given the presumed complexity of the caldera's sub-structure and the limited number of instruments used. The 2-D models to be considered will be defined relative to the horizontal x -coordinate along the array azimuth line and the z -coordinate vertically downward. The problems will be solved for in-plane P-wave sources, allowing only for P-SV wave conversions due to scattering at irregular interfaces in the models. In Chapter 3 we show that these simplifications necessarily preclude the existence of a transverse component of motion. Thus we can only attempt to model the variations in the vertical and radial components in this thesis. However, for completeness we will show the spectral ratio results for all three components in the following figures.

The spectra used to calculate the amplitude ratios were obtained by Fast Fourier Transforming (FFT) the exact data windows shown for the seismograms plotted. These windows represent 34.133 secs of data and all windows for each event begin at the same absolute time. The DC offset was removed from each seismogram and the ends were tapered smoothly to zero before transforming. The raw amplitude spectra were then smoothed using a 3-point triangular window which was passed through the spectra five times. This method of smoothing was preferred over the frequency-bandwidth averaging method because the triangular window will always be strongly peaked at its center regardless of how many times it is passed

through the spectra. Thus, for a desired degree of smoothness, the triangular window method produces less contamination from higher and lower frequencies than the bandwidth averaging method does. It is ideally suited for removing large peaks or troughs from the spectra without significantly degrading the remaining samples. We mention this here because large local troughs in the spectra used for the denominators will cause erroneously large values for the amplitude ratio at that frequency. This is a very common problem to users of spectral ratios and has prompted authors such as *Owens, Zandt & Taylor* [1984] to employ the “water level” technique of *Clayton & Wiggins* [1976] for removing large holes in the denominator spectra. We have tested the water level method against the simpler triangular smoothing method and discovered that both are equally effective for removing localized spectral troughs. The water level method has an advantage in that it only removes troughs that fall below some preset threshold value and leaves the remainder of the spectrum unaffected. However, when it is acceptable to smooth the entire spectrum, as in our case, it is not necessary to also employ the water level method.

After all of the amplitude spectra were smoothed as above, the relative instrument amplitude corrections were applied next, as described in Section 2.2. The corrected amplitude spectra were then averaged over the six sites and used as the denominator in equation (2.5). Figures 2.14 through 2.19 show the resultant single-event spectral amplitude ratios over the frequency band 0.1 to 1.0 Hz for the six teleseisms plotted before in Figures 2.6 through 2.11. Originally we had hoped to use both the amplitude ratio and phase delay spectra in the modeling analysis. If successful, this would have represented true full-waveform modeling and would

OBSERVED SPECTRAL RATIOS FOR
 DATA FROM ANDREANOF ISLANDS EVENT REGION RECORDED ON JEMEZ ARRAY 2
 NUMERATORS: single event DENOMINATOR: average over 6 sites
 σ_{HHS}^2 (log): V=0.202E+00 R=0.480E+00 T=0.259E+00 Total=0.314E+00

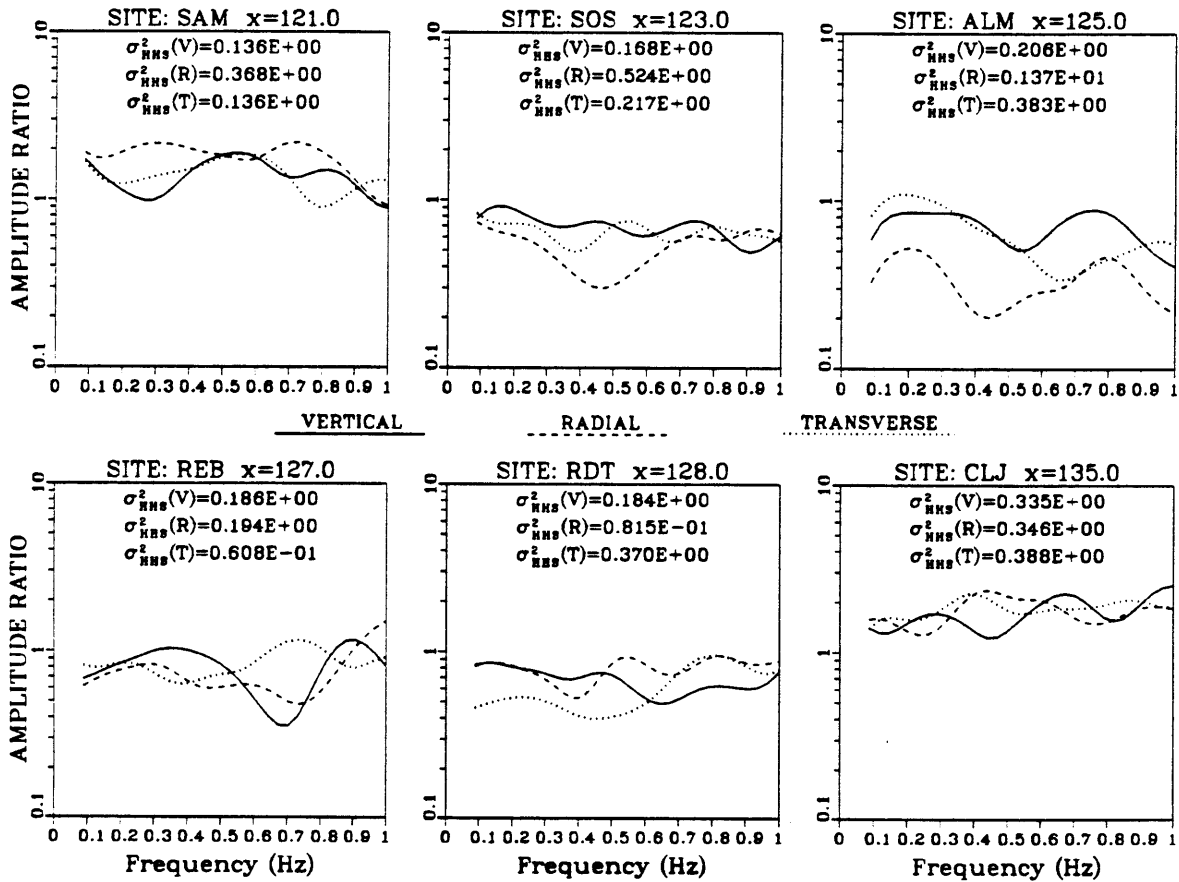


Figure 2.14 Spectral amplitude ratios for the Andeanof Islands event shown in Figure 2.6 for the frequency band 0.1 to 1.0 Hz. The ratios for each component were computed at each site relative to the average over all six sites. Residual variance for ratios predicted by a homogeneous halfspace model (HHS) are listed for each site and component as well as for the entire data set.

**OBSERVED SPECTRAL RATIOS FOR
DATA FROM JUJUY, ARGENTINA EVENT REGION RECORDED ON JEMEZ ARRAY 2**
 NUMERATORS: single event DENOMINATOR: average over 6 sites
 σ_{HHS}^2 (log): V=0.276E+00 R=0.302E+00 T=0.288E+00 Total=0.289E+00

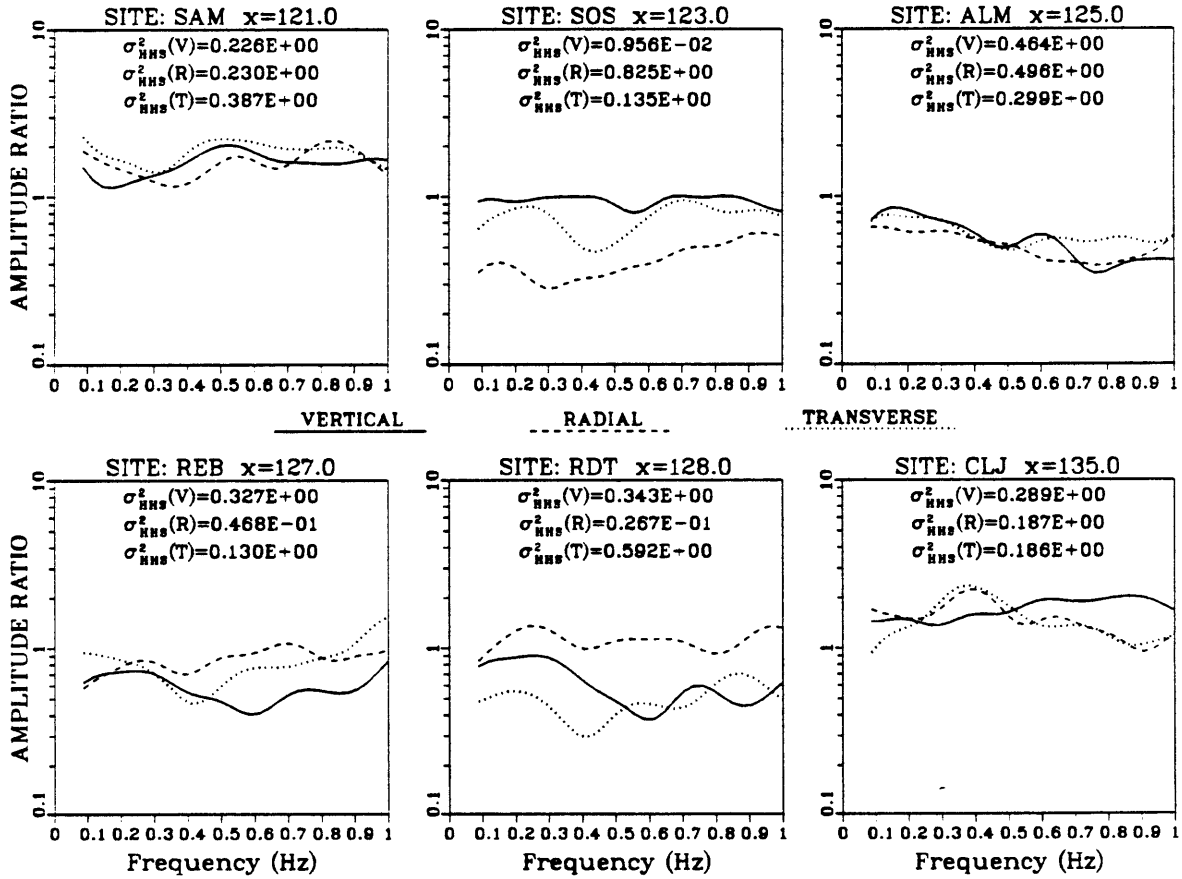


Figure 2.15 Spectral amplitude ratios for the Jujuy, Argentina event shown in Figure 2.7.

OBSERVED SPECTRAL RATIOS FOR
 DATA FROM HONSHU, JAPAN EVENT REGION RECORDED ON JEMEZ ARRAY 2
 NUMERATORS: single event DENOMINATOR: average over 6 sites
 σ_{HNS}^2 (log): V=0.222E+00 R=0.418E+00 T=0.268E+00 Total=0.303E+00

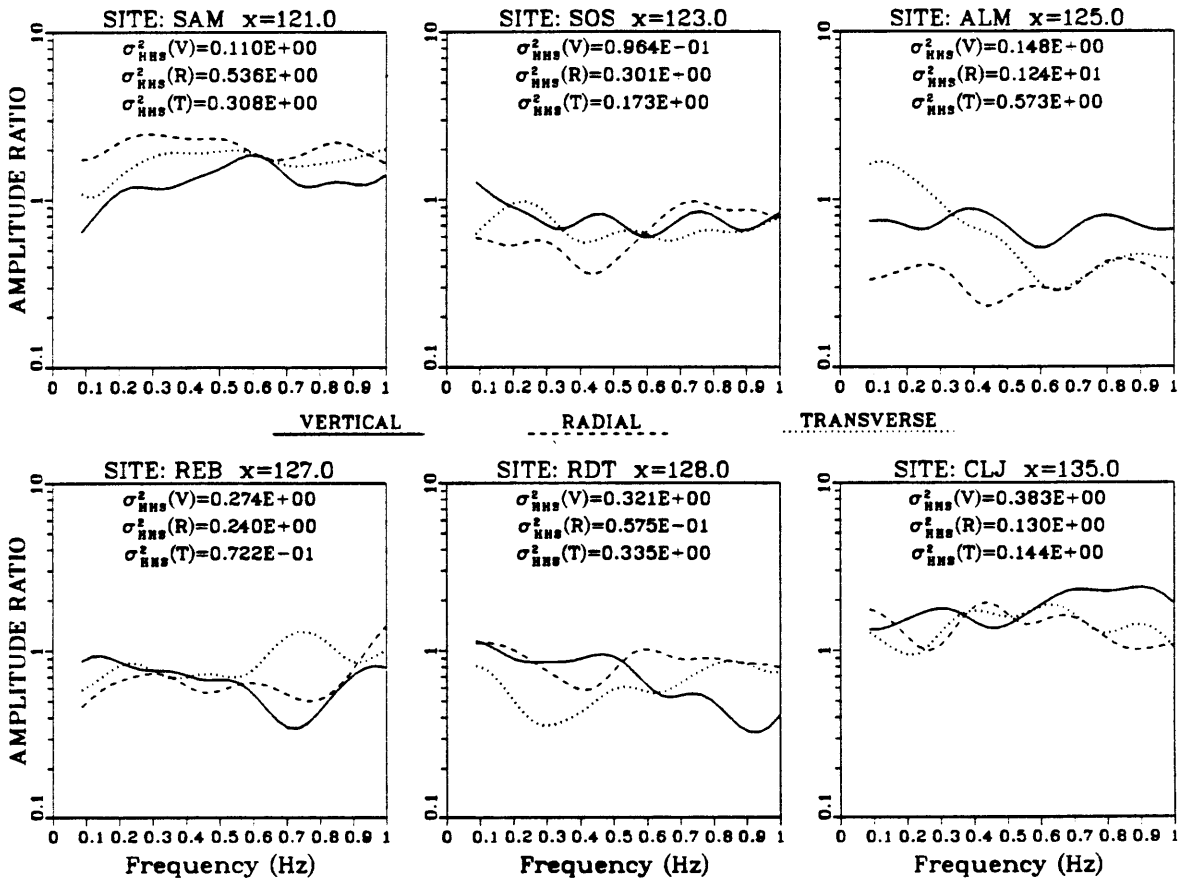


Figure 2.16 Spectral amplitude ratios for the Honshu, Japan event shown in Figure 2.8.

OBSERVED SPECTRAL RATIOS FOR
 DATA FROM ECUADOR EVENT REGION RECORDED ON JEMEZ ARRAY 2
 NUMERATORS: single event DENOMINATOR: average over 6 sites
 σ_{HNS}^2 (log): V=0.322E+00 R=0.649E+00 T=0.365E+00 Total=0.446E+00

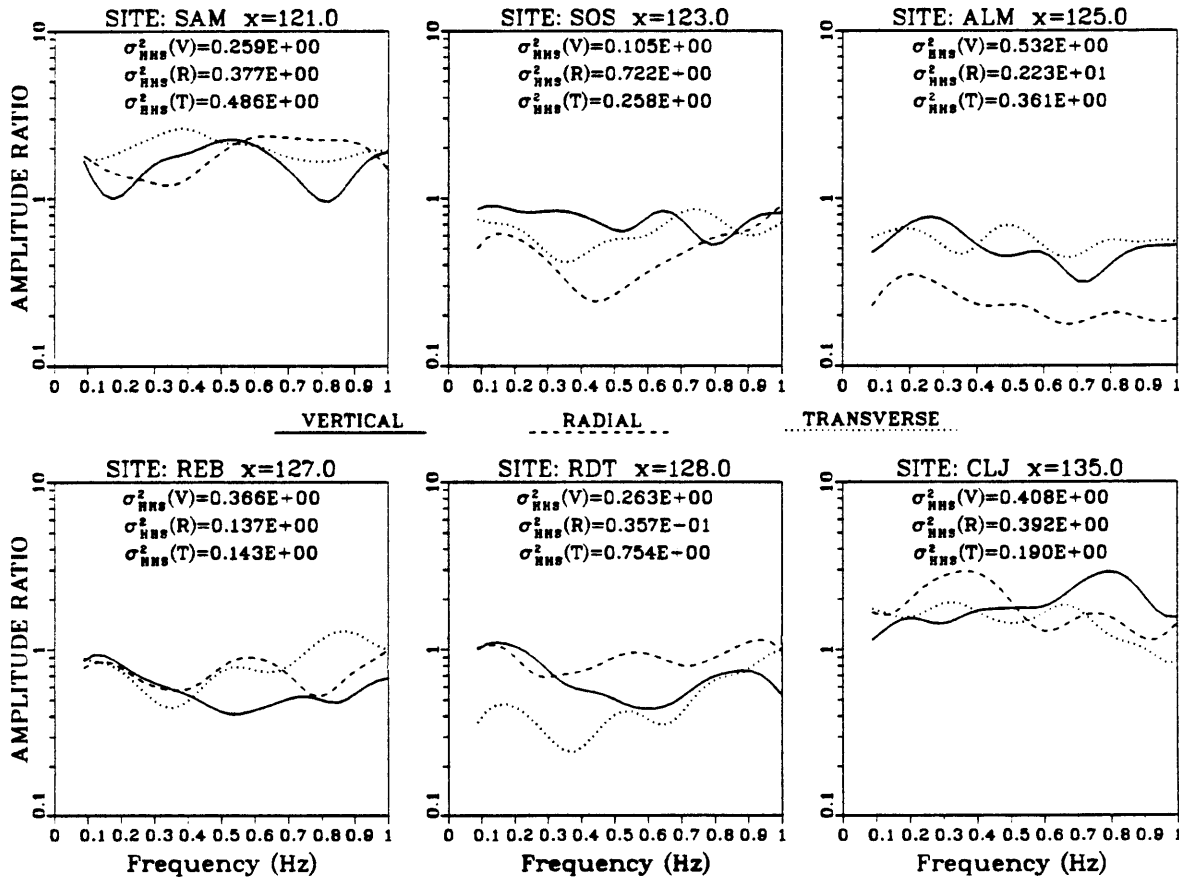


Figure 2.17 Spectral amplitude ratios for the Ecuador event shown in Figure 2.9.

**OBSERVED SPECTRAL RATIOS FOR
DATA FROM KOMMANDORSKY ISLANDS EVENT REGION RECORDED ON JEMEZ ARRAY 1**
 NUMERATORS: single event DENOMINATOR: average over 6 sites
 σ_{HNS}^2 (log): V=0.120E+00 R=0.349E+00 T=0.437E+00 Total=0.302E+00

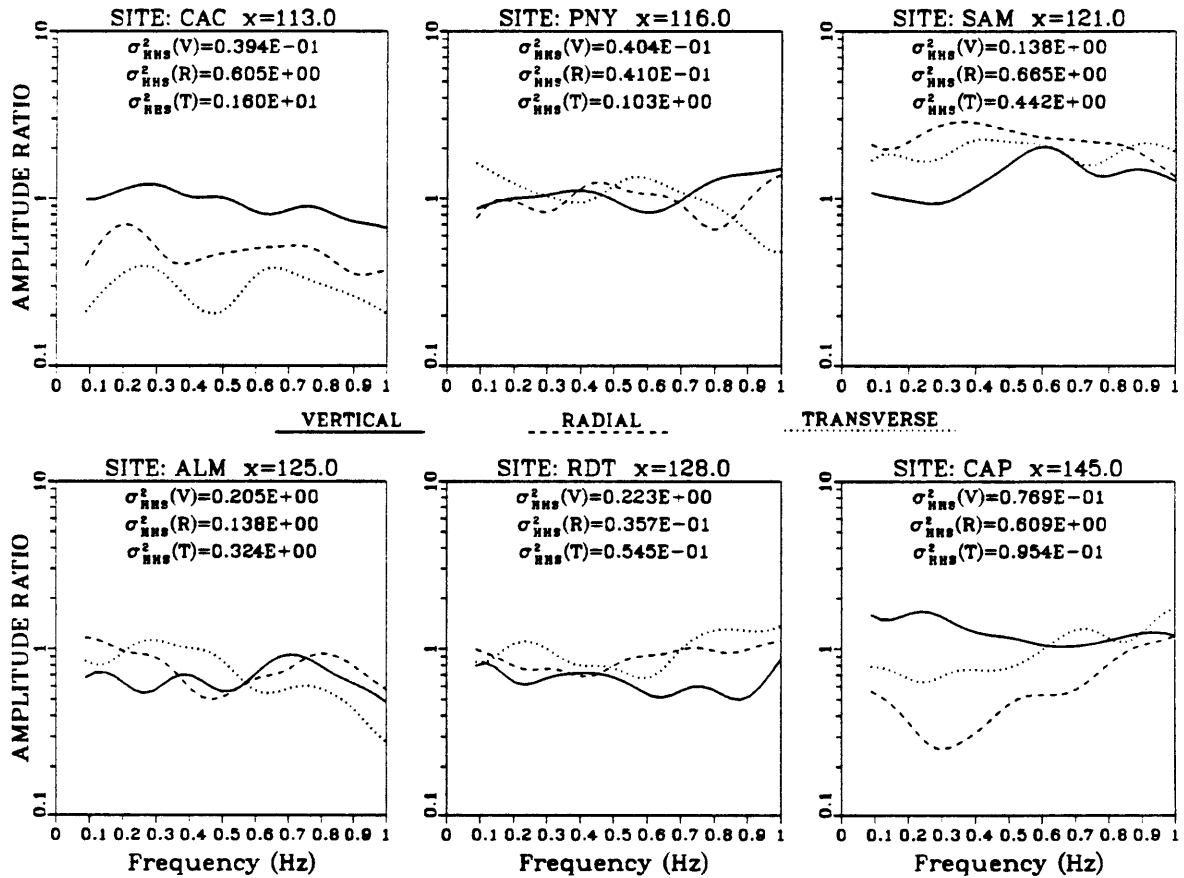


Figure 2.18 Spectral amplitude ratios for the Kommandorsky Islands event shown in Figure 2.10.

**OBSERVED SPECTRAL RATIOS FOR
DATA FROM CENTRAL CHILE EVENT REGION RECORDED ON JEMEZ ARRAY 1**
 NUMERATORS: single event DENOMINATOR: average over 5 sites
 σ_{HNS}^2 (log): V=0.237E+00 R=0.394E+00 T=0.450E+00 Total=0.360E+00

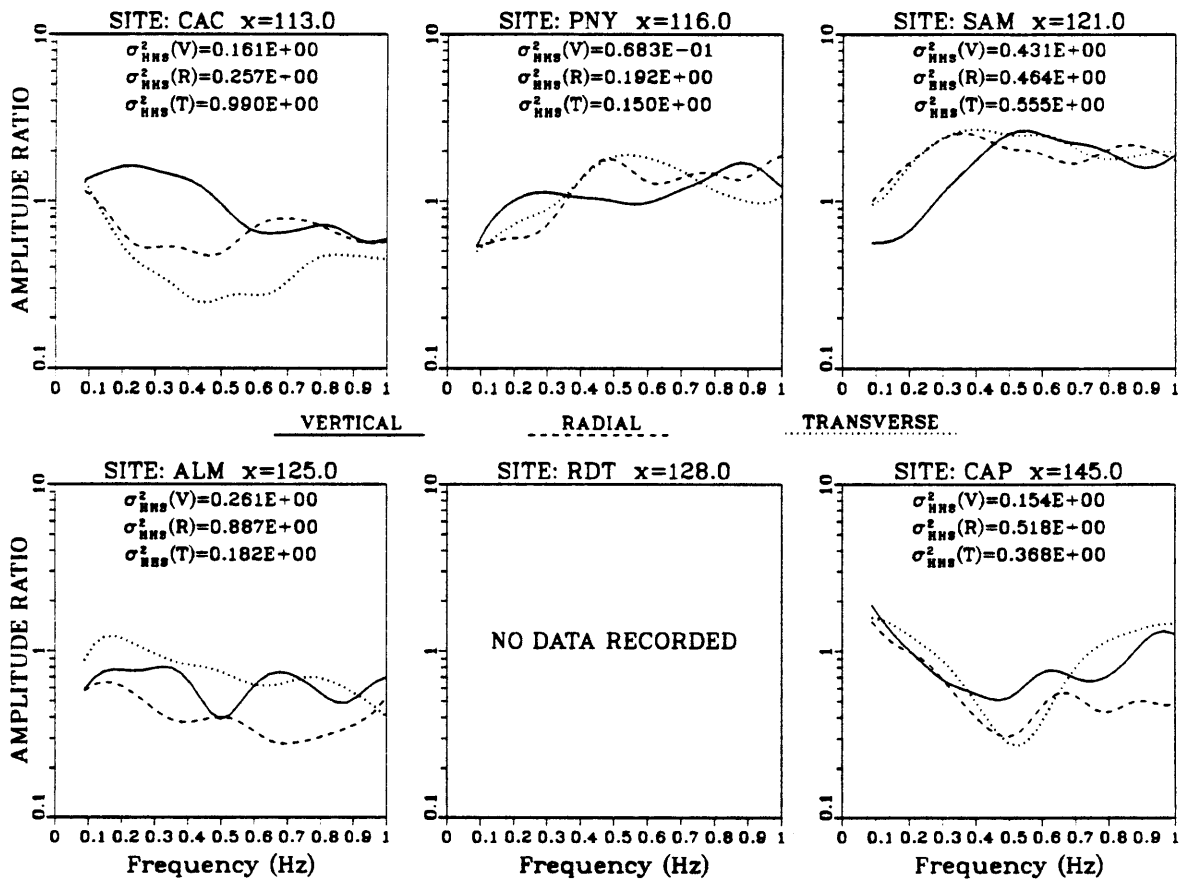


Figure 2.19 Spectral amplitude ratios for the Chile event shown in Figure 2.11. The data at site RDT were not included due to log-truck noise.

have allowed comparisons of observed and synthetic seismograms in the time domain. Unfortunately, as mentioned above, the phase spectra obtained for almost all of the recorded seismograms were far too erratic to be used confidently in this study. We believe this to be due to the complexity of the scattered waves which we have chosen to examine. We will show an example of this after first discussing the amplitude variations. We will, however, use the observed travel-time variations of the first motions to study the P-wave velocity structure beneath the caldera. This amounts to using only phase information that is uncontaminated by scattered waves and we will discuss this in more detail in the next section of this chapter.

In the previous section we showed qualitatively that the amplitudes are significantly lower for seismograms recorded inside the caldera than for those recorded on the ring fracture and that this observation is reasonably independent of incidence angle and source direction. These observations are born out quantitatively in the amplitude ratios for the four events shown for array 2, Figures 2.14 through 2.17. Although there are clearly some secondary effects which do apparently vary with incidence angle, such as relative shifts in the positions and amplitudes of certain peaks and troughs, the primary pattern is quite clear. The amplitudes for all three components are much lower at the 4 inner sites, SOS, ALM, REB and RDT, relative to the same components at SAM and CLJ. Also, the relative variations in the radial components are significantly larger than for the vertical components. In Chapter 5 we will discuss these observations in much more detail as we attempt to model and explain them.

To characterize how good any particular model is at fitting the data we will calculate the "residual variance reduction" for the synthetic and observed amplitude ratios relative to what we would expect for a homogeneous halfspace (HHS)

model. Clearly such a model will have the same response at any position along its free surface and the synthetic spectral amplitude ratios for all components and frequencies will be unity at all surface locations. Since we will require any acceptable model to be an improvement over the HHS case, we will in turn require the residual variance to be smaller. This will allow the identification of the best acceptable models as well as of the unacceptable models which produce larger variances than the HHS case. So, for reference, we have listed the HHS residual variances on all plots of observed spectral amplitude ratios. The HHS variances for each component at each site are listed separately inside the box for each site containing the ratio curves. The total variances for each component over all sites and the total over all components and sites are listed in the plot headings. The residuals were computed as the difference between $\ln(\text{amplitude ratio})$ for the observed and synthetic results at each frequency. The residual variance was then obtained by the general formula:

$$\sigma^2 = \frac{1}{N} \sum_{n=1}^N [\ln(R_n^{\text{obs}}) - \ln(R_n^{\text{syn}})]^2, \quad (2.7)$$

where N is the total number of ratio data points considered.

For single components at each site, $N = N_f$, where N_f is the total number of frequencies considered in the amplitude ratios. For single components over all sites, $N = K \cdot N_f$, where, as before, the total number of sites used is given by $K \leq 6$. For the total variance, $N = K \cdot N_c \cdot N_f$, where N_c is the number of components considered. R_n^{obs} is the observed amplitude ratio for the n^{th} point and R_n^{syn} is the corresponding synthetic value. Clearly for the HHS model, $\ln(R_n^{\text{syn}}) \equiv 0$, and the residual variance relative to this model, σ_{HHS}^2 , represents simply the mean square

of the natural log of the observed amplitude ratios. So σ_{HHS}^2 may be viewed as a measure of “how badly” an irregular model is needed in order to best explain the amplitude data. The variance reduction for a particular irregular model can be defined simply as the percentage:

$$V_{\text{MOD}} = \frac{\sigma_{\text{HHS}}^2 - \sigma_{\text{MOD}}^2}{\sigma_{\text{HHS}}^2} \cdot 100, \quad (2.8)$$

and if this number is positive then the model gives a better fit to the data than the HHS case does. Obviously, if the variance reduction is +100%, then $\sigma_{\text{MOD}}^2 = 0$ and the model yields a perfect fit to the data. On the other hand, a negative value for the variance reduction indicates that the model produces results which, on the average, display no consistency with the data. In these cases the HHS case is preferable and the model is worse than having no model at all. We give these formulas here, although we will not use them systematically until Chapter 5, because they set the framework for relating the model results directly to the data.

To summarize the amplitude ratio results for all data recorded on array 2 for distinctly different source locations, we have plotted the single-event ratios versus 8 incidence angles for each component and for 5 separate frequencies in Figures 2.20 through 2.22. The different symbol shapes mark the different frequencies listed in the legend. Figure 2.20 shows the vertical component, Figure 2.21 shows the radial and Figure 2.22 the transverse. Recall that positive incidence angles correspond to northwestern events and negative angles to southeastern events. These figures confirm, for a wider range of incidence angles, the observations we discussed previously for only four individual events. The similarity of all relative amplitudes at each site

VERTICAL COMPONENT SPECTRAL RATIOS VS. 8 INCIDENCE ANGLES
 DATA RECORDED IN JEMEZ MOUNTAINS ON ARRAY 2
 NUMERATORS: single events DENOMINATORS: average over 6 sites

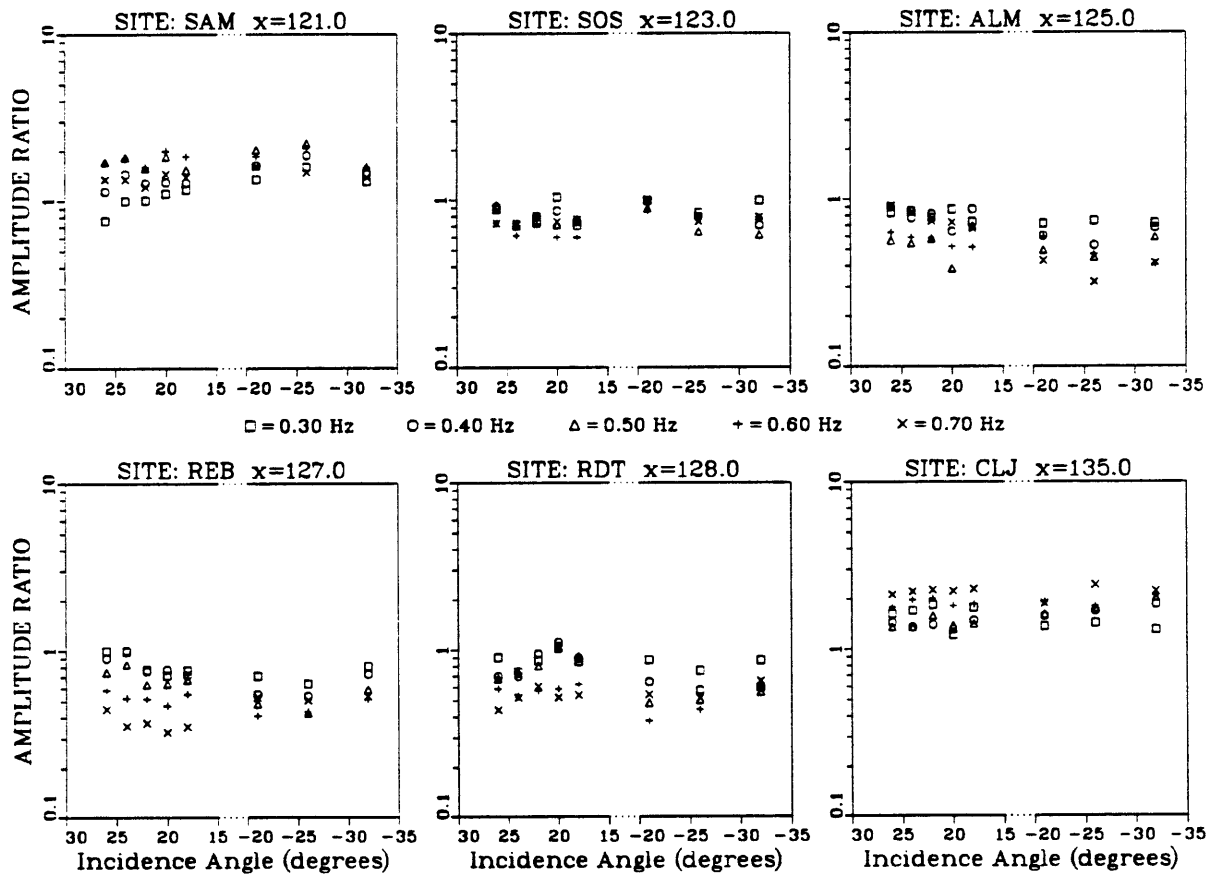


Figure 2.20 Spectral amplitude ratios for the vertical component of motion plotted versus 8 incidence angles at each site for 5 separate frequencies. Represented are all single-event ratios for distinct incidence angles for the data recorded on array 2.

RADIAL COMPONENT SPECTRAL RATIOS VS. 8 INCIDENCE ANGLES
 DATA RECORDED IN JEMEZ MOUNTAINS ON ARRAY 2
 NUMERATORS: single events DENOMINATORS: average over 6 sites

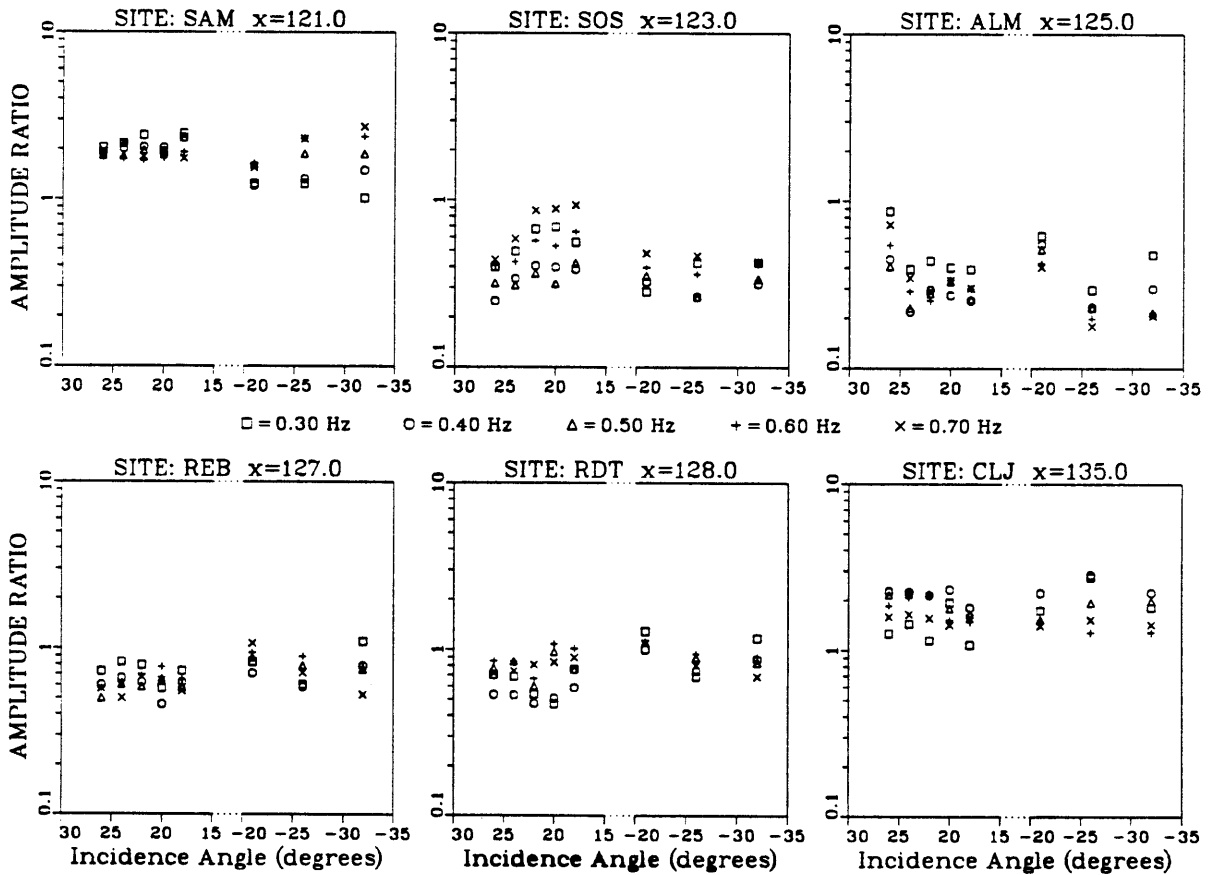


Figure 2.21 Same as Figure 2.20 but for the radial component of motion.

TRANSVERSE COMPONENT SPECTRAL RATIOS VS. 8 INCIDENCE ANGLES
 DATA RECORDED IN JEMEZ MOUNTAINS ON ARRAY 2
 NUMERATORS: single events DENOMINATORS: average over 6 sites

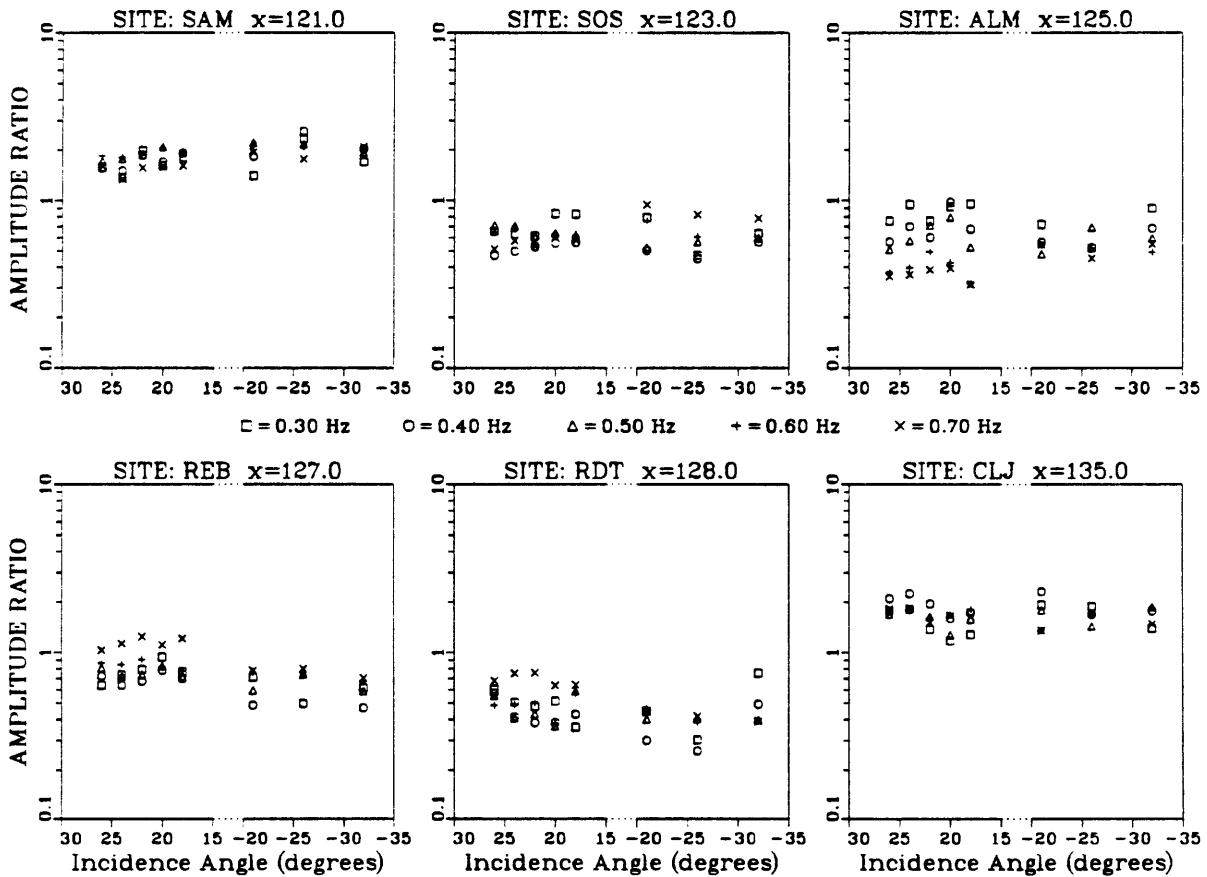


Figure 2.22 Same as Figure 2.20 but for the transverse component of motion.

is clearly the dominant behavior which we wish to reproduce. The similarities are particularly strong for the vertical component and for positive incidence angles. In Chapter 5 these dominant effects will be shown to be best explained by a shallow attenuating body beneath the caldera. We will find also that the complexity of the problem will not allow the secondary effects of relative peak movements to be readily explained through forward modeling efforts.

The next two figures show examples of the observed instability for phase spectra of the scattered waves, which we mentioned earlier. Figure 2.23 shows a radial component seismogram (top) and its velocity amplitude and phase spectra (bottom) for a magnitude $m_b = 5.7$ event from the Kuril Islands recorded at SAM. Figure 2.24 shows the radial seismogram, recorded at the same site, for another Kuril event with an almost identical location and magnitude, ($m_b = 5.6$), as the previous one. Note the obvious differences between the seismograms. One has very large amplitude near the first arrival and the other has larger amplitude later on in the scattered waves. Although the amplitude spectra are very similar, the phase spectra are quite different. These phase spectra were obtained by unwrapping the principal value of the phase using a simple discontinuity-detection scheme. When the difference between two successive phase values, i.e., $[\phi(\omega_2) - \phi(\omega_1)]$, is less than $-\pi$, an appropriate multiple of 2π is added to the latter value, $\phi(\omega_2)$. If the phase is well-behaved, this method should produce phase curves that are reasonably continuous and which increase linearly with frequency. On the contrary, the phase curves in Figures 2.23 and 2.24 contain several large discontinuities. Furthermore, although the phase curve for Figure 2.23 is approximately linear, the curve for Figure 2.24 is not.

EVENT REGION: KURIL ISLANDS $M_s=5.7$
ORIGIN TIME: 1987/09/06 15:27:22.400 $\Delta=68^\circ$
RADIAL COMPONENT DATA RECORDED AT SITE: SAM
START TIME: 1987/09/06 15:38:18.203 $V_{max} = 3.5000$ microns/sec

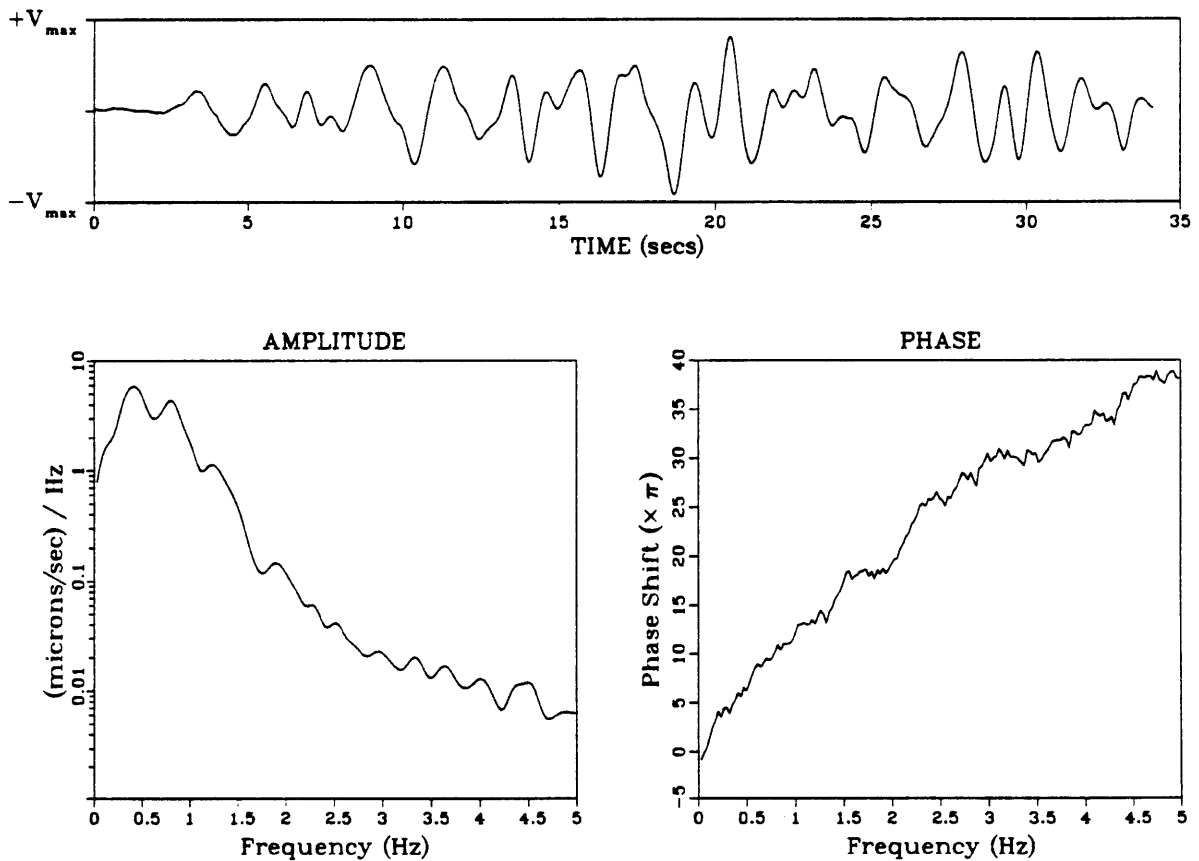


Figure 2.23 Radial component seismogram (top) and amplitude and phase spectra (bottom) for a magnitude 5.7 event from the Kuril Islands recorded at site SAM. These plots should be compared with Figure 2.24.

EVENT REGION: KURIL ISLANDS $M_s=5.6$
ORIGIN TIME: 1987/09/08 13:35:16.100 $\Delta=68^\circ$
RADIAL COMPONENT DATA RECORDED AT SITE: SAM
START TIME: 1987/09/08 13:46:04.489 $V_{max} = 3.5000$ microns/sec

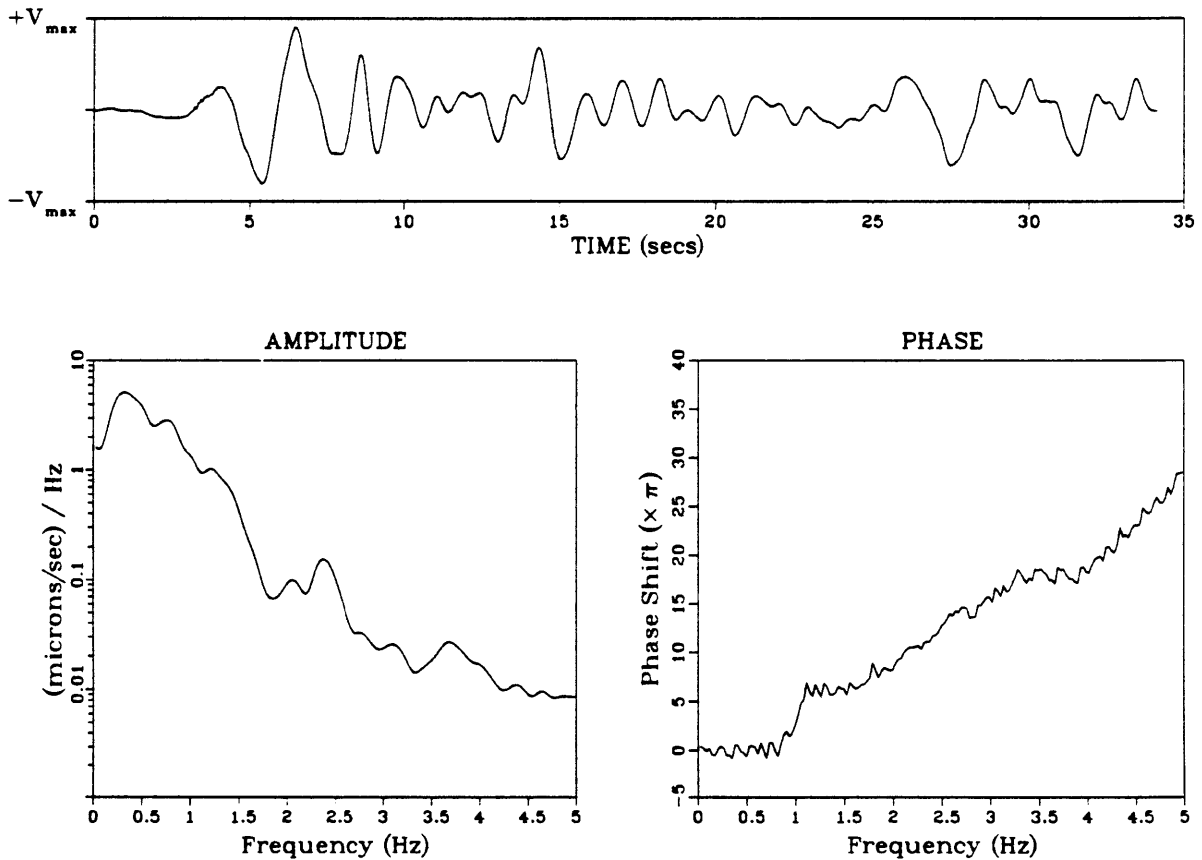


Figure 2.24 Radial seismogram and spectra for a magnitude 5.6 Kuril Islands event recorded at site SAM. Comparison with the Figure 2.23 shows that, although the events had nearly identical magnitudes, locations and amplitude spectra, the phase spectra are quite different.

Since the amplitude ratios remained quite stable despite the difference in phase, we were forced to consider the phase variations in the scattered waves as secondary effects which are extremely unstable and therefore impossible to model in 2-D. This instability is probably due to the complexity of the scattered waves and therefore to the details of the crustal structure which generate them. The elimination of spectral phase data from our modeling efforts is further justified by our innumerable attempts at obtaining continuous phase curves for even one seismogram, all of which failed. These attempts involved the use of every known technique for unwrapping phase that we could find, including the complex cepstrum method of *Tribolet* [1977]. Since we cannot use the phase of the scattered waves in the waveform modeling, we will do the next best thing and model travel time delays across the caldera for the first-arriving P wave.

We now conclude this section with the spectral amplitude ratio results obtained for spectra averaged over multiple events, using equation 2.6. We will note two desirable effects that this approach yields in our observations. First is the noise reduction that we mentioned before. Secondly, the averaging will enhance the primary behavior that is common to all events considered and will reduce the secondary effects that differ with incidence angle and source direction. We consider here only the data recorded on array 2.

To demonstrate the noise reduction we chose the four events recorded from the Kuril Islands source region listed at the bottom of Table 2.2. The single-event spectral amplitude ratios for each of these are shown in Figures 2.25 through 2.28. Notice that the ratios are much more stable from event to event for frequencies above 0.3 Hz than for the lowest frequencies. Furthermore, we would expect the variations

OBSERVED SPECTRAL RATIOS FOR
 DATA FROM KURIL ISLANDS (A) EVENT REGION RECORDED ON JEMEZ ARRAY 2
 NUMERATORS: single event DENOMINATOR: average over 6 sites
 σ_{HNS}^2 (log): V=0.163E+00 R=0.331E+00 T=0.249E+00 Total=0.248E-00

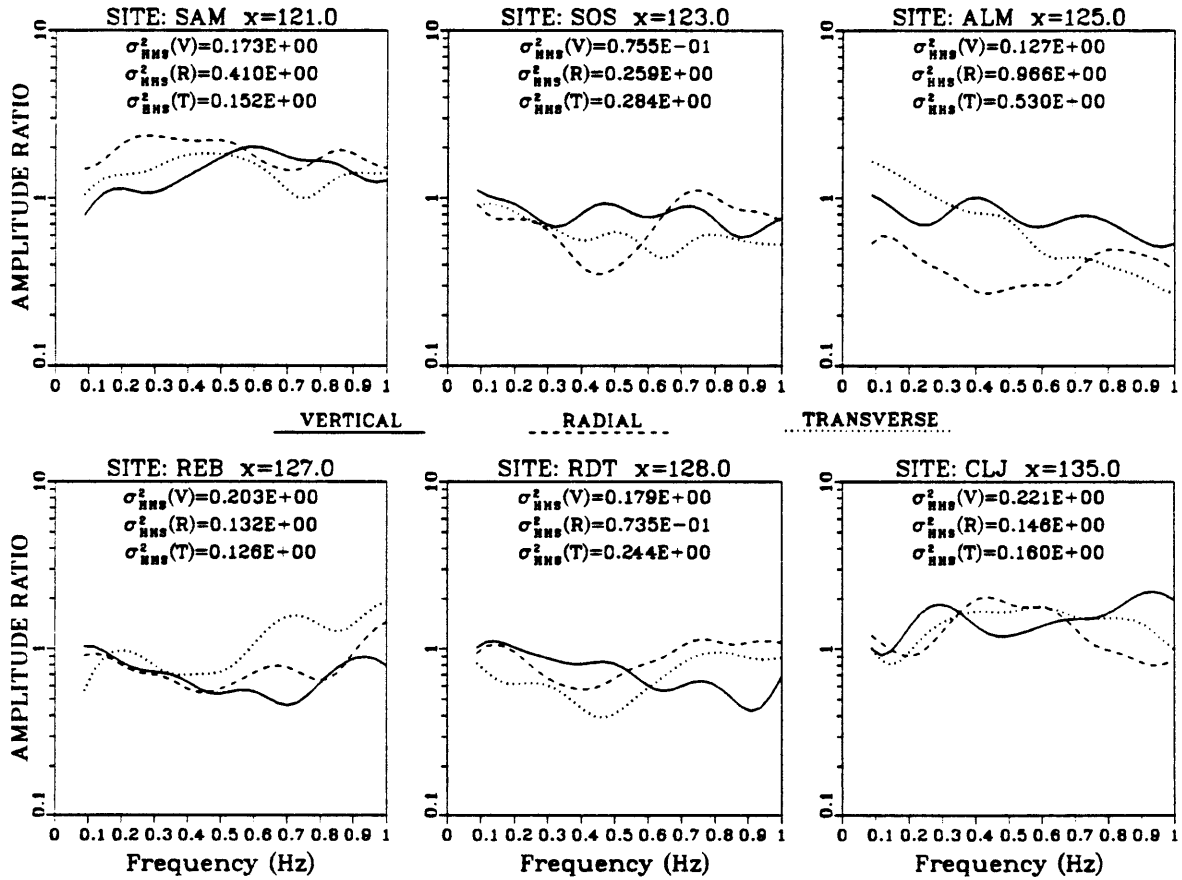


Figure 2.25 Single-event spectral amplitude ratios for the first Kuril Islands event to be used in the 4-event averaged results.

OBSERVED SPECTRAL RATIOS FOR
 DATA FROM KURIL ISLANDS (B) EVENT REGION RECORDED ON JEMEZ ARRAY 2
 NUMERATORS: single event DENOMINATOR: average over 6 sites
 σ_{HHS}^2 (log): V=0.158E+00 R=0.457E+00 T=0.256E+00 Total=0.290E+00

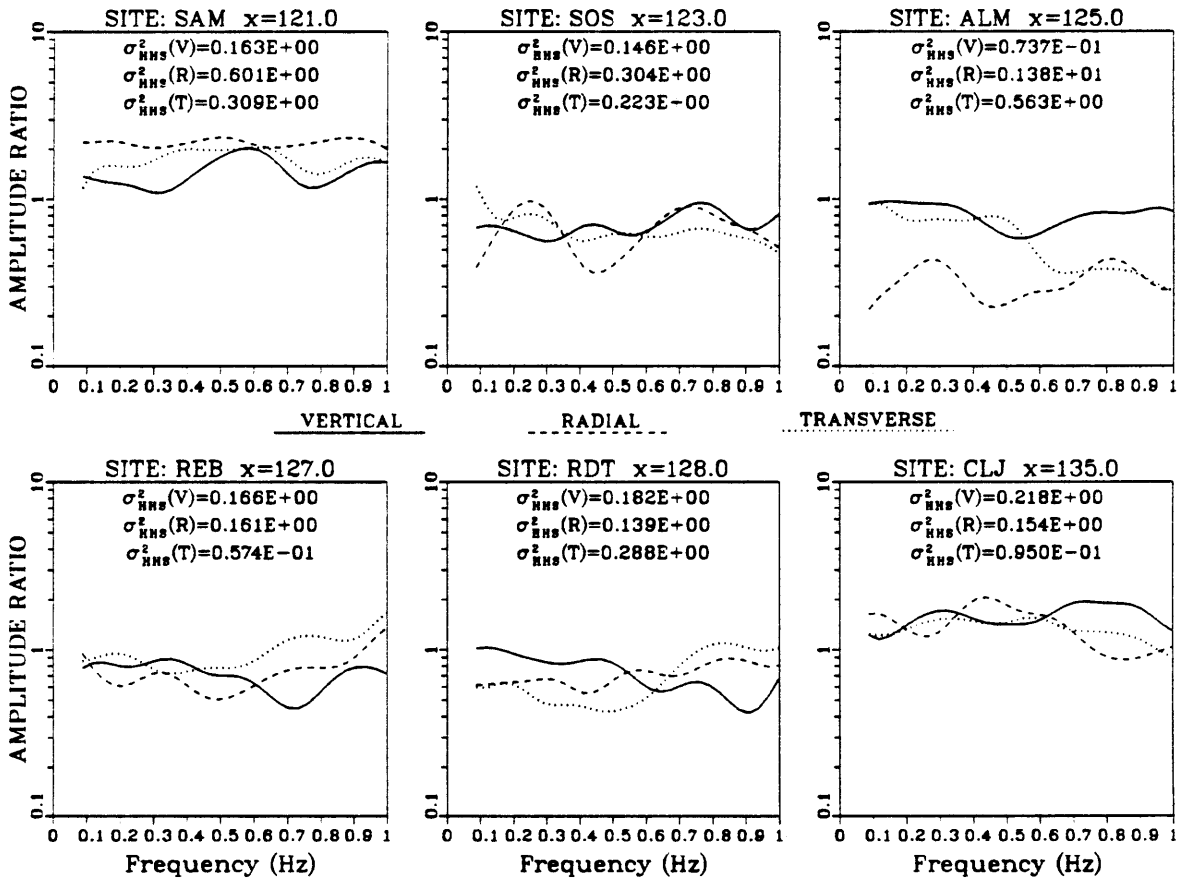


Figure 2.26 Single-event spectral amplitude ratios for the second Kuril Islands event to be used in the 4-event averaged results.

OBSERVED SPECTRAL RATIOS FOR
 DATA FROM KURIL ISLANDS (C) EVENT REGION RECORDED ON JEMEZ ARRAY 2
 NUMERATORS: single event DENOMINATOR: average over 6 sites
 σ_{HNS}^2 (log): V=0.199E+00 R=0.455E+00 T=0.323E+00 Total=0.326E-00

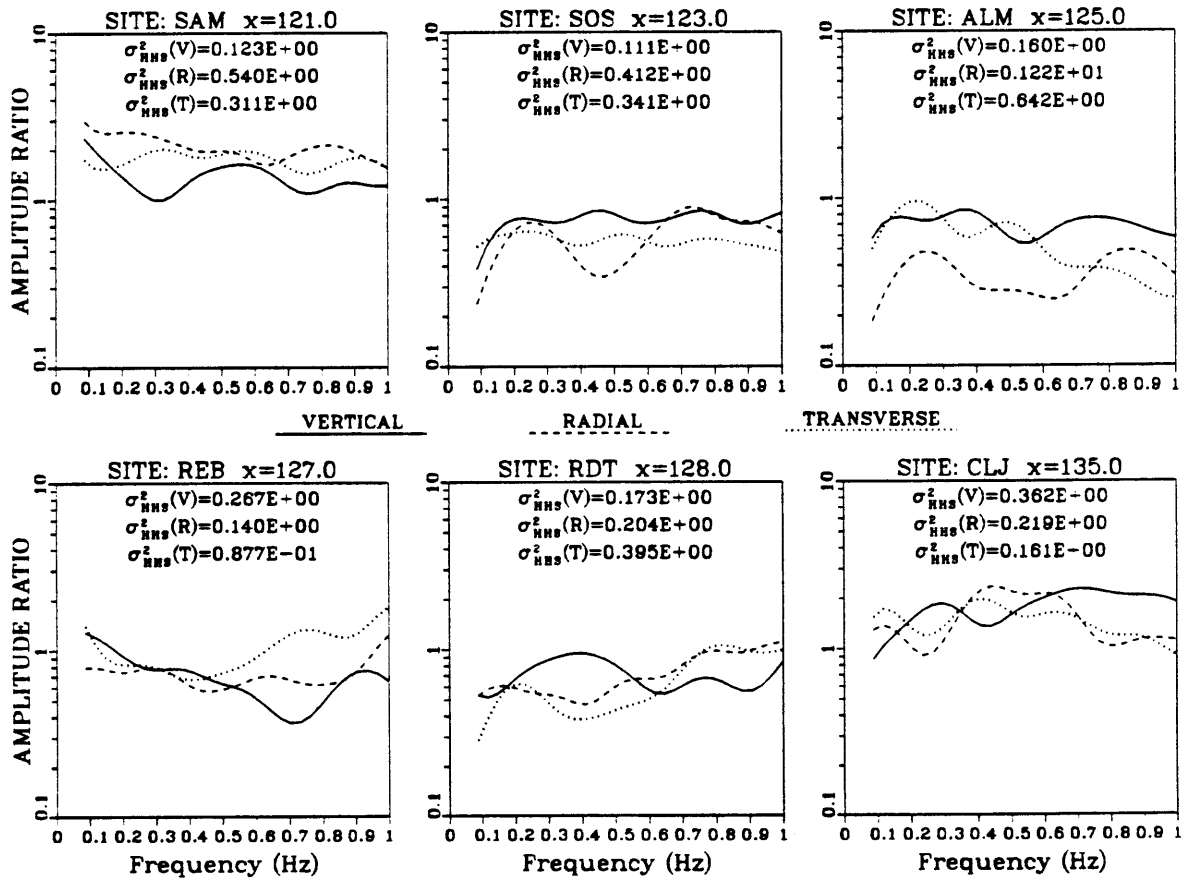


Figure 2.27 Single-event spectral amplitude ratios for the third Kuril Islands event to be used in the 4-event averaged results.

OBSERVED SPECTRAL RATIOS FOR
 DATA FROM KURIL ISLANDS (D) EVENT REGION RECORDED ON JEMEZ ARRAY 2
 NUMERATORS: single event DENOMINATOR: average over 6 sites
 σ_{HHS}^2 (log): V=0.272E+00 R=0.395E-00 T=0.278E+00 Total=0.315E+00

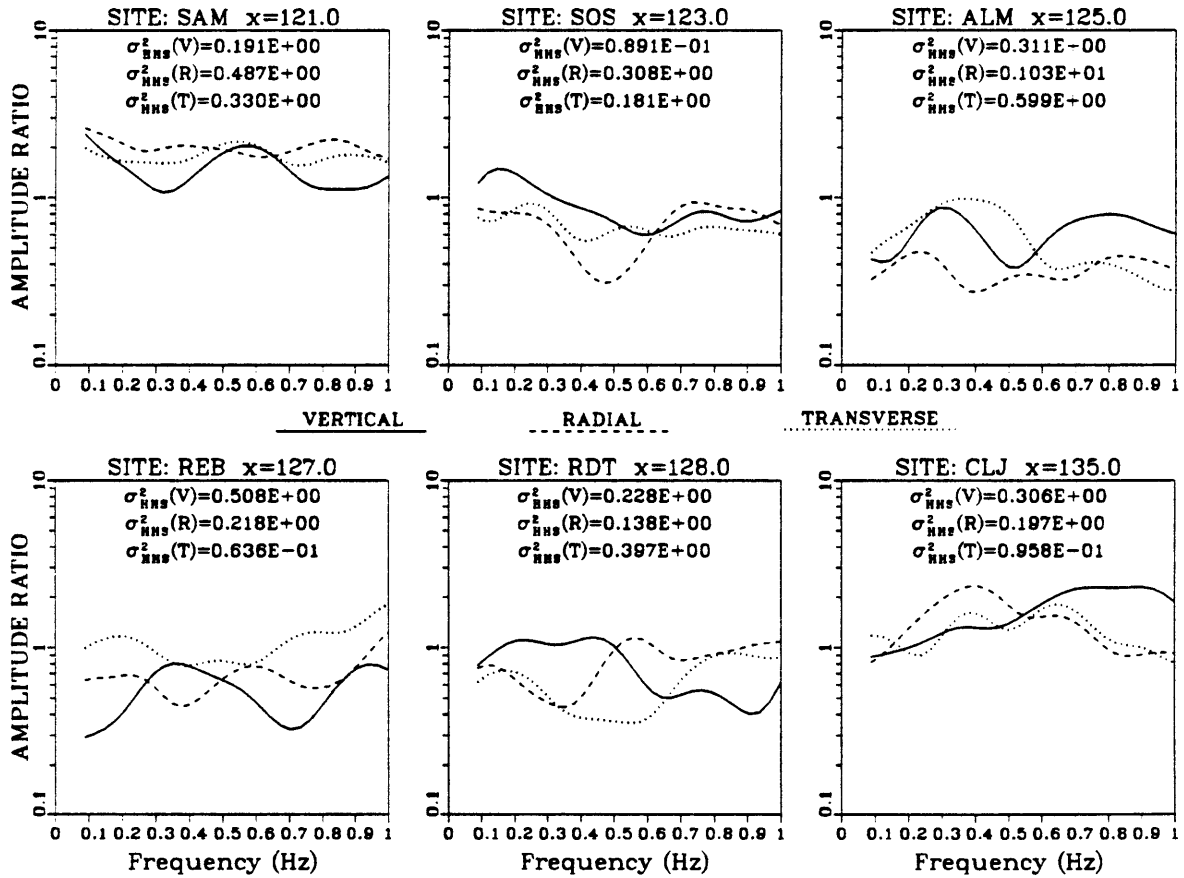


Figure 2.28 Single-event spectral amplitude ratios for the fourth Kuril Islands event to be used in the 4-event averaged results.

from site to site to decrease for lower frequencies as the wavelength becomes much larger than the presumed maximum size of structural anomalies beneath the caldera. This will be confirmed by the modeling results in Chapter 5. We assume then that the variability observed for the lowest frequencies is due to background noise, as discussed in section 2.3. Figure 2.29 shows the results after averaging the spectra at each site over all four events. We now see that the ratios above 0.3 Hz are virtually unchanged and that the lower frequencies have stabilized near unity for most of the sites. This in turn allows us to assume that most of the useful information in the data occurs for frequencies above 0.2 Hz and that this is where we should concentrate our modeling efforts. We will be using almost exclusively the averaged Kuril Islands data shown here for comparisons with synthetic data in Chapter 5 to determine the best models, since we believe it to be the most noise-free representation of the primary observations that we wish to explain. The models that produce the best fits with the Kuril data will then be tested against the remaining data to see just how much can be explained by any single model.

Next, we averaged all available data for the northwestern and southeastern events separately to see if there are any major direction-dependent effects that should be considered. Figure 2.30 shows the ratio results for the seven northwestern events recorded on array 2 and Figure 2.31 shows the results for three southeastern events. We have used only events that were recorded at all six sites. The only significant differences between these two plots occur at the four inner sites, SOS, ALM, REB and RDT, where the amplitude ratios are slightly higher for the northwestern events than for the southeastern events, although they are still considerably lower in both cases than for the ring fracture sites.

OBSERVED SPECTRAL RATIOS FOR
 DATA FROM KURIL ISLANDS (A,B,C,D) EVENT REGION RECORDED ON JEMEZ ARRAY 2
 NUMERATORS: average over 4 events DENOMINATOR: average over 6 sites
 σ_{HHB}^2 (log): V=0.173E+00 R=0.369E+00 T=0.248E+00 Total=0.264E+00

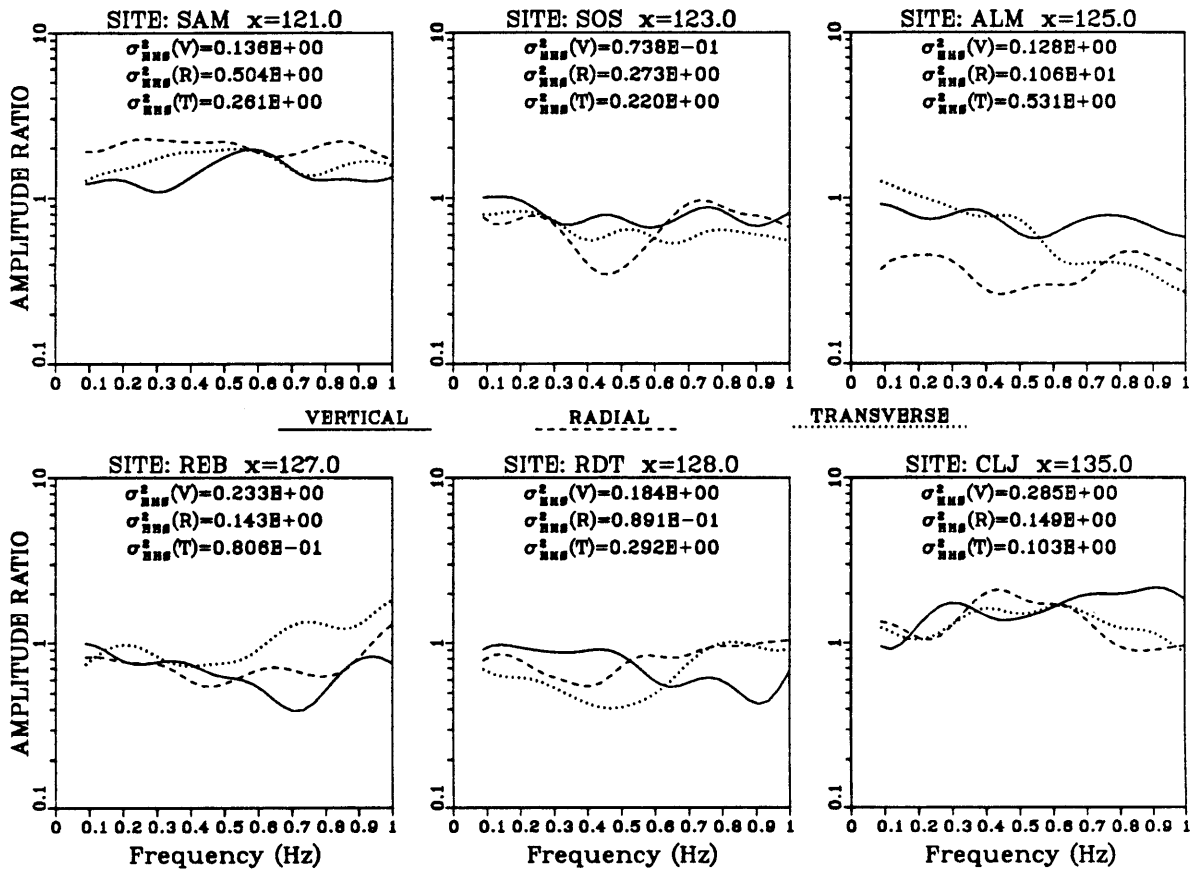


Figure 2.29 Spectral amplitude ratios obtained from the averaged amplitude spectra for the 4 Kuril Islands events.

OBSERVED SPECTRAL RATIOS FOR
 DATA FROM NORTHWESTERN EVENT REGION RECORDED ON JEMEZ ARRAY 2
 NUMERATORS: average over 7 events DENOMINATOR: average over 6 sites
 σ_{HHS}^2 (log): V=0.177E+00 R=0.363E+00 T=0.240E+00 Total=0.260E+00

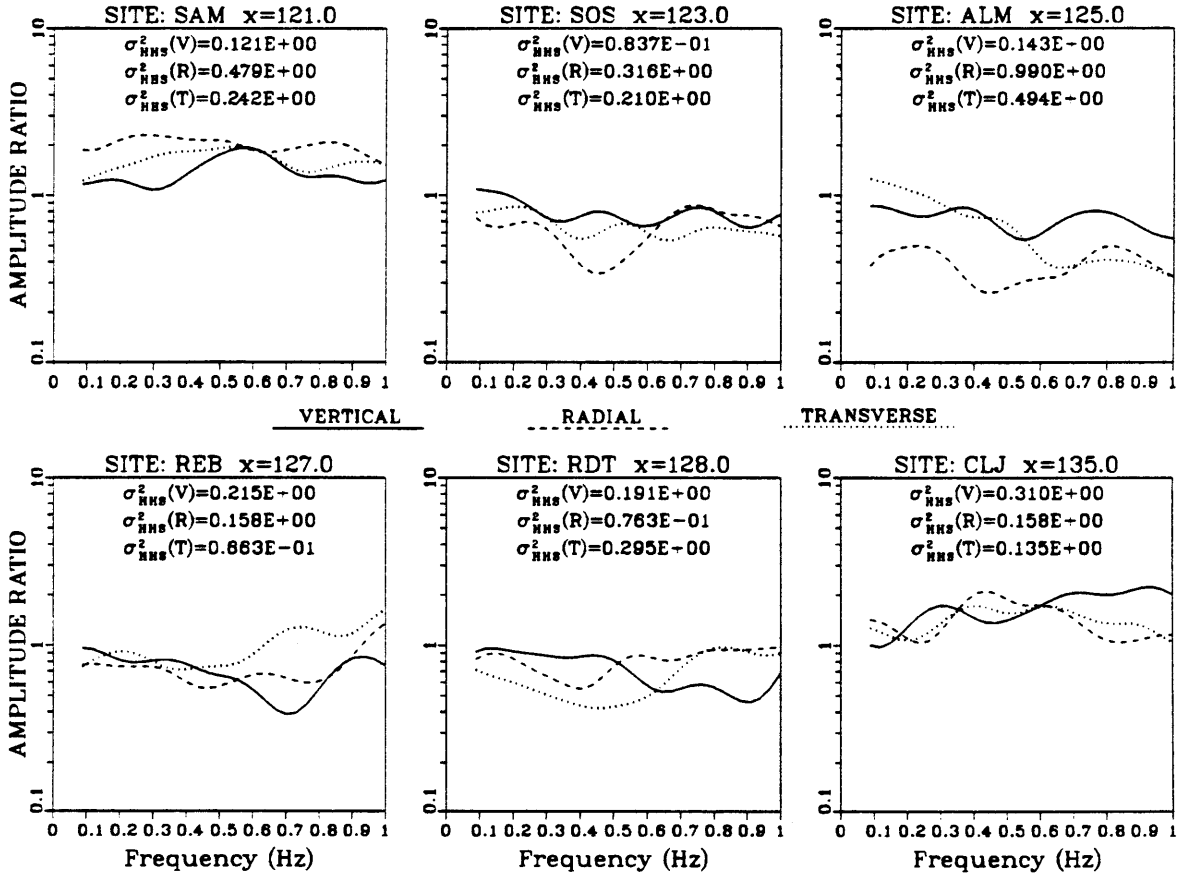


Figure 2.30 Spectral amplitude ratios for data averaged over all northwestern events. A total of 7 events were used in the average.

OBSERVED SPECTRAL RATIOS FOR
 DATA FROM SOUTHEASTERN EVENT REGION RECORDED ON JEMEZ ARRAY 2
 NUMERATORS: average over 3 events DENOMINATOR: average over 6 sites
 σ_{HNS}^2 (log): V=0.291E+00 R=0.381E+00 T=0.269E+00 Total=0.314E+00

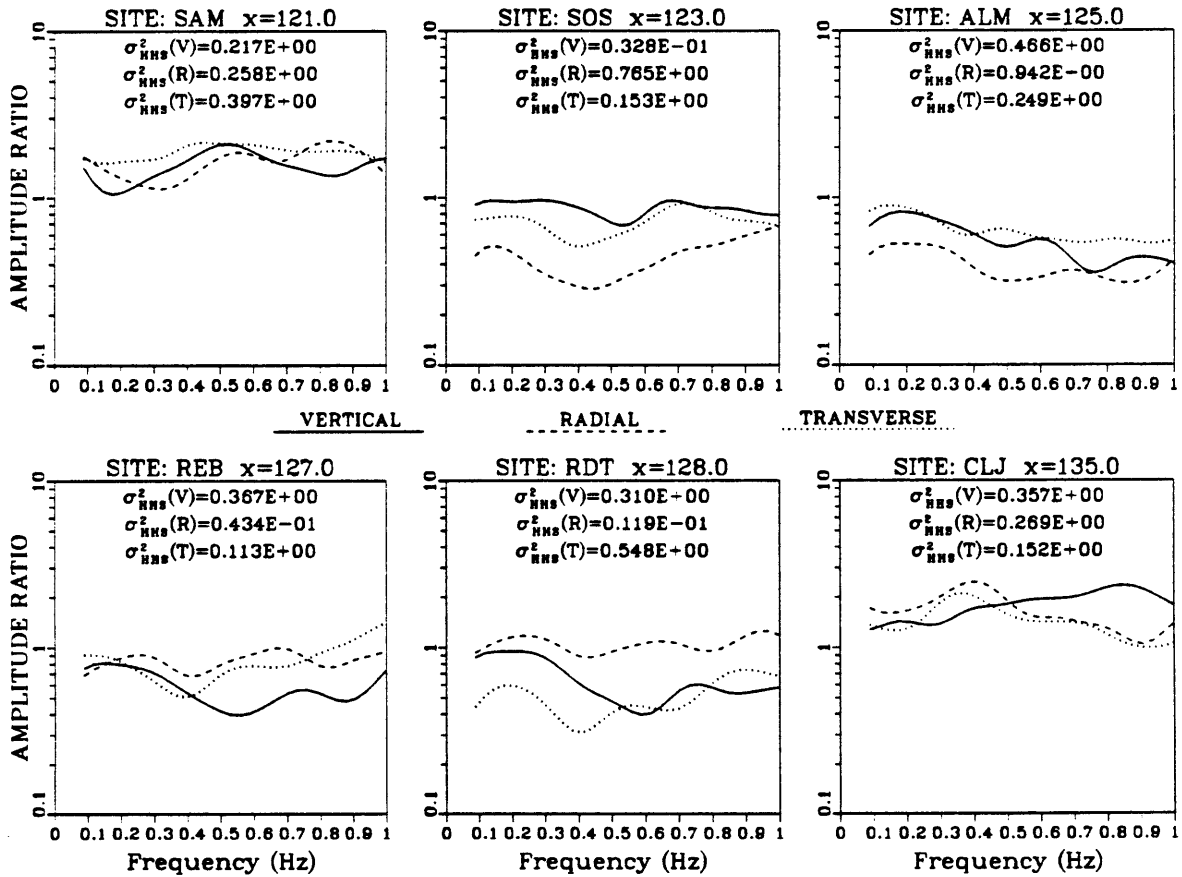


Figure 2.31 Spectral amplitude ratios for data averaged over all southeastern events. A total of 3 events were used in the average.

OBSERVED SPECTRAL RATIOS FOR
 DATA FROM NORTHWEST & SOUTHEAST EVENT REGION RECORDED ON JEMEZ ARRAY 2
 NUMERATORS: average over 10 events DENOMINATOR: average over 6 sites
 σ_{HHS}^2 (log): V=0.235E-00 R=0.355E+00 T=0.241E+00 Total=0.277E-00

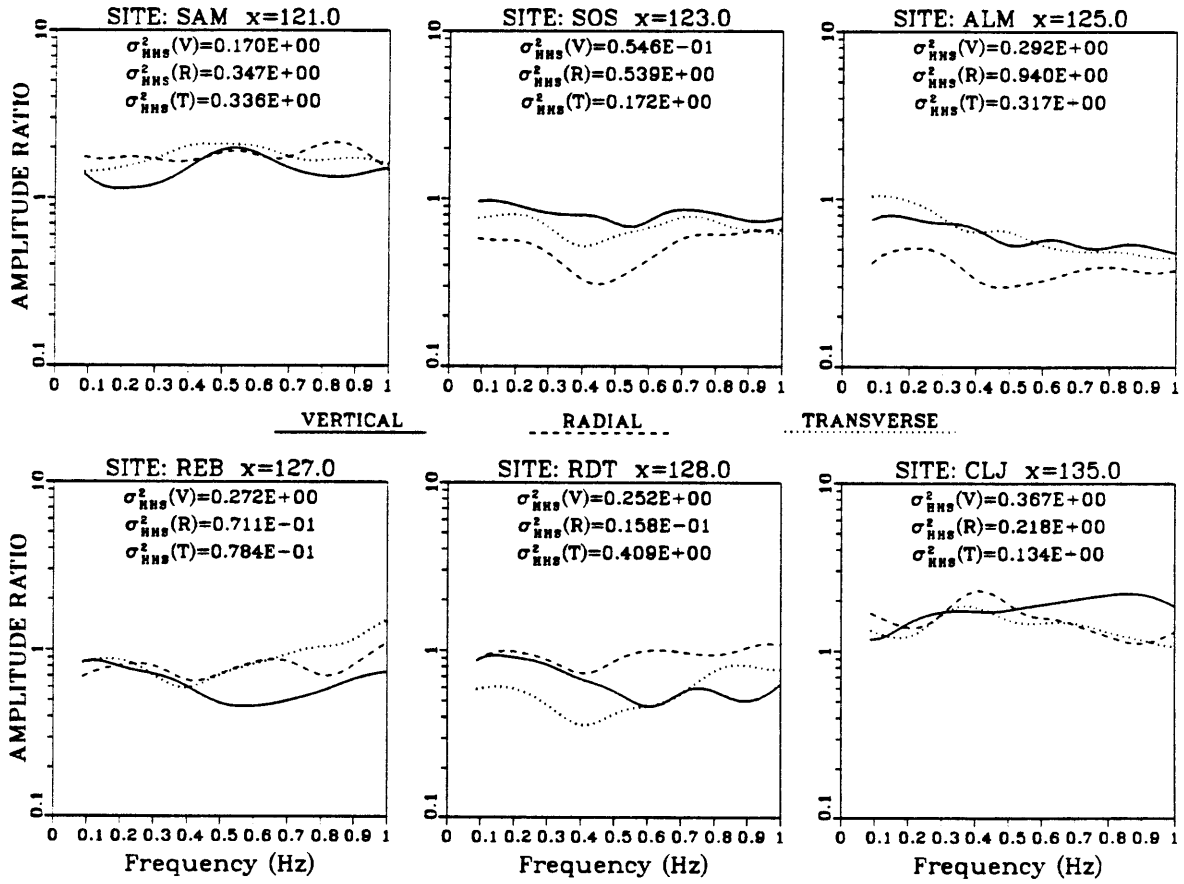


Figure 2.32 Spectral amplitude ratios average over both the 7 northwestern and 3 southeastern events shown in Figures 2.30 and 2.31.

Finally, Figure 2.32 shows the amplitude ratios obtained by averaging all events from all incidence angles and both directions, ten events in all. This figure is very similar to Figure 2.29 for the four Kuril events and suggests that the primary effects which are independent of incidence angle and directions may be adequately represented by the Kuril data. We make this statement with some caution, though, since the total average here is probably dominated by the fact that we have used more northwestern events in the average than southeastern events.

2.5 Measured P-Wave Arrival Time Delays

The direct P waves recorded for almost all of the 24 events listed in Table 2.2 showed very clear first motions at all nine sites used for both arrays. The vertical component seismograms shown previously in Figures 2.6 through 2.11 are typical of the quality obtained for the first arrivals. Although not all of the 24 events were recorded at all sites in operation, we managed to select a total of 116 high quality first arrivals from this data set. Since three sites were shared by both instrument arrays, it was easy to combine the arrival time observations from both deployments by measuring time delays for the first motion at each site relative to one reference site common to all recorded events and both arrays. This allowed the time delay due to upper-crustal P-wave velocity structure to be characterized as a function of site location and incidence angle. Data reduced in this way allow the application of standard travel time inversion and ray tracing methods for determining the P-wave structure which best explains the observed travel time anomalies. In the present section we will present the time delay results and discuss the data reduction steps

used to obtain them. We will comment on possible interpretations only qualitatively here. The quantitative modeling will be discussed in detail in Chapter 4.

The only site at which every event in Table 2.2 was recorded was SAM. Therefore we chose it as the reference site mentioned above. This was somewhat fortuitous because this site always had the largest amplitudes, as we showed in the previous section, and therefore usually had the sharpest first motion, making it an ideal choice above its necessity as the only common site. To measure the delays relative to this site as accurately as possible we used a cross-correlation technique in which the first half-cycle of the first motion in the vertical component was isolated from the rest of the signal at each non-reference site and then correlated with that at SAM for each event. The resulting time lag was then measured at the peak value of the cross-correlation series obtained for each signal pair. We used the spectral technique for computing cross-correlation rather than the time domain overlap-shift method. After manually windowing and isolating the first half-cycle from each seismogram, the beginnings were padded with zeros so that the FFT windows for the signals at all sites for each event started at the same absolute time. The ends were also zero-padded to obtain a wide enough window, relative to the length of actual signal used, to avoid undesirable endpoint overlap effects [e.g., *Brigham*, 1974]. After computing the FFT's of the windowed signals for each event, the cross-correlations were obtained by multiplying the complex spectrum at each site by the conjugate of the reference spectrum and then computing the inverse FFT of the result:

$$d_{\text{cor}}^{(jk)}(t) = \text{IFFT} \left\{ D_k^{(j)}(\omega) \cdot \overline{D_{\text{ref}}^{(k)}(\omega)} \right\}, \quad (2.9)$$

where j = event index, k = site index, $D_k^{(j)}$ is the complex spectrum of the first half-cycle of the P wave at site k for event j , $D_{\text{ref}}^{(j)}$ is the spectrum at the reference site for event j , and $d_{\text{cor}}^{(jk)}$ is the correlation time series for site k and event j relative to the reference site.

Since we have selectively windowed only the first half-cycle of the first arrival, the desired time delay will correspond to the location of the maximum positive value of $d_{\text{cor}}^{(jk)}$, which will have a smooth bell shape. We chose to use only the first half-cycle to decrease the width of the correlation peak and thus to increase the precision with which the peak may be located. In all cases we found that the peak could be selected to within one sampling interval, which in our case represents a precision of ± 4 msec. However, we also discovered that by adjusting the width of actual data in the FFT window by as little as ± 10 samples the location of the peak could shift by as much as ± 10 msec and we consider this to be a conservative estimate of the accuracy obtainable with this method. Also, we mentioned earlier that the accuracy to which we trust the clock times recorded by the instruments is typically ± 10 msec, except for cases where absolute drift measurements could not be obtained. The worst cases of clock measurement error were assigned an accuracy of ± 100 msec. Thus the typical accuracy with which the relative arrival time delays can be measured is ± 20 msec, which is quite good. The worst case yields errors of ± 110 msec, which is still acceptable for our purposes.

There are two forms in which the measured time delays may be presented. The first form has the normal moveout due to non-vertical incidence built into the delays so that naturally the delay will always increase with distance along the

earth's surface. These delays are obtained from the unaltered results of the cross-correlation above and we will see in Chapter 4 that this is the most useful form to have the data in when comparing with the results of ray-tracing. For the second form, several additional processing steps are taken with the aim of displaying the features in the delay observations which may be attributable to inhomogeneous velocity structure. This involves subtracting an estimate of the normal moveout, described below, correcting for differences between the array azimuth and source direction and subtracting the average delay over all sites from these results for each event. This would be the best form to use for travel time inversion since any delays left over after making these corrections can then be modeled in terms of slowness perturbations distributed along the associated ray paths relative to some simple initial model.

Since the moveout-corrected delays contain mainly information about irregular structure, it is more informative to examine these first to get some idea of what the major structural features are. Once these are known, the details can be determined by fitting ray-tracing results to the uncorrected delays. Figure 2.33 shows examples of the moveout-corrected delays for two events recorded at all six sites on array 2. The first, marked by open squares, is for one of the Kuril Islands events to the northwest and the second is for the Jujuy, Argentina event to the southeast. The epicentral distances, Δ , to the central site RDT and incidence angles, θ_0 , are listed at the bottom of the figure. Recall that positive θ_0 corresponds to northwestern events and negative θ_0 to southeastern events. Each marked point corresponds to the moveout-and-azimuth-corrected delay at one site relative to the average over all six sites. The site names are marked along the top of the figure at their correct

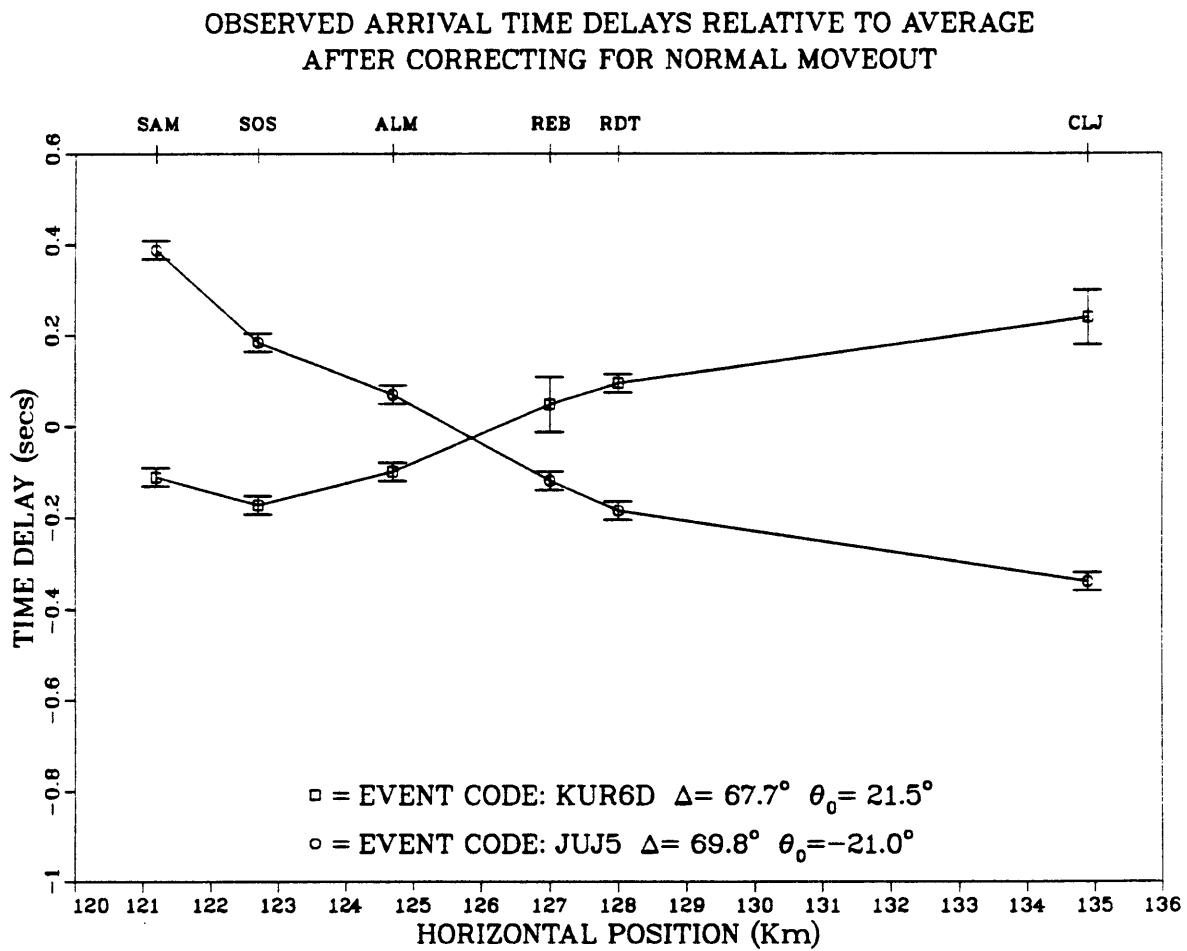


Figure 2.33 Observed arrival time delays relative to the average after correction for normal moveout and azimuth for two events recorded on array 2. Open squares are for a northwestern event and open circles for a southeastern event. Vertical bars on each point represent the estimated error in the observed delay times. θ_0 is the estimated Richter incidence angle, positive for northwestern events and negative for southeastern events. Δ is the epicentral distance in degrees to the central site RDT.

horizontal location. The vertical bars show the estimated errors discussed previously which for the most part are ± 20 msec. The larger errors at REB and CLJ for the Kuril event are due to clock drift measurement problems.

The moveout correction was calculated using the estimated incidence angles listed and a moveout velocity of 6.34 km/sec. This is simply the surface velocity which applies for the incidence angle tables in *Richter* [1958] used here to estimate θ_0 from Δ . The following simple formula was used to estimate the normal moveout delay time between any two given sites:

$$T_{mov} = \frac{X \sin \theta_0}{\alpha_{mov}}, \quad (2.10)$$

where X is the horizontal distance between the two sites, θ_0 is the incidence angle and α_{mov} is the moveout velocity. Since we have subtracted the normal moveout for each event, a homogeneous flat-layered structure for the caldera would yield a zero relative delay at all sites. If we had not subtracted the average delay from all sites for each event, then both plots would have zero delay at the reference site, SAM.

The most obvious feature of the plots in Figure 2.33 is that the largest time delays are observed on the side of the caldera furthest from the source, i.e., at REB, RDT and CLJ for the Kuril event and at SAM, SOS and ALM for the Jujuy event. The largest delay, relative the average, is observed at SAM for the southeastern event. Furthermore, the difference between the maximum and minimum delays is nearly twice as large for the southeastern event, ~ 700 msec, than for the northwestern event, ~ 400 msec. This pattern is very typical of all events recorded on array 2 and strongly suggests the existence of a low velocity zone (LVZ) at a

significant depth beneath the caldera. We will see in Chapter 4 that the width and horizontal location of the zone of largest delays along the surface, as well as the strength of the delays, will allow us to constrain the width and average depth of this LVZ, as well as its minimum height and velocity.

Figure 2.34 shows similar plots for two events recorded on array 1. Here the northwestern event was from the Kommandorsky Islands and the southeastern event was from Chile. Although the record of the Chile event at RDT, shown in Figure 2.11, was unusable for amplitudes, the cross-correlation method did yield a distinct peak which we used to obtain the delay point plotted here. However, we have assigned a large error to this point because the correlation peak was wider than for other data. Figure 2.34 shows that the delay zone is largely localized to the caldera sites, SAM, ALM and RDT and again the largest delay relative the average is observed at SAM for the southeastern event. However, we must also note that the delays at CAP for the northwestern event and at PNY for the southeastern event are considerably larger than we would expect from normal moveout alone. Otherwise these points would fall very close to the minimum delay in each case. This suggests that the structure is probably much more complex than the simple localized LVZ we have proposed. We will show that some of this complexity may be accounted for by an irregular low velocity surface layer and some by allowing the deep LVZ to take on very bizarre shapes or by adding separate smaller inclusions. At any rate these added complexities do not contradict the basic properties of the deep LVZ and may be considered as secondary details of our desired structural model.

Finally, in Figure 2.35 we have plotted all of the 116 time delay observations in a manner which is partially qualitative yet extremely illustrative and convincing.

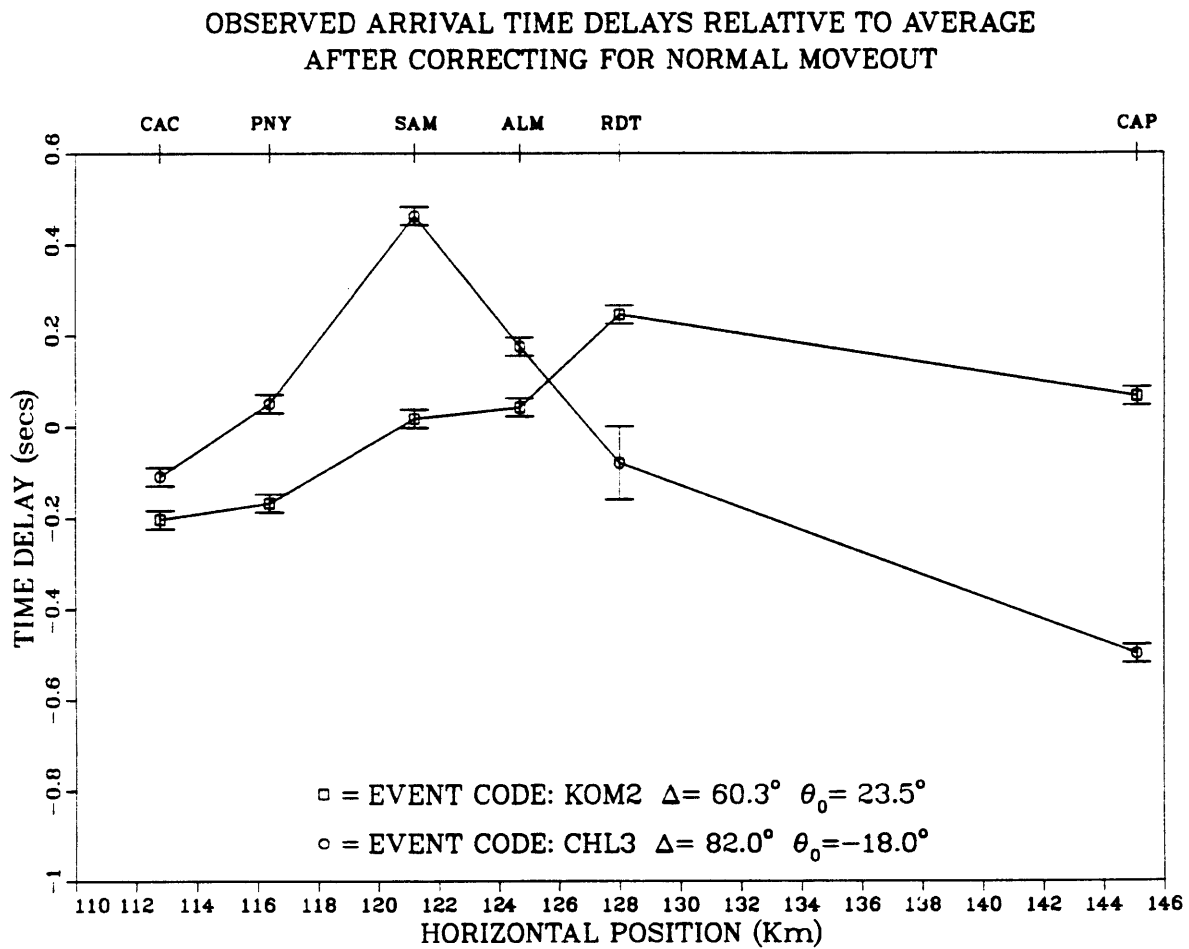


Figure 2.34 Same as Figure 2.33 except that the data plotted are for two events recorded on array 1.

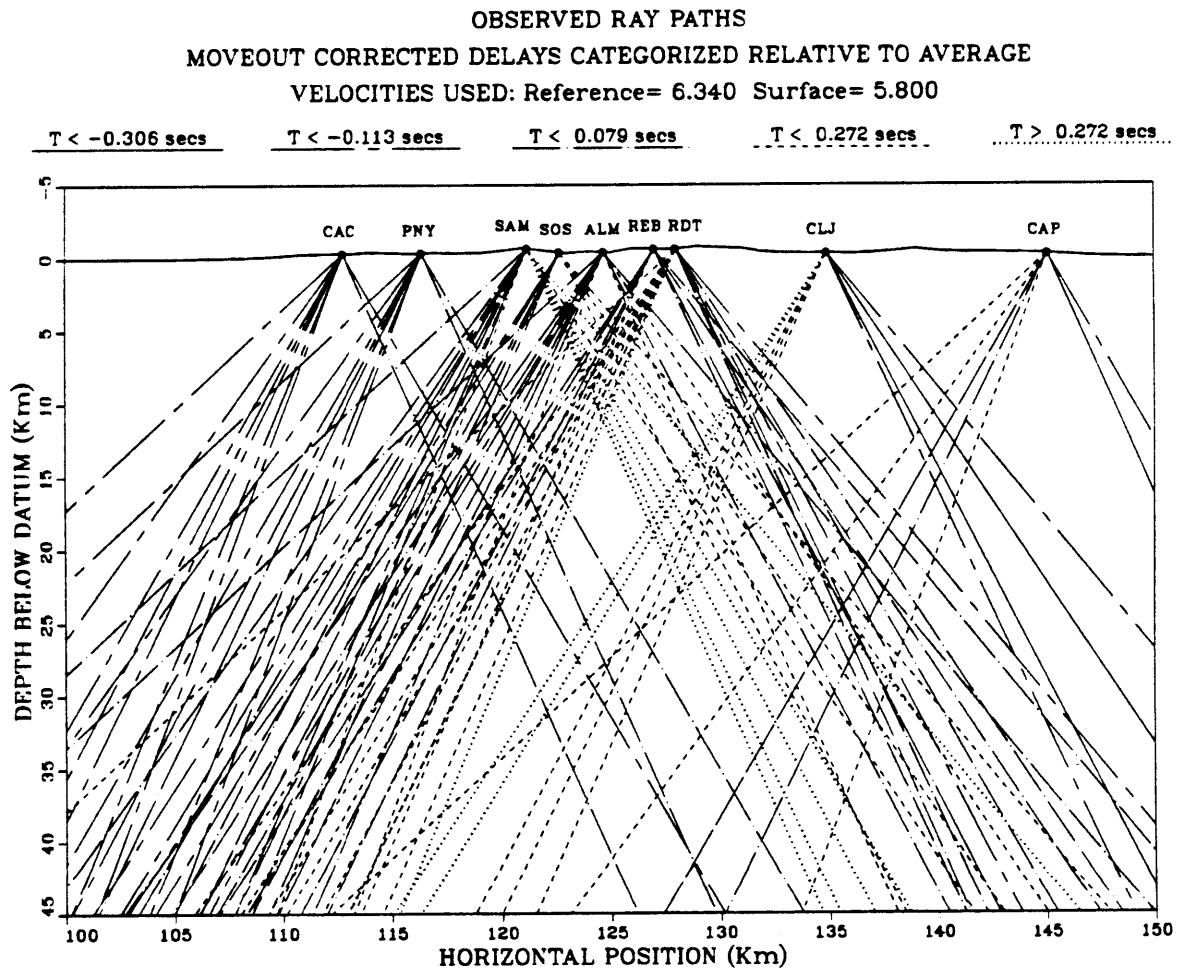


Figure 2.35 Observed ray paths for all events recorded on both arrays 1 and 2. Incidence angles were estimated from *Richter* [1958] and corrected for the lower near-surface P-wave velocity for the Valles Caldera region. Rays are categorized according to the strength of the arrival time delay for each one and plotted in different line styles indicated in the legend. Site codes are listed near their locations along the free surface topography profile where the rays end at the top of the figure.

The approach is very similar to that used by *Steeple & Iyer* [1976] for delineating a low velocity zone beneath the Long Valley Caldera in California. The data are plotted as straight ray paths with incidence angles derived from the Richter angles estimated previously. The surface velocity of 6.34 km/sec used in Richter's tables is higher than what other investigators have found for the basement granite in the Jemez Mts. region [e.g., *Olsen et al.*, 1986; *Ankeny et al.*, 1986], so we have corrected the Richter angles to account for the more reasonable basement velocity of 5.8 km/sec, thereby steepening the estimated incidence angle for each event. The ray endpoints at the top correspond to the 9 site locations labeled by name along the surface topography profile for the Jemez Mountains. Next, each ray was categorized according to the value of the time delay observed at the site where the ray ends. In this way all of the observed ray paths were broken down into 5 separate categories represented by different line styles. The legend indicates the lower bound of each delay category. The upper bound of each category is simply the lower bound of the next highest category. The smallest delays are represented by solid lines and the largest by dotted lines. In general, the more broken the line, the stronger the delay. Ray paths are plotted to a depth sufficient to show where the major structural anomalies must be located to produce the observed delay pattern at the surface.

Clearly regions where strongly delayed rays intersect less delayed rays must be excluded as possible locations for a low velocity inclusion. This means the LVZ must be at least 5 km deep since this is approximately the minimum depth where the strongest delayed rays, beneath ALM, REB and RDT, intersect each other without interfering with any of the more weakly delayed rays. We can also begin to constrain the horizontal location and maximum width of the LVZ in a similar

manner. We might even go so far as to suggest that the inclusion could be lens-shaped, with its left and right edges tapering out gradually, since there is a very clear horizontal gradation pattern beginning with the strongest delays at approximately ($x = 128$ km, $z = 18$ km) and decreasing steadily to either side. Of course the major assumption here is that the inclusion is homogeneous with a uniform P-wave velocity. Since this entire discussion is largely qualitative we will end any further intuitive modeling here and defer the remaining analysis of the delay data to the ray-tracing and formal inversion methods. The fact that we can actually draw so many intuitive yet convincing conclusions based on a simple plot like Figure 2.35, however, gives us confidence that the quality and coverage of the arrival time data should allow us to obtain reliable detailed models from the ray-tracing results in Chapter 4.

CHAPTER 3

The Aki-Larner Discrete Wavenumber Method

3.1 Introduction and History

The discrete wavenumber method for computing synthetic waveform spectra has been in existence in a practical form since Keiiti Aki first developed the algorithm for solving the plane SH-wave scattering problem for layered models with irregular interfaces. Kenneth Larner, at the time a student under Aki, revised the method and contributed to the first publication, [Aki & Larner, 1970], which gave a concise exposition of the algorithm for SH waves in a single layered model with flat free surface and irregular layer-halfspace interface. In his doctoral thesis, Larner [1970] extended the algorithm to P-SV scattering problems and presented the explicit formulation needed to set up problems for multiple irregular interfaces. The basics of the formulation were published in Aki & Richards [1980], where it was referred to as the “Rayleigh-Ansatz Method” for reasons which will become clear in the next section. It has also been commonly identified generically by the name “Discrete Wavenumber Method.” The next person to use the method extensively was another of Aki’s students, Michel Bouchon. Subsequently Bouchon and his students began to refer to the technique as the “Aki-Larner Method” in almost all of their publications. This name is now in wide use since it gives credit to the original developers of the method, and we also will use it throughout this thesis. This chapter is devoted to reviewing the history and details of the method from its initial form to its present state of extended capability. Attention here is focused on

in-plane P-SV scattering problems, as this is the main subject of the present thesis. The historical review is followed by an in-depth presentation of the general P-SV formulation and method of solution for the problem of multiple irregular layers over a half-space. It should be pointed out first that the Aki-Larner Method has stood the test of time well, suffering few revisions, and nearly all subsequent advances have involved changing the source or increasing the complexity of the model in response to a steady increase in computer storage and speed over the last 18 years.

The original method as presented in *Aki & Larner* [1970] and *Larner* [1970] uses steady state plane waves as the source. This limitation restricts the applicability of the method to studies of ground motion due to incident teleseismic waveforms. This is not a serious restriction at all since teleseismic data can be obtained at almost any region on the earth. The most complex problems solved in *Larner* [1970] included an irregular free surface, at most one irregular buried interface and allowed topographic variations only in two dimensions, the x - z model plane. The resulting models were thus “washboard” features and solutions were obtained for the scattered wavefield generated for three distinct cases of incident plane wavefields: 1.) in-plane SH waves, 2.) in-plane P or SV waves and 3.) arbitrary azimuth P, SV or SH waves. The first two cases are completely uncoupled from each other because there can be no conversions between P-SV and SH motions for in-plane waves when the topography is two-dimensional. The third case involves coupling between all three waves types because the wavefield is no longer restricted to being normal to the y -axis. By combining the Aki-Larner and Thomson-Haskell methods [*Thomson*, 1950; *Haskell*, 1953, 1960, 1962], Larner was able to include additional flat layers in

his models without significantly increasing the size of the problem. Additional irregular interfaces expand the problem considerably, however, and computers available in the late 1960's were not large enough or fast enough to handle problems with more than one or two irregular interfaces.

Following on the work presented in *Aki & Larner* [1970] the method was compared with the finite difference technique by *Boore et al.* [1971]. Surface motion was calculated for a crust-mantle model and a soft basin model and excellent agreement was obtained between the results of the two methods. This was the first time that the validity of the Aki-Larner method had been checked against another independent solution for identical problems.

The Aki-Larner method was used next by *Bouchon* [1973] to study the effects of topographic irregularities on ground motion. The results were successfully applied to the Pacoima Dam accelerograph record of the 1971 San Fernando earthquake. An improvement to the Aki-Larner method was also presented in which the residual stress at the free surface is used to make corrections to the computed surface displacement. However, this correction is usually not necessary since the residual stress, as will be demonstrated later in this thesis, is normally very small. *Bouchon* [1973] also succeeded in synthesizing time domain seismograms from the single-frequency solutions.

The next improvements to the Aki-Larner method involved the introduction of non-plane wave sources as inputs to the models. This allowed the placement of point or line sources within the model which in turn allowed comparisons with local and regional data. The works of *Bouchon* [1976], *Bouchon & Aki* [1977] and *Bouchon* [1979] were devoted to the development and application of the source

representation. The work in this thesis utilizes teleseismic data, allowing the use of plane waves as sources in the Aki-Larner method. No further mention will be made concerning the discrete wavenumber representation of sources.

Bard & Bouchon [1980a,b] next performed exhaustive studies on sedimentary basin and alluvial valley problems for the SH and P-SV plane wave scattering cases and found that surface waves generated at the valley edges were a major component of the resulting ground motion. They also described a practical approach for synthesizing realistic seismograms from multiple single-frequency steady-state solutions through convolution with a Ricker source wavelet. Next, *Bard & Bouchon* [1985] used the same method again to study specific 2-dimensional resonance patterns for sediment-filled valleys. Some of their results were compared with the integral equation method of *Sanchez-Sesma & Esquivel* [1979], and excellent agreement was observed even for fairly steep interface slopes. They demonstrated that 2-D resonance behavior differs significantly from that predicted by traditional 1-dimensional theory.

The most recent improvements to the Aki-Larner method were performed by *Bard & Gariel* [1986] and *Kohketsu* [1987]. In the former paper the method was extended to allow the study of 2-dimensional sediment-filled valleys containing vertically stratified structures. They also were the first investigators to include anelastic attenuation as a model parameter. Although their work is very thorough and convincing, they gave very few details on how they introduced these changes to the Aki-Larner method. *Kohketsu* [1987] presents the ground work for a very tantalizing new algorithm which allows the Aki-Larner method to be extended to deal with an arbitrarily large number of irregular interfaces with only minor increases

in computation time. Currently this method has been formulated only for the SH scattering problem and also was presented in a form which is not very accessible or reproducible.

Kohketsu makes a claim that one of the major sources of error in the Aki-Larner method can be eliminated simply by adding a transparent dummy layer to the models in the medium containing the incident wave. The source of error in question is the Rayleigh ansatz representation of scattered waves in a halfspace, which we will discuss in detail in the next section of this chapter. Let it suffice here to point out that the ansatz error is inherent to the method and cannot be removed by so simple a trick. Just to be sure, though, we have tried Kohketsu's suggestion with the P-SV algorithm used in this thesis and it has absolutely no effect on the solutions for a wide range of problems tested.

Since Kohketsu's work has not been extended to the P-SV case yet, the following presentation of the traditional Aki-Larner P-SV formulation should still be useful. We will use a very generalized notation which can be extended to any number of irregular interfaces. But, since the size of the problem grows rapidly in computation and storage requirements as more interfaces are added, we have been able to solve problems only for a maximum of four irregular interfaces. This is limited purely by the size, speed and precision of available computers and is the largest problem that could be run reliably on a VAX 8650. Appendix 1 contains the detailed formulas required to program the 4-interface P-SV problem.

3.2 Formulation

The formulation of the Aki-Larner method presented here adheres closely to the notation used in *Aki & Larner* [1970] and in *Larner* [1970] and is largely a detailed review of those works. The aim of the following presentation is to provide the specific formulation used to extend the method for multiple irregular interface problems. *Larner* [1970] provided a detailed formulation for P-SV-SH scattering problems in which the models were strictly 3-dimensional layered structures with only one irregular interface. He reduced the problem to be pseudo 2-dimensional by assuming the irregularity to be dependent only on the x and z model coordinates. The irregularity will resemble a washboard in 3 dimensions and its strike will be parallel to the y axis. Thus the model can be described completely by defining a 2-D vertical plane perpendicular to the y -axis. This means that all partial derivatives with respect to the y coordinate encountered in the 3-D formulation will vanish and the in-plane P-SV motions will be completely decoupled from the transverse SH motion. This allows the scattering problems for P-SV and SH motions to be solved separately. By employing a clever coordinate rotation tensor *Larner* [1970] combined the P-SV and SH solutions to obtain the total 3-D wavefield for arbitrary azimuth problems with the washboard structures. For the present study, however, a washboard structure would be a very poor model for the Valles Caldera. We would not expect to gain much additional information over a 2-D model by synthesizing the scattered SH component under such restrictive structural conditions. So for the purposes of this thesis we will reduce the formulation, at the appropriate stage, to that for the strictly 2-dimensional P-SV problem alone and will allow waves to propagate only in the (x,z) model plane. We begin, as in *Larner* [1970], by

assuming the structures have no y -dependence. In general, the Fourier Transform of the wavefield must satisfy the vector wave equation:

$$-\rho\omega^2\hat{\underline{U}}(x, y, z, \omega) = (\lambda + 2\mu)\nabla(\nabla \cdot \hat{\underline{U}}) - \mu\nabla \times (\nabla \times \hat{\underline{U}}), \quad (3.1)$$

where $\hat{\underline{U}} = (\hat{u}, \hat{v}, \hat{w})$ is the total integrated displacement vector. The basis of the method is to first represent the total displacement field in each layer as a superposition of individual fields characterized by their x -component of wavenumber, k [Larner, 1970]:

$$\hat{\underline{U}}(x, y, z, \omega) = \int_{-\infty}^{+\infty} \underline{U}(x, y, z, \omega, k) dk. \quad (3.2)$$

The k -decomposed wavefields, \underline{U} , are themselves made up of a mixture of P, SV and SH waves, and in order to apply boundary conditions we must first separate these wave types so that individual expressions for each component of motion, u , v and w may be obtained. To do this we make use of the familiar Helmholtz theorem which expresses \underline{U} as a combination of scalar and vector wave potentials:

$$\underline{U} = \nabla\tilde{\Phi} - \nabla \times (\underline{B} + \nabla \times \underline{C}), \quad (3.3)$$

where the vector potentials may be represented by:

$$\underline{B} = (0, 0, \tilde{\Upsilon}),$$

$$\underline{C} = (0, 0, \tilde{\Psi}).$$

The three scalar potentials $\tilde{\Phi}$, $\tilde{\Upsilon}$ and $\tilde{\Psi}$ correspond respectively to the P, SH and SV wave contributions to \underline{U} . Using equation (3.3) we may now expand $\underline{U} = (u, v, w)$

to obtain:

$$\begin{aligned}
u(x, y, z, \omega, k) &= \frac{\partial \tilde{\Phi}}{\partial x} - \frac{\partial \tilde{\Upsilon}}{\partial y} - \frac{\partial^2 \tilde{\Psi}}{\partial x \partial z}, \\
v(x, y, z, \omega, k) &= \frac{\partial \tilde{\Phi}}{\partial y} - \frac{\partial^2 \tilde{\Psi}}{\partial y \partial z} + \frac{\partial \tilde{\Upsilon}}{\partial x}, \\
w(x, y, z, \omega, k) &= \frac{\partial \tilde{\Phi}}{\partial z} + \frac{\partial^2 \tilde{\Psi}}{\partial x^2} + \frac{\partial^2 \tilde{\Psi}}{\partial y^2}.
\end{aligned} \tag{3.4}$$

These expressions represent the general solution to equation (3.1) for a homogeneous body. For the specific problem at hand, this body is bounded by irregular interfaces. Since the irregularities have no y -dependence, all partial derivatives with respect to y will vanish in equations (3.4). Furthermore, we will now impose the 2-D restriction on the wavefield, mentioned above, and allow only for P-SV motion propagating in the (x, z) plane of model symmetry. Thus we will require only the $\tilde{\Phi}$ and $\tilde{\Psi}$ wave potentials above and will obtain solutions only for $\underline{U} = (u, 0, w)$. Then by first making the substitution $\tilde{\Upsilon} = \partial \tilde{\Psi} / \partial x$, we can rewrite equations (3.4) as:

$$\begin{aligned}
u(x, z, \omega, k) &= \frac{\partial \tilde{\Phi}}{\partial x} - \frac{\partial \tilde{\Psi}}{\partial z}, \\
v(x, z, \omega, k) &= 0, \\
w(x, z, \omega, k) &= \frac{\partial \tilde{\Phi}}{\partial z} + \frac{\partial \tilde{\Psi}}{\partial x}.
\end{aligned} \tag{3.5}$$

$\tilde{\Phi}$ and $\tilde{\Psi}$ must satisfy the scalar wave equations:

$$\begin{aligned}
\left(\nabla^2 + \frac{\omega^2}{\alpha^2} \right) \tilde{\Phi} &= 0, \\
\left(\nabla^2 + \frac{\omega^2}{\beta^2} \right) \tilde{\Psi} &= 0,
\end{aligned} \tag{3.6}$$

where α = acoustic velocity and β = shear velocity of the elastic solid. The solutions to equations (3.6) for the k -decomposed plane wave potentials, $\tilde{\Phi}$ and $\tilde{\Psi}$, are given in terms of spatially independent up-going and down-going potentials by:

$$\begin{aligned}\tilde{\Phi}(x, z, \omega, k) &= \Phi^d(\omega, k) e^{i(kx + \nu z)} + \Phi^u(\omega, k) e^{i(kx - \nu z)}, \\ \tilde{\Psi}(x, z, \omega, k) &= \Psi^d(\omega, k) e^{i(kx + \nu' z)} + \Psi^u(\omega, k) e^{i(kx - \nu' z)},\end{aligned}\tag{3.7}$$

where k = x -component of wavenumber and ν and ν' are the z -components (positive downward in this case) of the P and S wavenumbers respectively. Defining the characteristic P and S wavenumbers (which are simply the magnitudes of the wavenumber vectors), K_α and K_β , the vertical components can be obtained by:

$$\begin{aligned}\nu &= (K_\alpha^2 - k^2)^{1/2}, \\ \nu' &= (K_\beta^2 - k^2)^{1/2}, \\ K_\alpha &= \frac{\omega}{\alpha}, \\ K_\beta &= \frac{\omega}{\beta}.\end{aligned}\tag{3.7a}$$

The first major source of error in the Aki-Larner method arises from the use of the Rayleigh ansatz representation of the scattered wavefield in the halfspace [Rayleigh, 1907]. The ansatz is a particular form of equations (3.7) which only allows scattered waves in a halfspace to propagate away from its bounding interface. The ansatz cannot completely represent the total scattered wavefield if the interface is significantly irregular because it cannot account for waves which may be scattered inward toward the interface. In particular, for an up-going incident P wave in a

halfspace bounded above by an irregular interface, the ansatz representations of the wave potentials in the halfspace are:

$$\begin{aligned}\tilde{\Phi}(x, z, \omega, k) &= \Phi^d(\omega, k) e^{i(kx + \nu z)} + e^{i(k_0 x - \nu_0 z)}, \\ \tilde{\Psi}(x, z, \omega, k) &= \Psi^d(\omega, k) e^{i(kx + \nu' z)}.\end{aligned}\tag{3.8}$$

where k_0 and ν_0 are the horizontal and vertical wavenumbers of the incident P wave for an incidence angle θ_0 (defined clock-wise from vertically upward) and are given by:

$$\begin{aligned}k_0 &= K_\alpha \sin \theta_0, \\ \nu_0 &= K_\alpha \cos \theta_0.\end{aligned}\tag{3.8a}$$

Clearly, this representation cannot account for any waves which may be scattered upward by the interface irregularity because only down-going potentials are allowed. Thus the Rayleigh ansatz will give reliable results only if the irregularity is smooth relative to the wavelengths being considered. The ansatz error has been discussed thoroughly by *Aki & Larner* [1970], *Larner* [1970], *Aki & Richards* [1980] and by nearly all other authors who have used the method. Rather than dwell on this and other sources of errors separately we will instead check the overall reliability of our solutions by examining the boundary condition residuals and the wavenumber spectra of the various wave potentials obtained.

The expressions in equations (3.7) and (3.8) may be used to formulate the total wavefields for any model composed of multiple isotropic layers with the top-most layer bounded above by a free surface and the bottom-most layer bounded below by a halfspace. Figure 3.1 shows a typical 2-D model geometry for this type of

PROBLEM CONFIGURATION FOR MULTIPLE IRREGULAR INTERFACE MODELS

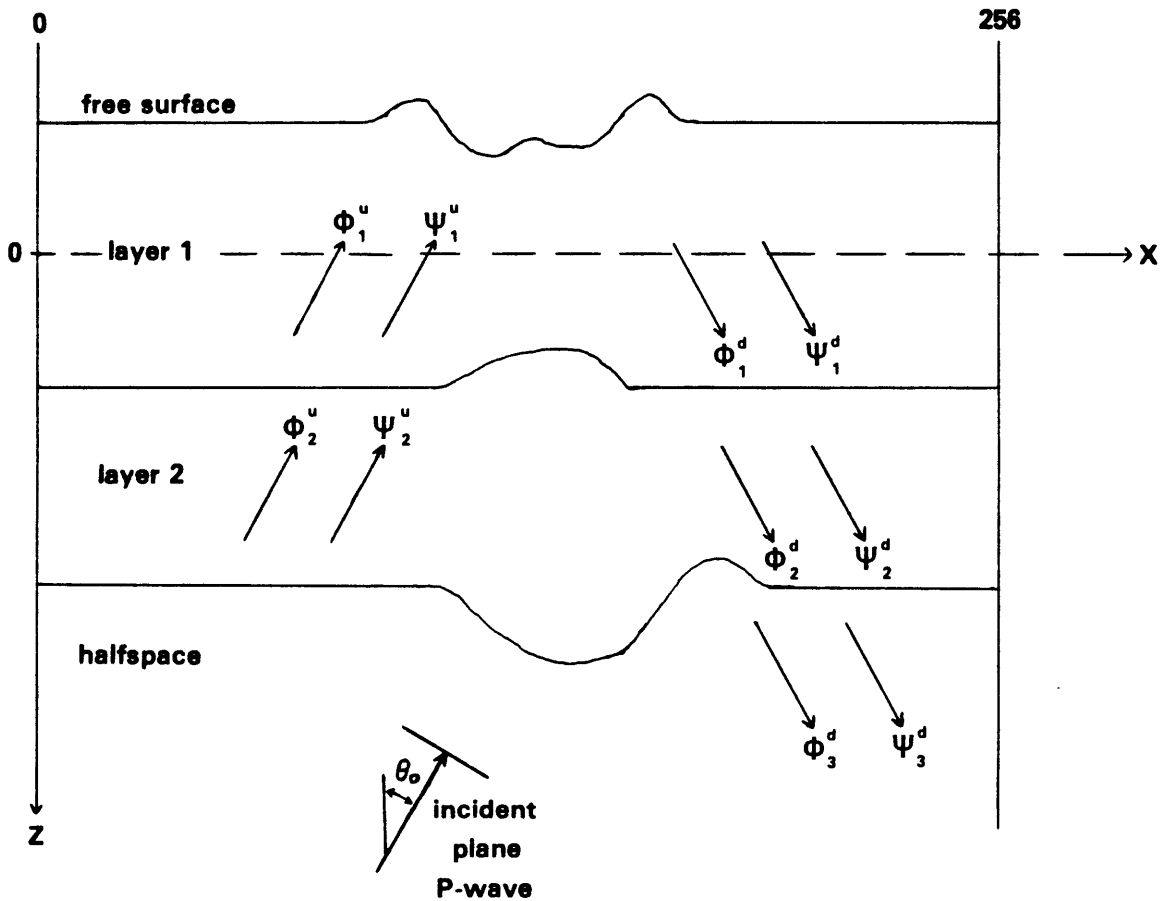


Figure 3.1 Example of 2-D model geometry and problem setup for the P-SV scattering case. Arrows in each medium represent up-going and down-going unknown wave potentials to be solved for. Problem is shown for a plane P-wave source with incidence angle θ_0 arriving from below. Irregular interfaces are functions only of the x -coordinate. The z -coordinate is defined to be positive downward.

problem with the various up-going and down-going wave potentials labeled in each medium. The interface shapes are functions only of x and can be written in the general form $z = \zeta(x)$, where $\zeta(x)$ may be either an analytic functional form (such as a simple cosine shape) or could represent a digitized series of topography samples for some arbitrary shape. The source wave in this case, and throughout this thesis, is a steady-state plane P wave with unity potential amplitude.

We need to find solutions for all of the up-going and down-going wave potentials in each medium as functions of k for each frequency ω so that equation (3.5) and a discrete-summation version of equation (3.2) may be used to construct the displacements at arbitrary locations in the model. This is done by satisfying exactly in the wavenumber domain the boundary conditions of vanishing stress at the free surface and continuity of stress and displacement across each buried interface. If the model contains P layers above the halfspace, then there will always be $4P + 2$ unknown potential functions to solve for (4 in each layer and 2 in the halfspace). In the following presentation the model layers are indexed from the free surface down as $[p = 1, 2, \dots, P + 1]$, where $p = P + 1$ corresponds to the halfspace. Similarly, the interfaces are indexed as $[p = 0, 1, \dots, P]$ so that interface p defines the bottom of layer p , and $p = 0$ corresponds to the free surface. Using this notation, the boundary conditions may be summarized as follows:

- (1) Vanishing horizontal traction along the free surface ($p = 0$):

$$\hat{T}_{x,1}(x, z = \zeta_0(x), \omega) = 0,$$

- (2) Vanishing vertical traction along the free surface ($p = 0$):

$$\hat{T}_{z,1}(x, z = \zeta_0(x), \omega) = 0,$$

.....

(4P - 1) Continuity of horizontal displacement along interface $p = P$:

$$\hat{u}_P(x, z = \zeta_P(x), \omega) = \hat{u}_{P+1}(x, z = \zeta_P(x), \omega)$$

(4P) Continuity of vertical displacement along interface $p = P$:

$$\hat{w}_P(x, z = \zeta_P(x), \omega) = \hat{w}_{P+1}(x, z = \zeta_P(x), \omega)$$

(4P + 1) Continuity of horizontal traction along interface $p = P$:

$$\hat{T}_{x,P}(x, z = \zeta_P(x), \omega) = \hat{T}_{x,P+1}(x, z = \zeta_P(x), \omega)$$

(4P + 2) Continuity of vertical traction along interface $p = P$:

$$\hat{T}_{z,P}(x, z = \zeta_P(x), \omega) = \hat{T}_{z,P+1}(x, z = \zeta_P(x), \omega).$$

Equations (3.5) are used to obtain expressions for the k -decomposed displacements, $u(x, z, \omega, k)$ and $w(x, z, \omega, k)$, which are used to evaluate the boundary conditions for the total displacements, \hat{u} and \hat{w} , above. The tractions are obtained from the same expressions for u and w by way of the stress tensor and Hooke's law as follows. The traction vector for layer p evaluated at a point on interface p is related to the stress tensor through the unit normal to the interface:

$$\underline{\hat{T}}_p(x, \zeta_p(x), \omega) = \underline{\hat{S}}_p(x, \zeta_p(x), \omega) \cdot \underline{n}_p(x), \quad (3.9)$$

where $\underline{\hat{S}}$ is the integrated stress tensor and $\underline{\hat{T}}$ is the integrated traction vector:

$$\begin{aligned} \underline{\hat{S}}(x, z, \omega) &= \int_{-\infty}^{+\infty} \underline{S}(x, z, \omega, k) dk, \\ \underline{\hat{T}}(x, z, \omega) &= \int_{-\infty}^{+\infty} \underline{T}(x, z, \omega, k) dk. \end{aligned} \quad (3.10)$$

The unit normal \underline{n} is defined to point away from the bottom of the interface toward the positive z direction. Its components may be written either in terms of the interface slope, $s(x) = d\zeta(x)/dx$, or in terms of the angle γ between the interface tangent and the x -axis:

$$\underline{n}(x) = \begin{pmatrix} n_x \\ n_y \\ n_z \end{pmatrix} = \begin{pmatrix} -s(x)(1+s^2(x))^{1/2} \\ 0 \\ (1+s^2(x))^{1/2} \end{pmatrix} = \begin{pmatrix} -\sin \gamma \\ 0 \\ \cos \gamma \end{pmatrix}. \quad (3.11)$$

The required traction components may then be written as:

$$\begin{aligned} \hat{T}_x &= \hat{S}_{xx}n_x + \hat{S}_{xz}n_z \\ \hat{T}_z &= \hat{S}_{zx}n_x + \hat{S}_{zz}n_z. \end{aligned} \quad (3.12)$$

So the tractions may be obtained using only three components of the stress tensor and these are derived from \hat{u} and \hat{w} using Hooke's law:

$$\begin{aligned} \hat{S}_{xx} &= \lambda\Theta + 2\mu\frac{\partial\hat{u}}{\partial x}, \\ \hat{S}_{zz} &= \lambda\Theta + 2\mu\frac{\partial\hat{w}}{\partial z}, \\ \hat{S}_{xz} &= \mu\left(\frac{\partial\hat{u}}{\partial z} + \frac{\partial\hat{w}}{\partial x}\right), \end{aligned} \quad (3.13)$$

$$\text{where: } \Theta = \frac{\partial\hat{u}}{\partial x} + \frac{\partial\hat{w}}{\partial z}.$$

The boundary conditions at each buried interface may be written in a general form as the vector integral equations:

$$\begin{aligned} \int_{-\infty}^{+\infty} \underline{U}_p(x, \zeta_p(x), \omega, k) dk &= \int_{-\infty}^{+\infty} \underline{U}_{p+1}(x, \zeta_p(x), \omega, k) dk, \\ \int_{-\infty}^{+\infty} \underline{T}_p(x, \zeta_p(x), \omega, k) dk &= \int_{-\infty}^{+\infty} \underline{T}_{p+1}(x, \zeta_p(x), \omega, k) dk, \end{aligned} \quad (3.14)$$

and at the free surface:

$$\int_{-\infty}^{+\infty} \underline{T}_1(x, \zeta_0(x), \omega, k) dk = 0. \quad (3.15)$$

The full expressions for \underline{T}_p and \underline{U}_p are needed to expand equations (3.14) and (3.15) into a form which may be solved directly for Φ_p^d , Φ_p^* , Ψ_p^d and Ψ_p^* . These expressions are very long and messy and are presented in Appendix 1 rather than here. They will take on two basic forms, the first requiring four unknown potentials when the medium is a layer, and the second requiring only two unknown potentials when the medium is a halfspace. Evaluation of the appropriate forms on either side of a buried interface or at the free surface will in turn lead to three particular forms for the boundary integral equations (3.14) and (3.15), depending on whether the interface is the free surface, separates two layers or separates a layer from the halfspace. All three particular forms may be generalized and combined, by first moving all functions of k to the left-hand sides of equations (3.14), to yield one compact expression representing all $4P + 2$ boundary conditions:

$$\int_{-\infty}^{+\infty} \left[\sum_{j=1}^{4P+2} A_j(\omega, k) g_{ij}(x, \omega, k) \right] e^{ikz} dk = h_i(x, \omega) e^{ik_0 z} \quad [i = 1, \dots, 4P + 2], \quad (3.16)$$

where i is the index over all $4P + 2$ boundary conditions, j is the index over all unknown wave potential functions, A_j are the $4P + 2$ unknown wave potential functions, g_{ij} are the known motion-stress components for scattered waves evaluated on either side of an interface, and h_i are the known motion-stress components for the source wave in the halfspace evaluated at the bottom-most interface. Appendix

1 gives the full detailed formulas for all g_{ij} and h_i for the case of a three-layered model with irregular free surface, which is the most complex that we will deal with in this thesis. Equation (3.16) represents a square linear system of integral equations which may be written equivalently for a single value of x and ω as:

$$\int_{-\infty}^{+\infty} \left[\underline{g}(k) \cdot \underline{A}(k) \right] e^{ikx} dk = \underline{h} e^{ik_0 x}. \quad (3.16a)$$

As we will show below, the solution of this system to obtain the unknown potentials vector \underline{A} requires discretizing all expressions for the left-hand and right-hand sides of this equation over both the x and k variables.

In equation (3.16) there will be only four non-zero components for h_i , corresponding to the horizontal and vertical displacements and tractions at the bottom-most interface due to the impinging source wave in the halfspace below. Also at the bottom interface only six A_j will contribute to the traction and displacement because the Rayleigh ansatz does not allow for up-going scattered waves, Φ_{P+1}^* and Ψ_{P+1}^* , in the halfspace. So the first of the three particular forms mentioned above for equation (3.16) will involve only six non-zero g_{ij} and one non-zero h_i for each of the four boundary conditions [$i = 4P - 1, \dots, 4P + 2$] at the bottom interface. Moving up to a boundary condition for a layer-layer interface, for which [$2 < i < 4P - 1$], eight of the unknown A_j will contribute to each of the four boundary conditions in this case, requiring eight non-zero g_{ij} . Also all four h_i will vanish since there is no source wave contribution above the halfspace. The third and final particular form is for the free surface. In this case there are only two boundary conditions, [$i = 1, 2$], for vanishing traction and only the four A_j for the top-most

layer are involved, requiring four non-zero g_{ij} , and two h_i which are zero. There are also two degenerate forms which occur only when the model contains no layers. The first is for an interface separating two halfspaces and requires four boundary conditions, four unknown A_{ij} and four non-zero h_i . The second is for a single halfspace bounded by a free surface and requires only two A_{ij} and two non-zero h_i .

The general form of equation (3.16) is deceptively simple. Some care must be taken with the ordering of the elements involved in setting up the complicated non-symmetric linear system. As more layers are added to the models the sparsity of the matrix \underline{g} increases rapidly and it becomes harder to keep track of where in this matrix all of the zero and non-zero elements should be placed. An intimate knowledge of the particular forms that all possible boundary condition equations may assume is important for assuring the proper placement of these components within the matrix and within the source and unknown potential vectors. This also allows one to extend the formulation for simpler models to more complex models by simply augmenting the linear system with boundary conditions for additional layers.

3.3 Solution of the Integral Equations

The integral equations (3.16) clearly cannot be solved analytically. The originality of the Aki-Larner method lies in the technique used to solve them numerically. The notation used by *Aki & Larner* [1970], which has already been introduced in equation (3.16), will be adhered to in the following. If we were to simply discretize equation (3.16) over both x and k then the accuracy of the approximation will depend strongly on the step intervals chosen for Δx and Δk . Aki and Larner forced

the integral equations to reduce exactly to infinite-sum equations by assuming the model structure to be periodic in the x -component with period length L . This means that now all $\zeta_p(x)$ and $s_p(x)$ are periodic and thus all h_i and g_{ij} in equation (3.16) must also be periodic since they depend on x only through the topography and slope functions. The first step in reducing equation (3.16) to an infinite sum is to multiply both sides by e^{-ik_0x} and then substitute $\tilde{k} = k - k_0$, which yields:

$$\int_{-\infty}^{+\infty} \left[\sum_{j=1}^{4P+2} A_j(\omega, k) g_{ij}(x, \omega, k) \right] e^{i\tilde{k}x} dk = h_i(x, \omega) \quad [i = 1, \dots, 4P + 2]. \quad (3.17)$$

Due to the imposed periodicity, all functions of x must repeat for $x_n = x + nL$. In order for the exponential term, $e^{i\tilde{k}x}$, to obey this restriction \tilde{k} can only assume discrete values which are integer multiples of $2\pi/L$. This restriction in turn reduces equation (3.17) to the desired infinite-sum equation:

$$\sum_{n=-\infty}^{+\infty} \left[\sum_{j=1}^{4P+2} A_n^{(j)}(\omega) g_n^{(ij)}(x, \omega) \right] e^{i(2\pi n x)/L} = h_i(x, \omega) \quad [i = 1, \dots, 4P + 2], \quad (3.18)$$

$$\begin{aligned} \text{where: } A_n^{(j)}(\omega) &= A_j(\omega, k_n) \Delta k_n & [j = 1, \dots, 4P + 2], \\ g_n^{(ij)}(x, \omega) &= g_{ij}(x, \omega, k_n) & [i, j = 1, \dots, 4P + 2], \\ k_n &= k_0 + n\Delta k_n, \\ \Delta k_n &= 2\pi/L. \end{aligned} \quad (3.18a)$$

Equation (3.18) is an exact representation of the boundary conditions in the wavenumber domain because Δk_n is fixed by the choice of the periodicity length

L . However, the use of periodic models can introduce errors into the displacement solutions caused by contamination from scattered energy arriving from adjacent model periods. This is the second major source of possible errors in the method. This effect can be minimized very easily by choosing L to be much larger than the maximum length of the interface irregularities and by including either attenuation or damping in the ansatz through the use of complex wavenumbers. This is discussed in detail in the next section. In order to evaluate equation (3.18) numerically it is first necessary to truncate the infinite sum to yield the following approximation:

$$\sum_{n=-N1}^{N2} \left[\sum_{j=1}^{4P+2} A_n^{(j)}(\omega) g_n^{(ij)}(x, \omega) \right] e^{i(2\pi n x)/L} = h_i(x, \omega) \quad [i = 1, \dots, 4P + 2]. \quad (3.19)$$

We now have a finite number of unknown wave potentials to solve for over a finite set of discrete horizontal wavenumbers. In theory equation (3.19) could be solved by discretizing it over the x variable and applying generalized inverse theory to the resulting set of linear equations in x and k . This would mean, however, that the inverse problem could be either under-determined, exact or over-determined depending on the total number of discrete x values used in digitizing the model. It is preferable to use an exact method of solution which is independent of the particular choices for L and Δx used for defining the model. Also, as we will discuss further below, the dependence of the solutions on k should be directly related to the degree of flatness in the model interfaces [Aki & Larner, 1970], and this implies that there should be a correspondence between the elements of $g_n^{(ij)}$, as functions of k , and their variations as functions of x . As we have seen, the discrete wavenumber

spacing, Δk_n is determined solely by L . Also, since L is the model period, the Fourier Transform of any function of x in equation (3.19) will share the same Δk_n as defined in equations (3.18) regardless of the choice for Δx . Thus if we compute values of each $g_n^{(ij)}(x_m, \omega)$ for all discrete values of x_m , where $[m = 0, \dots, M - 1]$ and M is the total number of samples in one model period, and then compute the Fast Fourier Transform (FFT) of the resulting series we obtain wavenumber spectra which characterize the variations in the motion-stress terms as functions of k_m along each interface involved. Similarly, the FFT of $h_i(x_m)$ will describe the spectral content of variations in the source terms along the bottom-most interface. Also, since $n\Delta k_n = 2\pi n/L = k_n - k_0$, then by substitution we can write $m\Delta k_m = 2\pi m/L = k_m - k_0$. Then, since $\Delta k_m = \Delta k_n$, it follows that the FFT's of $g_n^{(ij)}$ and h_i will be centered around $k_{m=0} = k_0$ and their complete spectra will be defined for both positive and negative wavenumbers relative to k_0 for $[m = -(M/2), \dots, 0, \dots, +(M/2) - 1]$. As long as we have chosen $M/2$ (the number of points in half the model period) to be greater than the largest of the wavenumber truncation limits in equation (3.19), $N1$ or $N2$, then the Fourier spectra of $g_n^{(ij)}$ and h_i may truncated exactly as before. Specifically, we first write the Fourier Transforms of $g_n^{(ij)}$ and h_i as:

$$G_{mn}^{(ij)}(\omega) = \frac{1}{L} \int_0^L g_n^{(ij)}(x, \omega) e^{i[2\pi(n-m)x]/L} dx, \quad (3.20)$$

$$H_{im}(\omega) = \frac{1}{L} \int_0^L h_i(x, \omega) e^{-i(2\pi mx)/L} dx.$$

Finally, if we now truncate the Fourier index m from $-N1$ to $+N2$ as before we can write the Discrete Fourier Transform (i.e. FFT) of equation (3.19)

approximately as:

$$\sum_{n=-N1}^{+N2} \left[\sum_{j=1}^{4P+2} A_n^{(j)}(\omega) G_{mn}^{(ij)}(\omega) \right] = H_{im}(\omega) \quad [i = 1, \dots, 4P + 2],$$

$$[m = -N1, \dots, 0, \dots, +N2](3.21)$$

$$\text{or: } \underline{\underline{G}} \cdot \underline{A} = \underline{H}$$

This equation represents a square linear system of $(4P + 2) \cdot (N1 + N2 + 1)$ equations in the same number of unknowns. By solving this system for all potential coefficients $A_n^{(j)}$ we will be matching the boundary conditions exactly in the wavenumber domain for one input source frequency, ω , at a time. Since the system is square it can be solved directly using LU decomposition and Gaussian elimination. Once we have obtained the solutions for the potential coefficients above, they may be used in the appropriate formulas, derived using equations (3.8), (3.7), (3.5) and (3.2), for calculating the displacements at any (x, z) location in the model. These formulas, as well as those used to calculate tractions, are given in detail in Appendix 1.

The explicit structure of the matrix $\underline{\underline{G}}$ in equation (3.21) is rather confusing at first glance. In fact this matrix can have two different forms depending on the order in which the two summations are taken. The order preferred in this thesis is achieved by interchanging these summations so that the inner sum is over the discrete wavenumber index and the outer sum is over the wave potential index. It is useful to define here the two wavenumber domains contained in the matrix. The first corresponds to the rows of $\underline{\underline{G}}$ and is the discrete wavenumber domain (over n) defined

by equations (3.18). The second we will call the Fourier wavenumber domain (over m), defined by equations (3.20), and corresponds to the columns of \underline{G} . Each row represents one Fourier component of one boundary condition over all contributing wave potentials and discrete wavenumbers. Each column represents one discrete wavenumber component of one wave potential over all Fourier components of all boundary conditions. Thus the entire matrix is made up of $(4P + 2)^2$ square sub-matrices, each with dimensions $(N1 + N2 + 1) \times (N1 + N2 + 1)$. Obviously the vector \underline{A} must be ordered according to the matrix row pattern and \underline{H} must be ordered according to the column pattern. More details on setting up the matrix are given in Appendix 1.

As mentioned above, the dependence of the displacement solutions on k is directly related to the flatness of the model interfaces. In particular, if all interfaces are flat then only the incident wavenumber, k_0 , will contribute to the solution. In this case, all sub-matrices, $G_{mn}^{(ij)}$, in equation (3.21) will have non-zero entries only when $n = m$, that is, they will be diagonal. So the use of the FFT to transform on the x -dependence of the motion-stress terms in equation (3.19) allows one to control the stability of the solutions directly through the degree of flatness of the interfaces. This was the main reason that Aki decided to use the Fourier Transform to construct the linear system of equations (K. Aki, personal communication, 1989). If any problems are encountered in solving the linear system, i.e., because of singularities in the matrix, then flattening the model interfaces should help.

The truncation of the infinite sum equation (3.18) introduces the third and final major source of error in the method. If $N1$ and $N2$ are not chosen large enough to adequately account for all possible scattered waves it will be impossible to match all

of the boundary conditions when the interfaces are significantly irregular. Ideally the wavenumber magnitude spectra for the potential coefficients $A_n^{(j)}$ should all converge towards zero as n approaches $-N1$ and $+N2$. Strictly speaking, this criterion is the main justification for the wavenumber truncation. If they do not converge then it may be necessary to include higher scattering orders by increasing $N1$ and $N2$. As we will see, however, this condition is often overly conservative and difficult to satisfy for complicated models. Frequently we will find that the boundary conditions are being satisfied reasonably well even though some of the coefficient wavenumber spectra do not converge to zero. Further, even *Larner* [1970] points out that increasing the wavenumber index will not always ensure convergence and may even be undesirable. Much of this problem is due to the inadequacy of the Rayleigh ansatz in the halfspace and, in fact, the spectra for the down-going potentials leaving the bottom interface almost never converge even though the boundary conditions are being satisfied. We will demonstrate later, in Chapter 5, that the reliability of the displacement solutions at the free surface of the model may be assured by the requirements that the boundary condition residuals are small and that the coefficient spectra should converge at least for the wave potentials used to calculate the displacement solutions. We will not present a detailed discussion of the three sources of error in this thesis. This subject has already been addressed sufficiently by *Larner* [1970]. However, in the course of modeling the observed amplitude data for the Valles Caldera, these errors were dealt with as they occurred, and it is necessary to know how to recognize them. The effects of either the Rayleigh ansatz or wavenumber truncation errors will be clearly manifested as misfits or oscillations in the boundary conditions. The effects of the periodic interfaces will not show

up in the boundary conditions but may be controlled by adjusting the amount of attenuation in the model or damping in the wavefield. This is discussed in detail in the next section.

Concerning the choices for the wavenumber truncation limits, $N1$ and $N2$, in general $N1 \neq N2$ for the following reasons. The scattered discrete wavenumbers, given by $k_n = k_0 + n\Delta k_n$, represent waves which are scattered either forward or backward in the x direction relative to the incident wavenumber, k_0 , depending on whether n is positive or negative, respectively. Since $k_0 = K_\alpha \sin \theta_0$, we can write the expression for the sine of the propagation angle of the n^{th} scattered P wave as [Larner, 1970]:

$$\sin \theta_n^P = \sin \theta_0 + \frac{n\Delta k_n}{K_\alpha}, \quad (3.22)$$

and for the corresponding scattered S wave:

$$\sin \theta_n^S = \frac{\beta}{\alpha} \sin \theta_0 + \frac{n\Delta k_n}{K_\beta}. \quad (3.23)$$

Ideally we would wish to include in our displacement solutions at least all possible homogeneous scattered wave angles over the range: $[\sin \theta_n = -1, \dots, 0, \dots, +1]$ for both P and S waves. Larner [1970] showed that in order to satisfy the boundary conditions in most cases it is necessary to include inhomogeneous waves as well, for which $|\sin \theta_n^S| > 1$ and/or $|\sin \theta_n^P| > 1$. For the present discussion we merely wish to point out that in general $\theta_0 \neq 0$ and for sufficiently shallow incidence angles it is usually necessary to choose $N1 \neq N2$ so that the range of wavenumbers used is approximately symmetric and centered around $k_{n_0} = 0$. As mentioned earlier, examination of the boundary condition residuals is an adequate test of the choices

for N_1 and N_2 . Lerner concludes that as long as the total number of wavenumbers, $N_1 + N_2 + 1$, is chosen large enough, then for moderately shallow incidence angles, say $|\theta_0| \leq 45^\circ$, the boundary conditions will be met adequately by letting $N_1 = N_2 = N$ and performing the wavenumber discretization over the symmetric range: $[n = -N, \dots, 0, \dots, +N]$. We will use this convention throughout this thesis since, for teleseismic P waves, we will never have to consider incidence angles greater than $|\theta_0| \approx 30^\circ$.

Finally, one should notice that in order to cover the entire range of homogeneous scattered angles for the S waves it is always necessary to choose N large enough to extend the P-wavenumbers into the inhomogeneous region. This is because for a given wavenumber index n_P , for which $\sin \theta_{n_P}^P = 1$, the corresponding S-wave angle is given by $\sin \theta_{n_P}^S = \beta/\alpha < 1$. Thus to include all possible homogeneous S waves in the solution, N must be chosen sufficiently larger than n_P so that $|\theta_{\pm N}^S| \geq 1$. This means that, in general, all P-SV scattering problems must necessarily include inhomogeneous P waves in order to adequately represent the scattered S-wavefield. This requirement of course is dependent on the severity (steepness and amplitude) of the interface irregularities and may be relaxed for sufficiently gentle model geometries. As discussed above, in the extreme limiting case where all interfaces are flat, no scattered waves are generated and k_0 is the only wavenumber which contributes to the solutions. In this case we can simply choose $N = 0$, which is equivalent to solving the 1-dimensional problem using the Thomson-Haskell method [Thomson, 1950; Haskell, 1953, 1960, 1962].

3.4 Wavefield Damping and Complex Wavenumbers

It is well known to users of the Aki-Larner method that complex wavenumbers must be employed to make it work. The primary reason for this is the need to damp out the energy arriving from adjacent model periods, which would produce erroneously large amplitudes for the displacement solutions. By introducing an imaginary part to K_α and K_β , the plane wave representations given by equations (3.7) and (3.8) will now contain real-valued exponential decay factors which attenuate the steady-state waves with increasing travel distance and time. The imaginary part traditionally has been introduced by making the frequency, ω , complex [e.g. *Aki & Larner, 1970; Larner, 1970; Bouchon, 1973; Bard & Bouchon, 1980a,b*]. This approach is the simplest in terms of formulation and does succeed in eliminating the unwanted arrivals as long as the imaginary part of frequency is chosen large enough. This approach will be termed the “wavefield damping method” here since it is completely artificial in nature and any displacement solution obtained must ultimately be corrected by appropriately removing this damping from it. An alternative approach, which provides the benefit of being physically meaningful, is to make the wavenumbers complex by including attenuation as a realistic physical parameter in the models. We will show below that this approach may be implemented in the Aki-Larner method by using familiar formulas relating the seismic quality factor, Q , to material dispersion characteristics in the form of complex, frequency-dependent phase velocity. We will call this the “ Q method” here and it has a two-fold advantage over the damping method in that it allows one to model the effects of attenuation on seismic waves, and since these effects are realistic there is no need to correct for them in the displacement solutions. *Bard & Gariel [1986]*

were the first ones to employ the Q method in the Aki-Larner technique, but they gave no details in that work on how to successfully implement it. Since this is a relatively new and fairly tricky improvement to the method, we will discuss its implementation in some detail below.

A secondary reason for the use of complex wavenumbers arises for models involving layers bounded by parallel plane interfaces. In these cases, when K_α and K_β are real, the existence of poles in the horizontal wavenumber summation path at $k_n = K_\alpha$ and at $k_n = K_\beta$ will introduce singularities in the matrix \underline{G} of equation (3.21) corresponding to trapped modes in the plane layers. *Larner* [1970] discussed this point in some detail, pointing out that these poles can be completely avoided by allowing k_n and ν_n to be complex. He also pointed out that the matrix singularities will not exist if all of the model interfaces contain irregularities. Since this will be the case for all models presented in this thesis we will not dwell on this point except to aid in the discussion below of the wavenumber summation paths which result when K_α and K_β are complex.

The following discussion applies for both P and S waves using the generalized expression for the complex characteristic wavenumber:

$$K = K_R + iK_I = \frac{\omega}{c(\omega)}, \quad (3.24)$$

where $c(\omega)$ is the phase velocity for either P or S waves. In general, equation (3.24) implies that either ω or $c(\omega)$ or both may be complex and that $c(\omega)$ may also be frequency-dependent. The incident horizontal and vertical wavenumber components may still be written as before, but with the addition of the imaginary part:

$$\begin{aligned} k_0 &= K \sin \theta_0 = K_R \sin \theta_0 + iK_I \sin \theta_0, \\ \nu_0 &= K \cos \theta_0 = K_R \cos \theta_0 + iK_I \cos \theta_0. \end{aligned} \quad (3.25)$$

The discrete horizontal scattered wavenumbers, k_n , will all share the same imaginary part as k_0 because the wavenumber increment, Δk_n is real:

$$k_n = k_0 + \Delta k_n = \text{Re}\{k_0\} + \Delta k_n + i \text{Im}\{k_0\}, \quad (3.26)$$

and the corresponding vertical wavenumbers are written as before, remembering that now all quantities are complex:

$$\nu_n = (K^2 - k_n^2)^{1/2}. \quad (3.27)$$

So the previous formulation for real wavenumbers generalizes perfectly to the complex case. The only difficulty arises in resolving the ambiguity inherent to evaluating the complex square root of equation (3.27). To fully understand the behavior of k_n and ν_n summation paths needed to solve equation (3.21), it is helpful to study these quantities in terms of their positions on the top sheet of the complex wavenumber plane. We will elaborate here on the discussions of *Aki & Larner* [1970] and *Larner* [1970] by describing the paths taken by ν_n as well as k_n and by providing more details concerning the way in which the ambiguities in the complex square root are resolved.

It is well known [*Lapwood*, 1949] that the top and bottom sheets of the complex k -plane correspond to values of k for which $\text{Im}\{\nu\} > 0$ and $\text{Im}\{\nu\} < 0$, respectively. These two Riemann sheets are connected by a branch line along which $\text{Im}\{\nu\} = 0$ and which includes the branch point at $k = K$ where $\nu = 0$. *Larner* [1970] explained that for halfspaces and non-plane layers, branch points are located only at the characteristic P and S wavenumbers, $+K_\alpha$ and $+K_\beta$, and we need not concern ourselves with the possible branch points at $-K_\alpha$ and $-K_\beta$. For the case

when K is real, the branch line follows the real k -axis from the branch point to the origin and then follows the imaginary k -axis from the origin to $k = + i\infty$ [Lapwood, 1949]. The top sheet thus is defined by this branch line and by choosing $Im\{\nu\} > 0$. When K is complex the branch point at K is displaced away from the real axis into the first quadrant along a line with slope $\epsilon = K_I/K_R$ and the branch line becomes a hyperbola with the real and imaginary axes as asymptotes. The summation path for k_n , according to equations (3.25) and (3.26), will now follow a straight line parallel to the real axis with a constant imaginary part: $K_I \sin \theta_0$. If we now write:

$$\begin{aligned}\nu^2 &= \nu_R^2 - \nu_I^2 + 2i\nu_R\nu_I \\ &= K^2 - k^2 \\ &= (K_R^2 - K_I^2 - k_R^2 + k_I^2) + 2i(K_RK_I - k_Rk_I),\end{aligned}\tag{3.28}$$

then clearly the branch line defined by $Im\{\nu\} = \nu_I = 0$ is also equivalently defined by:

$$\frac{1}{2}Im\{\nu^2\} = K_RK_I - k_Rk_I = 0.\tag{3.29}$$

So the branch line can be calculated easily by either of the equivalent formulas:

$$\begin{aligned}k_I &= \frac{K_RK_I}{k_R}, \\ \text{or : } k_R &= \frac{K_RK_I}{k_I},\end{aligned}\tag{3.29}$$

which, as mentioned, represent a hyperbola passing through the point $k = K$ and asymptotic to the real and imaginary axes. For values of k falling below this hyperbola, that is when $k_Rk_I < K_RK_I$, we see that $Im\{\nu^2\} > 0$ and the two choices

for ν are given by:

$$\nu = \pm (|\nu_R| + i|\nu_I|).$$

Similarly, when k falls above the hyperbola, $Im\{\nu^2\} < 0$ and:

$$\nu = \pm (|\nu_R| - i|\nu_I|).$$

So the complex square root will be single-valued if we use only the top Riemann sheet, which fixes $Im\{\nu\} > 0$. Then we can define ν unambiguously by using the following rule:

$$\begin{aligned} \nu &= +|\nu_R| + i|\nu_I| \quad \text{for } k_R k_I \leq K_R K_I, \\ \nu &= -|\nu_R| + i|\nu_I| \quad \text{for } k_R k_I > K_R K_I. \end{aligned} \tag{3.30}$$

This simple rule is important to observe when it comes time to implement the Aki-Larner method on a computer because most programming languages will return a value for the complex square root which defaults to always having a non-negative real part. Physically this rule implies that up-going waves will always attenuate in the upward direction and down-going waves will attenuate downward. However, *Larner* [1970] discusses the fact that this simple interpretation breaks down when the branch line is crossed; that is when $k_R k_I > K_R K_I$. In this case the real part of ν is negative, so that now “up-going” waves will appear to be propagating downward but will still attenuate upward. So no physically realistic meaning can be attached to these waves. Their existence must be accepted as an artificial aspect of the method which is required in some general cases to satisfy the boundary conditions. In particular cases, though, such as problems involving near vertical incidence, these non-physical waves will not be involved because the k_n summation path will

lie entirely on or close to the real axis and thus will never cross the branch line. It is only for fairly shallow incidence angles that these waves will begin to contribute significantly. The following figures illustrate this more clearly.

Figure 3.2 shows portions of typical summation paths for k_n and ν_n on the top sheet of the complex wavenumber plane for four different angles of incidence. Figure 3.2a is for $\theta_0 = 0^\circ$ (vertical incidence), Figure 3.2b is for $\theta_0 = 20^\circ$, Figure 3.2c is for $\theta_0 = 45^\circ$ and Figure 3.2d is for $\theta_0 = 90^\circ$ (grazing incidence). In each plot the solid curve represents the branch line, given by equation (3.29), and the dashed curve is a plot of the so-called epsilon line: $K_I = \epsilon K_R$, for any arbitrary choice for the damping factor $\epsilon = K_I/K_R$. The characteristic wavenumber K is the branch point and will always lie exactly at the intersection point of the branch line and epsilon line. The (+) symbols mark the discrete values for k_n and the (∇) symbols mark the corresponding values for ν_n . The large open circles mark the locations of k_0 and ν_0 for the incident wave. The two dotted lines mark the origins of the real and imaginary axes and are plotted in order to show the asymptotic behavior of the branch line and to demonstrate the change in sign for $Re\{\nu_n\}$ when k_n crosses the branch line. The horizontal wavenumber spacing chosen for these plots is $\Delta k_n = 0.1K_R$ and the maximum scatter order index used is $N = 40$. The negative scatter orders for the horizontal wavenumbers, k_{-40} through k_{-1} , lie to the left of k_0 and the positive orders are to the right. For non-vertical incidence ν_{-40} is the uppermost point to the right of the branch line and ν_{+40} is the last point to the left. For vertical incidence the positive and negative scatter orders for ν are identical and lie exactly on the branch line because in this case $Im\{k_n\} = 0$.

NORMALIZED COMPLEX WAVENUMBER SUMMATION PATHS

$\Delta k = 0.10 K_R$ $N = 40$

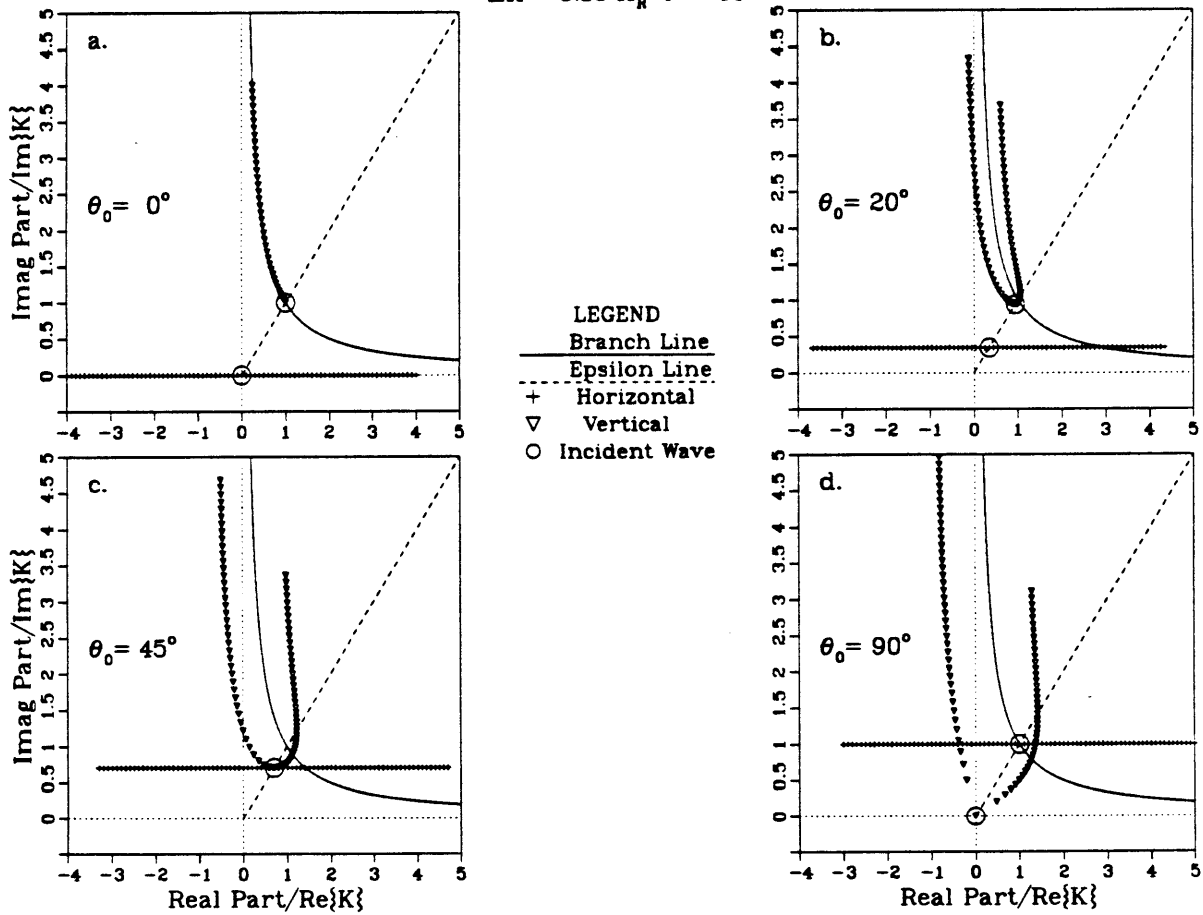


Figure 3.2 Summation paths, epsilon and branch lines on the top sheet of the complex wavenumber plane. The real axis is normalized by $Re\{K\} \equiv K_R$ and the imaginary axis by $Im\{K\}$ so that all plots are generalized for arbitrary choices of K_R and ϵ . The various plots are marked as shown in the legend.

All plots have the real axis normalized by K_R and the imaginary axis by K_I so that the figures are independent of any particular choices for K and ϵ .

It may appear that Figure 3.2 shows only the paths for non-negative incidence angles and for down-going scattered waves since all imaginary parts are positive. Equivalent inverted paths in the lower two quadrants must exist also. Strictly speaking this is true since for negative θ_0 the k_n summation line will lie in the third and fourth quadrants. However, the conventions and branch test rules for determining the correct sign of ν_n are unaffected by the sign of $Im\{k_n\}$. Furthermore, the Rayleigh ansatz contains separate terms for up-going and down-going waves and thus only the positive roots of equation (3.27) are required for ν_n and these are independent of the sign of θ_0 .

There are four major features in these plots which are common to all incidence angles. First, the incident wavenumber components, k_0 and ν_0 , always lie somewhere along the epsilon line, in accordance with equation (3.25). Second, as already mentioned, the k_n summation paths always follow straight lines parallel to the real axis, due to the discretization scheme given by equation (3.26). Third, the ν_n summation paths, obtained by evaluation of equation (3.27) for each k_n and following the rules in equations (3.30), always make a loop around the branch point and branch line due to the fact that k_n has a constant imaginary part. Finally, in all cases the k_n and ν_n paths are roughly orthogonal to each other, especially for large positive or negative n . The implications of this last point are discussed below in terms of the propagation and attenuation direction angles.

The major differences in the summation paths with increasing incidence angle may be summarized as follows. First, the k_n summation line shifts upward and

to the right as θ_0 increases. This is due to the fact that $Re\{k_0\}$ and $Im\{k_0\}$ are proportional to $\sin \theta_0$ and $Im\{k_n\} = Im\{k_0\} = \text{constant}$. This also causes k_n to cross the branch line for smaller positive values of n as θ_0 increases. Secondly, the ranges of values covered by $Re\{\nu_n\}$ and $Im\{\nu_n\}$ increase in width as θ_0 increases. Examination of Figure 3.2 reveals that $|Im\{\nu_{-N}\}| \propto |Re\{k_{-N}\}|$ and $|Im\{\nu_{+N}\}| \propto |Re\{k_{+N}\}|$ so that as θ_0 increases $Im\{\nu_{-N}\}$ decreases and $Im\{\nu_{+N}\}$ increases. Also, the width of the range of values for $Re\{\nu_n\}$ is proportional to $Im\{k_n\}$.

The complicated relations described above can best be understood in terms of the propagation vector, \vec{P} , and the attenuation vector, \vec{A} , associated with general plane waves when the wavenumber vector, \vec{K} is complex. The following discussion will apply for both the damping and Q methods mentioned earlier and we use the term "attenuation" in both cases. We will see in the next section, though, that true anelastic attenuation requires the elastic parameters, λ and μ , to be complex, and this is not the case for the simple damping method.

Borcherdt [1973, 1977] has shown that the propagation factor for general plane waves in anelastic materials should be written for the 2-D case as:

$$e^{i\vec{K}\cdot\vec{r}} = e^{i\vec{P}\cdot\vec{r} - \vec{A}\cdot\vec{r}},$$

$$\text{where : } \vec{r} = (x, z),$$

$$\vec{K} = (k, \nu), \tag{3.31}$$

$$\vec{P} = (Re\{k\}, Re\{\nu\}),$$

$$\vec{A} = (Im\{k\}, Im\{\nu\}).$$

Recalling that $K = \omega/c(\omega) = \|\vec{K}\|$, the following relations will hold for K , \vec{P} , and \vec{A} :

$$\begin{aligned}\vec{P} \cdot \vec{P} - \vec{A} \cdot \vec{A} &= \text{Re}\{K^2\}, \\ \vec{P} \cdot \vec{A} &= \frac{1}{2} \text{Im}\{K^2\} = P A \cos \gamma,\end{aligned}\tag{3.32}$$

where γ is the angle between \vec{P} and \vec{A} , $P = \|\vec{P}\|$ and $A = \|\vec{A}\|$. *Buchen* [1971] and *Borcherdt* [1973] used these relations to show that inhomogeneous waves exist when $\gamma \neq 0$, that is when the direction of maximum attenuation differs from the direction of propagation. Also, the medium may be considered to be elastic when either $A = 0$ or $\gamma = \pi/2$. The class of inhomogeneous plane waves in anelastic media is then clearly defined by $A \neq 0$ and $0 < \gamma < \pi/2$ [*Aki & Richards*, 1980].

Figure 3.3 shows plots of the direction angles (clockwise from vertical) for \vec{P} and \vec{A} and the differences, γ , for the wavenumber summation paths of Figure 3.2. Using the same values calculated for k_n and ν_n before, the three angles, θ_n for \vec{P}_n , ϕ_n for \vec{A}_n and γ_n for the difference may be calculated very easily with formulas derived from equations (3.31) and (3.32):

$$\begin{aligned}\theta_n &= \arctan(\text{Re}\{k_n\}/\text{Re}\{\nu_n\}), \\ \phi_n &= \arctan(\text{Im}\{k_n\}/\text{Im}\{\nu_n\}), \\ \gamma_n &= \arccos\left(\frac{\vec{P} \cdot \vec{A}}{P A}\right).\end{aligned}\tag{3.33}$$

In Figure 3.3 these angles are plotted versus $\text{Re}\{k_n\}/\text{Re}\{K\}$, which is equivalent to using the scattering index, n , as the ordinate with $n = -N$ at the far left as in Figure 3.2. In these plots the (+) symbols mark the discrete propagation directions, θ_n , for the scattered waves. The (x) symbols mark the directions of

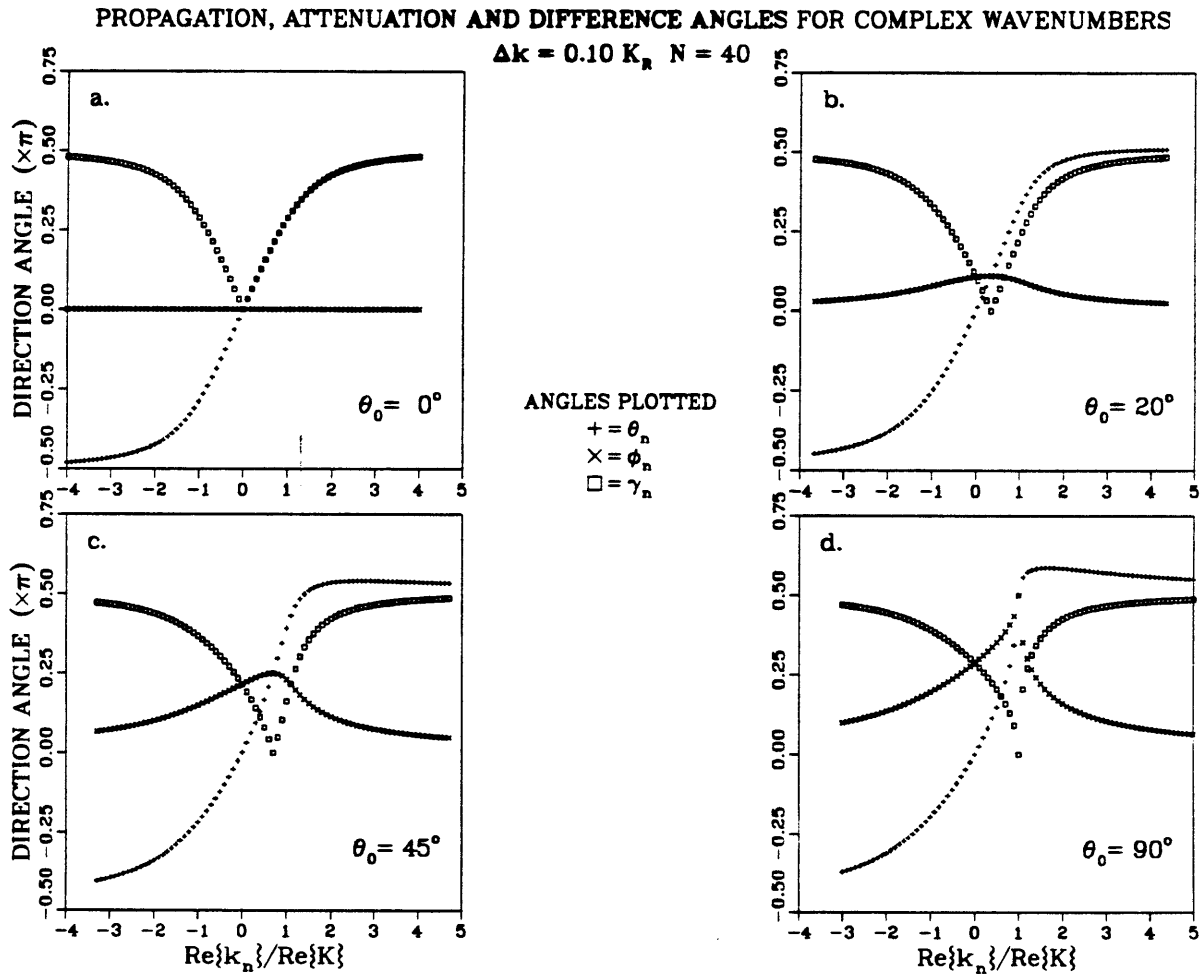


Figure 3.3 Propagation, attenuation and difference angles plotted for the discrete wavenumber summation paths of Figure 3.2. Angles are plotted as multiples of π versus $Re\{k_n\}/Re\{K\}$. Plots are labeled as shown in the legend.

maximum attenuation, ϕ_n , and the open squares mark the angles, γ_n , between \vec{P}_n and \vec{A}_n .

There are four basic wave types represented in these plots. First, for large positive and negative scatter orders, i.e. $|Re\{k_n\}| \geq 2K_R$, we see that $\gamma_n \approx \pi/2$ for all incidence angles. This case corresponds to inhomogeneous interface waves which attenuate vertically away from a boundary and these waves may exist regardless of whether the medium is anelastic or elastic. Second, the point where the θ_n curve intersects the ϕ_n curve corresponds to the incident wave. For any incidence angle then, we can obviously write: $\theta_0 = \phi_0$, and $\gamma_0 = 0$. Since $A \neq 0$ the incident wave in all cases is a homogeneous attenuating plane wave. The third wave type is the general inhomogeneous plane wave, characterized by $A \neq 0$ and $0 < \gamma_n < \pi/2$ [Aki & Richards, 1980]. These waves lie in the region $|Re\{k_n\}| \leq 2K_R$, and as we will see later, contribute strongly to the scattered wavefield. Finally the fourth wave type is the aforementioned non-physical wave for which $Re\{\nu_n\} < 0$ and $\theta_n > \pi/2$. As θ_0 increases, these waves become more prevalent and overlap the range of general inhomogeneous plane waves just mentioned. These waves will not contribute significantly to solutions for $\theta_0 \leq 30^\circ$.

The incident wave is always homogeneous simply because k_0 and ν_0 both lie on the epsilon line due to their definitions in equations (3.25). Actually both of Figures 3.2 and 3.3 are simplified because strictly they apply only for the medium containing the incident wave (i.e., the halfspace). In a medium with a different velocity than in the halfspace the point $\nu_{n=0}$ will no longer lie on the epsilon line because, although k_0 and all k_n are identical in all media, now K will be different. Thus there will be no homogeneous waves on the opposite side of the bottom-most

interface, even if this interface is flat. *Borcherdt [1977]* gives a detailed discussion of the interaction of plane waves with interfaces in anelastic media. Even for plane interfaces the anelasticity causes very complex behavior in all aspects of the wave motion. Fortunately, an in-depth knowledge of this complex behavior is not required for successfully implementing anelastic attenuation in the Aki-Larner method. The previous discussion and figures generalize perfectly for both approaches to making wavenumbers complex. With this background on complex k and ν in mind, we will now discuss how to implement Q in the Aki-Larner method.

3.5 Anelastic Attenuation and Parameterization of Q

We begin this section with a brief discussion of the wavefield damping method since this is the easiest to implement and has been used in all previous publications concerning the Aki-Larner method except one. Simply, a small imaginary part is added to the frequency :

$$\omega = \omega_R (1 + i\epsilon), \tag{3.34}$$

$$\text{where normally : } \epsilon = \frac{\omega_I}{\omega_R} \ll 1.$$

In practice, ϵ is chosen large enough to damp out unwanted arrivals from scatterers at some prescribed distance from the desired observation points in the model. The minimum value for ϵ required to significantly damp out arrivals from adjacent model periods would be:

$$\omega_I = 1/\tau,$$

$$\text{where : } \tau \approx L/2c_{max}, \tag{3.35}$$

$$\text{and : } c_{max} = \text{highest model velocity.}$$

This will damp out waves by a factor of e^{-2} at a time $t = L/c_{max}$. The damping may also be increased to remove resonance and scattering effects near the observation point if one wishes only to study the earlier parts of seismograms. As mentioned in the previous section, this type of damping is basically artificial since it will cause first arrivals to attenuate with travel distance at a rate which is arbitrary and physically meaningless since ω_I is not a model parameter. Therefore it is necessary in the end to remove the damping from the solutions either in the wavenumber domain or in the time domain. The time domain correction can be used only when synthetic seismograms have been calculated by obtaining individual Aki-Larner solutions for many equally spaced frequencies. In this case ω_I must be frequency independent so that the time series can be corrected simply by multiplying it by $e^{\omega_I t}$. To correct in the wavenumber domain, the displacement solution at (x, z) for each single frequency is multiplied by $e^{Im\{k_0\}x - Im\{\nu_0\}z}$. Complex frequency actually can be used to obtain one of the definitions for Q, namely the “temporal Q” described in *Aki & Richards* [1980]. We will show below, though, that the Aki-Larner solutions obtained using this temporal Q differ significantly from the solutions obtained using the same value for Q but parameterized in terms of complex velocity instead of frequency.

The most common definition for Q used in seismology relates $1/Q$ to the fractional loss of energy per wave cycle due to heat generated by internal friction [*Knopoff*, 1964; *Aki & Richards*, 1980]:

$$\frac{1}{Q} = -\frac{\Delta E}{2\pi E}. \quad (3.36)$$

This relation can be easily converted to express $1/Q$ in terms of the time derivative of the log of wave amplitude:

$$\frac{d(\ln A)}{dt} = -\frac{\omega}{2Q}, \quad (3.37)$$

or in terms of the spatial derivative in 1-D:

$$\frac{d(\ln A)}{dx} = -\frac{\omega x}{2Qc}. \quad (3.38)$$

Integration of these two equations yields the familiar relations expressing amplitude attenuation in terms of temporal or spatial Q [*Aki & Richards*, 1980]:

$$\frac{A(t)}{A_0} = \exp\left[-\frac{\omega t}{2Q}\right], \quad (3.39)$$

$$\frac{A(x)}{A_0} = \exp\left[-\frac{\omega x}{2Qc}\right].$$

From the discussion in the previous section it would seem natural to introduce attenuation in the plane wave representations simply by letting $\omega = \omega_R(1 + i/2Q)$ for temporal Q , or $K = K_R(1 + i/2Q)$ for spatial Q . But, as demonstrated in *Aki & Richards* [1980] this simple approach violates causality requirements. Also, tests of the shapes of attenuated impulses do not agree with the shapes of observed pulses that have traveled through an attenuating material. The attenuated impulse, $p(x, t)$, for the above definition of Q may be calculated very easily using the Inverse Fourier Transform formula given in *Aki & Richards* [1980]:

$$p(x, t) = \frac{1}{2\pi} \int_{-\infty}^{+\infty} e^{ikx} e^{-\omega t} d\omega, \quad (3.40)$$

$$\text{where now : } k = \frac{\omega}{c} + i \frac{|\omega|}{2Qc}.$$

The attenuated pulse obtained when the phase velocity is non-dispersive has a non-zero amplitude before $t = 0$, is symmetric in shape and has too large a rise time as compared with measurements of observed attenuated pulses [Stacey *et al.*, 1975]. These problems were alleviated by Azimi *et al.* [1968] who used the Hilbert Transform to introduce dispersion in the phase velocity in such a way that the lower frequency components of the pulse are delayed in time relative to the higher frequencies. Their approach yielded the familiar logarithmic dispersion law which may be written in its most useful form as [Aki & Richards, 1980]:

$$c(\omega) = c(\omega_0) \left[1 + \frac{1}{\pi Q} \ln \left(\frac{\omega}{\omega_0} \right) \right]. \quad (3.41)$$

In this relation the phase velocity increases logarithmically with increasing frequency at a rate inversely proportioned to Q . In practice the only trick involved in using it lies in the choice of the reference frequency, ω_0 . Also, several assumptions were made in the derivation of this law and the one which will concern us the most in this thesis is the assumption that $Q \gg 1$. We will discuss these two issues in some detail below. The final step in constructing the attenuation law is to introduce the imaginary part to K in a way that is physically meaningful. Anelasticity has a profound effect on the interaction of waves with an interface [Lockett, 1962; Cooper & Reiss, 1966; Shaw & Bugl, 1969; Borchardt, 1977]. In order for the effects of anelasticity to manifest themselves in the traction boundary conditions, it is necessary for the elastic parameters of the various media, λ_p and μ_p , to be complex. Clearly then we must make the phase velocities, α_p and β_p , complex instead of the frequency. We have already seen that the characteristic wavenumber may be

written as $K = K_R(1 + i/2Q)$. This is equivalent to writing the phase velocity as $c = c_R/(1 + i/2Q)$. After rationalizing this expression and dropping a $1/4Q^2$ term from the denominator, the full complex dispersive phase velocity formula may be obtained by substituting equation (3.41) for c_R :

$$c(\omega) = c(\omega_0) \left[1 + \frac{1}{\pi Q} \ln \left(\frac{\omega}{\omega_0} \right) \right] \cdot (1 - i/2Q). \quad (3.42)$$

To implement this in the Aki-Larner method, we simply replace α and β throughout the model with equation (3.42), using the original non-dispersive model velocities for $c(\omega_0)$ in each case. It can be easily verified that the resulting plane wave expressions will still satisfy the wave equation and that the general discussion of the propagation and attenuation vectors presented in the last section will still hold. We will now turn to a discussion of the reference frequency and high-Q assumption and then conclude this chapter with an example comparing displacement solutions obtained using the damping method with those obtained for the Q method.

Figure 3.4 shows the behavior of the logarithmic dispersion law, equation (3.41) for $Q = 20, 10, 5, 2$ and 1 , plotted as $c(\omega)/c(\omega_0)$ versus ω/ω_0 . Note the rapid increase in the strength of the dispersion as Q decreases. Note also that the function has a zero at a value of ω/ω_0 which increases as Q decreases, and that below this value $c(\omega)$ is actually negative. These zero-crossings occur specifically at $\omega/\omega_0 = e^{-\pi Q}$ and clearly the portion of the curves for which $\omega/\omega_0 \leq e^{-\pi Q}$ cannot be used.

So if one is considering using low values for Q , it is wisest to chose ω_0 to be smaller than the lowest frequency that will be used in the modeling. It is also

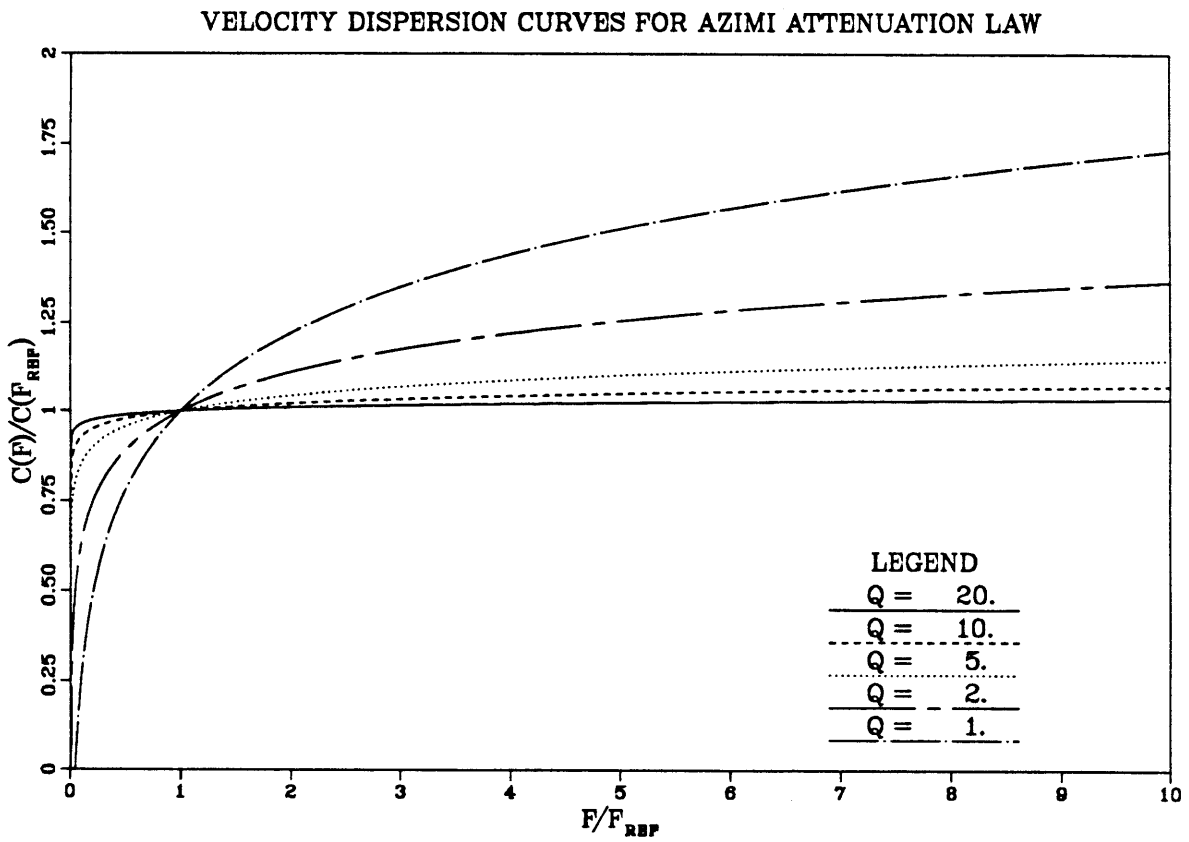


Figure 3.4 Plots of the Azimi et al. dispersion law, equation (3.41), for five different values of Q as indicated in the legend.

desirable to avoid the early portion of the curves where the slope changes rapidly since this can lead to erratic behavior in the comparisons of displacement solutions for multiple frequencies. Thus we have chosen $\omega/\omega_0 = 5$ as a reasonable minimum value used to determine ω_0 . Since our minimum frequency to be modeled in this thesis is $f = 0.05 \text{ Hz}$, we will use a reference frequency of $f_0 = 0.01 \text{ Hz}$ throughout. This is not a very critical issue when Q is fairly large, and most other users of equation (3.41) have simply chosen $f_0 = 1.0 \text{ Hz}$ for this reason [Aki & Richards, 1980; Lokshtanov, 1987]. However, in this thesis we wish to push the dispersion law as far as possible to try modeling very strongly anelastic material. Since this will encroach on violating the high Q assumption used to derive the law we need to determine how low Q can be allowed to go before we need to question the validity of our solutions. So it becomes very important in this case to choose the reference frequency as carefully as possible.

As a means of determining how big is big in the assumption $Q \gg 1$, we used equation (3.40) with the dispersion law added to examine the attenuated pulse shapes obtained for the same Q values used in Figure 3.4. The results of this are shown in Figure 3.5. Here we have calculated the various pulse spectra for a frequency spacing of $\Delta f \approx 0.05 \text{ Hz}$, which is the same spacing we will use in the modeling calculations. Using $f_0 = 0.01 \text{ Hz}$, the spectra were calculated for 512 points up to a Nyquist frequency of 25.0 Hz. This was done simply to increase the smoothness of the resulting time series and to eliminate aliasing effects. The pulses were allowed to propagate a distance x such that $x/c \approx 10 \text{ s}$ to produce the amount of attenuation, A/A_0 , indicated by the amplitude axis. The time axis is normalized by the minimum travel time, t_{min} , corresponding to the arrival of the frequency

ATTENUATED IMPULSES FOR COMPLEX DISPERSIVE PHASE VELOCITY

$$f_{ref} = 0.010000; \Delta f = 0.048828; f_{nyq} = 25.000$$

$$T_{MAX} = 20.480 \text{ secs.}; \text{ Delay time} = 10.240 \text{ secs.}$$

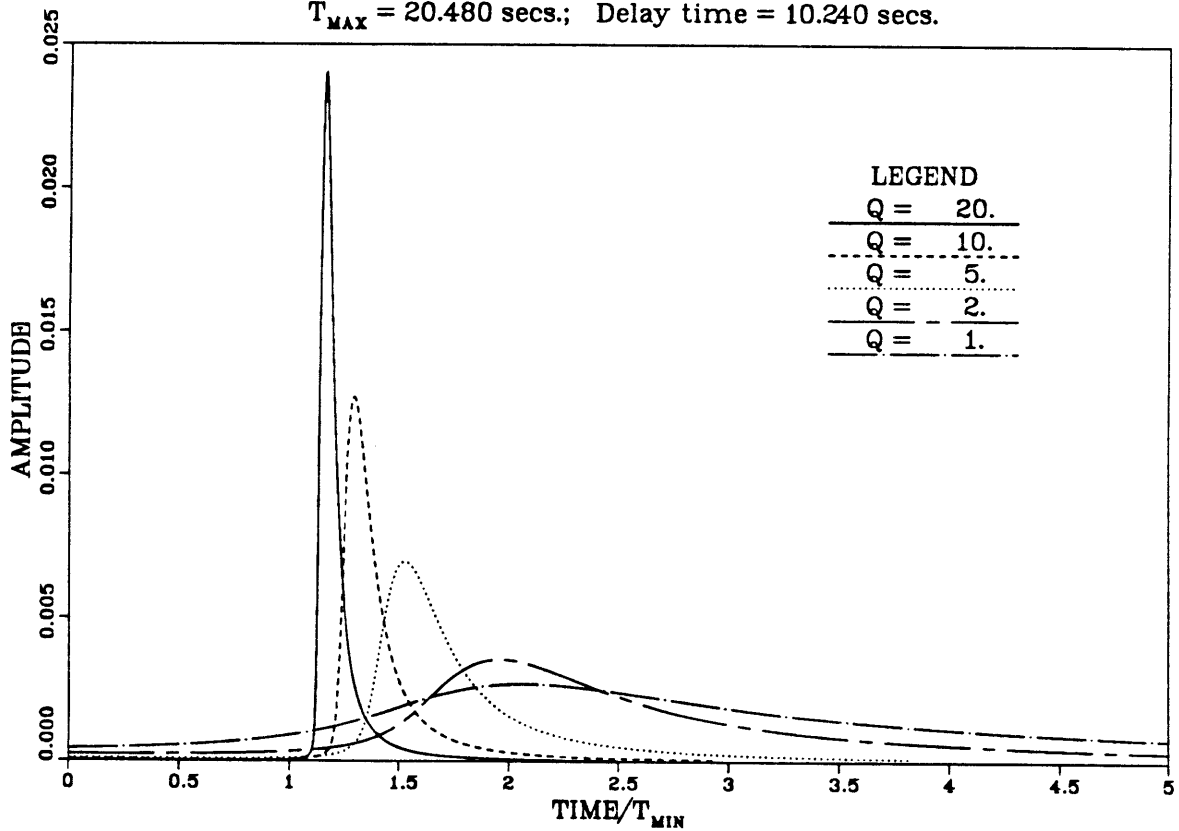


Figure 3.5 Attenuated pulse shapes obtained using the logarithmic dispersion law for the five values of Q used in Figure 3.4. Pulses are plotted versus t/t_{min} , where t_{min} is earliest arrival time expected for the frequency component with the highest phase velocity in each case.

component with the highest phase velocity. If the dispersion law holds, t_{min} should correspond to the travel time of the first motion.

In all cases the pulse shape appears to be correct. The decay time is longer than the rise time, and the rise time increases as Q decreases. However, the causality requirement is satisfied well only down to $Q = 5$. For $Q = 2$ there is a significant but very small non-zero amplitude before $t = 0$, but the main part of the pulse does not begin until after $t/t_{min} = 1$, as required. For $Q = 1$ the non-zero amplitude is even larger, and now the main pulse arrives earlier than $t/t_{min} = 1$. So it is reasonable to expect the Aki-Larner method to give reliable results at least for Q as low as 5 and possibly as low as 2. This is rather surprising, since apparently the dispersion law holds even for very strongly attenuating materials. Further, since causality is determined only by the phase spectrum and since the pulse shapes are correct in all cases, it is possible that even results for $Q = 1$ may be meaningful as long as we are looking only at amplitudes and not phase. This is a very critical consideration in this thesis because we will see later on that the model which best explains the observed amplitude data for the Valles Caldera requires the use of $Q \approx 1$. Further justification for this will be presented with those results.

Finally we end this chapter by demonstrating the difference in results obtained using complex frequency versus complex dispersive phase velocity. For this test we used a specific single-layered model taken from *Larner* [1970] which was used to study a dented MOHO problem. The model geometry, velocities and densities are shown in the top of Figure 3.6. The source is a steady-state plane P wave with vertical incidence. The model period used was $L = 256$ km and the maximum scatter

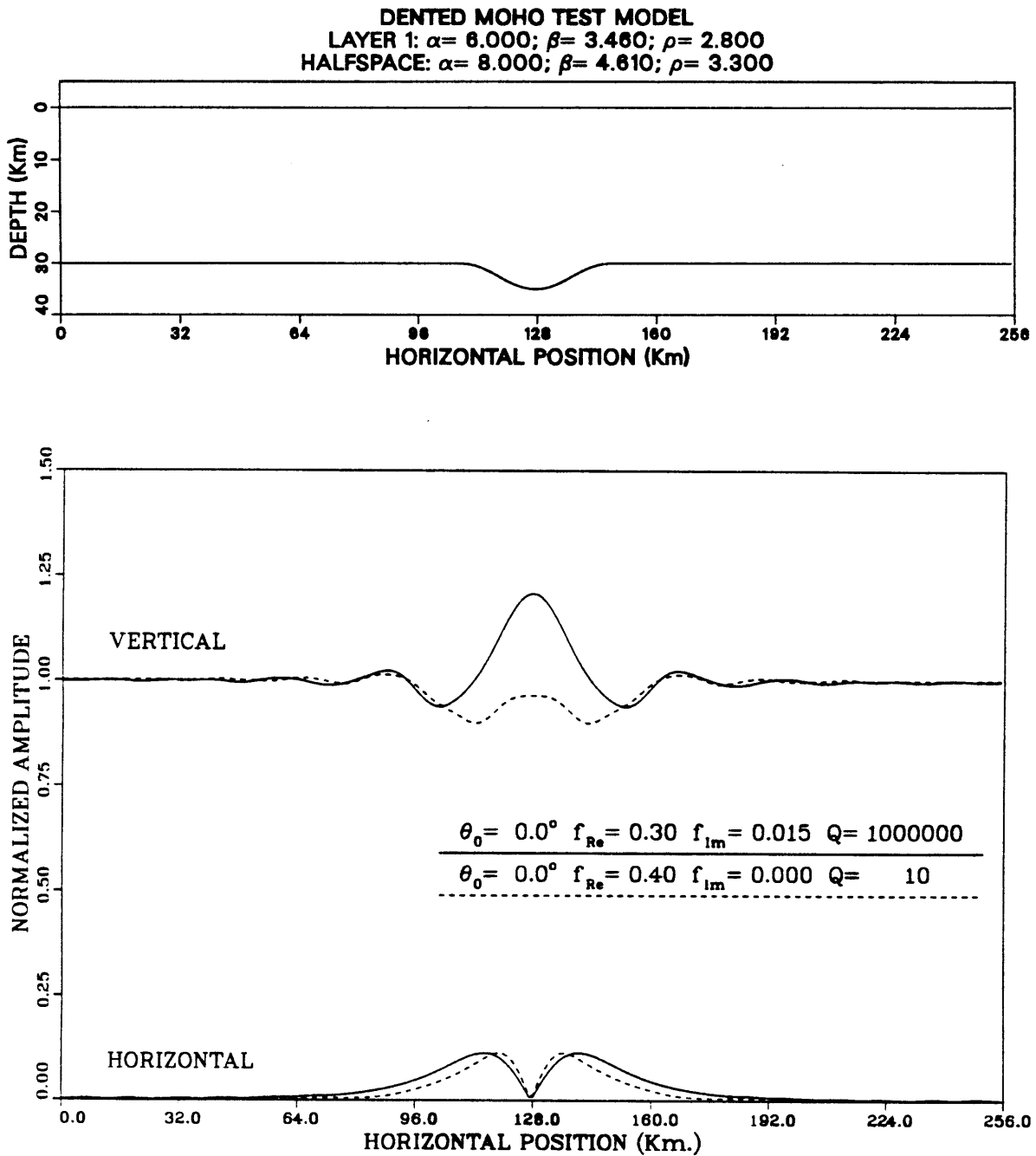


Figure 3.6 Comparison of results for the wave damping method and Q method for the dented MOHO problem shown at the top of the figure for a vertically incident P wave [after *Larner*, 1970]. The displacement amplitude solutions for vertical and horizontal motion are shown at the bottom for a single frequency versus horizontal position along the model surface. The amplitudes for both components are normalized by the vertical solution away from the irregularity in each case. The damping method results are shown as solid lines and the Q method results as dashed lines.

order index was $N = 39$. The bottom of Figure 3.6 shows the vertical and horizontal (radial) displacement amplitude solutions for a single frequency plotted versus horizontal positions along the surface of the model. The amplitudes are normalized by the flat-layered solution for the vertical component away from the interface irregularity. The solid lines are for Larner's solution using complex frequency with $f_I = 0.015$ and constant, real phase velocities. The dashed lines are the solutions obtained for real frequency and complex dispersive velocities using $Q = 10$ in both the layer and the halfspace. In both cases $K_I = 0.05K_R$ for the halfspace due to the choices for ω_I and Q . Also, because the dispersion causes a reduction in K_R , we have used $f_R = 0.4 \text{ Hz}$ for the low- Q case and $f_R = 0.3 \text{ Hz}$ for the complex frequency case so that both results share the same value of K_R in the halfspace. So the only difference between these two problems is that λ and μ are complex for the low- Q case and real for the complex frequency case. The difference in the solutions is quite striking, especially for the vertical component. With Q correctly parameterized in the model there is a zone of attenuation associated with the region above the interface irregularity, whereas the complex frequency case predicts amplification here. This shows that although K_R and K_I are identical in both cases it is not correct to attempt parameterization of Q in terms of complex frequency since this will link the attenuation to the wavefield itself rather than to the elastic parameters of the model.

CHAPTER 4

Modeling of Arrival Time Delays

4.1 Introduction

In Chapter 2 we demonstrated that the pattern of observed teleseismic P-wave arrival time delays strongly suggests the presence of a large, deep low velocity zone (LVZ) beneath the Valles Caldera. We used a simple plot of straight raypaths in Figure 2.35, categorized according to the strength of delay, to estimate qualitatively the maximum dimensions and minimum depth of this LVZ. In the present chapter we will present the best results for the P-wave velocity structure obtained from ray tracing analysis of the delay data. Our approach was to obtain a first order estimate of the deep structure primarily from Figure 2.35, and then to use this information to guide the ray tracing efforts which we performed completely as a forward modeling study.

We first attempted to run a formal travel time inversion of the delay data, using the method of *Aki, Christofferson & Husebye* [1976] (ACH). However, these results were inconclusive for two main reasons. First, the ACH inversion requires the use of block-grid model geometries, and unless the ray coverage is extremely dense this gives rise to under-sampling problems which depend on the size of the grid spacing. Although our ray coverage was good, it was not dense enough to adequately sample every block of the initial models that we used. Increasing the block size, to compensate for the under-sampling, yielded models which were too coarse to provide any useful information about the velocity structure. The main

deficiencies in the data were that we had no stations in between sites RDT and CLJ and we had too few southeastern events. The most obvious holes in the coverage are clearly displayed in Figure 2.35 directly below the caldera, between SAM and RDT at depths of about 10 km and larger. Secondly, we could only use flat-layered structures for our initial models and this severely restricted the amount of a priori information we could use. In particular, the near-surface structure is highly irregular in shape and, if not corrected for adequately, will directly affect the solution for the shape and location of the LVZ, which is our primary concern here. Despite these problems, the ACH inversion did yield a velocity image which favored a vertical band of low velocity blocks centered beneath the caldera, but it did not provide any additional information, particularly concerning depth, beyond what we have already qualitatively discussed for Figure 2.35. Therefore we will not discuss these results in this thesis.

Our specific approach to modeling the delay data, then, was to combine an initial estimate of the size, depth and velocity of the LVZ with an a priori estimate of the near-surface structure, and then to use this as an initial model to test with ray-tracing. By carefully adjusting the initial model, we were able to obtain a reasonable fit between the majority of the observed and calculated delays. The minimum structural requirements of the best-fitting model are that it have an irregular low velocity surface layer and a large, deep, low-velocity inclusion, as we expected from our intuitive examination of the delay data. Although more complex models would be required to completely explain all of the observations, our data coverage was insufficient to constrain adequately any additional features beyond the two mentioned above. Thus, we will maintain the simplicity of the two-component

structure throughout this chapter. We will discuss how this in itself is a very complex problem because of the extreme sensitivity that ray tracing exhibits for small variations in interface slopes and velocity contrasts.

4.2 Description of Ray Tracing Method

To perform the ray tracing we used a FORTRAN program written by W.H.K. Lee, R.P. Comer, Franklin Luk and J.P. Yang which was supplied to us by Scott Phillips of Los Alamos National Laboratory. The basic method is described in *Lee & Stewart* [1981] and we will discuss only the practical aspects of its application to our problem here. The models are defined over a two-dimensional rectangular grid with velocities assigned at the grid points. The grid spacing in both the x and z coordinates can be chosen arbitrarily and may vary within the model since the grid point locations are stored explicitly in arrays in memory. This was particularly convenient for our purposes because it allowed us to use the same types of layered models as in the Aki-Larner method by simply digitizing the P-velocity structures over a sufficiently dense grid. The ray-tracing itself is a shooting method and requires the specification of a starting point within the model boundaries and a take-off angle for each desired ray. Partial derivatives with respect to x and z of the velocity at each grid point are used to obtain the velocity gradients within the model. These in turn determine the ray-bending angles which obey Snell's law. The rays are terminated when they hit any of the four edges of the model box and the total path length from the starting point to the ending point, the travel time for this path and the apparent velocity are calculated for each ray. The program calculates only the shortest paths between the starting and ending points and thus

only refraction and total reflection are considered. This is appropriate for studying the earliest arrival at any given site.

The locations of the ending points for rays which reach the top edge of the model were used in our study to obtain travel time curves versus horizontal position, since the top of the model represents the free surface where our sites were located. Since our teleseismic data represent plane-wave arrivals with a specific angle of incidence, θ_0 , we traced suites of parallel rays, with takeoff angle θ_0 , which all began at points along a horizontal line near the bottom of the models. We chose θ_0 for each event by correcting the estimated Richter incidence angle for the P-wave velocity at the bottom of the model, as discussed in Chapter 2. The resulting travel times to the surface, then, do not contain the additional delays due to normal moveout and this must be added in before we can compare with the observed delays. This is a very important point which we will discuss in more detail below. We made several modifications to Lee's program. The most important one was the addition of free surface topography since this can cause significant differences in travel time from site to site. We simply changed the program code so that rays will terminate along a pre-defined profile of x and z values rather than being allowed to continue to the top of the model box.

The accuracy of the travel time calculations obtainable from the program for a given ray is a function of the total path length, model grid spacing and machine precision. The grid spacing, if too coarse, can severely influence the details of the shortest path taken, particularly for fairly complex velocity structures, and this will alter the location of the ending point and the travel time. We will show examples of this in the next section. Regardless of the grid spacing, the absolute accuracy of the

travel time calculation decreases as the ray path length increases. This is because the desired accuracy is defined internally by the program in terms of significant digits rather than in absolute seconds. So if we started the parallel rays along an inclined line rather than a horizontal line, the accuracy of the travel times will vary from ray to ray as the path length increases even if the model is a homogeneous halfspace. The use of inclined starting points would be a natural way to represent a plane wave front, since then the normal moveout is automatically included in the results. But to maintain consistent accuracy it was necessary instead to use a horizontal starting line and add the normal moveout to the results afterwards. This also allows the model box to be smaller since we don't need to increase the depth or width of the boundaries to accommodate shallower incidence angles. By following these procedures, then, we were able to calculate travel times with an accuracy of about 10 msec.

To compare the calculated travel times with the observed delay times, two things must be done to the ray results. First, as we have already mentioned, the normal moveout must be added in. This is necessary in order to correctly delay each ray so that the true first arrival at each site can be detected. We will see that the model structures are capable of bending rays very sharply forward or backward, and there are many cases in which two or more rays arriving at the same surface location will arrive in the wrong order unless the moveout is included. The moveout correction is simply the opposite of what we did to the observed delays in Chapter 2 to display only the effects of irregular structure. We use equation (2.10) as before, but now we choose an arbitrary reference location along the ray starting line and calculate moveout delays for all other rays, based on their starting points, relative

to the reference point. These delays are then added to the ray travel times. Next we must convert the calculated absolute travel times to relative delay times, as with the observed data. This is simply a matter of finding the smallest ray travel time to a reference site and subtracting this from the travel time for each ray. The reference site must be the same one used for the observed data. Recall that we used one common site, SAM, as the reference for all recorded data in order to obtain Figure 2.35. This choice was helpful for reducing the data in a way which allows simultaneous comparison of all recorded events. However, we will see that SAM is a poor choice for the reference site for southeastern events in the ray-tracing results. This is because the best models produce numerous multiple arrivals near this location for negative θ_0 , and it is usually difficult to choose the best value to normalize by. It is better to use a site with the fewest multiple arrivals, and this is usually the site closest to the event. For array-1 data we will use CAC as the reference site for northwestern events (positive θ_0) and CAP for southeastern events. For array 2 we will use SAM and CLJ, respectively.

Due to the complexity of the structures that we have modeled and the extreme sensitivity of ray-tracing to velocity contrast and interface shape, it is almost impossible to predict where any given ray should start so that it terminates exactly at a particular site location. Possible multiple arrivals further complicate this problem. Thus, in order to get adequate coverage so that at least one ray will always emerge near each site, we had to trace approximately 4000 rays for each incidence angle tested. Even then, there were cases where observed delay points happened to fall within small gaps in the calculated delay points. These gaps produce large residuals which may be erroneous if the trend in the calculated delays on either side of a gap

would normally pass through the observed delay point. In other cases there were so many ray arrivals near a site that it was very difficult to choose a reasonable value for the delay to be used to obtain the residual. We dealt with these cases by averaging the calculated delays over a 1.0-km width of horizontal coordinates centered around the observed delay point. For the average we used only the calculated delays which fell below the upper error bar for the observed delay at the site. If there were no ray delays earlier than this, we simply used the earliest ray delay at the site location to obtain the residual. We then obtained the residual variance of the calculated delays for each observed event separately and for all events combined, using a formula similar to equation (2.7) for comparing amplitude ratios:

$$\sigma^2 = \frac{1}{N} \sum_{n=1}^N [T_n^{obs} - T_n^{ray}]^2. \quad (4.1)$$

For a single event, N is the total number of sites (other than the reference site) at which the event was recorded. For multiple events, N is the total number of observed time delays in the combined data set. As with the amplitude ratios we will quantify how good a model is by calculating the variance reduction relative to the homogeneous halfspace (HHS) case. The HHS time delay curve is a straight line which passes through the reference site delay point, and has slope equal to $\sin \theta_0 / \alpha_H$ for incidence angle θ_0 and halfspace P velocity α_H . Any acceptable model should yield a residual variance smaller than for the HHS case. So we will use the variance reduction formula exactly as given in equation (2.8) to characterize how well a particular model fits the observed delay data.

4.3 Delay Time Modeling Results

In this section we will present the best ray model and discuss its validity in terms of which features are or are not well constrained by the data. Since the ray coverage was not sufficient to provide reliable results from a formal travel time inversion, we should not expect to be able to determine all features of the structure uniquely. However, for models with a simple two-component structure, namely caldera fill and low velocity inclusion, we found that the observed pattern of time delays at the surface does place reasonable constraints on the width, average depth and approximate shape of the LVZ. We can also determine the minimum height and velocity. But the depths to the top and bottom of the LVZ are less well constrained because of the limited ray coverage.

We began the modeling by first trying to fit as much of the observed data as possible with only the free surface topography and irregular caldera fill layer. Our aim here was to isolate the minimum effects which must be attributed to deeper structure. We used a priori estimates of the dimensions and shape of the caldera fill from *Self et al.* [1986] (see Figure 1.4) and a range of P velocities of 3.0 to 4.5 km/sec [*Ankeny et al.*, 1986] to set limits on the variability of the initial caldera fill model. By carefully adjusting the shape, thickness and velocity of the caldera fill we were able to fit quite well all observed delays at sites CAC through RDT for the northwestern events only. The best fits were obtained for velocities between 3.0 and 3.5 km/sec. However, the observed delays at CLJ for northwestern events and at all non-reference sites for southeastern events were significantly stronger than the delays predicted by the caldera fill layer alone.

This is demonstrated quite clearly in the following figures. Figure 4.1a shows the caldera fill correction model used, including the surface topography and nine site locations shown previously in Figures 2.1a,b. We used a velocity of 3.2 km/sec in the caldera fill and 5.8 km/sec in the granite basement. Figure 4.1b shows the comparison of the calculated ray delays for this model with the raw observed delays, relative to the reference site SAM, for the Kuril Islands event shown previously in Figure 2.33. The estimated incidence angle used was $\theta_0 = +21.5^\circ$. The straight solid line represents the HHS solution, which is simply the normal moveout relative to the reference site. The residual variance for the HHS case, σ_{HHS}^2 , and for the caldera fill model, σ_{MOD}^2 , are listed at the top of each figure along with the variance reduction for the model. Figure 4.1c shows the delays relative to CLJ for the Jujuy event, also shown before in Figure 2.33, with $\theta_0 = -21.0^\circ$. The calculated and observed delays in both figures have been normalized to zero at the reference site location.

For the Kuril event, all observed delays are fit well except CLJ. On the contrary, the Jujuy delays are all significantly larger than what the caldera fill model predicts. This difference between northwestern and southeastern events is reflected clearly by comparison of the variance reduction, which is positive and large for the Kuril event but negative for Jujuy. In fact, for the Jujuy data, the model predicts delays smaller than for the HHS case at all but one site. This is because the caldera fill is thickest beneath the reference site, CLJ. Thus, we next require the addition of the low velocity zone. We will also require that the LVZ must significantly improve the variance reduction for all southeastern events and increase the relative delay at CLJ for northwestern events without affecting the remaining four sites.

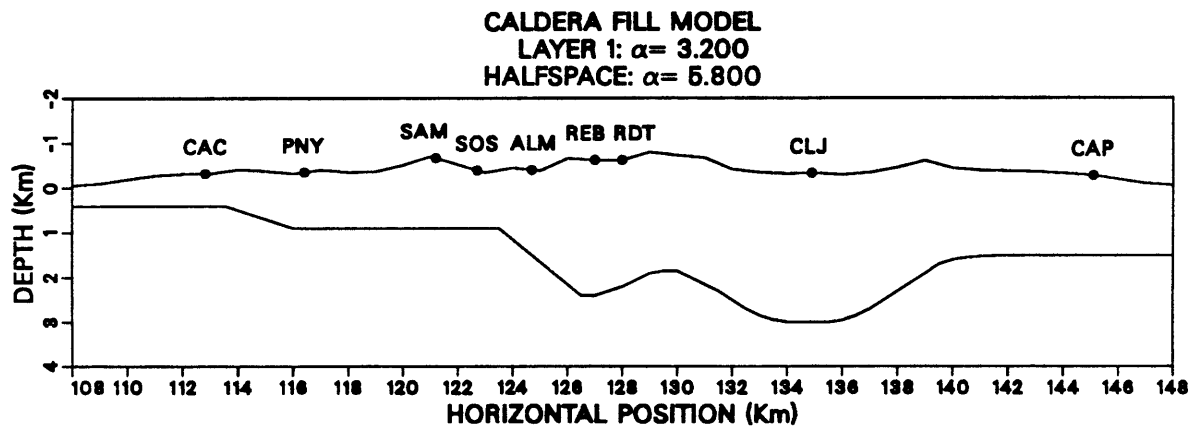


Figure 4.1a Caldera fill correction model used to fit the observed delays for northwestern events.

CALCULATED RAY DELAYS FOR CALDERA FILL MODEL
PLANE WAVEFRONT: INCIDENCE ANGLE = 21.5°
OBSERVED P-WAVE DELAYS FOR EVENT FROM: KURIL ISLANDS
REFERENCE SITE: SAM LOCATION: X = 121

$\sigma_{\text{HHS}}^2 = 0.385\text{E-}01$ $\sigma_{\text{MOD}}^2 = 0.466\text{E-}02$ Variance Reduction = 87.9%

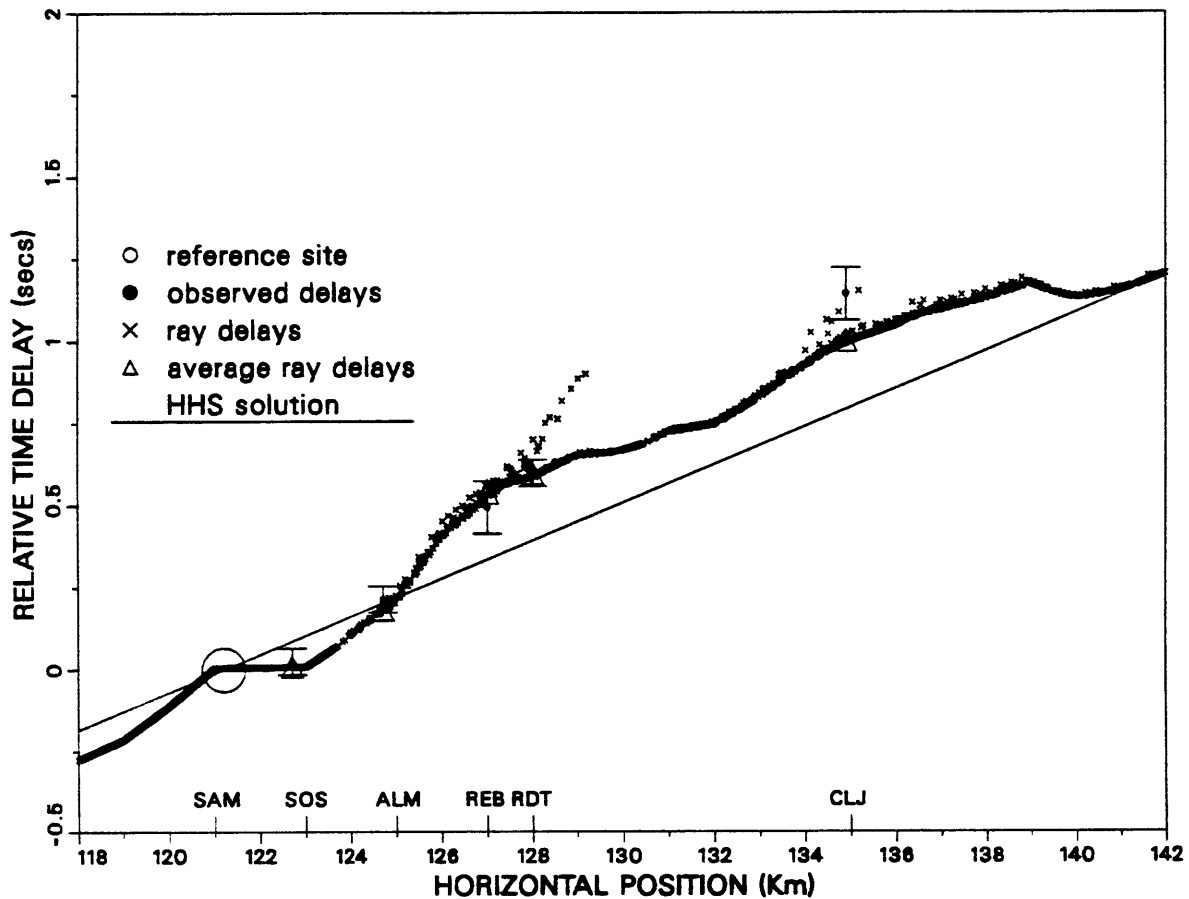


Figure 4.1b Comparison of ray tracing results (x's) for the caldera fill model in Figure 4.1a with observed delays (solid dots with error bars) for an event from the Kuril islands. The large open circle marks the reference site location. Incidence angle used was $\theta_0 = +21.5^\circ$. The solid line shows the predicted solution for the homogeneous halfspace (HHS) model. Open triangles mark the average ray delay near each site used to calculate the residual variance for the model. The variances for the model and for the HHS are listed at the top of the figure, along with the variance reduction.

CALCULATED RAY DELAYS FOR CALDERA FILL MODEL
PLANE WAVEFRONT: INCIDENCE ANGLE = -21.0°
OBSERVED P-WAVE DELAYS FOR EVENT FROM: JUJUY, ARGENTINA
REFERENCE SITE: CLJ LOCATION: X = 135

$\sigma_{\text{HHS}}^2 = 0.207\text{E}+00$ $\sigma_{\text{MOD}}^2 = 0.368\text{E}+00$ Variance Reduction = -77.8%

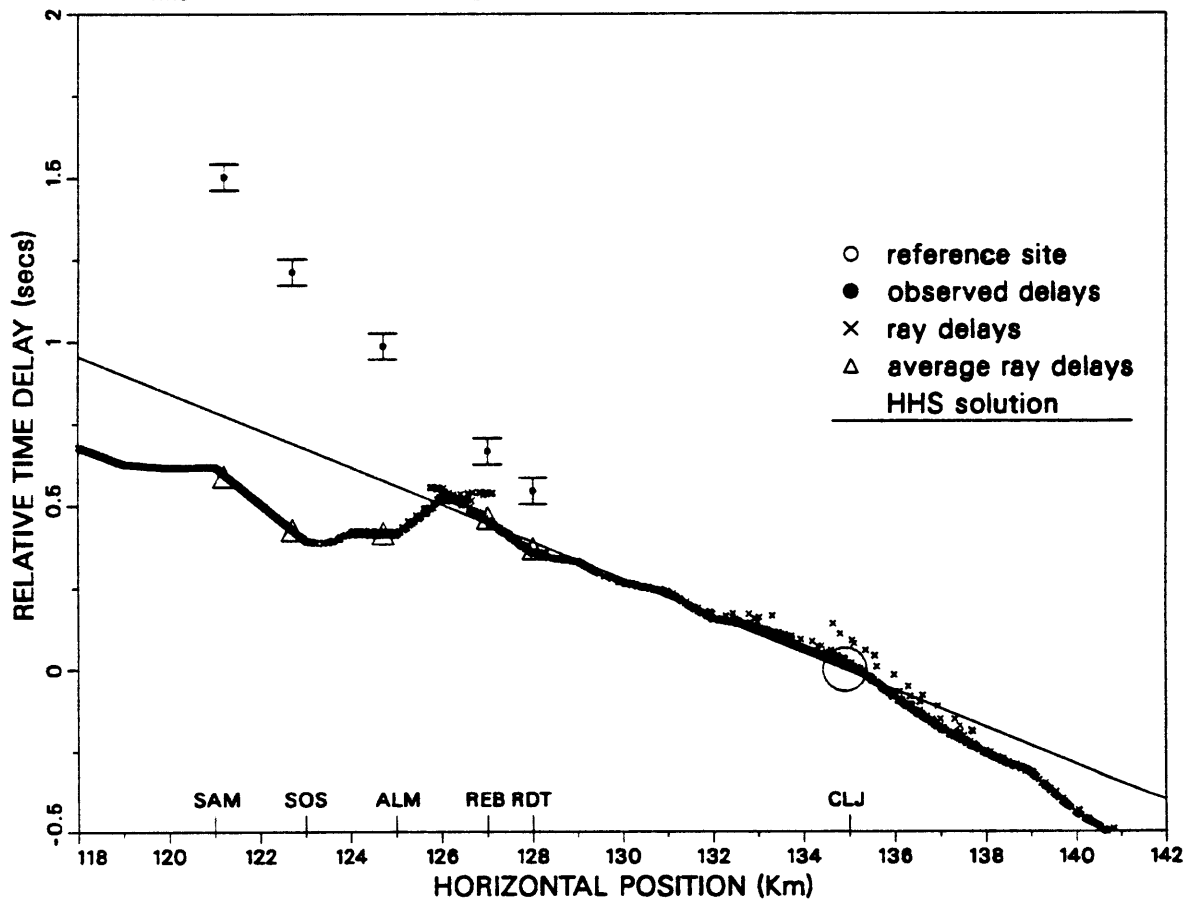


Figure 4.1c Same as Figure 4.1b except ray tracing results are compared with observed delays for an event from Jujuy, Argentina. Incidence angle used was $\theta_0 = -21.0^\circ$.

Figures 4.1b,c show that the width of the observed zone of delays at the surface, beyond the caldera fill affect, is on the order of 7 to 10 km. The southeastern data show this zone beginning approximately at RDT and extending at least to SAM. For northwestern data the zone begins beyond RDT and is significantly reduced at CLJ, where the additional non-caldera delay is much smaller than for the southeastern data at SAM. The thickened caldera fill beneath CLJ accounts for a large portion of the observed delay at that site. We found that a circular low velocity inclusion, 8 km in diameter, placed beneath the caldera fill succeeds in delaying a region of sufficient width at the surface and that the location of this delayed region as a function of incidence angle puts reasonable constraints on the depth and horizontal position of the inclusion. However, the delays produced for southeastern incidence angles were much too strong at RDT, REB and ALM. The circular shape of the inclusion caused very severe refraction near its left and right edges so that all rays which came in contact with it were either delayed by almost the same large amount or scattered away from the caldera completely.

The trend in the observed delays for the Jujuy event in Figure 4.1c is approximately linear between RDT and SAM, with a slope significantly steeper than either the HHS or the caldera fill models can predict. This implies that between RDT and SAM the portions of the ray paths which lie inside the inclusion must increase gradually in length from ray to ray away from the source or that the effects of refraction must cause an increase in the total path length from the bottom of the model to successively further sites. We were able to reproduce this effect and minimize the strong edge refractions by tapering the left and right edges of the inclusion to produce a lens-shaped structure. This eliminates the steepest slopes

of the circular shape and allows rays to pass through the inclusion with minimal refraction. It also allows the path length inside the inclusion to increase gradually for successively later rays.

Figure 4.2 shows the model we eventually obtained by carefully adjusting the shape, size, velocity and location of the LVZ. This is the simplest model we obtained which best fits all of the data. The P-wave velocity used for the LVZ was 3.7 km/sec. The total width of the LVZ, between the ends of the tapered regions, is 17 km and its overall height is 8 km. The average width is approximately 8 km. In Figure 4.3 we show examples of typical raypaths through this model for a positive incidence angle of $\theta_0 = +15^\circ$ at the top and for a negative angle of $\theta_0 = -15^\circ$ at the bottom. Although the travel time calculations were performed for 4000 rays, we have only shown about 50 raypaths here to avoid cluttering the figures. First, notice that in both cases there is a very distinct region at the surface within which the only arrivals arise from rays which have passed through the LVZ. These arrivals clearly will be delayed relative to the rest. The width of the surface delay zone is directly determined by the width of the LVZ. Furthermore, the position of this zone will shift horizontally if the location of the LVZ is shifted in any direction. A shift in the LVZ location to the right will cause the surface delay zone to shift the right also. For positive incidence angles, a downward shift of the LVZ will move the delay zone to the right, and for negative incidence it will shift to the left. So we can use the observed width and locations of the delay zone versus incidence angle to constrain the width and location of the LVZ. Given adequate ray coverage for a wide range of incidence angles, we would also be able to constrain the height. But we will see that this is not the case with our teleseismic data.

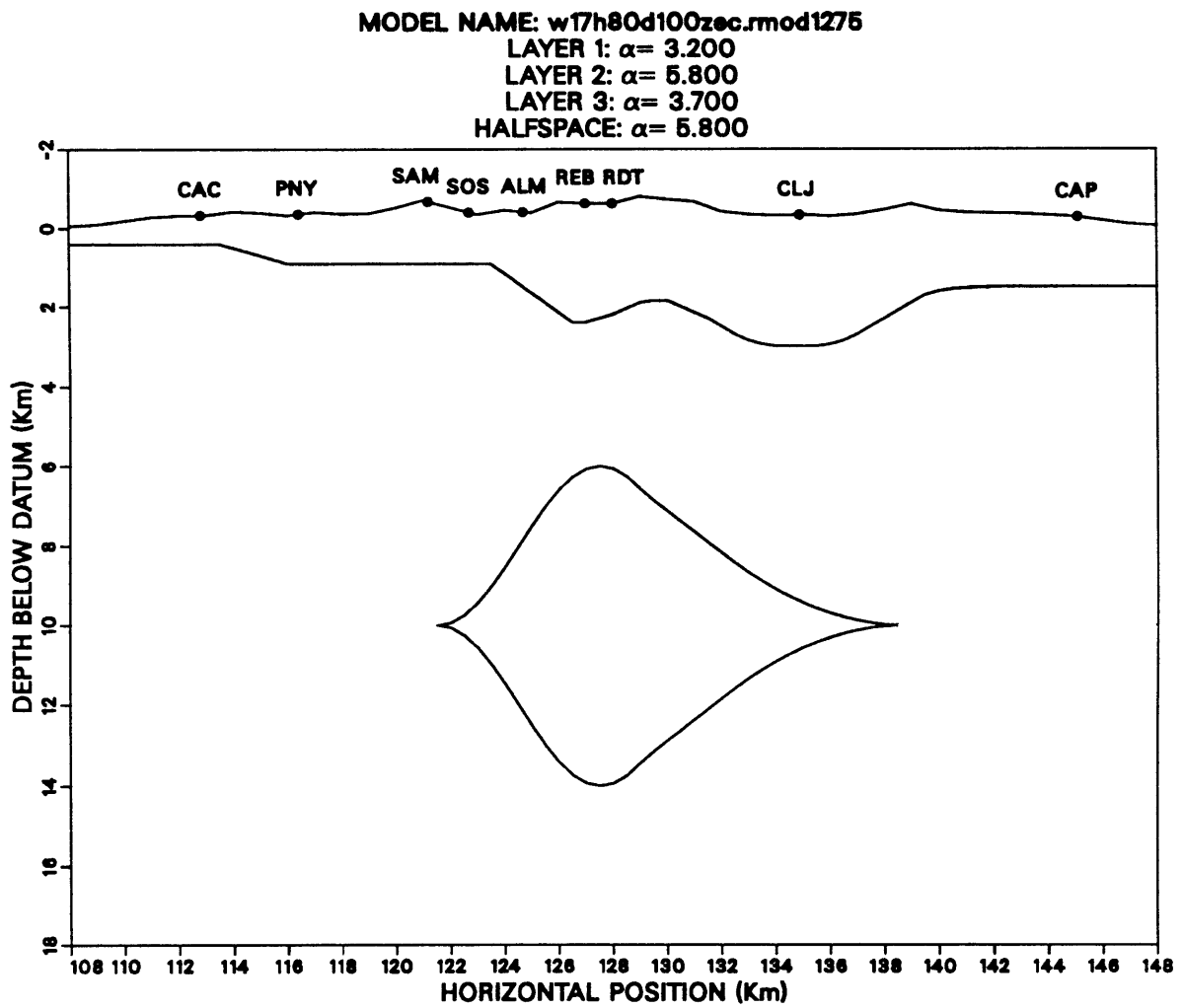


Figure 4.2 LVZ model geometry and velocities which gives the best fit to all observed delay data recorded on both instrument arrays. Caldera fill layer is the same as shown previously in Figure 4.1

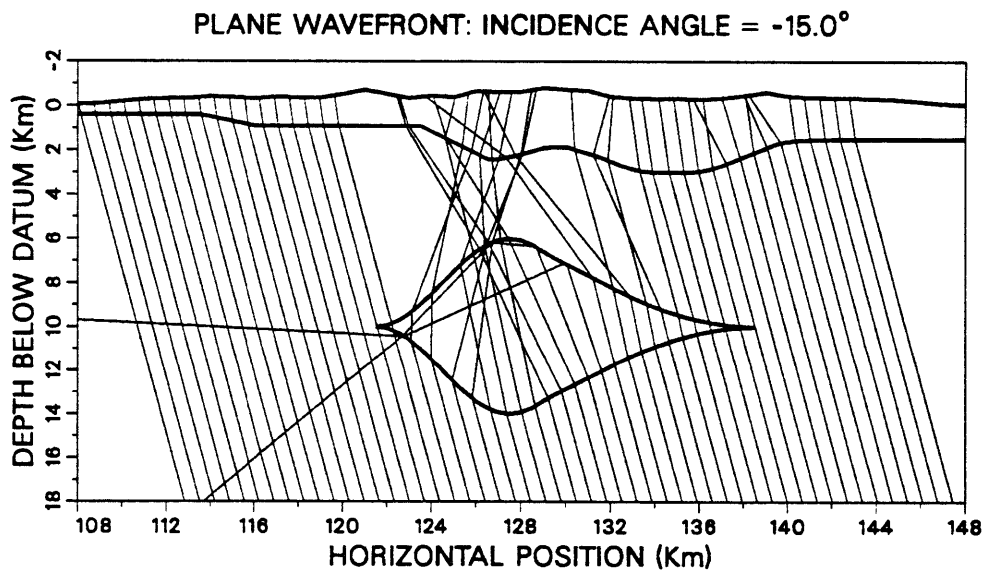
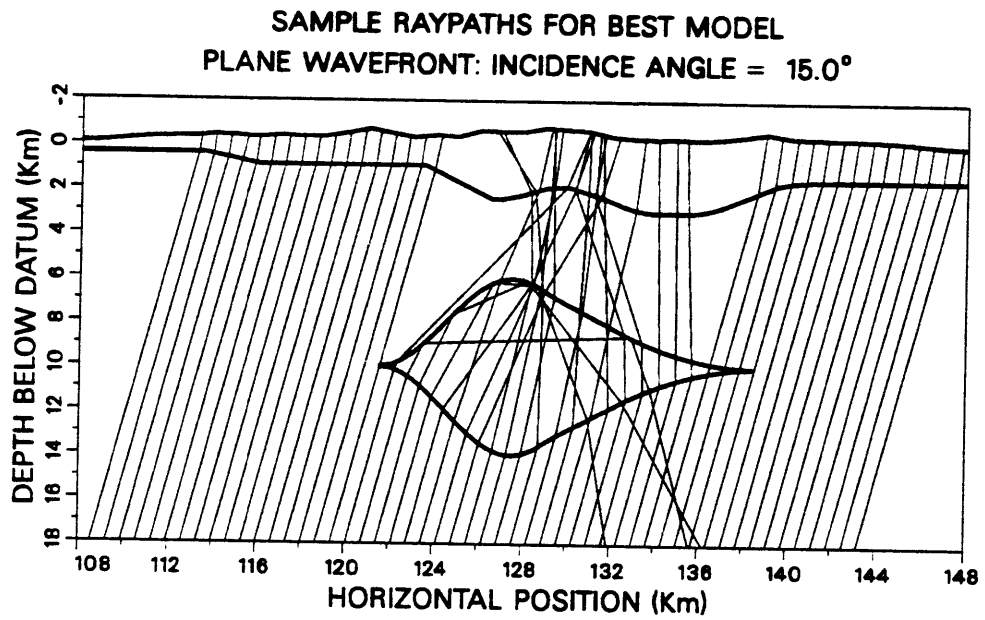


Figure 4.3 Typical raypaths for the best model shown in Figure 4.1 for positive incidence angle $\theta_0 = +15^\circ$ (top) and negative incidence, $\theta_0 = -15^\circ$ (bottom).

The rays in Figure 4.3 which pass through the LVZ can take a variety of complicated paths. Some rays experience total reflection at the top of the LVZ and never make it to the surface. Most rays which pass through the tapered zones of the LVZ follow predictable paths to the surface discussed previously. The remaining rays are refracted through the largest portions of the LVZ and either emerge at the surface on opposite sides of the caldera from where they first entered the LVZ, or are focused near the center. Careful inspection of these plots reveals that a few rays appear to bend at angles inconsistent with the local interface slope. This is caused by the finite grid spacing mentioned in the previous section, which creates localized step-like shapes at grid points which lie on or very close to an interface. This effect is due to the way in which the program calculates velocity gradients and cannot be completely eliminated. This is one of the reasons why we have averaged the ray delays near each site to obtain the residuals.

Figures 4.4a,b shows the comparison of the ray time delay results for the model with the same array 2 data shown previously in Figures 4.1b,c. Notice the immense improvement over the caldera fill model in the variance reduction for the Jujuy event in Figure 4.4b. Also note that the Kuril data in Figure 4.4a are fit much better at CLJ than before. The pattern of delays created by the LVZ reveals three main features related to the ray paths discussed above for Figure 4.3. First, in both cases there is a region corresponding to the weakest of the anomalous delays, which exhibit roughly linear dependence on x . For positive incidence angles this region of delays nearly intersects the observed delay at CLJ and has virtually zero slope. For negative angles the slope is strongly negative and passes through the observed delays at ALM, REB and RDT. This feature is due to the tapered zone at the right

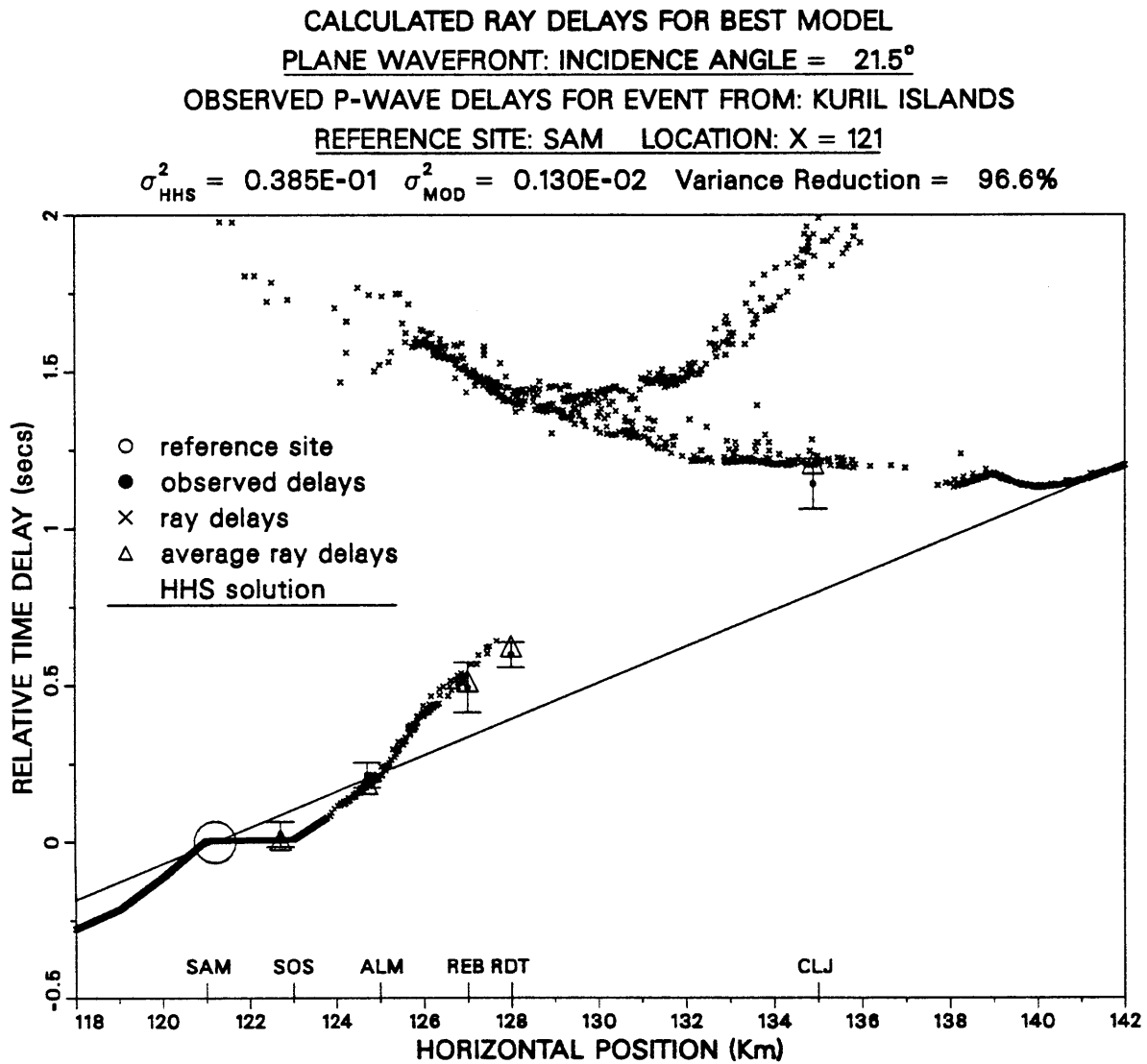


Figure 4.4a Comparison of ray tracing results for the best model, Figure 4.2, with observed delays for the Kuril Islands event shown previously in Figure 4.1b.

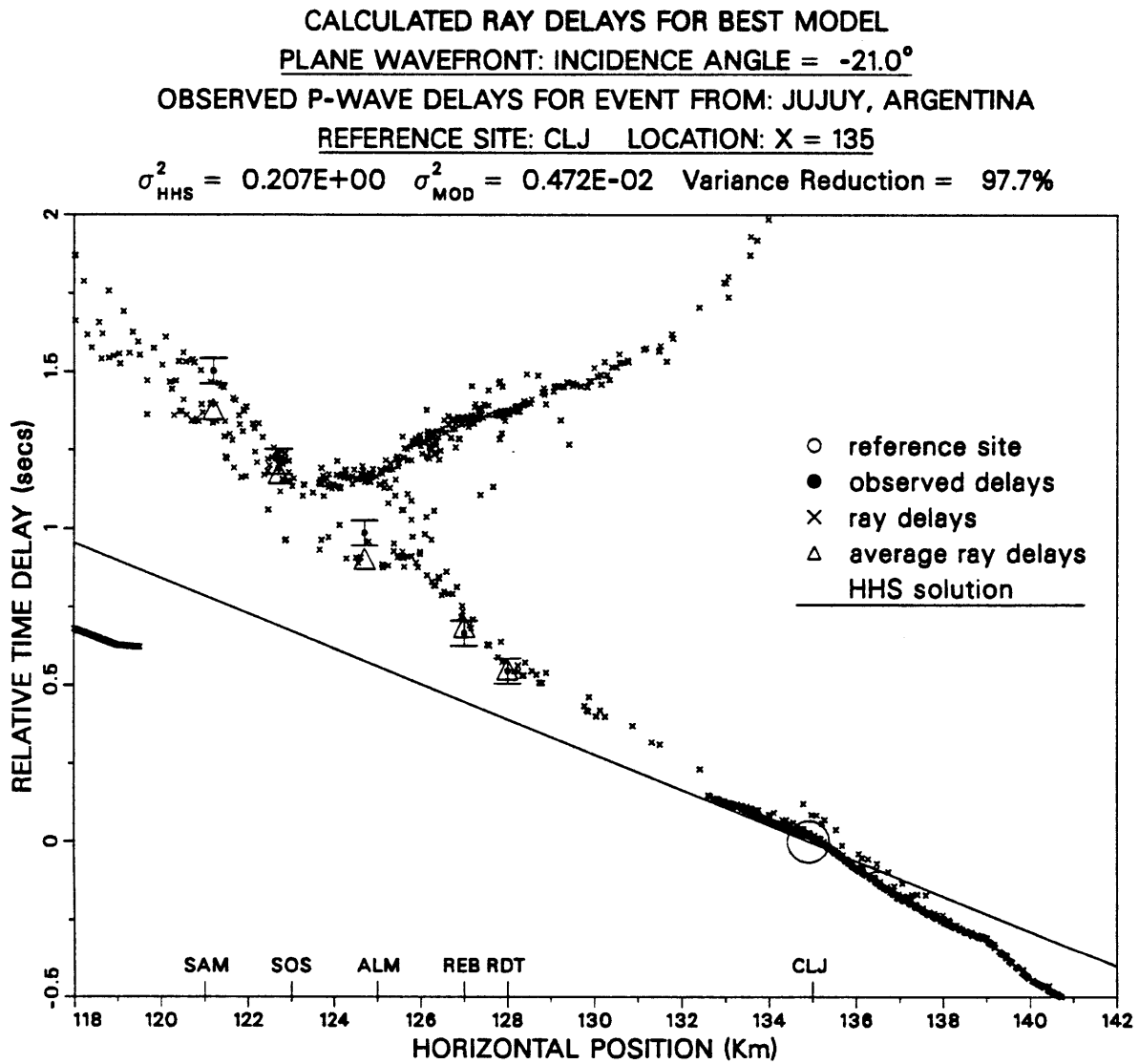


Figure 4.4b Comparison of ray tracing results for the best model with observed delays for the Jujuy event shown previously in Figure 4.1c.

edge of the LVZ. For positive incidence the taper causes the LVZ delays to decrease with increasing x in proportion to the increasing normal moveout delay, and this cancellation of effects yields the flat behavior shown. For negative angles these two effects add rather than cancel, to yield the steep slope necessary to fit the Jujuy data. The second major feature is the upward-curving pattern representing the strongest delays. These delays are due to the rays refracted across the largest portions of the LVZ and shown previously in Figure 4.3. The strongest observed delays, at SAM and SOS for negative incidence, thus represent the primary constraints on the minimum height or maximum velocity of the LVZ. The final important feature is the concentration of arrivals with similar delays near ALM for negative incidence. Although there is a spread of approximately 250 msec between the smallest and largest delays here, this is small enough that for teleseismic data these arrivals would appear to be nearly coincident. This focusing should produce large amplitudes near the first arrivals at certain sites inside the caldera, depending on the location of the LVZ. This is contrary to the observations we presented in Chapter 2, where the entire seismogram for each event, including the first arrival, was consistently smaller inside the caldera. In Chapter 5 we will show that the low amplitudes in the caldera are produced by a shallow attenuating body in the caldera fill and thus the focusing predicted by the ray-tracing is not in contradiction with the amplitude data. But it does allow us to exclude defocusing as a possible cause for the low amplitudes.

The width of the delay zone at the surface in Figures 4.4a,b produced by the LVZ is approximately 10 km for both positive and negative incidence angles. Increasing the width of the LVZ would create delays for negative incidence angles

which are too strong at RDT, REB and ALM. For positive angles the delay zone would extend too far to the left and this would cause a sudden, large increase in the delay at RDT. A wider LVZ could be moved to the right to avoid the problem at RDT for positive angles, but this would only aggravate the problem for negative angles. If the LVZ was significantly narrower, the range of approximately linear delays produced between RDT and SAM for negative incidence would be progressively pinched-out, leaving only the weaker caldera fill delays and the very large delays due to strong refraction through the largest portions of the LVZ. Thus, we will keep the tapered width and horizontal position fixed as in Figure 4.2 for the remainder of this chapter and discuss how well the data can constrain the height, depth and velocity of the LVZ. These are perhaps the most important parameters for defining the characteristics of an inclusion which might be interpreted as a remnant magma chamber.

In Figures 4.5a,b modeling results are compared with observed delays for two events recorded on array 1. Figure 4.5a is for an event from the Kommandorsky Islands to the northwest, shown previously in Figure 2.34, with incidence angle $\theta_0 = +23.5^\circ$. Figure 4.5b is for an event from Central Chile to the southeast, with $\theta_0 = -18.0^\circ$, also shown before in Figure 2.34. The reference sites used were CAC and CAP. These data show a very similar pattern as for array 2 but on a larger scale. The largest delays relative to the HHS case are observed at the inner three sites, SAM, ALM and RDT, for both northwestern and southeastern events. The Kommandorsky data, except for CAP, are fit well entirely by the effects of the caldera fill alone. For the Chile data, the delays inside the caldera, relative to CAC, are reproduced at least as well by the model as the Jujuy data were, relative to CLJ.

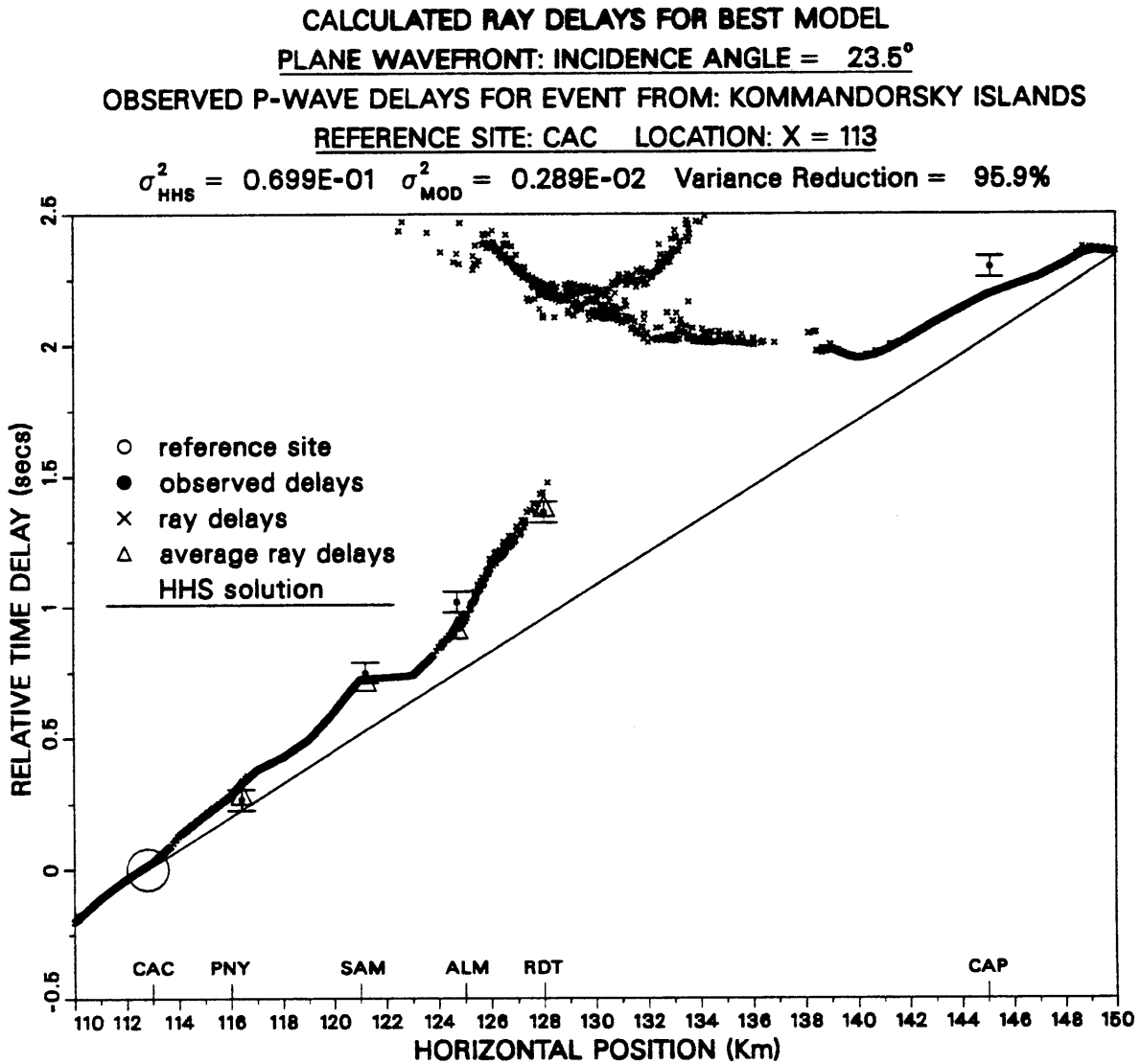


Figure 4.5a Same as Figures 4.4a,b except ray tracing results for best model are compared with observed delays for an event from the Kommandorsky Islands recorded on array 1. Incidence angle used was $\theta_0 = +23.5^\circ$.

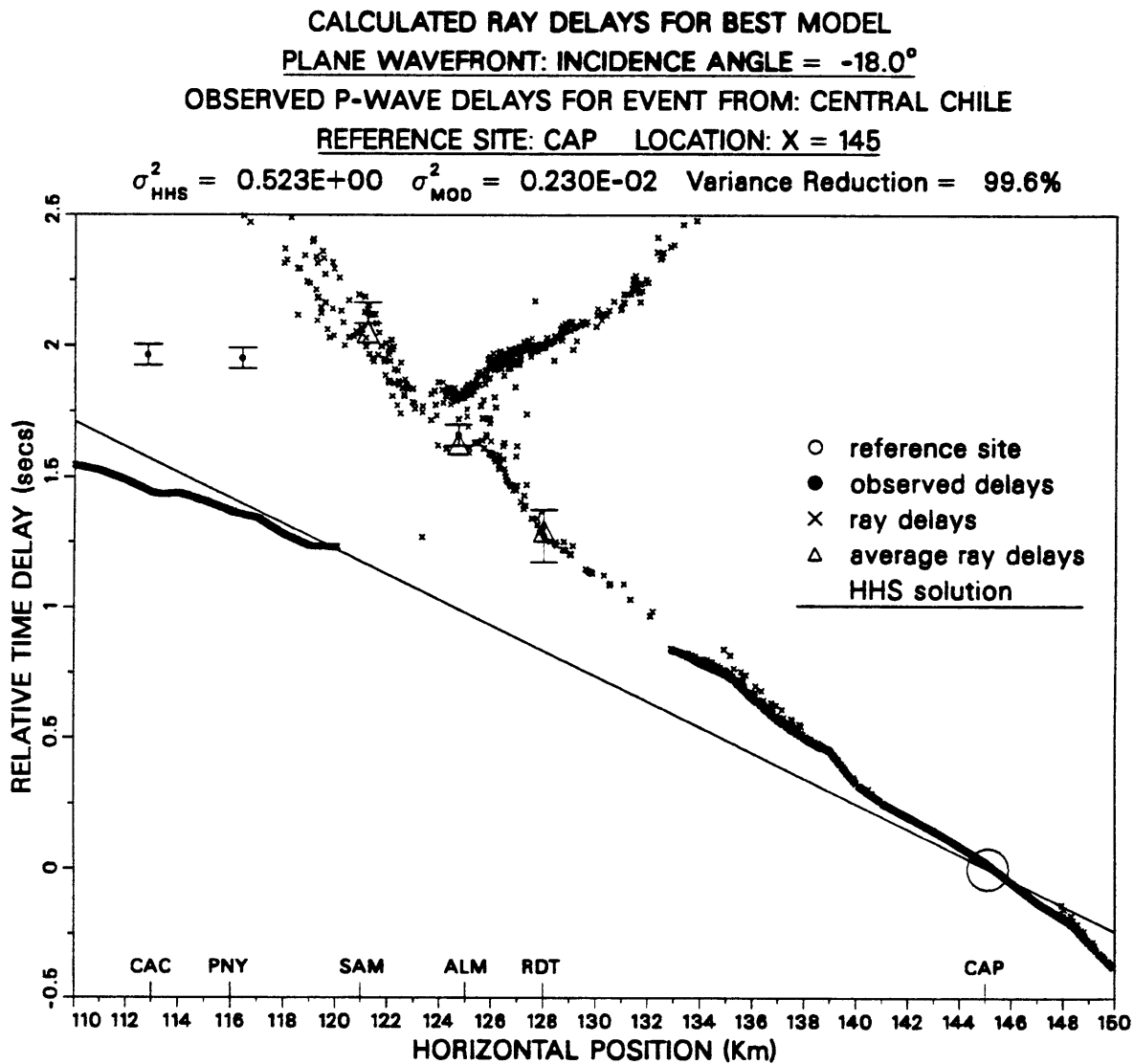


Figure 4.5b Same as Figure 4.5a except ray tracing results are compared with observed delays for an event from Central Chile. Incidence angle used was $\theta_0 = -18.0^\circ$.

But the delays at CAP for the Kommandorsky event and at CAC and PNY for the Chile event are larger than predicted by the caldera fill and smaller than predicted by the LVZ. These delays cannot be explained by a local thickening of the surface layer beneath these sites because this would reduce the relative ray delays in the caldera for opposite-azimuth incidence, which already fit the data well. Therefore, these outlying delays must be due to deeper structure. However, the Chile data at CAC and PNY cannot be explained by extending the LVZ to the left because this would in turn interfere with positive incidence rays arriving at the caldera sites and the ray delays at these sites would be much too large as a result. The same arguments apply to the Kommandorsky delay at CAP, although the model comes much closer in this case than for the Chile data at CAC and PNY. The Chile data can only be reproduced by placing some additional low velocity structure to the left of the LVZ and beneath the caldera fill. We made numerous attempts at determining this secondary structure but since we only had two southeastern events recorded at CAC and PNY we could not constrain this feature adequately. Since these outlying delays do not contradict the effects of the localized LVZ but do contribute very large residuals, we removed these points from the variance calculations and concentrated entirely on the local caldera structure. So the variance and variance reductions listed at the top of the Chile plot represent only the three caldera sites. Likewise, we eliminated the residual at CAP for the Kommandorsky event.

The true test of the present model is to compare ray results with data for a wide range of positive and negative incidence angles. The northwestern data covered a range of θ_0 from about $+15^\circ$ to $+40^\circ$ and the southeastern data covered from -18° to -32° . Table 4.1 lists the residual variance for the HHS and model and

TABLE 4.1
Residual Variance and Variance Reduction for
Best Ray Model Compared with 21 Events

Event Region	θ_0	# of Points	σ_{HHS}^2	σ_{MOD}^2	Variance Reduction
Guatemala	-32.0	5	0.0776	0.0065	+91.7%
Ecuador	-26.5	5	0.2010	0.0571	+71.6%
Southern Peru	-23.0	2	0.2090	0.0649	+68.9%
Northern Chile	-21.0	4	0.2180	0.0046	+97.9%
Jujuy, Argentina	-21.0	5	0.2070	0.0047	+97.7%
Chile-Argentina	-19.0	3	0.1820	0.0049	+97.3%
Central Chile	-18.0	3	0.5230	0.0023	+99.6%
South of Honshu	+15.0	3	0.1160	0.0360	+68.9%
Coast of Honshu	+17.0	3	0.2050	0.0218	+89.4%
Coast of Honshu	+18.0	5	0.0449	0.0044	+90.2%
Kuril Islands	+20.0	4	0.1450	0.0145	+90.0%
Sea of Okhotsk	+20.0	3	0.0762	0.0149	+80.4%
Kuril Islands	+20.0	5	0.0282	0.0049	+82.5%
Kuril Islands	+21.5	4	0.1070	0.0077	+92.8%
Kuril Islands	+21.5	5	0.0385	0.0013	+96.6%
Kommandorsky I.	+23.5	4	0.0833	0.0027	+96.6%
Kommandorsky I.	+23.5	4	0.0894	0.0053	+94.1%
Andreanof Islands	+24.5	5	0.0586	0.0002	+99.7%
Fox Islands	+26.0	5	0.0466	0.0012	+97.4%
Kodiak Island	+28.5	4	0.0595	0.0021	+96.4%
Coast of Oregon	+40.0	4	0.0631	0.0011	+98.2%
TOTAL	-	95	0.1080	0.0097	+91.0%

the variance reduction for each of the usable events, 21 in all. The uncorrected Richter incidence angles used and the number of data points considered are also listed for each event. At the bottom of the table are listed the results for all data points combined, 95 in all. Although the model fits some events better than others, the total variance reduction of 91% is extremely good.

The next set of figures demonstrates the effects of varying the depth of the LVZ. In each figure we show the ray tracing results compared with the Kuril and Jujuy data, as in Figures 4.4a,b. In the following discussion we will define the "average depth" of the LVZ to be the depth from the zero datum to its center, that is, to the widest portion where the tapered edges pinch-out completely. The "lower" and "upper" depths are defined at the bottom and top, respectively, of the LVZ. The average depth of the model in Figure 4.2, then, is 10 km, and with the topography included, this corresponds to a "true average depth" of approximately 11 km from the peak of the resurgent dome. For the results in Figures 4.6a,b the LVZ was shifted upward by 1 km to an average depth below datum of 9 km. The remaining figures are for deeper LVZ's. Figures 4.7a,b are for 11 km average depth and Figures 4.8a,b are for 12 km.

Examination of these figures and Figures 4.4a,b reveals a clear pattern in the calculated delays which allows us to constrain the average depth of the LVZ. Figure 4.6a, for the 9-km-depth LVZ compared with the Kuril data, shows that the weaker ray delays for the caldera fill effect have been cut off just before RDT. The last of these rays arrives within 500 meters of the site, however, and since we average the arrivals over ± 500 meters around each observed point, the residual at RDT is still very small and the total variance reduction for the 9-km-depth LVZ model, over

CALCULATED RAY DELAYS FOR 9 Km AVERAGE DEPTH LVZ MODEL

PLANE WAVEFRONT: INCIDENCE ANGLE = 21.5°

OBSERVED P-WAVE DELAYS FOR EVENT FROM: KURIL ISLANDS

REFERENCE SITE: SAM LOCATION: X = 121

$\sigma_{\text{HHS}}^2 = 0.385\text{E-}01$ $\sigma_{\text{MOD}}^2 = 0.180\text{E-}02$ Variance Reduction = 95.3%

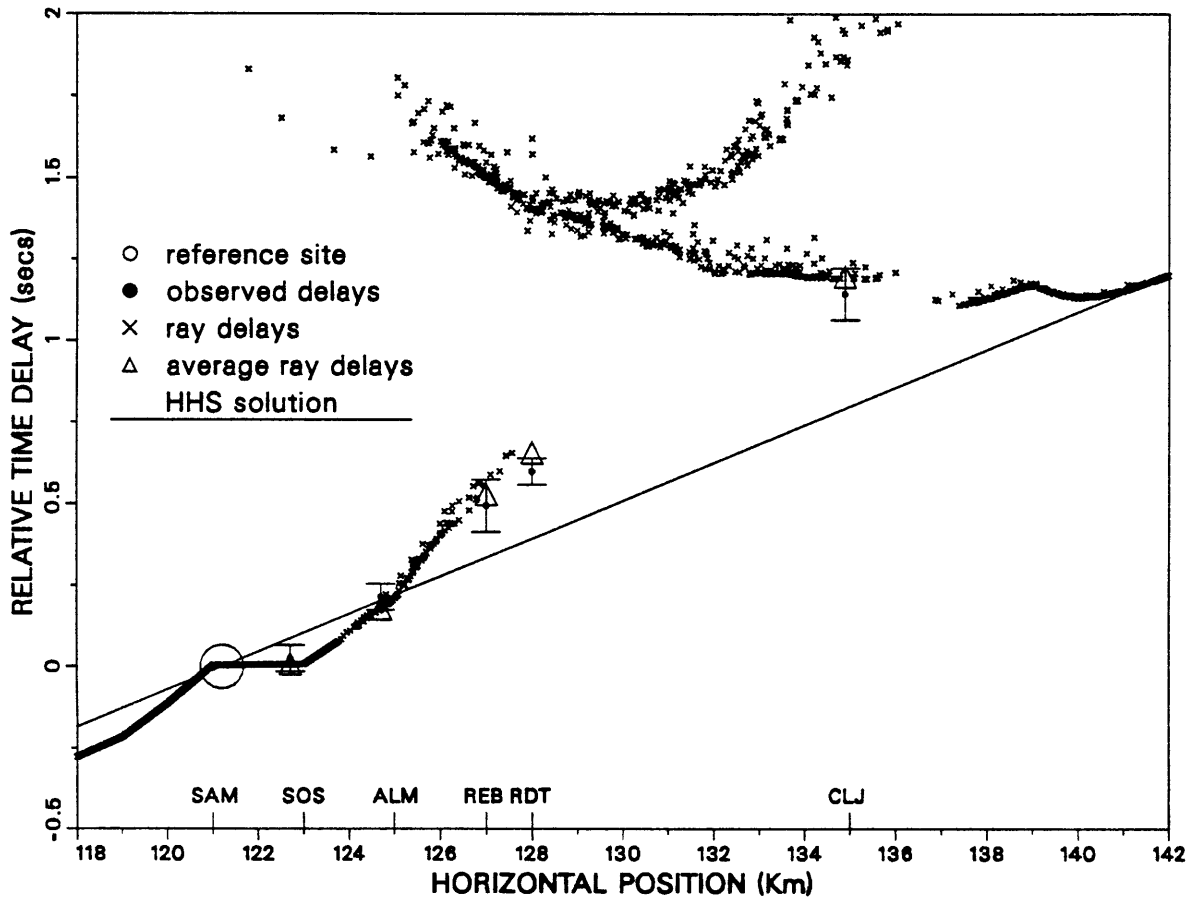


Figure 4.6a Ray tracing results for the best model with the LVZ shifted vertically upward by 1 km to an average depth of 9 km. Results are compared, as before in Figure 4.4a, with observed delays for the Kuril Islands event.

CALCULATED RAY DELAYS FOR 9 Km AVERAGE DEPTH LVZ MODEL
PLANE WAVEFRONT: INCIDENCE ANGLE = -21.0°
 OBSERVED P-WAVE DELAYS FOR EVENT FROM: JUJUY, ARGENTINA
REFERENCE SITE: CLJ LOCATION: X = 135

$\sigma_{HHS}^2 = 0.207E+00$ $\sigma_{MOD}^2 = 0.918E-02$ Variance Reduction = 95.6%

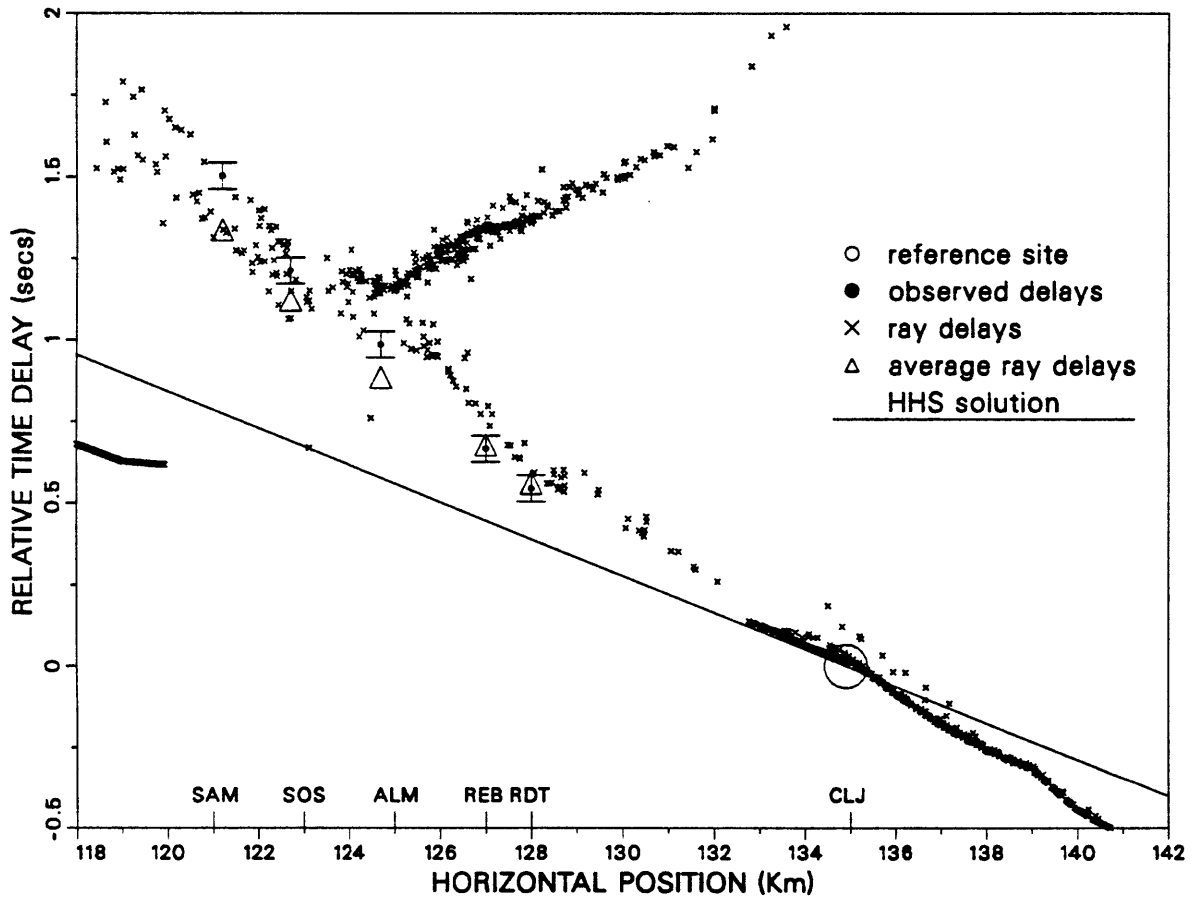


Figure 4.6b Same as Figure 4.6a except that the 9 km deep LVZ model is tested against delays for the Jujuy event.

CALCULATED RAY DELAYS FOR 11 Km AVERAGE DEPTH LVZ MODEL

PLANE WAVEFRONT: INCIDENCE ANGLE = 21.5°

OBSERVED P-WAVE DELAYS FOR EVENT FROM: KURIL ISLANDS

REFERENCE SITE: SAM LOCATION: X = 121

$\sigma_{\text{HHS}}^2 = 0.385\text{E-}01$ $\sigma_{\text{MOD}}^2 = 0.149\text{E-}02$ Variance Reduction = 96.1%

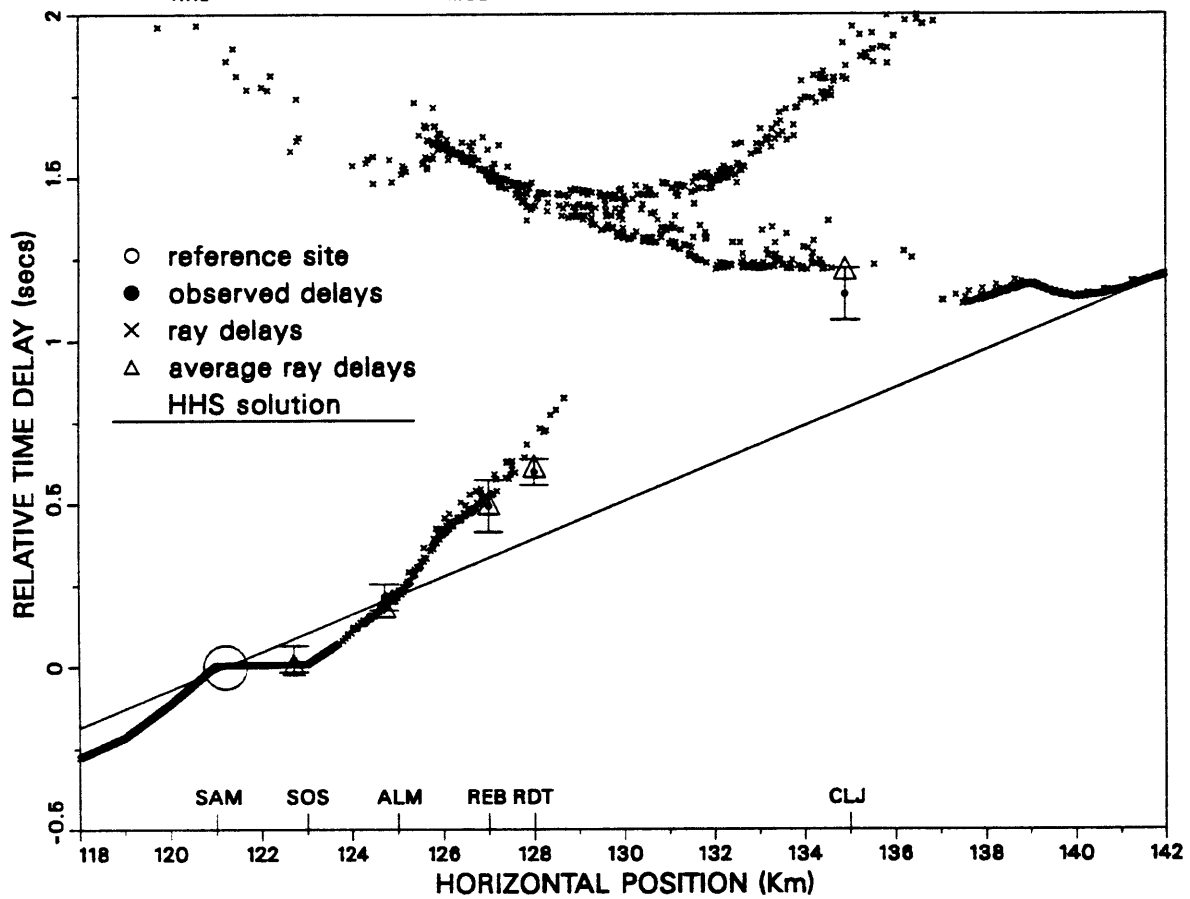


Figure 4.7a Same as Figure 4.6a except that the ray tracing results, compared with the Kuril data, are for the best model with the LVZ shifted downward by 1 km to an average depth of 11 km.

CALCULATED RAY DELAYS FOR 11 Km AVERAGE DEPTH LVZ MODEL
 PLANE WAVEFRONT: INCIDENCE ANGLE = -21.0°
 OBSERVED P-WAVE DELAYS FOR EVENT FROM: JUJUY, ARGENTINA
 REFERENCE SITE: CLJ LOCATION: X = 135

$\sigma_{\text{HHS}}^2 = 0.207\text{E}+00$ $\sigma_{\text{MOD}}^2 = 0.799\text{E}-02$ Variance Reduction = 96.1%

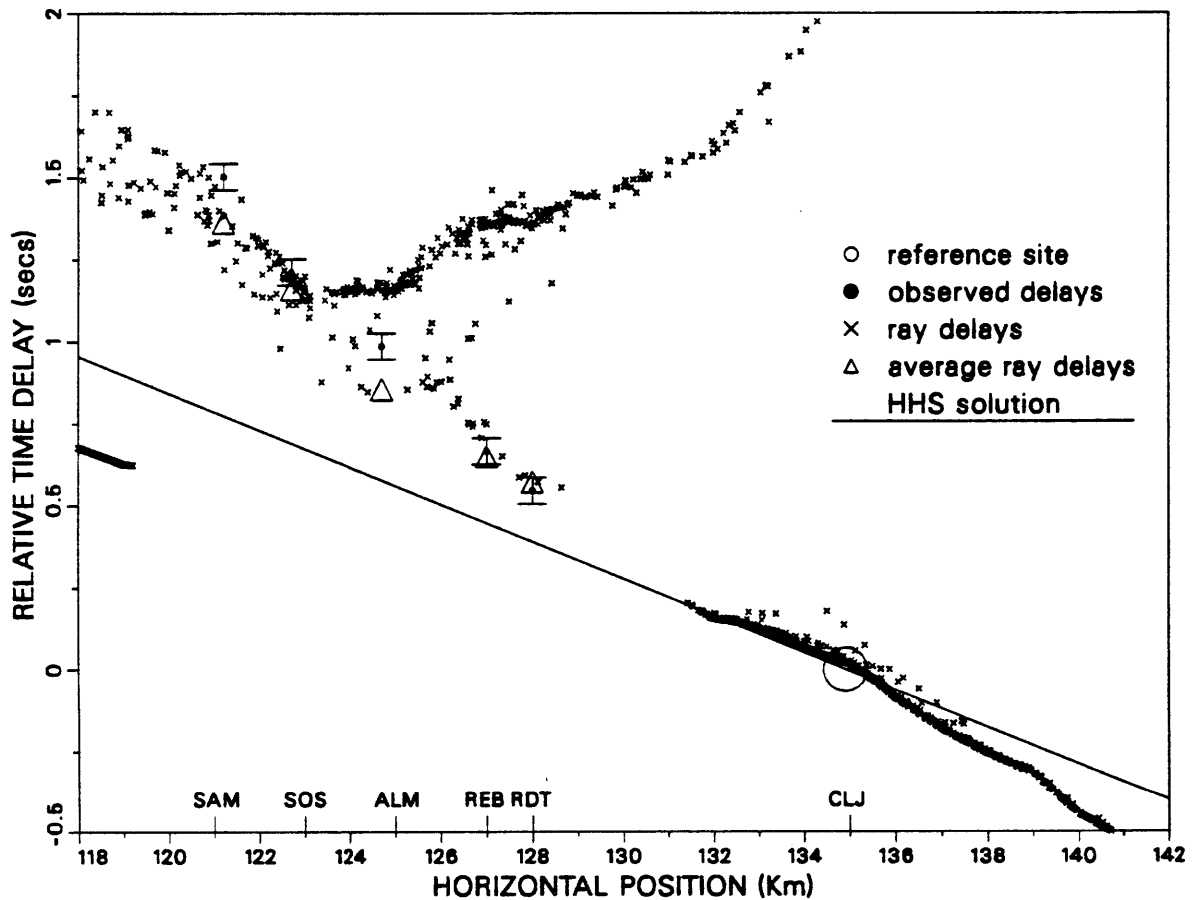


Figure 4.7b Same as Figure 4.7a except that the 11 km deep LVZ model is tested against delays for the Jujuy event.

CALCULATED RAY DELAYS FOR 12 Km AVERAGE DEPTH LVZ MODEL

PLANE WAVEFRONT: INCIDENCE ANGLE = 21.5°

OBSERVED P-WAVE DELAYS FOR EVENT FROM: KURIL ISLANDS

REFERENCE SITE: SAM LOCATION: X = 121

$\sigma_{HHS}^2 = 0.385E-01$ $\sigma_{MOD}^2 = 0.176E-02$ Variance Reduction = 95.4%

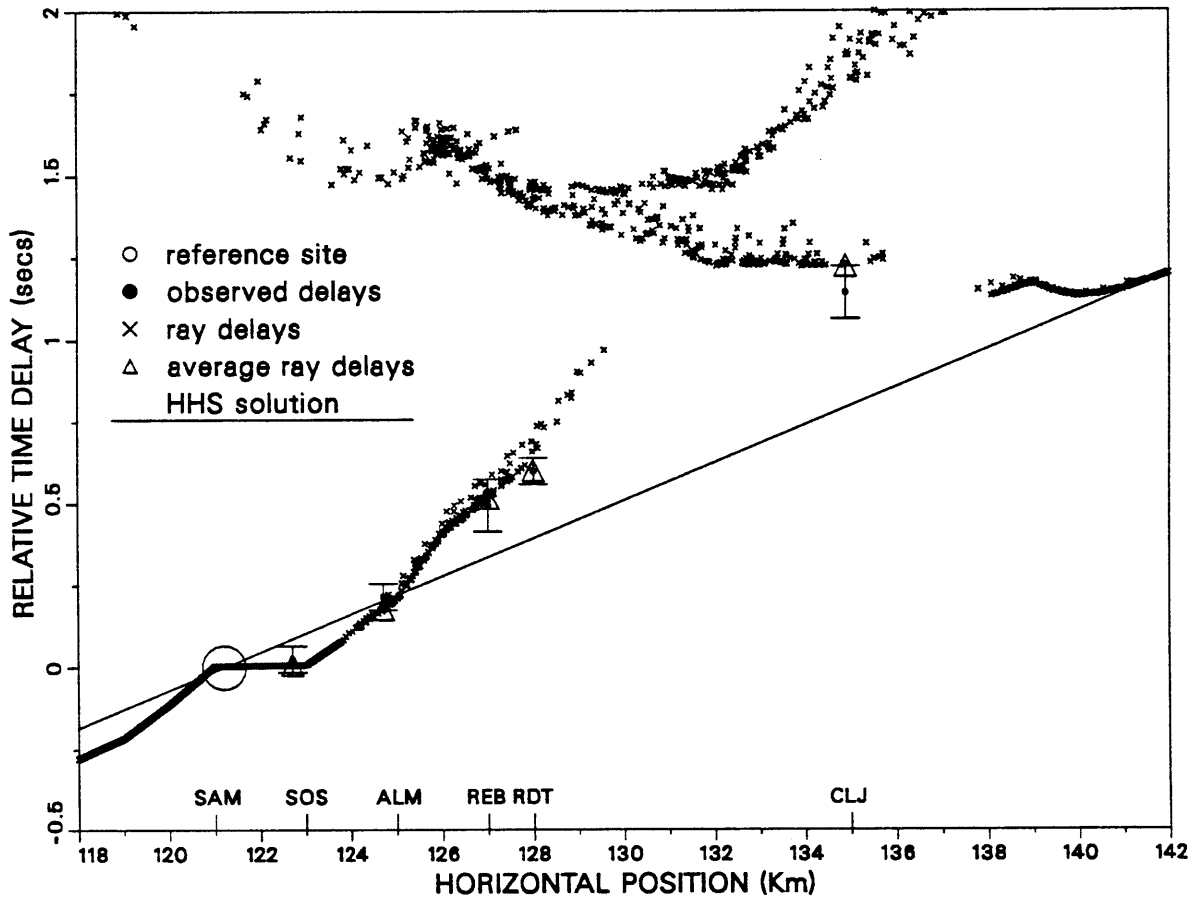


Figure 4.8a Same as Figure 4.6a except that the ray tracing results, compared with the Kuril data, are for the best model with the LVZ shifted downward by 2 km to an average depth of 12 km.

CALCULATED RAY DELAYS FOR 12 Km AVERAGE DEPTH LVZ MODEL

PLANE WAVEFRONT: INCIDENCE ANGLE = -21.0°

OBSERVED P-WAVE DELAYS FOR EVENT FROM: JUJUY, ARGENTINA

REFERENCE SITE: CLJ LOCATION: X = 135

$\sigma_{\text{HHS}}^2 = 0.207\text{E}+00$ $\sigma_{\text{MOD}}^2 = 0.110\text{E}-01$ Variance Reduction = 94.7%

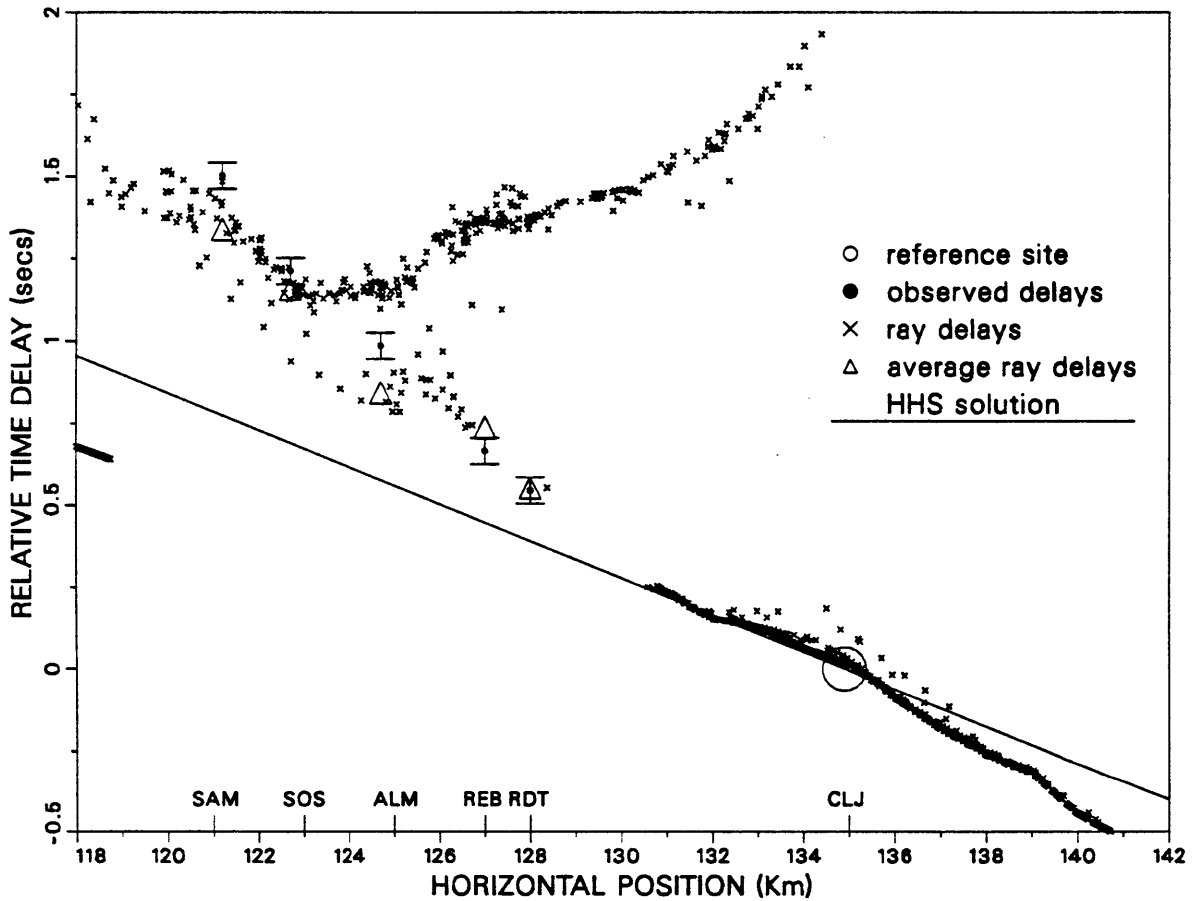


Figure 4.8b Same as Figure 4.8a except that the 12 km deep LVZ model is tested against delays for the Jujuy event.

all 21 events used, was approximately 89%, which is virtually the same as for the 10-km-depth LVZ in the best model. If the average depth is decreased any further, though, the average ray delay at RDT jumps suddenly into the upper LVZ delay curve and the residual at this site becomes very large. This is due to the effect discussed previously, where the horizontal position of the LVZ delay zone at the surface, for positive incidence angles, shifts to the left as the LVZ depth decreases. So we will consider 9 km to be the lower bound on the average depth of the LVZ. The Jujuy data in Figure 4.6b also support this lower limit because now, as the LVZ depth decreases, the entire pattern of ray delays shifts to the right, causing predicted delays which are, on the average, growing too large at ALM, REB and RDT.

The calculated delays compared with the Kuril data at CLJ demonstrate that as the LVZ depth increases, the ray delays at this site also increase. Compare Figures 4.6a, 4.4a, 4.7a and 4.8a, in that order, to observe this behavior. This trend is caused by successively later rays hitting the tapered zone at the right edge of the LVZ as its depth increases, and thus is due to normal moveout. Notice that the variance reduction for just the Kuril data is peaked at about 97% for 10 km average LVZ depth (Figure 4.4a) and decreases slightly to about 96% and 95% for 11 and 12 km depths in Figures 4.7a and 4.8a, respectively. This is due primarily to the increased residual at CLJ. For average depths greater than 12 km, the ray delays at CLJ fall significantly above the upper error bar for the observed delay. So 12 km can be taken as an upper bound for the average depth of the LVZ.

A similar comparison as above for the Jujuy data reveals that one rather subtle effect of increasing the average depth for negative incidence angles is a decrease in

the delays, due to the leftward shift of the surface delay zone. This effect is most pronounced at SAM, SOS and ALM by comparison of Figure 4.4b with Figure 4.8b. The decrease in variance reduction from about 98% for 10 km depth (Figure 4.4b) to about 95% for 12 km (Figure 4.8b) is due primarily to the decrease in the ray delays at these three sites. The most obvious effect of this leftward shift is shown clearly in Figure 4.8b, where there are very few early enough arrivals near REB and RDT. Although there were (barely) enough to obtain a small residual at these sites, this model is clearly a limiting case and, as we concluded from the Kuril data, the average depth of the LVZ can be no larger than 12 km.

Extending the above comparisons to multiple incidence angles yielded the same conclusions. The 21-event variance reduction showed a small decrease from 91% for the best model (10 km LVZ depth) to 88.9% for 9 km, 89.5% for 11 km and 86.9% for 12 km. Average depths larger than 12 km and shallower than 9 km produced sharp decreases in the total variance reduction, so, as before, these values represent reasonable upper and lower bounds on the depth of the widest part of the LVZ. So for a lens-shaped LVZ, 8 km high and 17 km in tapered width we can constrain its average depth to within ± 1.5 km.

The top and bottom of the LVZ cannot be constrained with the present data set because we do not have enough shallow incidence observations from both directions, and we had no recording stations between RDT and CLJ or between CLJ and CAP. With more stations and shallower incidence it should be possible to observe effects due to rays which first come into contact with the LVZ near its upper and lower edges rather than at its left and right edges. Furthermore, the only constraints that our data can place on the height and velocity of the LVZ arise from the strength of

the observed delays for southeastern events. The velocity must be low enough and the height large enough to reproduce the large caldera delays for negative incidence, particularly at SAM. Thus, we should be able to increase the height and velocity proportionally and still produce similar delays as for the 8 km height LVZ in Figure 4.2. For instance, we could increase the height to 12 km and the velocity from 3.7 to approximately 5.5 km/sec and still obtain a similar delay pattern. The only problem with this is that we must maintain the same 17 km tapered width discussed above. This means that to increase the height would also require increasing the interface slopes and this can significantly change the ray refraction pattern. On the other hand, decreasing the height and velocity will decrease the critical reflection angle at the top of the LVZ, making it more difficult for rays in the LVZ to reach the surface. Our best model already exhibits a significant degree of critical reflection, and tests with smaller LVZ's created severe shadow zones at the surface. So it is reasonable to say that the LVZ in Figure 4.2 has approximately the minimum dimensions and velocity permissible.

We also performed many tests with larger LVZ's. These tests included increasing the amplitude of the upper and lower interfaces defining the inclusion, and increasing the velocity as described above. We found that in general the largest delays at SAM and SOS for negative incidence angles could still be reproduced in most cases, but, for an increase in height larger than about 1 km, the gradual increase in delays between RDT and ALM could not. This was due to the fact that we had to alter the slope of the tapered section at the right edge, and we could find no particular shape which did not refract rays into the largest portions of the LVZ. This is basically the same behavior we observed for the circular inclusion discussed

previously. Thus, we can make no precise statements about the maximum height of the LVZ because this necessarily would require a characterization of how the details of its shape must change with increasing size. Clearly our data cannot provide this much information. This means that our assumption of a homogeneous lens-shaped inclusion breaks down when the height is increased beyond about 9 km. In turn, this is why our simplified model can only yield a lower bound on the height of the LVZ. Considering the actual structural complexity which must exist beneath the caldera, which we will discuss further in Chapter 6, it is most encouraging that the observed delay pattern is simple enough that our minimal model can reproduce it so well.

Our final test of the LVZ model in Figure 4.2 was a simple P-velocity perturbation study. Since there were many cases where the calculated delays around a given site location showed a significant degree of scatter, there should be a range of LVZ velocities over which we expect the variance reduction to remain fairly stable. We found that for velocities lower than about 3.5 km/sec, the critical reflection problem mentioned above began to eliminate most of the arrivals at RDT, REB and ALM for negative incidence angles. This caused a very sharp decrease in the variance reduction from about 89% for 3.5 km/sec to about 76% for 3.4 km/sec. Increasing the velocity not only decreases the maximum delay near each site, but also reduces the scatter in the delays because the refraction is less severe. This second effect actually increases the minimum delay at the caldera sites for negative incidence angles because earlier rays are no longer refracted forward at the right edge of the LVZ as sharply as before. These two effects combine so that the average delay remains nearly stationary until the velocity is large enough that the first effect

dominates. As the velocity increases above this maximum value, the delays become smaller and the residual variance begins to increase steadily. This maximum velocity was determined to be about 4.2 km/sec for the 10-km-average-depth LVZ. For this value, the variance reduction was reduced to about 88% from 91% previously. For 4.4 km/sec the variance had decreased to about 83% and at 4.8 to about 66%. So for the particular size and shape of the LVZ in Figure 4.2, the P-wave velocity can be constrained to lie between about 3.5 and 4.2 km/sec.

Since our approach here has been to model only relative time delays, there is an inherent non-uniqueness or ambiguity in the structure for the caldera fill correction layer. As long as a similar interface shape is maintained, the overall thickness of the layer can vary considerably without significantly degrading the synthetic results. In Figure 4.9 the best ray model is plotted again, but with the depth of the caldera fill interface increased by 3 km overall. The ray tracing results for this model are shown in Figure 4.10a for the Kuril Islands array-2 data, and in Figure 4.10b for the Jujuy, Argentina data. Although some of the details have changed in the calculated delays, the pattern for the first arrivals is virtually unaltered, and the variance reduction remains very large for both events. This demonstrates that many alternative models exist which simply change the delays at all sites by the same amount. This point will be an important consideration in Chapter 6, where we will discuss the consistency between the best ray model here, and the best amplitude model from Chapter 5.

The results of this chapter show very strong evidence for a large low velocity inclusion at significant depth beneath the approximate center of the Valles Caldera. Although we cannot constrain the maximum height of this inclusion, we can constrain the maximum width to about 17 km and the average depth to the widest

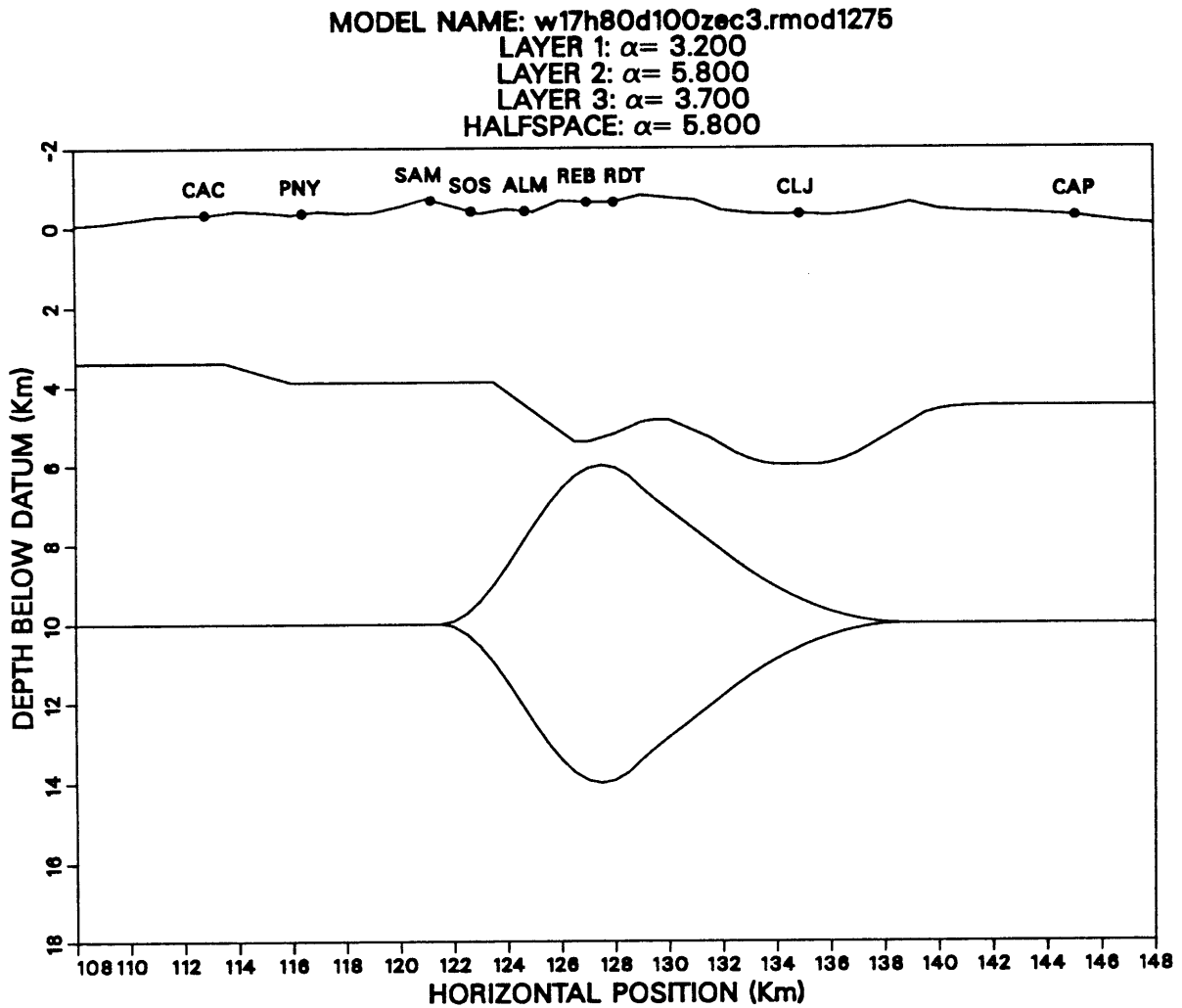


Figure 4.9 Same as best ray model plotted in Figure 4.2, except that the caldera fill layer has been increased in thickness by 3 km overall.

CALCULATED RAY DELAYS FOR THICK CALDERA FILL LVZ MODEL

PLANE WAVEFRONT: INCIDENCE ANGLE = 21.5°

OBSERVED P-WAVE DELAYS FOR EVENT FROM: KURIL ISLANDS

REFERENCE SITE: SAM LOCATION: X = 121

$\sigma_{HHS}^2 = 0.385E-01$ $\sigma_{MOD}^2 = 0.214E-02$ Variance Reduction = 94.4%

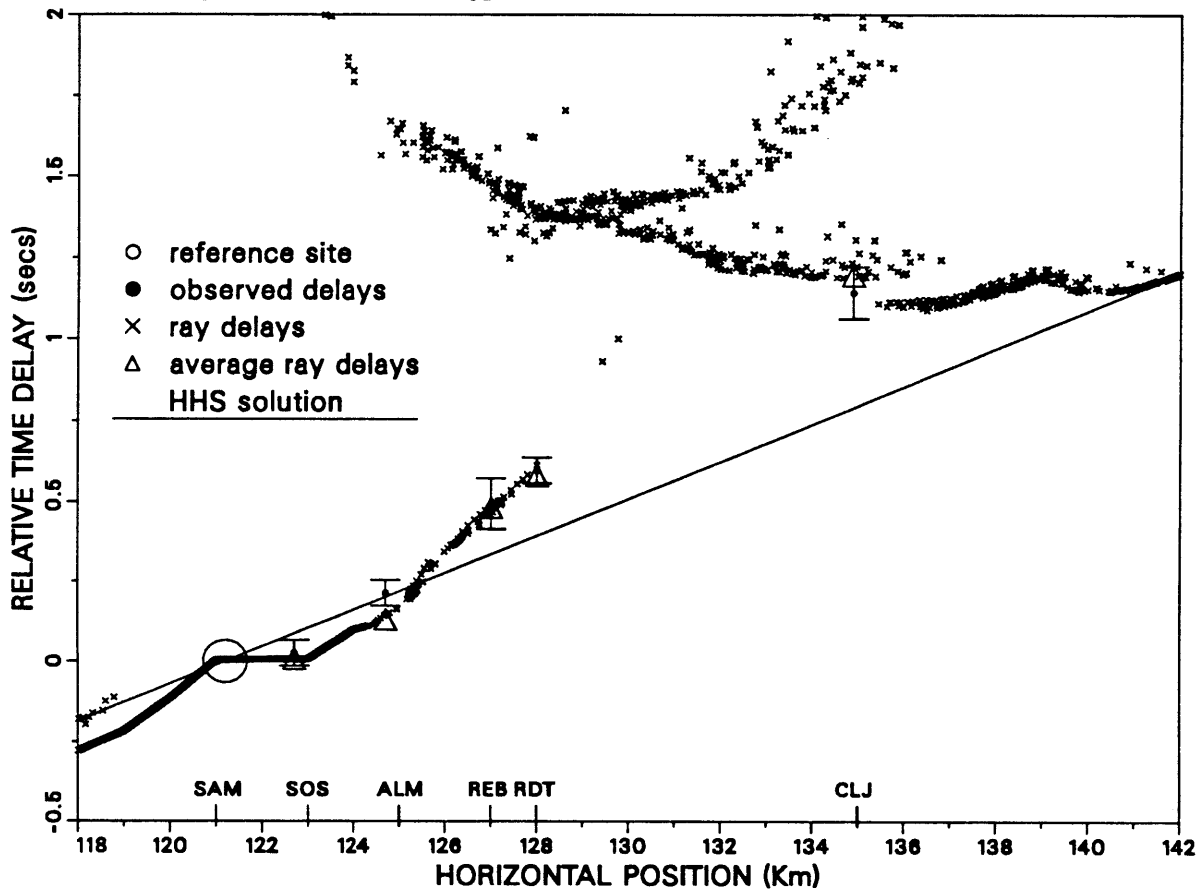


Figure 4.10a Ray tracing results for the thickened caldera fill model in Figure 4.9 compared with the Kuril Islands data used previously.

CALCULATED RAY DELAYS FOR THICK CALDERA FILL LVZ MODEL
 PLANE WAVEFRONT: INCIDENCE ANGLE = -21.0°
 OBSERVED P-WAVE DELAYS FOR EVENT FROM: JUJUY, ARGENTINA
 REFERENCE SITE: CLJ LOCATION: X = 135

$\sigma_{\text{HHS}}^2 = 0.207\text{E}+00$ $\sigma_{\text{MOD}}^2 = 0.564\text{E}-02$ Variance Reduction = 97.3%

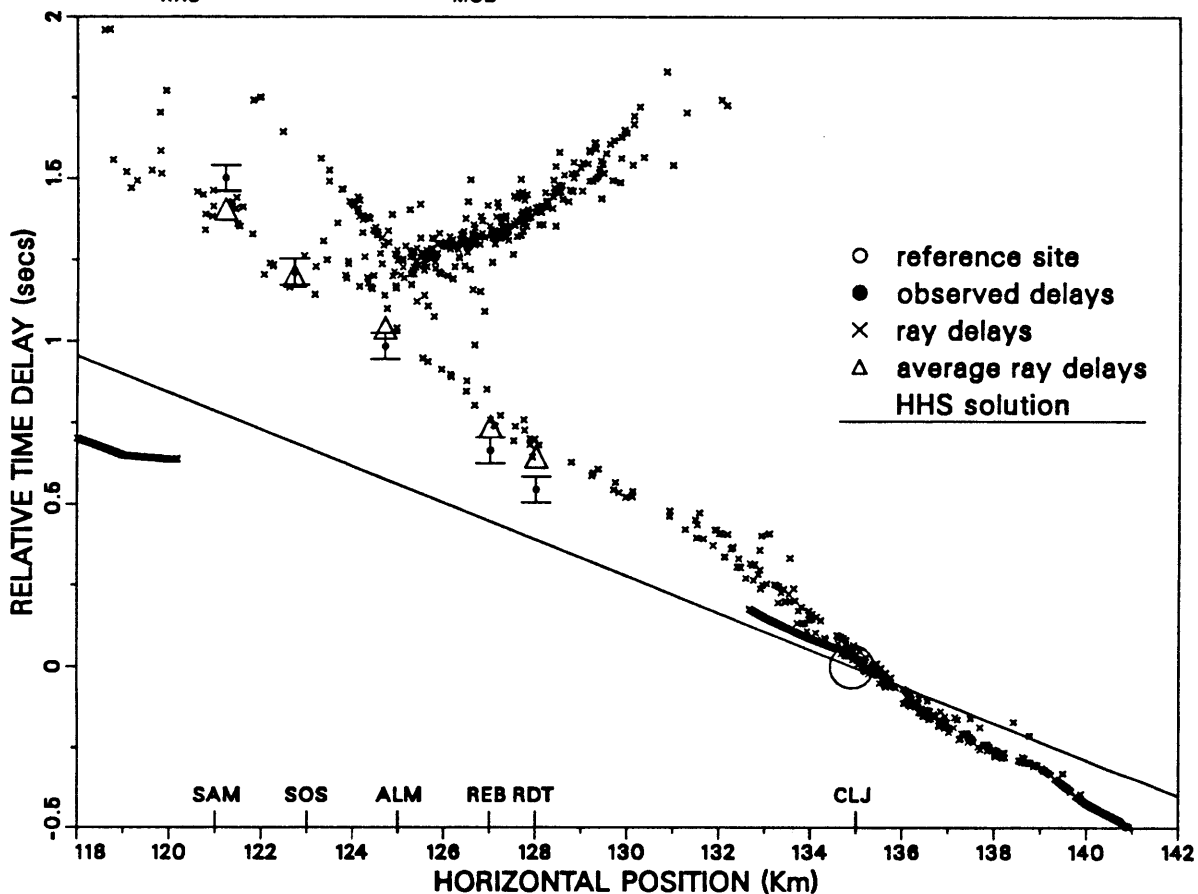


Figure 4.10b Same as Figure 4.10a, except that the ray tracing results are compared with the Jujuy, Argentina data used previously.

section can be limited to a range of 9 to 12 km. We also demonstrated a clear need for the inclusion to be lens-shaped. Given these constraints on the width and shape, we found that the minimum height and velocity permissible were approximately 8 km and 3.5 km/sec, respectively. With this particular geometry, the upper bound on the velocity was found to be about 4.2 km/sec, based on the stability of the variance reduction. Since the two-component structural model used is certainly an over-simplification of the true structure, we must realize that alternative combinations of different caldera fill and LVZ shapes might also be able to explain the observed delay data. This is particularly true in light of the varying degrees of structural ambiguity discussed above. However the fit of the present model to all available data is almost 91% better than for a homogeneous halfspace, and this very strongly supports the validity of at least the general features of the best model shown in Figure 4.2. We will discuss the validity of the LVZ further in Chapter 6, in terms of possible interpretations as a cooling magma chamber.

CHAPTER 5

Modeling of Spectral Amplitude Ratios

5.1 Introduction

In Chapter 4 we showed that the relative arrival time delays at each site varied strongly with incidence angle and that these variations could best be explained by the existence of a large, deep low velocity zone beneath the center of the caldera. In the present chapter we will demonstrate that this deep LVZ is not required to explain the spectral amplitude observations. We have already mentioned in Chapter 2 that the primary observation of low amplitude inside the caldera must be due to a shallow structural anomaly. This will be shown here to be the best way to fit the majority of the amplitude data. The major features of this anomaly include very low Q and low P and S velocities relative to its surroundings. The attenuating effect is so strongly dominant that, to first order, the amplitudes are insensitive to the deeper structure obtained in Chapter 4. In addition to this low Q zone (LQZ), the best fitting model requires an irregularly shaped caldera fill as a surface layer located directly above the anomaly. This surface layer, which we will refer to as the “upper caldera fill,” is bounded above by the free-surface topography shown previously in Figures 2.1a,b and below by the LQZ and a granitic basement halfspace. The surface layer geometry used is considerably different from the caldera fill used in Chapter 4 to isolate the effects of the deeper LVZ. These differences will be discussed in detail in Chapter 6. Although strictly we should refer to Q separately for P and S waves, we will use the same value for both wave types throughout. We tested different

models in which we allowed Q_α and Q_β to have different values, but discovered that both needed to be very low in the LQZ, relative to the surrounding material, in order to fit the data. Having fixed a single low value for Q in the LQZ, we found that it made no difference if Q_α or Q_β were allowed to vary independently in either the granite basement or in the upper caldera fill, as long as both were significantly higher than the value in the LQZ. We will demonstrate in the present chapter that the elimination of either the LQZ or the upper caldera fill from the model increases the residual variance and thus, these components represent the minimum structural requirements. We will also demonstrate by counterexample that the observed amplitude pattern on the whole cannot be explained by 2-dimensional resonance or directional scattering, since these effects produce surface motion which depends strongly on incidence angle and source direction.

We have used the forward modeling approach throughout this chapter to obtain the best model. In order for this approach to represent anything more than pure trial-and-error, one needs to combine as much a priori knowledge, common sense and intuition as possible to construct some reasonable initial models to be tested. This is particularly important here because now each medium in the model has four material parameters, α , β , ρ and Q , whereas for the ray-tracing we had only one, α . If any given initial model produces promising results, it may then be worthwhile to perturb its parameters in hopes of improving the fit to the data. This is the stage of the modeling which takes on a rather brute-force nature. Several hundred individual models were tested before obtaining the results in this chapter. Most of these models did not include attenuation and represent attempts at explaining the data through resonance and scattering effects alone. We will summarize some of our experiences

with these attempts since they may be useful for cases where attenuation is not as important as it is for the Valles Caldera. We will also demonstrate the sensitivity of the solutions to moderate perturbations in individual model parameters. By observing the changes in variance reduction, we will approximately define the upper and lower bounds on the most important parameters.

In Chapter 3 we discussed the limitations of the Aki-Larner method in terms of the various inherent sources of error and the range of frequencies that may be used for a given maximum amplitude of interface irregularity. When these limitations are violated, the boundary condition residuals become unacceptably large. We will rely almost entirely on this criterion as a means of assessing the reliability of our solutions. We will not go into great detail concerning the possible causes for any large boundary condition residuals we may encounter. Rather, we will accept only those solutions for which the residuals are small. We will see, however, that the Aki-Larner method will work only when the wavelength is comparable to or larger than the structural anomaly and this limits the range of possible models that we can obtain reliable solutions for at the highest frequencies considered. Specifically, we cannot test the deep LVZ model we obtained in Chapter 4 using the travel times because the inclusion is too large and its P velocity too low to allow us to use a reasonable choice for β without having S wavelengths smaller than half the height of the LVZ.

We will also discuss some of the possible implications of 3-dimensional structure. This cannot be addressed completely here because we only have the capability of modeling amplitudes in 2-D. In Chapter 2 we saw that the data contain strong transverse components which clearly indicate 3-D effects in the vicinity of

the caldera. On the other hand, all 3 components of motion displayed a similar pattern of amplitude variations across the two arrays regardless of incidence angle, and this suggests that the dominant effects on amplitude are localized beneath the array line. This is especially true because we are not trying to model the relative amplitudes between different components, but only the variations across the array for one component at a time. The observed pattern of low amplitude in the caldera is extremely fortuitous in this sense, because it means that we do not have to address directly the question of how the scattered waves are generated or how the three components of motion interact with each other. We will also show that the LQZ model produces a very good fit to the spectral amplitude variations of the first P-wave arrival pulse for the vertical component of motion, which should be nearly devoid of 3-D effects.

We will first present in detail the final results of the Aki-Larner amplitude modeling. Afterwards, the remainder of this chapter will be devoted to a discussion of the estimation of model parameter limits, implications of 3-D structure and counterexamples using models with no attenuation.

5.2 The Best Model

Figure 5.1 shows the model which produced the best fit to the 4-event averaged Kuril Islands data shown previously in Figure 2.29. The four irregular interfaces plotted are 1.) free surface topography showing array 2 site locations as in Figure 2.1b; 2.) bottom of surface layer representing primarily volcanic caldera fill material; 3.) top of low Q zone; and 4.) bottom of low Q zone. Note that the vertical

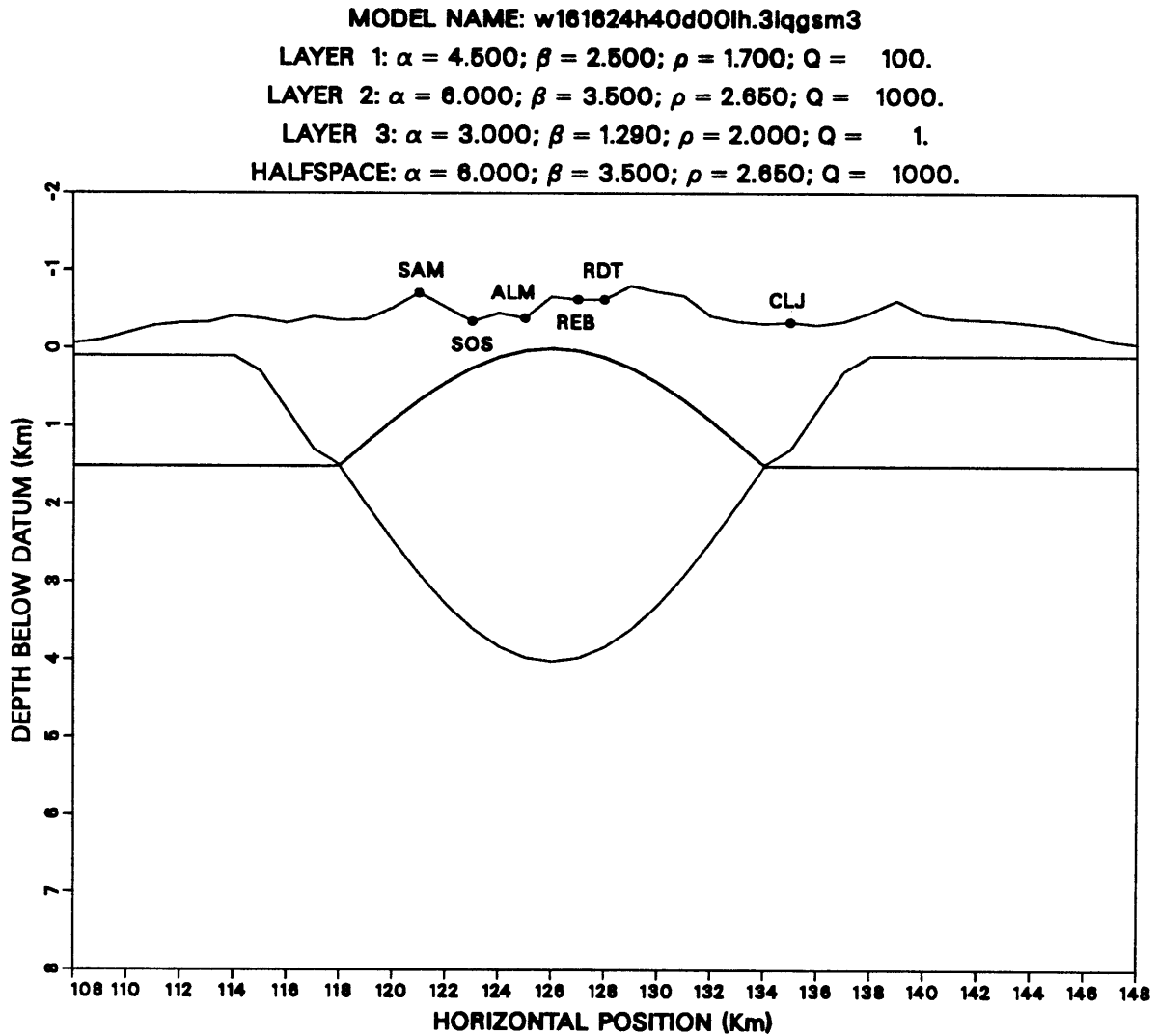


Figure 5.1 Model structure which yielded the best fit to the 4-event averaged Kuril Islands data shown in Chapter 2. All depths are relative to the arbitrary zero datum shown. Material parameters for each layer are listed at the top. Layer 1 is the upper caldera fill. Layers 2 and the halfspace are basement granite. Layer 3 is the low Q zone. The name of the model is also listed at top for reference.

exaggeration is approximately 4:1. As mentioned in Chapter 2, the caldera is centered at $x = 128$ km, corresponding to the site RDT. The total model periodicity length, as defined in Chapter 3, is $x = 256$ km and we have only plotted the central 40 km here to show the irregular portion. Layer 2 and the halfspace are both granite basement rock and the flat portions of the two LQZ interfaces are thus transparent. This is required by the strictly layered nature of the Aki-Larner formulation. At the top of the figure are listed the model name (for reference only) and α , β , ρ and Q for each layer, numbered sequentially from the uppermost layer down.

To avoid additional complexity, we have made all interface shapes symmetric, except for the known surface topography. Although this presents secondary problems in fitting the finer details of the data, we are only interested in determining the major larger-scale features of the caldera structure, and the additional complexity of asymmetric shapes is unwarranted in this case. The LQZ may be viewed as a sub-zone of the bowl-shaped caldera fill layer which has significantly lower α and β than the upper portion, as well as extremely low Q . The P-wave velocities for both the upper caldera fill and the granite basement, as well as the shape and depth of the entire caldera fill (including the LQZ), represent variations of the same components used in Chapter 4 for ray-tracing. The S-wave velocities and densities were estimated from published laboratory measurements made on numerous samples of granite, volcanic tuff and rhyolite listed in various handbooks of physical properties of rocks. This a priori information reduces the number of variable model parameters considerably. Most of the model adjustments can then be concentrated on the velocities, density, size and depth of the LQZ and on the Q values in all three media. This is discussed in more detail in Section 5.3.

The Aki-Larner displacement solutions for the model in Figure 5.1 were computed for 13 frequencies from 0.20 to 0.80 Hz using an incidence angle of $\theta_0 = +20^\circ$ as estimated for the Kuril Islands data. Vertical and radial synthetic spectra were obtained at each of the six x -locations corresponding to the array 2 sites. The spectra were then averaged over all six locations, and amplitude ratios were calculated relative to this average in exactly the same way as we described in Chapter 2 for the observed data. The results for the vertical component are plotted along with the Kuril data in Figure 5.2a and for the radial component in Figure 5.2b. We will refer to the radial component simply as “horizontal” in all of the modeling results since we will not be using the transverse component.

These figures show the amplitude ratios plotted for each site and for the frequency band 0.2 to 0.8 Hz with solid lines representing the observed data and dashed lines representing the synthetics. The lower limit of 0.2 Hz was dictated by the data, as discussed in Chapter 2. The upper limit of 0.8 Hz was the point above which the surface traction boundary condition errors for the synthetics became too large, as described below. The synthetic frequencies were spaced evenly every 0.05 Hz and the data were interpolated to match them. The residual variance, calculated using equation (2.7), and variance reduction, equation (2.8), are listed for each single component and site inside the corresponding plot box for each ratio pair. The variance and reduction for each component over all sites and for all data combined are listed at the top of each figure. Recalling that a variance reduction of +100% corresponds to a perfect fit to the data, the total reduction of 84.0% for this model should be considered excellent. The reduction for the vertical component, 80.7%, is slightly worse than for the horizontal, 85.4%. This is due primarily to the inability

VERTICAL COMPONENT SPECTRAL RATIOS

OBSERVED: KURIL ISLANDS (4 EVENTS) recorded in VALLES CALDERA (ARRAY 2)

SYNTHETIC: model= w161624h40d00lh.3lqgsm3 $\theta_0 = 20.0$ $f_{IM} = 0.0000$

$\sigma_{MOD}^2(\log)$: Vertical= 0.344E-01 Total= 0.486E-01

Variance Reduction (HHS): Vertical= 80.7% Total= 84.0%

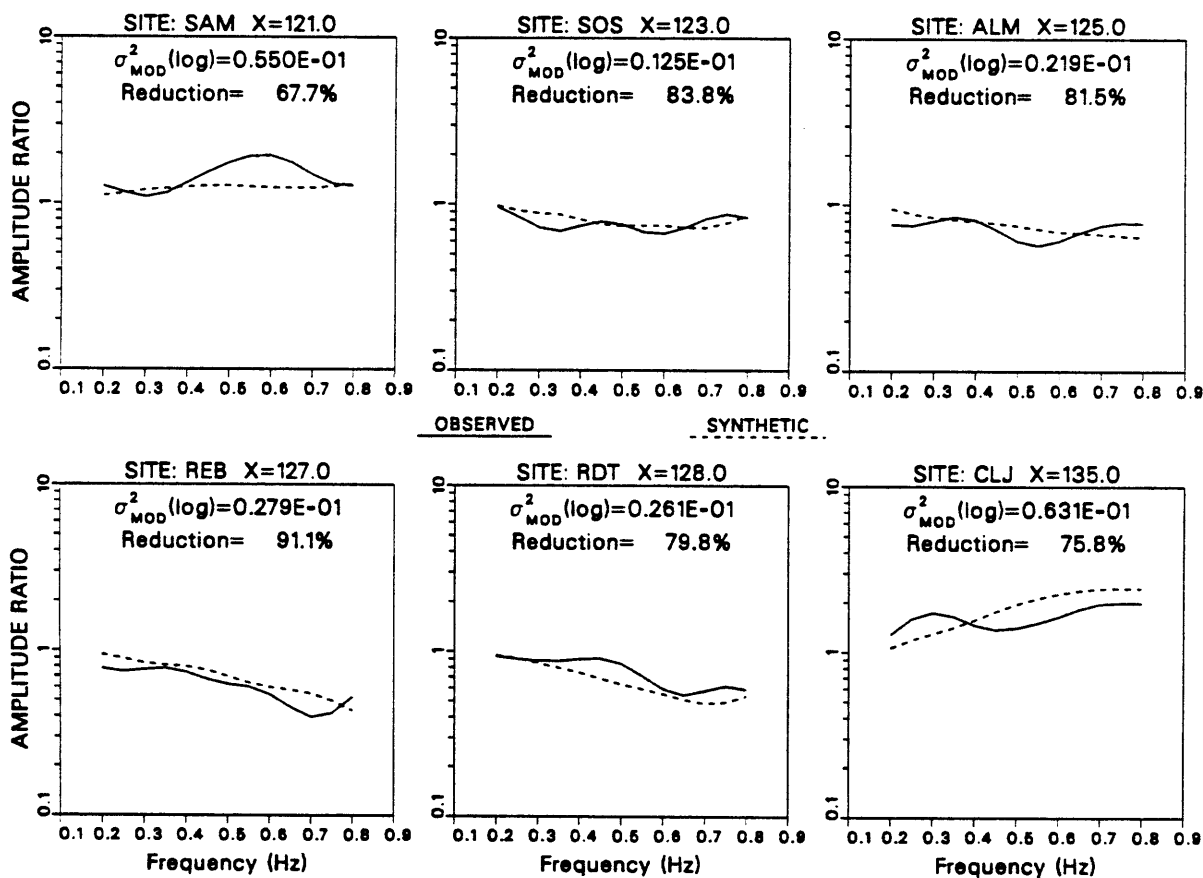


Figure 5.2a Vertical component spectral ratios for the synthetic Aki-Larner displacement solutions for the model in Figure 5.1 (dashed lines) compared with the observed ratios for the 4-event averaged Kuril Islands data (solid lines) shown previously in Chapter 2. Incidence angle used was $\theta_0 = +20^\circ$. Residual variance and variance reduction are shown in each sub-plot for each site. The total over all sites and over all results for both components are listed at the top of the figure.

HORIZONTAL COMPONENT SPECTRAL RATIOS

OBSERVED: KURIL ISLANDS (4 EVENTS) recorded in VALLES CALDERA (ARRAY 2)

SYNTHETIC: model= w161624h40d00lh.3lqgsm3 $\theta_0 = 20.0$ $f_{IM} = 0.0000$

$\sigma_{MOD}^2(\log)$: Horizontal= 0.627E-01 Total= 0.486E-01

Variance Reduction (HHS): Horizontal= 85.4% Total= 84.0%

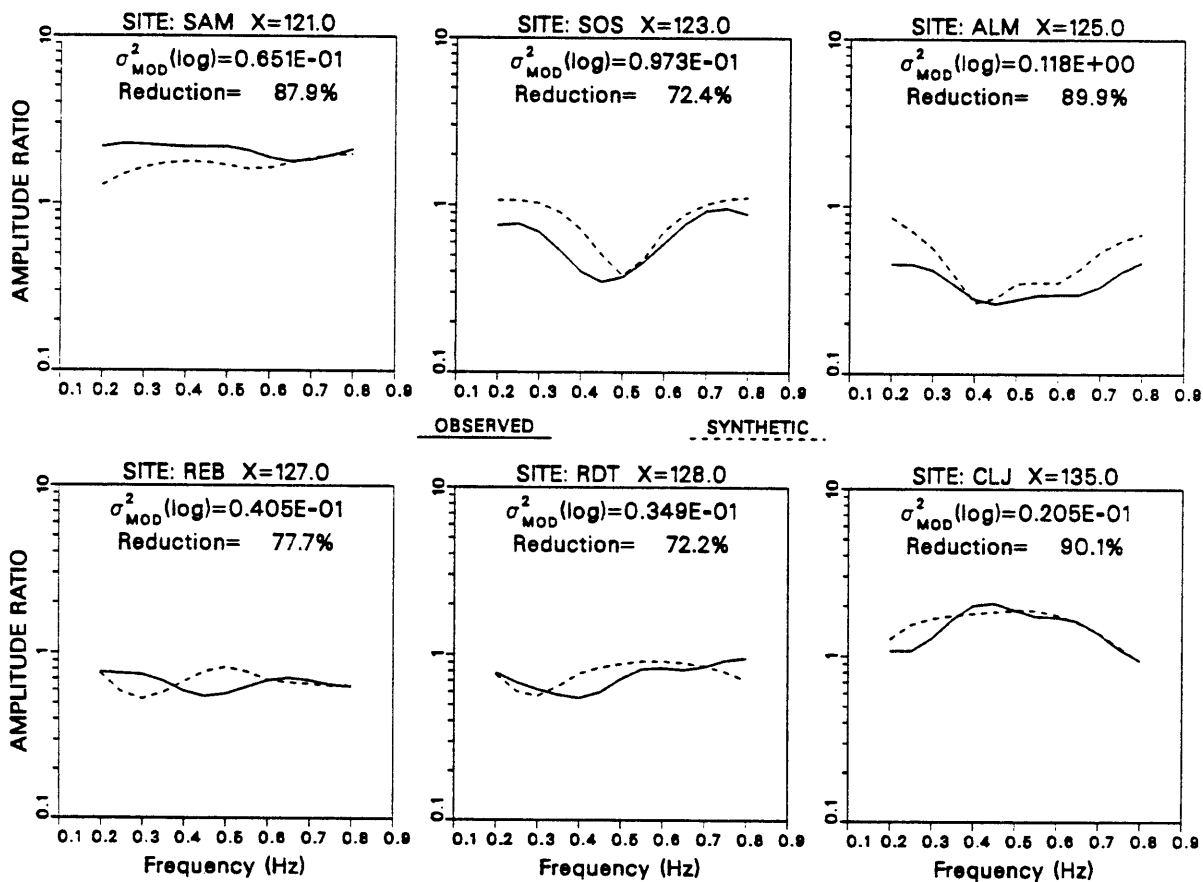


Figure 5.2b Same as Figure 5.2a except the results for the horizontal components are shown.

of the model to reproduce the peak in the vertical data near 0.6 Hz at SAM. This is the only case, among all sites and components, where the individual variance reduction is less than about 72%, and the peak in the observed ratios is probably due to secondary effects of resonance which are extraneous to the primary effect of relative attenuation.

For both components the general trends in the data versus frequency are reproduced quite well, although the secondary variations of peaks and troughs for the most part are not. Of particular interest is the horizontal component at ALM. The observed data here have the lowest relative amplitudes over the broadest range of frequencies and it is very encouraging that the model matches these data so well above 0.3 Hz. Examination of Figure 5.1 again shows that these results can be interpreted largely in terms of the local thickness of the low Q zone beneath each site. Thus, the lowest amplitudes for the vertical component are observed near the center of the caldera, and the expected Q effect of amplitude decreasing with increasing frequency is observed very clearly at REB and RDT. The horizontal data show a maximum attenuation at ALM relative to the amplitude at SAM by a factor of ~ 0.15 . This is considerably stronger than the maximum attenuation for the vertical, which at ~ 0.7 Hz is ~ 0.4 at REB relative to SAM. This makes sense because the wavelengths for S waves are shorter than for P waves and thus attenuate more rapidly. We will show next that the horizontal component is dominated by S waves and the vertical by P waves.

The Aki-Larner method allows one to calculate separately the P and S wave contributions to the total solution synthesized for each component of motion. In Figures 5.3a and 5.3b we show the synthetic spectral ratios for the total motion,

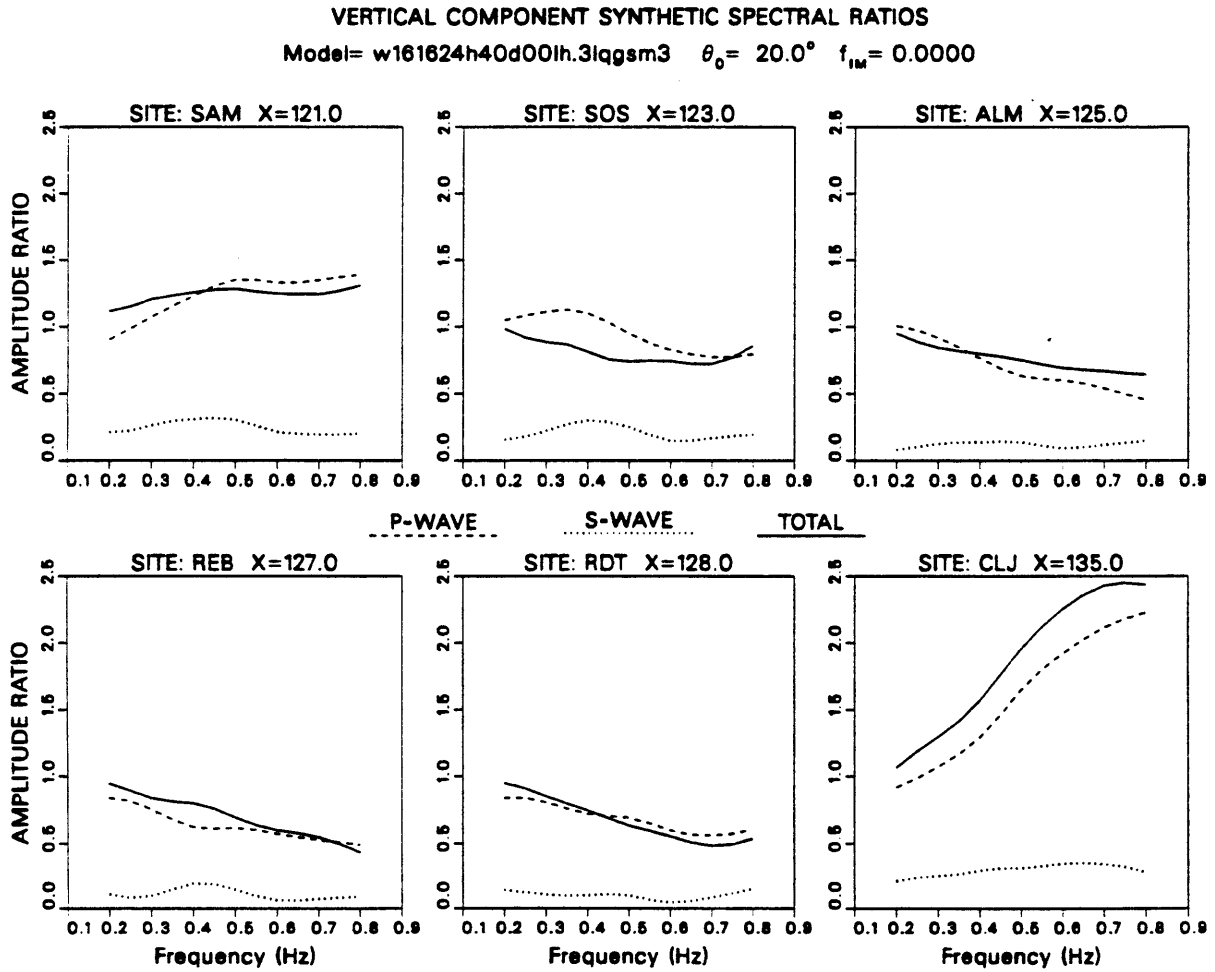


Figure 5.3a Vertical component synthetic spectral ratios from Figure 5.2a, showing the P-wave (dashed) and S-wave (dotted) contributions to the total solution (solid).

HORIZONTAL COMPONENT SYNTHETIC SPECTRAL RATIOS
 Model= w161624h40d00lh.3lqgsm3 $\theta_0 = 20.0^\circ$ $f_{IM} = 0.0000$

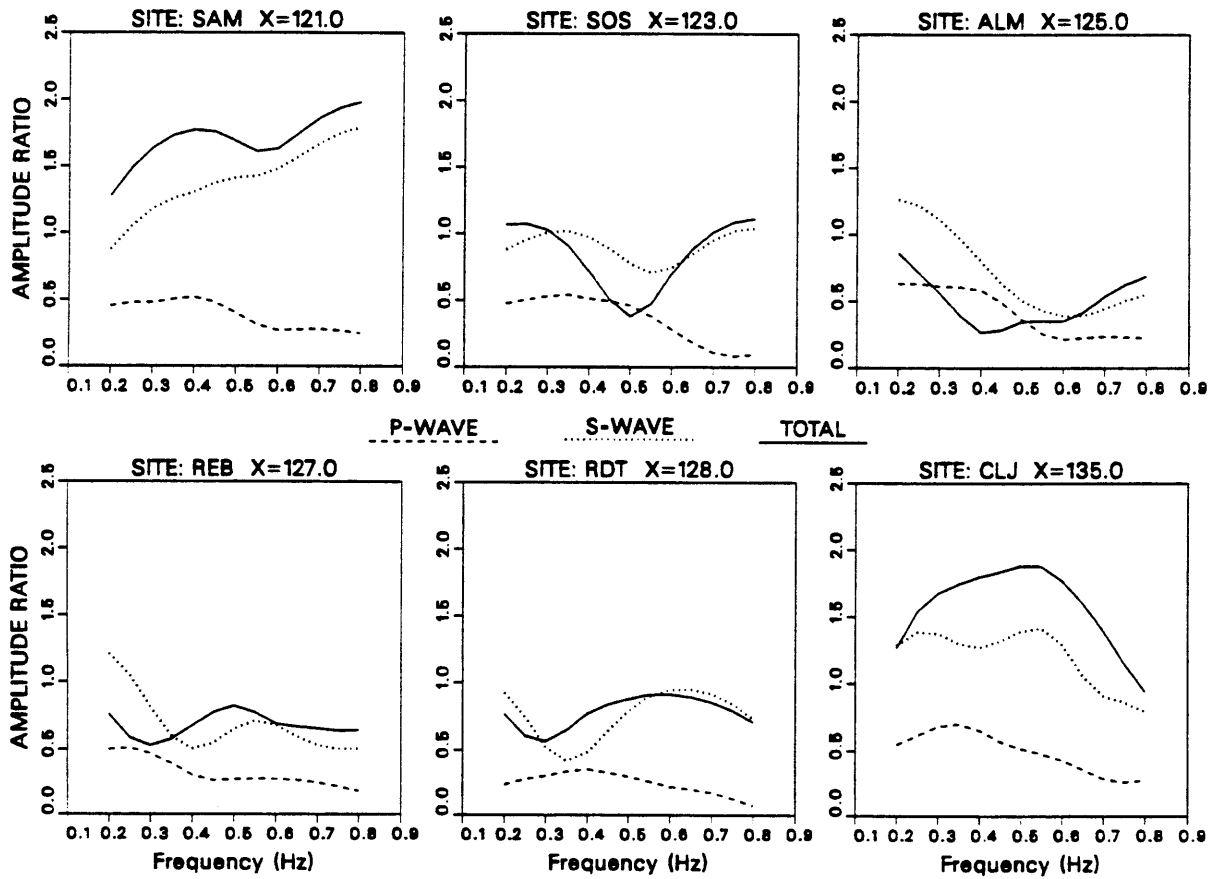


Figure 5.3b Same as Figure 5.3a except the horizontal components are shown.

shown already in Figures 5.2a and 5.2b, and the separate P and S contributions plotted together for each site. Figure 5.3a is for the vertical component and 5.3b for horizontal. Dashed lines show the P-wave contribution, dotted lines show the S-wave contribution and solid lines show the total. These plots demonstrate the effect mentioned above that the vertical component is clearly dominated by P waves and the horizontal by S waves. This is true primarily because of the relatively steep incidence angle for the source P wave. It is important to keep this in mind because it means that the horizontal component is more sensitive to the S-wave structure of the model and the vertical component is more sensitive to the P-wave structure.

To test the reliability of the synthetic solutions shown in Figures 5.2a,b, we calculated the boundary condition residuals along each interface in the model and for each frequency used. In Chapter 3 we discussed how this test will reveal problems arising from either the wavenumber truncation error or from the Rayleigh ansatz error. The combination of these two error sources will in general limit the applicability of the method to models in which the interface irregularities are comparable to or smaller than the smallest wavelength. For the model in Figure 5.1 the smallest wavelengths occur for S waves inside the low Q zone and range from 1.6 km at 0.8 Hz to 6.5 km at 0.2 Hz. The largest interface irregularity is for the bottom of the LQZ and has an amplitude of 2.5 km. So we would expect to have more problems matching boundary conditions at 0.8 Hz than for lower frequencies. The boundary conditions for any particular buried interface can be tested by calculating the two components of traction, T_x and T_z , and displacement, u and w , along the interface, using the appropriate potential coefficients and wavefield expressions for the media above and below. The formulas needed to do this are given in Appendix 1. We can

then calculate the root-mean-square-errors (RMSE) for each component of traction and displacement amplitude along the interface using the following formula given in *Larner* [1970]:

$$(RMSE)_{mi} = \frac{\left\{ \sum_{j=1}^J \left[\|u_{mij}^A\| - \|u_{mij}^B\| \right]^2 \right\}^{1/2}}{\left\{ \sum_{j=1}^J \|u_{mij}^A\| \cdot \|u_{mij}^B\| \right\}^{1/2}}, \quad (5.1)$$

where m is the interface index, i is the index over the 4 different types of boundary conditions and j is the horizontal x -position index. $\|u^A\|$ and $\|u^B\|$ represent the amplitudes of one of the components of either traction or displacement evaluated for the medium above and below the interface respectively. The tractions can be converted to equivalent units of displacement so that all four boundary conditions at each interface may be directly compared. We can then combine all four boundary conditions into one formula which gives the total RMSE for interface m [*Larner*, 1970]:

$$(RMSE)_m = \frac{\sum_{i=1}^4 \left\{ \sum_{j=1}^J \left[\|u_{mij}^A\| - \|u_{mij}^B\| \right]^2 \right\}^{1/2}}{\sum_{i=1}^4 \left\{ \sum_{j=1}^J \|u_{mij}^A\| \cdot \|u_{mij}^B\| \right\}^{1/2}}. \quad (5.2)$$

To convert the tractions to displacement units we will divide them by the same conversion factor used by *Larner* [1970], using the elastic constants in the halfspace: $\omega\rho_4(\alpha_4\beta_4)^{1/2}$. The index j above will be restricted to represent only the central 64 km of the models, from $x = 96$ km to $x = 160$ km, so that our error estimates will apply only for the irregular portions of the periodic structure. The errors for the

entire model period would be much smaller because the majority of each interface profile is flat.

The formulas above cannot be used for the vanishing stress condition at the free surface. Instead we will normalize all of the calculations by the amplitude of the incident source wave so that in cases where the free surface stress is not zero, we can set some threshold on it. If the stress exceeds this threshold significantly we must consider the corresponding displacement solutions to be unreliable, even if the remaining boundary conditions have been met adequately. We will use a value of 0.05 times the incident wave amplitude for this threshold and will require that no portion of the free surface stress components shall ever exceed this value. In the following we will see that this restriction limits the maximum frequency that we can model to 0.8 Hz.

Figures 5.4a and 5.4b show plots of the boundary conditions for the lowest and highest frequencies, 0.2 and 0.8 Hz respectively, for the solutions of the model in Figure 5.1. On the left are the vertical and horizontal components of traction converted to normalized displacement units so that 1.0 corresponds to the equivalent amplitude of the incidence wave. The true displacement components are plotted on the right of each figure. The free surface traction conditions are at the top of the figures and the deepest interface is at the bottom. The total RMS errors, using equation (5.2), are listed to left for each buried interface. Each sub-plot shows the corresponding solutions evaluated both above and below the interface with the individual RMSE, from equation (5.1), listed at the top of each box.

These plots represent the best and worst cases of internal error encountered for the current model. We will consider the largest error to be representative of the

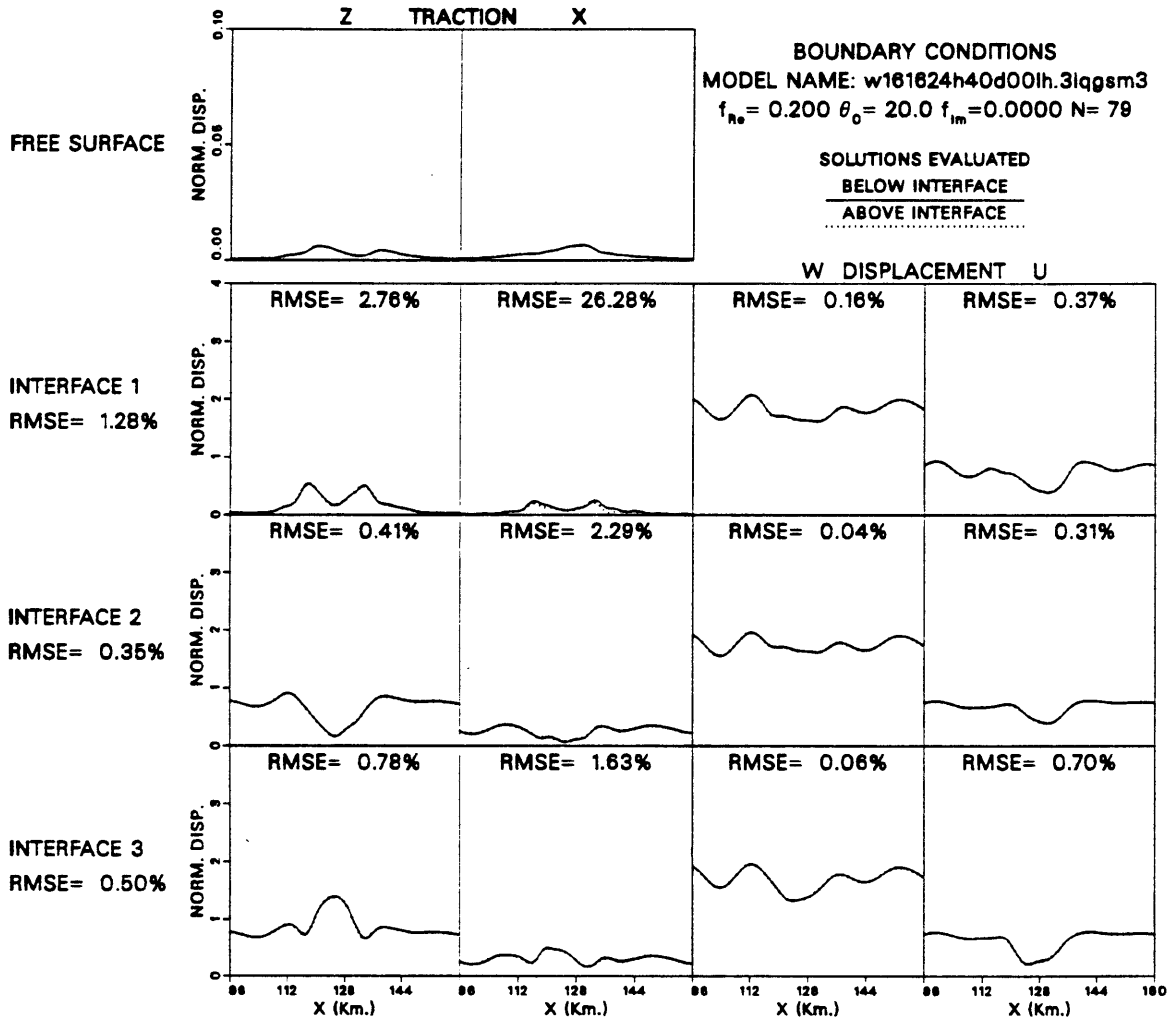


Figure 5.4a Boundary conditions and RMS errors for the 0.2 Hz Aki-larner solutions of the model in Figure 5.1. Traction conditions are on the left and displacement on the right. Interfaces are shown from the surface down starting at the top of the figure.

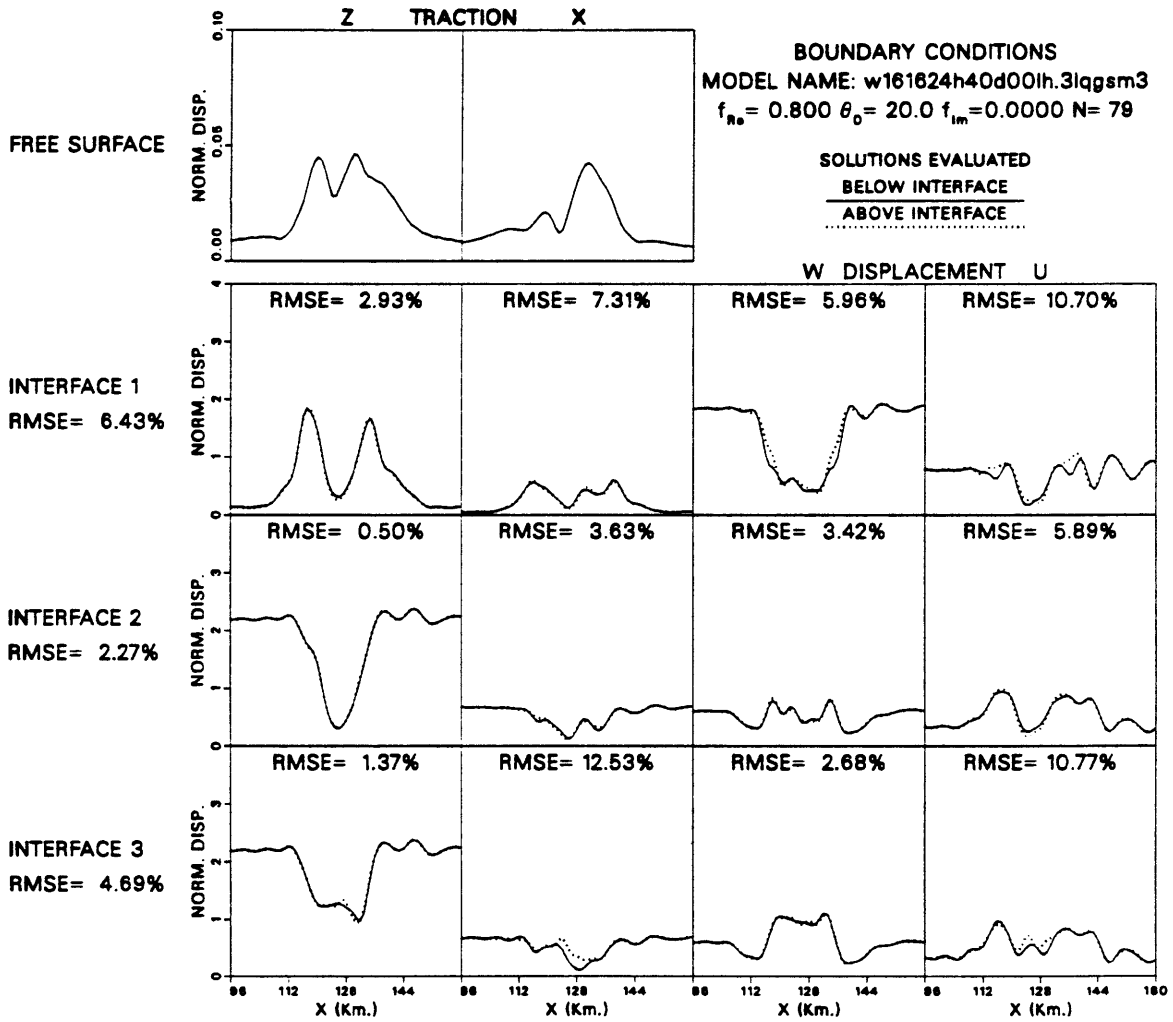


Figure 5.4b Same as Figure 5.4a except boundary conditions are shown for 0.8 Hz.

overall accuracy of our surface displacement solutions. *Larner* [1970] pointed out that this is probably a conservative estimate of the solution errors since the surface displacements are not very sensitive to larger errors in the boundary conditions on the buried interfaces. The largest total errors here are less than 7% and we consider this to be quite good. The maximum residuals in the free surface traction are also below the threshold of 0.05 that we set previously. However, for 0.8 Hz the maximum surface traction is approaching this value. Higher frequencies were eliminated from the modeling because this threshold was exceeded above 0.8 Hz. Table 5.1 lists the various RMS errors and maximum free surface tractions for the remaining frequencies. In some cases the errors are larger for individual traction or displacement components at certain interfaces, but the amplitudes in these cases are so small that they do not contribute significantly to the total RMS error for the interface.

TABLE 5.1
Boundary Condition % RMS Errors and
Maximum Surface Tractions for Best LQZ Model

Freq	Interface 3 RMSE (%)					Interface 2 RMSE (%)					Interface 1 RMSE (%)					Surf Tract	
	U	W	Tx	Tz	TOT	U	W	Tx	Tz	TOT	U	W	Tx	Tz	TOT	Tx	Tz
.20	0.70	0.06	1.63	0.78	0.50	0.31	0.04	2.29	0.41	0.35	0.37	0.16	26.28	2.76	1.28	.007	.006
.25	0.94	0.08	1.83	0.84	0.62	0.33	0.05	1.77	0.29	0.32	0.50	0.27	20.58	2.29	1.24	.008	.008
.30	1.12	0.18	2.12	0.56	0.66	0.43	0.08	1.63	0.24	0.35	0.75	0.41	17.65	2.04	1.39	.011	.010
.35	1.63	0.27	2.80	0.25	0.75	0.78	0.11	1.44	0.19	0.39	1.10	0.60	13.79	1.84	1.52	.014	.014
.40	2.23	0.44	3.37	0.62	1.11	0.97	0.08	0.95	0.23	0.35	1.51	0.89	9.26	1.71	1.63	.017	.019
.45	2.46	0.91	3.84	1.03	1.54	1.50	0.20	0.98	0.21	0.45	2.38	1.27	7.82	1.64	1.99	.017	.019
.50	4.62	1.43	7.68	1.33	2.63	2.41	0.41	0.81	0.21	0.56	3.33	1.72	6.18	1.57	2.34	.015	.021
.55	7.14	1.83	10.66	1.38	3.49	3.56	0.64	0.88	0.15	0.69	5.73	2.17	5.50	1.54	3.04	.013	.020
.60	14.13	2.68	17.31	1.55	5.58	4.17	0.83	1.38	0.07	0.81	7.80	2.48	5.46	1.61	3.62	.018	.021
.65	11.62	2.90	12.00	1.40	4.50	7.28	1.31	2.18	0.15	1.38	9.77	3.96	5.78	1.69	4.81	.023	.025
.70	11.59	3.28	12.90	1.55	4.88	7.84	2.09	2.85	0.25	1.85	9.59	4.92	5.57	1.91	5.27	.031	.032
.75	11.69	3.33	12.75	1.52	4.96	6.64	2.87	3.21	0.37	2.08	9.41	5.83	6.44	2.32	5.84	.036	.039
.80	10.77	2.68	12.53	1.37	4.69	5.89	3.42	3.63	0.50	2.27	10.70	5.96	7.31	2.93	6.43	.043	.046

Next we examined the wavenumber spectra for the magnitudes of the wave potential coefficients obtained by solving the linear system of boundary equations discussed in Chapter 3. As we mentioned then, a justification for truncating the infinite sum is that the coefficients should converge toward zero so that scatter orders higher than the truncation limits will not be needed. If this is not the case, then it may be impossible to satisfy the boundary conditions without including higher scatter orders. We have just shown above that this is not the case for our best model solution, and even if we find that some of the coefficient wavenumber spectra do not converge, this obviously does not matter since the boundary conditions are being satisfied quite well.

Figures 5.5a and 5.5b show the wavenumber magnitude spectra for all of the potential coefficients in each layer of the model for 0.2 Hz and 0.8 Hz respectively. The down-going and up-going P-wave potential are plotted on the left in decibels versus $Re\{k_n\}/(\omega/\alpha_4)$ and the S-wave potentials are on the right versus $Re\{k_n\}/(\omega/\beta_4)$. The potentials for the surface layer are at the top of the figure and the halfspace is at the bottom. On the horizontal axis we have also marked the locations of the characteristic wavenumbers, $Re\{K_{\alpha_p}\}$ for P waves and $Re\{K_{\beta_p}\}$ for S waves, for each layer and the halfspace as indicated in the legend. These points correspond to values of $Re\{k_n\}$ at and above which inhomogeneous interface waves will exist in the appropriate media, regardless of whether the wavenumbers are complex or not. For both 0.2 and 0.8 Hz all potential spectra except for the up-going S waves in layer 2 have a strong isolated peak at the incident wavenumber, k_0 . This is natural since the incident wave propagation direction should contribute the strongest component to the solutions in most cases. Above and below k_0 we can see that

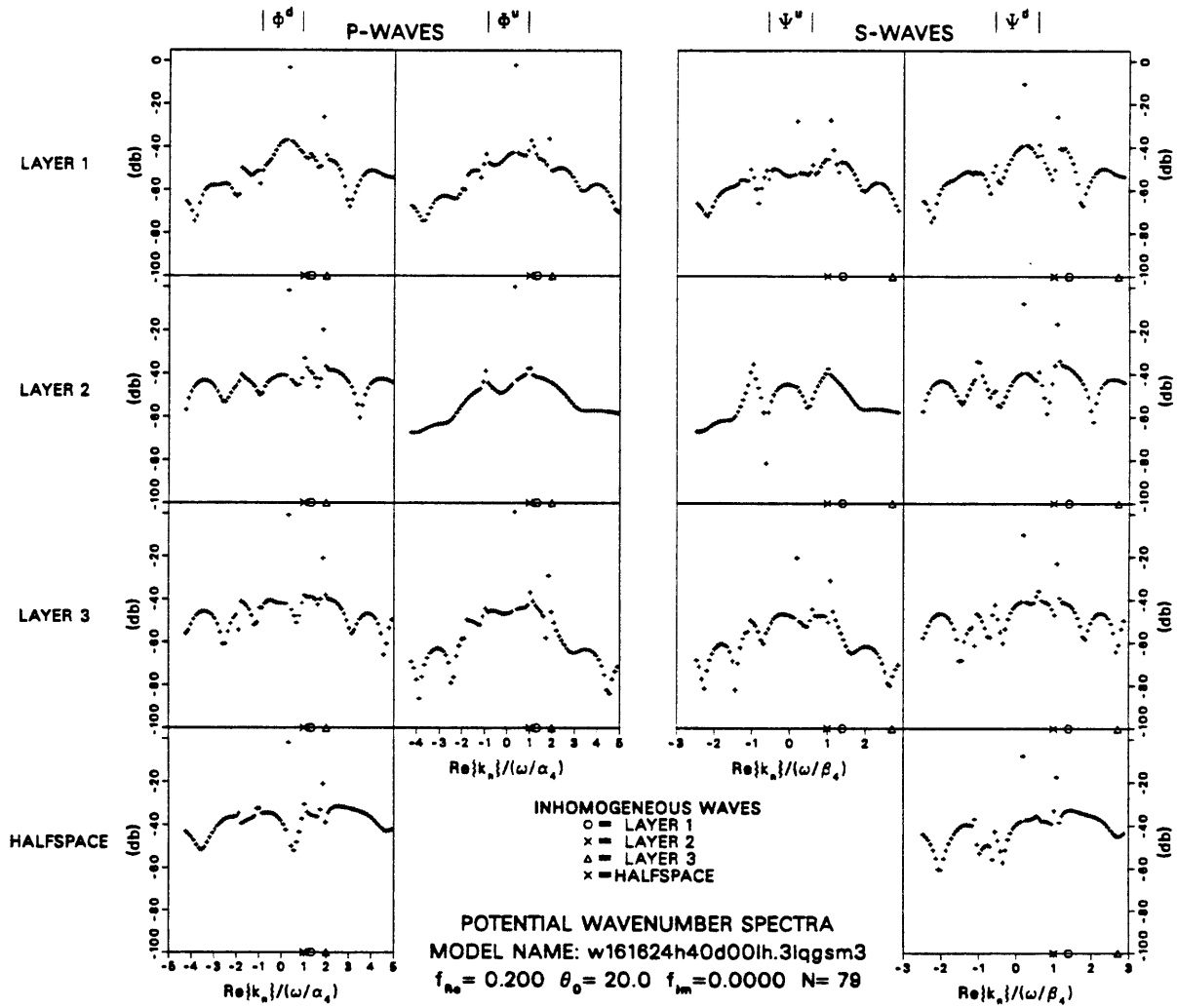


Figure 5.5a Potential wavenumber spectra for the 0.2 Hz solution of the best model. The vertical scale is in decibels.

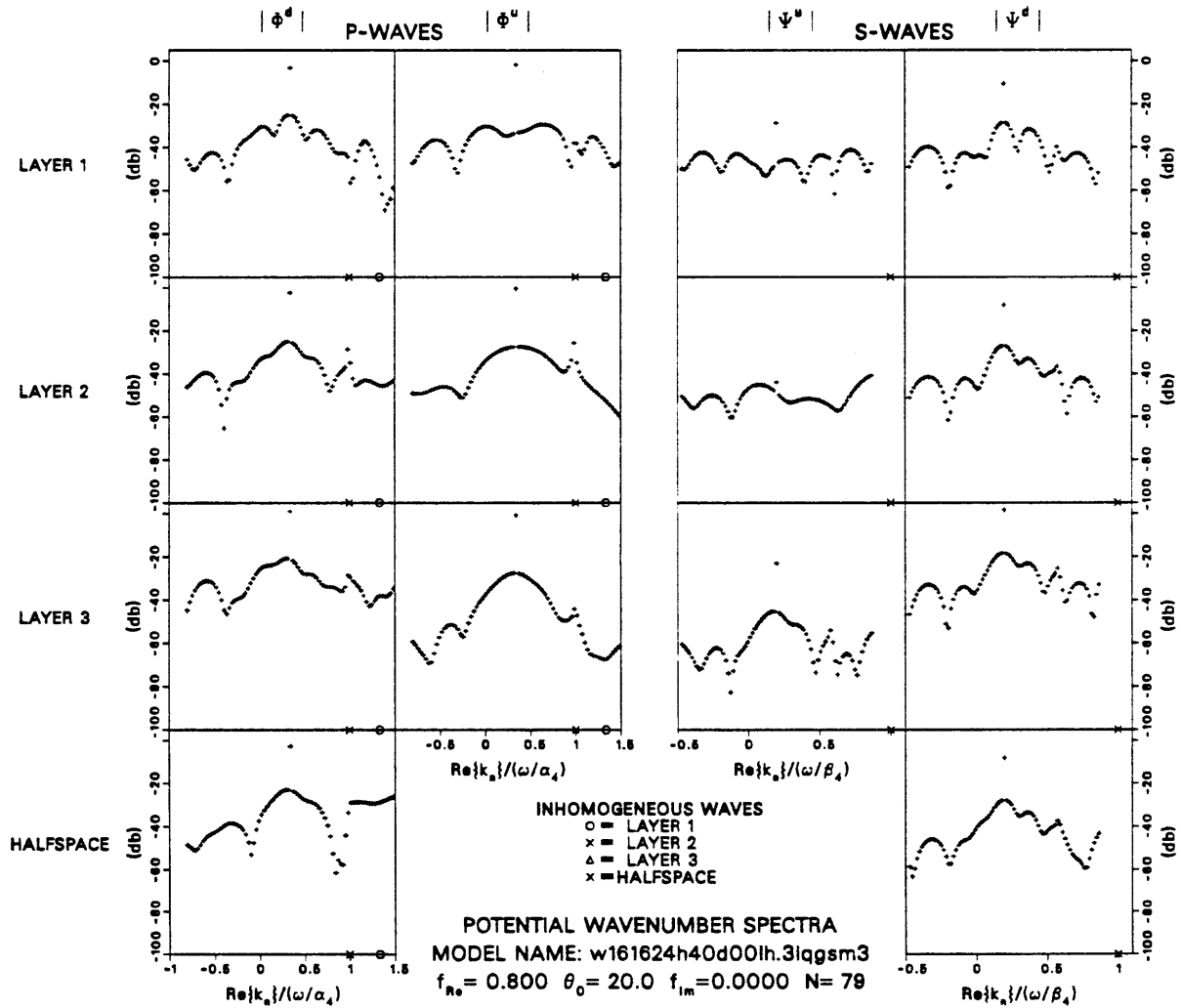


Figure 5.5b Same as Figure 5.5a except spectra are shown for 0.8 Hz.

there are several cases where the spectra do not converge uniformly towards zero. The S-wave potentials for 0.8 Hz in layer 1 (Figure 5.5b) are good examples of this. Apparently the convergence requirement may be relaxed in the present case since the boundary conditions are being fulfilled quite well. Actually, in almost every case for both 0.2 and 0.8 Hz, the potentials for the largest positive and negative wavenumbers are down by at least 40 db relative to the incident P-wave potential (0 db) and this should be sufficient justification for the truncation limits we have used here.

Note in Figure 5.5a, for 0.2 Hz, that there is an additional isolated peak in most of the spectra in the region of inhomogeneous interface waves mentioned above. This indicates a strong contribution of these wave types to the solution at 0.2 Hz, whereas apparently these wave types are not as important at 0.8 Hz since these peaks are much smaller in Figure 5.5b. In fact, at 0.8 Hz the P-wave potentials do not even extend up to K_{α_s} , the characteristic wavenumber in the low Q zone, and the S waves are completely within the homogeneous region of wavenumbers. (Note that the characteristic wavenumbers for the highest velocity media appear near the right-most limit for the S-wave plots.) This is because the wavenumber spacing, Δk_n , is independent of frequency, and we have used the same maximum scatter order index of $N = \pm 39$ for all frequencies. We tried increasing N for higher frequencies to include more inhomogeneous waves and discovered that the displacement solutions at the surface and the boundary conditions changed very little. Apparently interface waves are not very important for higher frequencies in the current model. This may be due to the strong attenuation present in this model, which causes higher frequency waves to attenuate more rapidly than for

lower frequencies. Interface waves which decay naturally away from the interface, even in high Q media, will now be attenuated even more strongly and thus should contribute very little to the solutions at higher frequencies. If this were not the case, then the boundary condition RMS errors would be much larger due to inadequate wavenumber coverage.

Now that the reliability of our solutions for the best model has been established, we wish to test the same model for different incidence angles to see if the stable pattern observed for all of the teleseismic data is adequately reproduced. In Chapter 2 we showed in Figures 2.30 through 2.32 that the spectral data averaged over the 7 northwestern events, the 3 southeastern events and all 10 events together yielded very similar amplitude ratio results. If the model in Figure 5.1 is reasonable, then it should be capable of producing a similarly stable pattern. The next set of figures shows these results. First for the northwestern events we simply compared the same synthetic spectral ratios shown in Figures 5.2a and 5.2b with the averaged ratios shown previously in Figure 2.30. The 7-event averaged data yielded ratio results almost identical to that for just the 4 Kuril Islands events, but the subtle differences did cause a very slight increase in the total variance reduction. The comparisons of the 7-event ratios with the synthetics is shown in Figure 5.6a and 5.6b. To test the model for negative incidence angles we calculated solutions for $\theta_0 = -20^\circ$ and compared them with the data for the 3 averaged southeastern events. These results are shown in Figures 5.7a and 5.7b plotted in the same way as before. Although the variance reduction is significantly smaller than for the northwestern data, the major features are still reasonably well represented by the model solutions. The fact that the total variance reduction of 63.7% is smaller

VERTICAL COMPONENT SPECTRAL RATIOS

OBSERVED: 7 NORTHWESTERN EVENTS recorded in VALLES CALDERA (ARRAY 2)

SYNTHETIC: model= w161624h40d00lh.3lqgsm3 $\theta_0 = 20.0$ $f_{IM} = 0.0000$

$\sigma_{MOD}^2(\log)$: Vertical= 0.305E-01 Total= 0.471E-01

Variance Reduction (HHS): Vertical= 83.2% Total= 84.3%

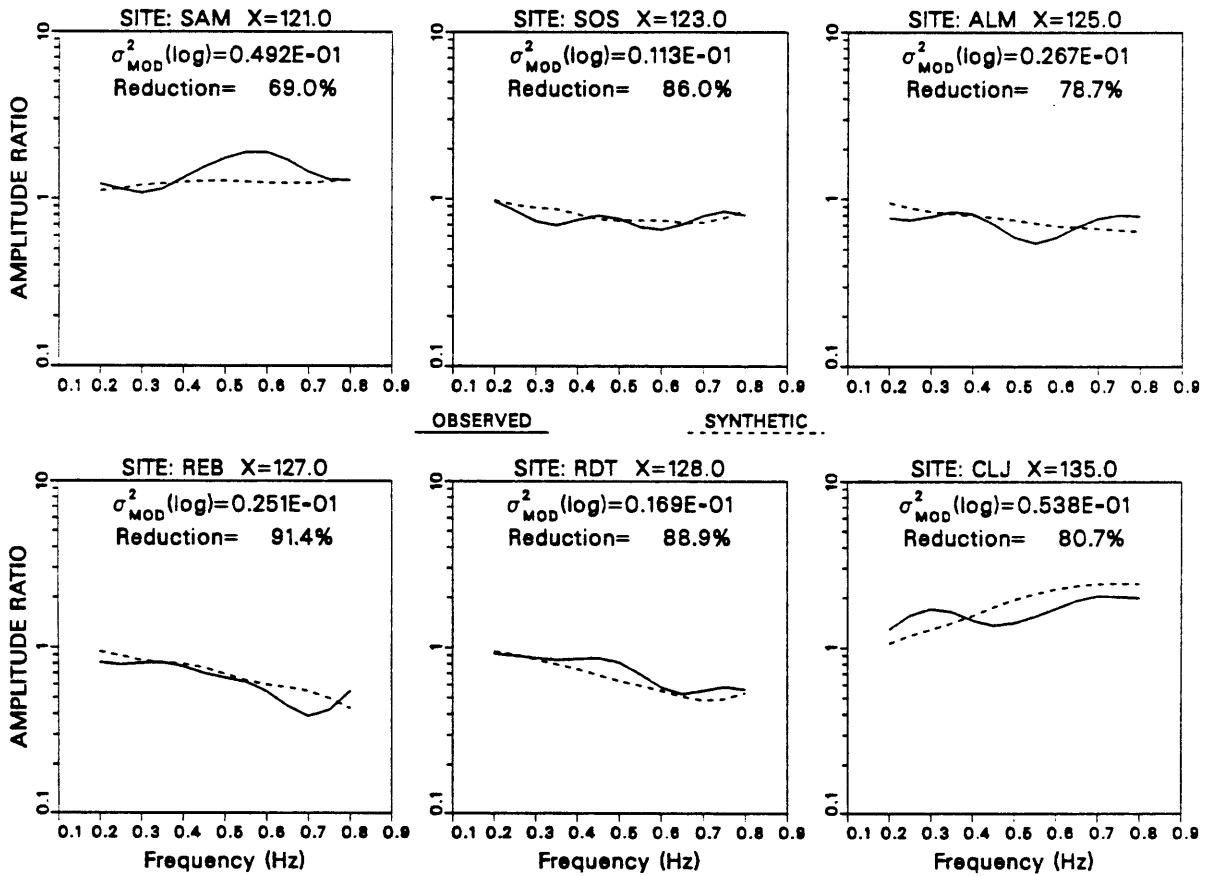


Figure 5.6a Comparison of the vertical component synthetic spectral ratios shown previously in Figure 5.2a with observed ratios for the 7-event averaged northwestern data. Incidence angle used was $\theta_0 = +20^\circ$.

HORIZONTAL COMPONENT SPECTRAL RATIOS

OBSERVED: 7 NORTHWESTERN EVENTS recorded in VALLES CALDERA (ARRAY 2)

SYNTHETIC: model= w161624h40d00lh.3lqgsm3 $\theta_0 = 20.0$ $f_{IM} = 0.0000$

$\sigma_{MOD}^2(\log)$: Horizontal= 0.637E-01 Total= 0.471E-01

Variance Reduction (HHS): Horizontal= 84.8% Total= 84.3%

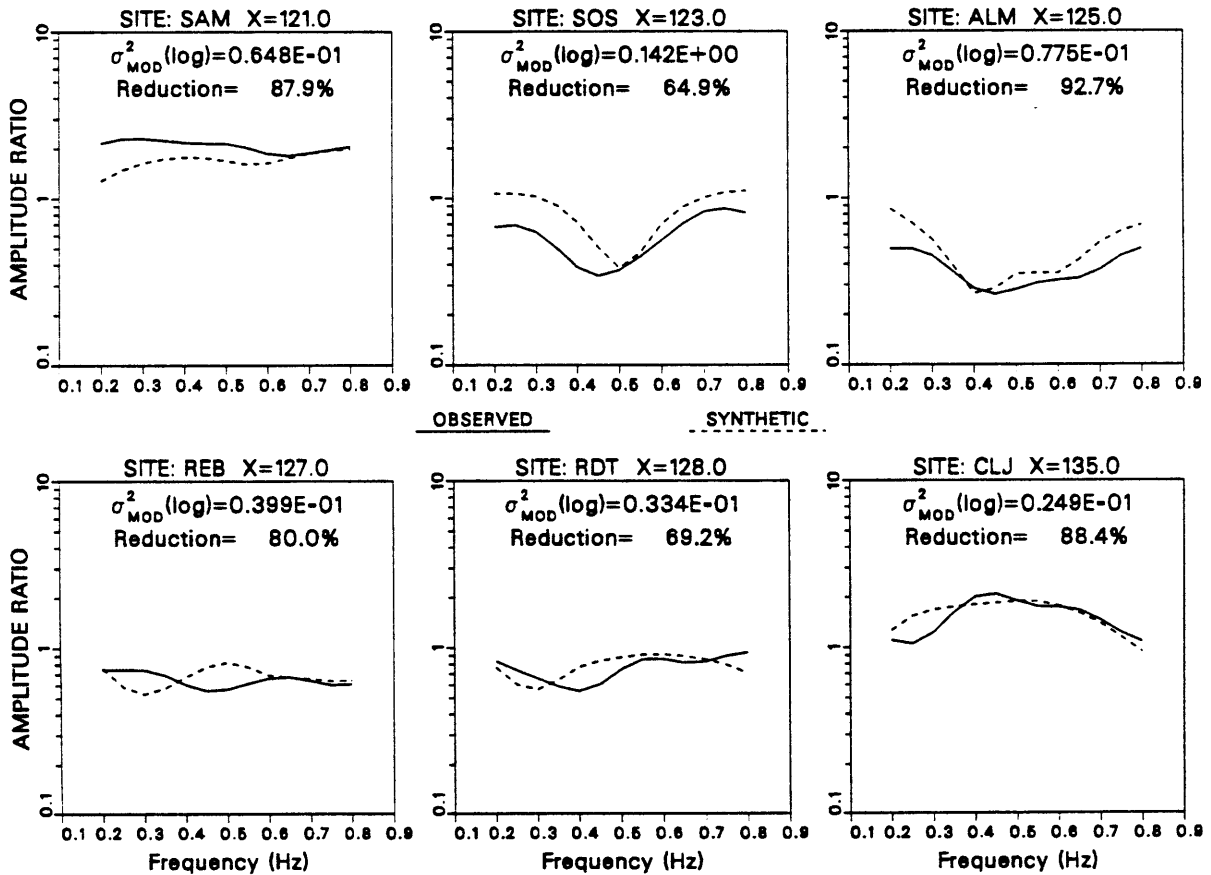


Figure 5.6b Same as Figure 5.6a except the horizontal components are shown.

VERTICAL COMPONENT SPECTRAL RATIOS

OBSERVED: 3 SOUTHEASTERN EVENTS recorded in VALLES CALDERA (ARRAY 2)

SYNTHETIC: model= w161624h40d00lh.3lqgm3 $\theta_0 = -20.0$ $f_{IM} = 0.0000$

$\sigma_{MOD}^2(\log)$: Vertical= 0.116E+00 Total= 0.132E+00

Variance Reduction (HHS): Vertical= 61.6% Total= 63.7%

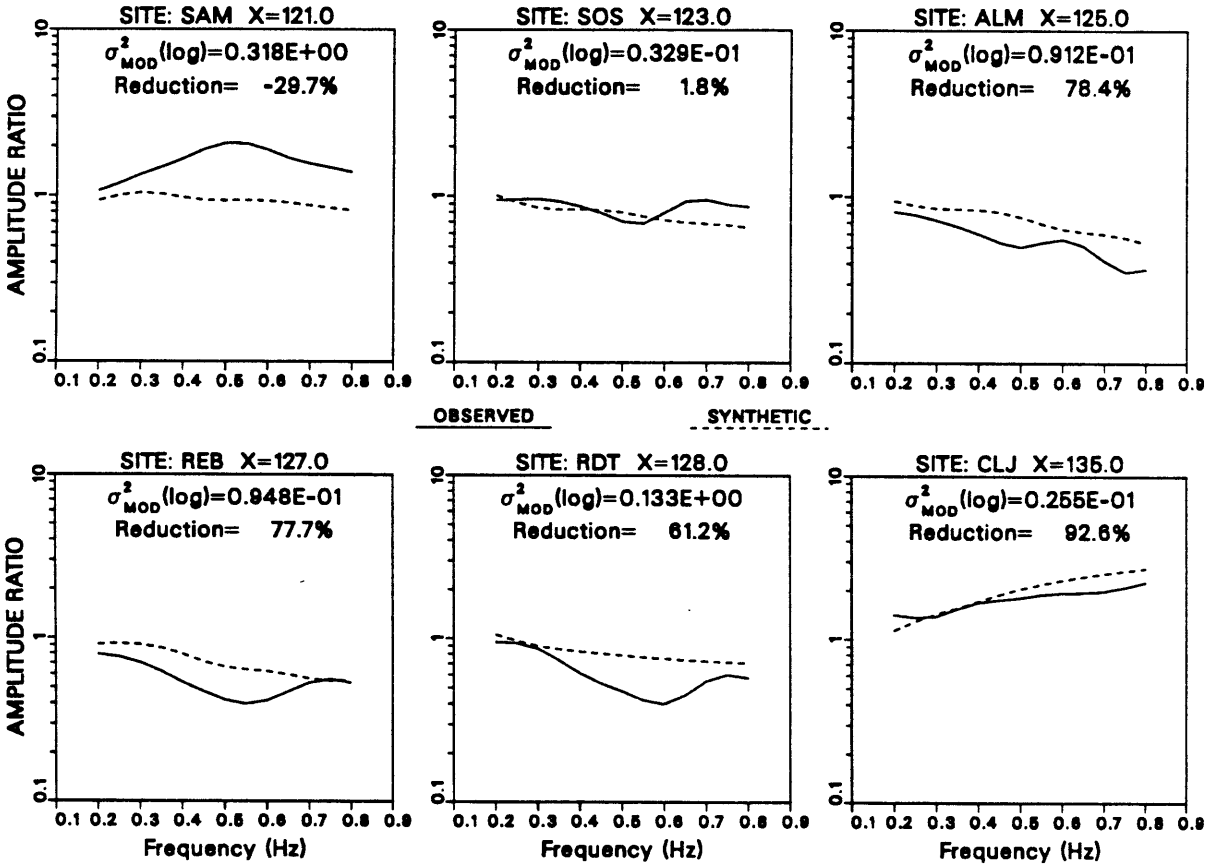


Figure 5.7a Vertical synthetic spectral ratios for best model with incidence angle $\theta_0 = -20^\circ$ compared with observed ratios for the 3-event averaged southeastern data.

HORIZONTAL COMPONENT SPECTRAL RATIOS

OBSERVED: 3 SOUTHEASTERN EVENTS recorded in VALLES CALDERA (ARRAY 2)

SYNTHETIC: model= w161624h40d00lh.3lqgsm3 $\theta_0 = -20.0$ $f_{IM} = 0.0000$

$\sigma_{MOD}^2(\log)$: Horizontal= 0.148E+00 Total= 0.132E+00

Variance Reduction (HHS): Horizontal= 65.2% Total= 63.7%

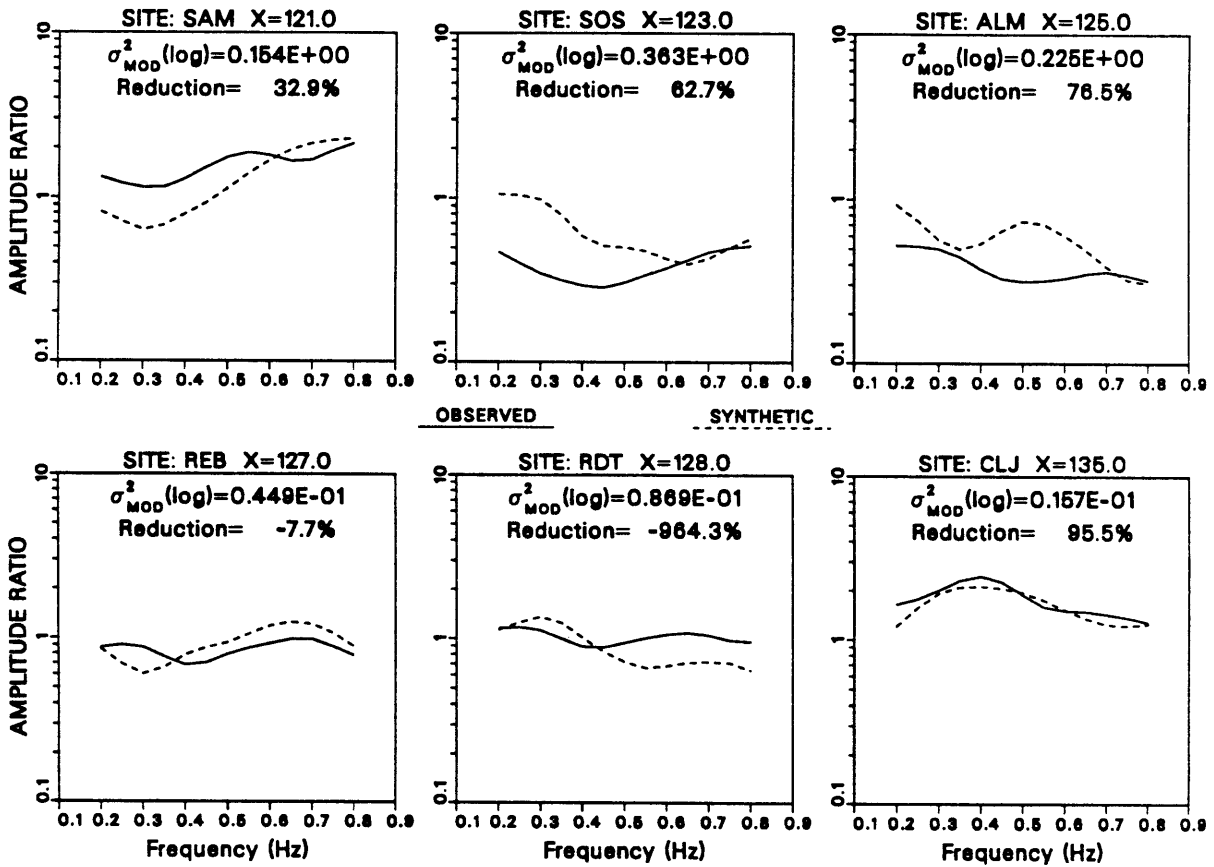


Figure 5.7b Same as Figure 5.7a except the horizontal components are shown.

than for the northwestern data indicates that the imposed symmetry of the model structure in Figure 5.1 is probably incorrect. This is certainly no surprise since there is no reason to expect the caldera's sub-structure to be symmetric beyond a simple first-order approximation, given the obvious complexity of the region [*Self et al.*, 1986]. However, we stated at the outset that we would only be attempting to determine large-scale first-order features of the structure in order to deal with the limited data set and to reduce the modeling procedure to a manageable form. With this simplification in mind, we consider the fit to the southeastern data to be acceptable. The fine tuning of the caldera sub-structure to improve this fit would require better data coverage and a more sophisticated modeling technique which would allow the study of more complex structures than the Aki-Larner method is capable of dealing with.

Finally, the results of the data averaged over all 10 events were compared with the model calculations for vertical incidence, in the belief that the average should minimize the effects due to positive or negative incidence angles. The comparisons between data and synthetics for this test are shown in Figures 5.8a and 5.8b. Here the total variance reduction of 76.0% is almost as high as for the northwestern data. Since now we can say that the model produces a very stable pattern which fits the data well for non-negative incidence angles, the partial breakdown of this pattern for negative incidence is clearly due to secondary structural features in the model which probably should be located in the southeastern half of the caldera. We feel, though, that Figure 5.1 is a good representation of the average dimensions and material properties for the large-scale shallow sub-structure of the caldera.

VERTICAL COMPONENT SPECTRAL RATIOS

OBSERVED: ALL 10 NW & SE EVENTS recorded in VALLES CALDERA (ARRAY 2)

SYNTHETIC: model= w161624h40d00lh.3lqgs3 $\theta_0 = 0.0$ $f_{IM} = 0.0000$

$\sigma_{MOD}^2(\log)$: Vertical= 0.666E-01 Total= 0.780E-01

Variance Reduction (HHS): Vertical= 73.4% Total= 76.0%

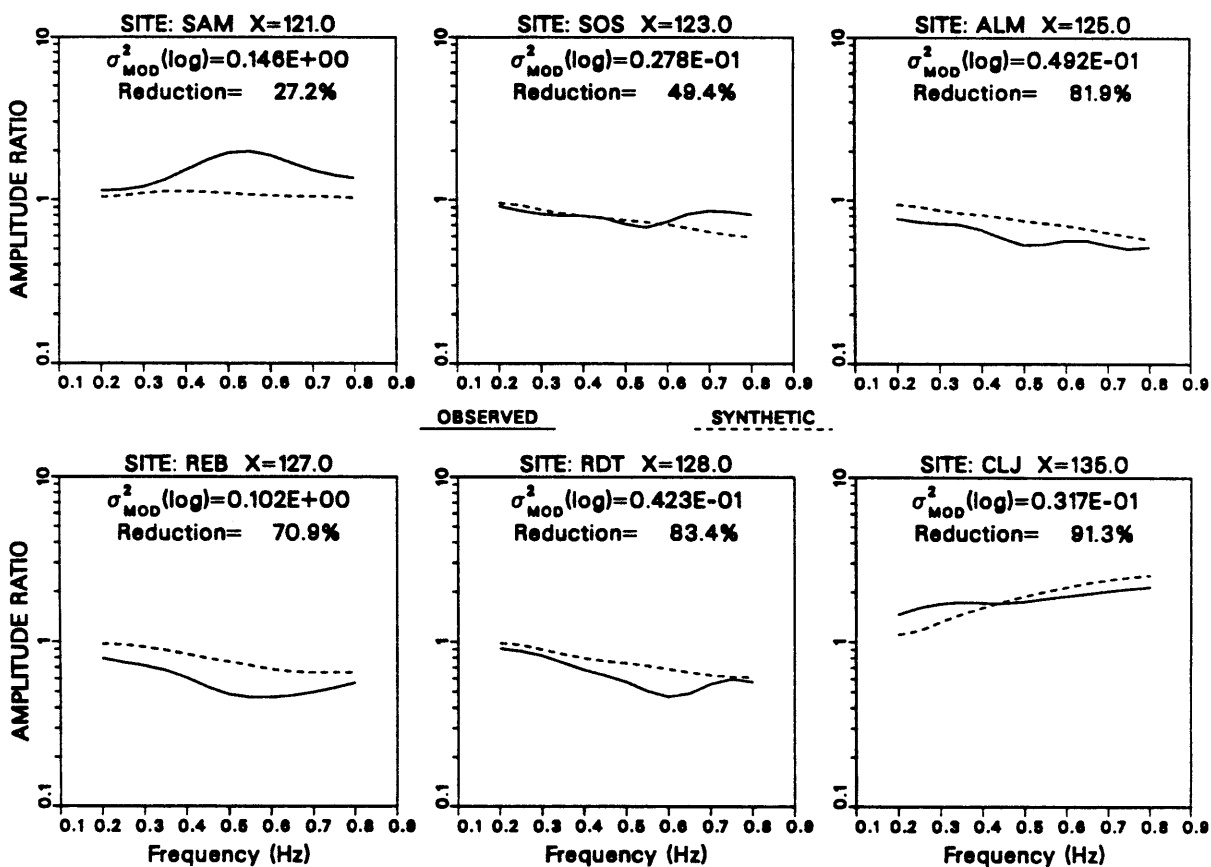


Figure 5.8a Vertical synthetic spectral ratios for best model with vertical incidence compared with observed ratios for the average of all 10 northwestern and southeastern events.

HORIZONTAL COMPONENT SPECTRAL RATIOS
OBSERVED: ALL 10 NW & SE EVENTS recorded in VALLES CALDERA (ARRAY 2)
SYNTHETIC: model= w161624h40d00lh.3lqgsm3 $\theta_0 = 0.0$ $f_{1M} = 0.0000$
 $\sigma_{MOD}^2(\log)$: Horizontal= 0.894E-01 Total= 0.780E-01
Variance Reduction (HHS): Horizontal= 77.6% Total= 76.0%

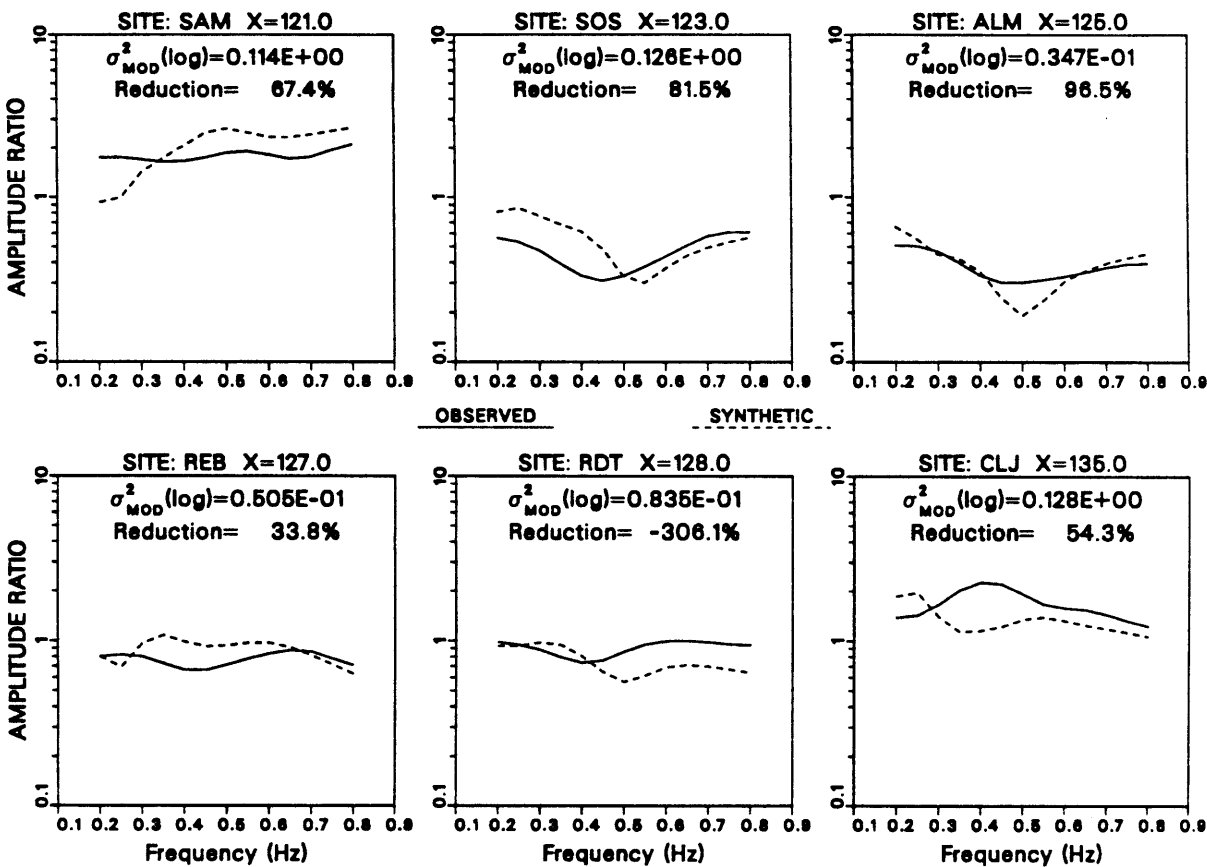


Figure 5.8b Same as Figure 5.8a except the horizontal components are shown.

In Figures 5.9a and 5.9b we compare the best model results with one of the Kommandorsky Islands events recorded on the wide aperture array 1. Although the relative differences between the ratios at SAM, ALM and RDT are similar as before, the model clearly fails to explain the overall variations for all six sites. In particular, the horizontal synthetic ratios at CAC and CAP do not predict low enough amplitude relative to the average over all sites. We mentioned in Chapter 2 that the low scattered wave amplitudes outside of the caldera could be explained by a decrease in the strength of scattering or resonance due to less complex structural irregularities relative to the caldera. We also discussed evidence in the data which indicates that the amplitudes at ALM and RDT are in fact anomalously low, rather than “normal”. So our assumption that the scattering is stronger near the caldera should be valid. The model structure shown in Figure 5.1 is clearly less complex at locations corresponding to CAC ($x = 113$ km) and CAP ($x = 145$ km) than for locations nearer the caldera. Apparently, then, our model does not produce strong enough scattering or resonance effects near the caldera to create the large scattered-wave amplitudes at SAM relative to CAC. Some additional features must be needed beneath the shallow caldera structure shown in Figure 5.1. Most likely the deep low velocity zone discovered in Chapter 4 is the major feature that is missing from the model.

Unfortunately our modeling capabilities with the Aki-Larner method are too limited to allow the inclusion of this feature in our calculations and thus we can only speculate as above about the discrepancies for the array-1 scattered-wave data. However, the array 2 data are much more localized and should be less subject to large differences in the strength of scattering effects from site to site. Therefore

VERTICAL COMPONENT SPECTRAL RATIOS
OBSERVED: KOMMANDORSKY ISLANDS recorded in VALLES CALDERA (ARRAY 1)
SYNTHETIC: model= w161624h40d00lh.3lqgm3 $\theta_0 = 20.0$ $f_{IM} = 0.0000$
 $\sigma_{MOD}^2(\log)$: Vertical= 0.120E+00 Total= 0.305E+00
Variance Reduction (HHS): Vertical= -6.0% Total= -19.8%

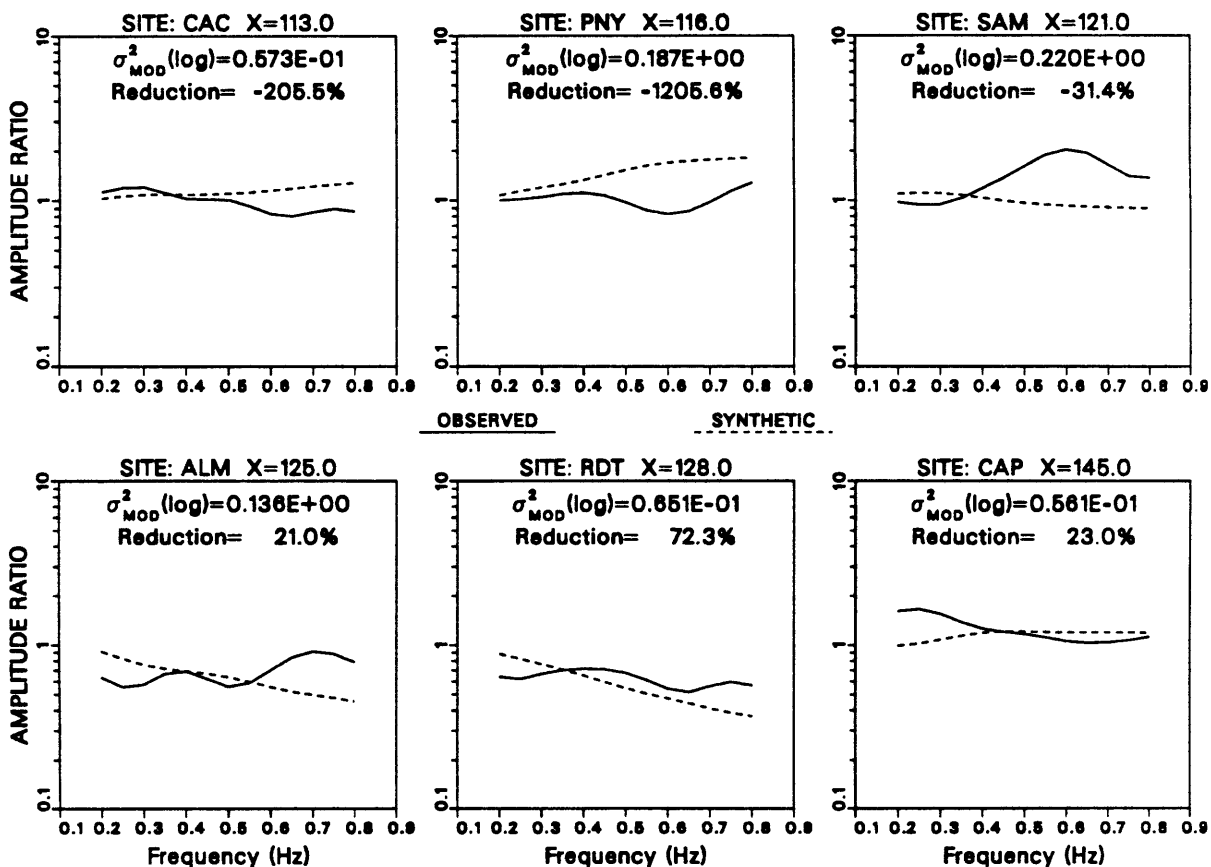


Figure 5.9a Vertical synthetic spectral ratios for the best model compared with observed ratios for a northwestern event from the Kommandorsky Islands recorded on array 1. Incidence angle used was $\theta_0 = +20^\circ$.

HORIZONTAL COMPONENT SPECTRAL RATIOS
OBSERVED: KOMMANDORSKY ISLANDS recorded in VALLES CALDERA (ARRAY 1)
SYNTHETIC: model= w161624h40d00lh.3lqgam3 $\theta_0= 20.0$ $f_{IM}= 0.0000$
 $\sigma_{MOD}^2(\log)$: Horizontal= 0.489E+00 Total= 0.305E+00
Variance Reduction (HHS): Horizontal= -23.7% Total= -19.8%

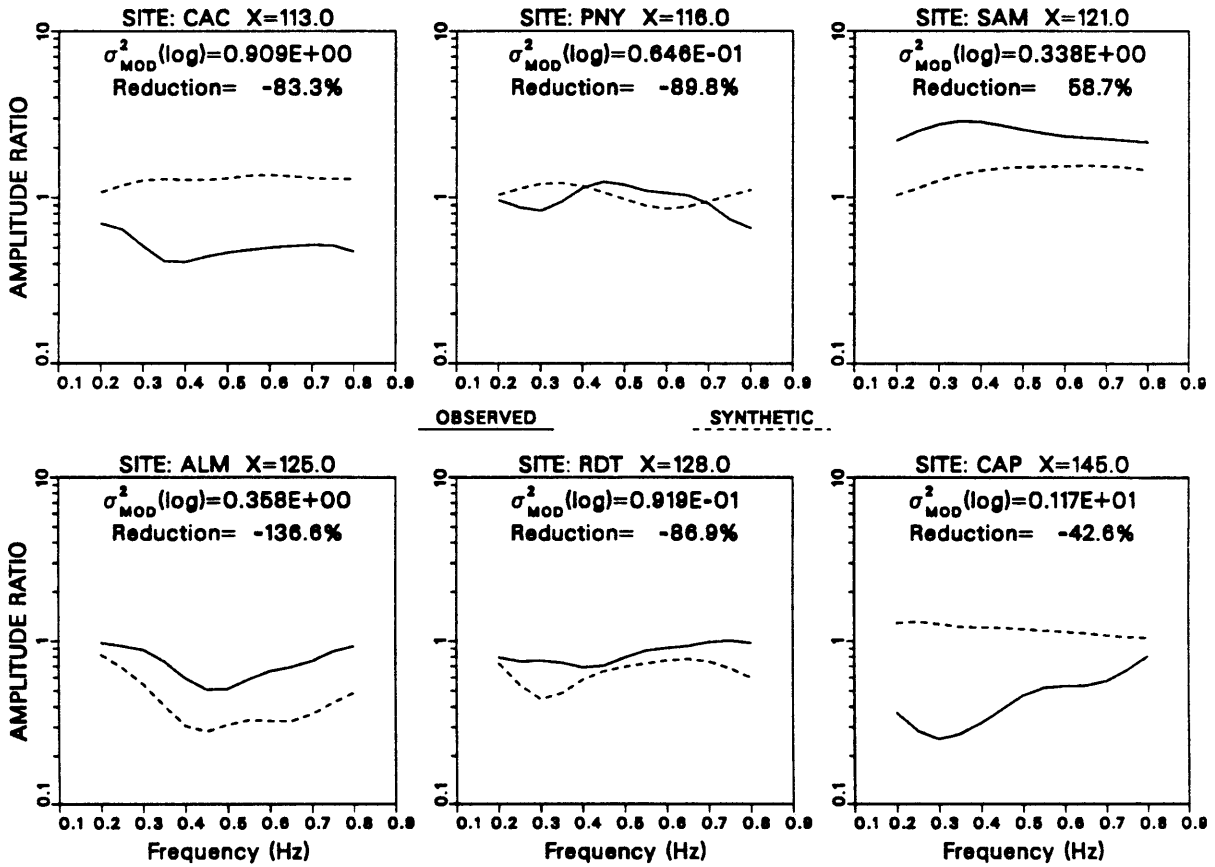


Figure 5.9b Same as Figure 5.9a except the horizontal components are shown.

we do not believe the array-1 data pose a contradiction to the shallow, localized Q structure of the best model. The Q effect simply dominates over relative scattering strength on the smaller scale represented by the array-2 data. In Section 5.4 we will present further evidence, using array-1 data, that on the larger scale the model in Figure 5.1 still holds for the Q structure, even though the scattering and resonance structure, as shown here, is not well represented.

The one feature of the best fitting model presented here which is most apt to be questioned is the extremely low value of $Q = 1$ used in the low Q zone. Although it may be physically possible for a material to have such a low Q [O'Connell & Budiansky, 1977], the major question here is how accurately can the Aki-Larner method predict the corresponding effects on seismic waves. In Chapter 3 we showed that the dispersion law of Azimi *et al.* [1968], used to incorporate Q in the wavefield expressions, holds well only down to about $Q = 5$. The major defect in attenuated pulses for lower values than 5 is the violation of causality. However, we mentioned in that discussion that perhaps the observance of causality is a strict requirement only when the phase spectrum is of importance. This is not the case here because, first, we are only modeling amplitudes and, secondly, each component of motion is largely dominated by a single wave type. Some of the observed ratio data exhibit features which are typical of Q effects, namely, a decrease in relative amplitude with increasing frequency for the vertical component at certain sites (i.e., REB and RDT) and a stronger relative decrease in amplitude from site to site for the horizontal component than for the vertical. We showed above that the second effect is due to S waves dominating the horizontal component. Since these effects were observed at fairly low frequencies we should expect that Q must be very low because

of its definition in terms of energy loss per wave cycle. In section 5.3 we will see that by increasing Q in the LQZ, the attenuating effects on the amplitude decrease in a predictable manner. The results for $Q \geq 2$ still display similar patterns as for $Q = 1$, but the relative amplitude variations are smaller and thus the higher Q models do not fit the data as well. This is a strong indication that indeed Q needs to be very low. We can also first do a simple calculation here using the basic definition for amplitude attenuation in terms of spatial Q given by equation (3.39, bottom). Since this formula is free from any assumptions about Q it can be used to see if the synthetic solutions in Figures 5.2a and 5.2b are reasonable. In Figure 5.2a for the vertical component, we estimate for the synthetics a decrease in amplitude at 0.4 Hz by a factor of approximately 0.5 between the two sites SAM and RDT. For the horizontal, Figure 5.2b, the decrease between SAM and ALM at 0.4 Hz is by a factor of approximately 0.15. Using $\alpha = 3.0$ in the low Q zone for the vertical component, $\beta = 1.29$ for the horizontal and a travel distance of $z = 4$ km for the maximum height of the LQZ, we can solve equation (3.39) directly to yield $Q \approx 2.1$ for the horizontal and $Q \approx 2.4$ for the vertical solutions. This is certainly within a reasonable range of $Q = 1$ used for the model, and these rough estimates may be high because the estimated travel distance of 4 km through the LQZ used at RDT and ALM is probably too large. But this simple calculation shows that the synthetic solutions are consistent with what we should expect from the model. The perturbation study in the next section will help to corroborate this further. So it appears that the Azimi dispersion law is good enough for our case. Since the Azimi law is primarily a phase correction, its success here for low Q may be due to the

fact that each component of motion is dominated by one wave type and the phase interactions between scattered P and S waves are minimal in most cases.

5.3 Parameter Perturbation Study and Uniqueness

The forward modeling approach used here inherently cannot provide a quantitative measure of a model's uniqueness the way that a formal inversion can. Strictly speaking, an infinite number of counterexamples would be required to prove uniqueness. In many cases, though, the data display a pattern that is systematic enough to rule out large classes of possible phenomena. This is the case with the present data set. There are very few ways in which the stable pattern of low amplitudes in the caldera can be explained. One possibility would be defocusing due to ray bending effects. This can be ruled out for two reasons. First, the amplitudes we are modeling are low frequency observations relative to the size of the structural anomaly, and ray theory will not hold in this case. Secondly, in Chapter 4 we demonstrated that lens-shaped low velocity inclusions tend to focus rather than defocus rays. Another mechanism which could produce low amplitudes is 2-dimensional resonance or anti-resonance similar to that discussed in detail by *Bard & Bouchon* [1985]. A low velocity inclusion can trap energy through resonance if the dominant mode is one in which the walls of the inclusion do not move. This would cause low amplitude on the opposite side of the inclusion, but this effect will be strongly frequency dependent, and the locations of low amplitudes on the surface will vary considerably with incidence angle. Anti-resonance in the surface layer could also produce low amplitude but again the pattern will not be as stable as what we observed in the Valles Caldera. Finally, the various mechanisms of scattering can produce distinct

amplitude patterns at the surface, depending on the type of scattering anomaly and its size relative to the wavelength. For a velocity anomaly, such as the low Q zone of our best model, that is smaller than the wavelength being considered we can expect a significant degree of Rayleigh scattering to occur, which will have an isotropic radiation pattern. But for higher frequencies, where the wavelength is comparable to the size of the anomaly, the scattering pattern becomes directionally dependent [Aki & Richards, 1980]. Both of these scattering regimes should be expected to exist in our caldera model for the frequency range we are using. Thus, in the absence of anelastic attenuation, we should expect to observe scattered wave amplitudes at the surface which depend on frequency and incidence angle. The Aki-Larner method can reproduce the effects of model resonance and scattering quite well and we will show in section 5.4 that these effects alone are too strongly dependent on frequency and incidence angle to explain the amplitude observations as well as we can with a low Q zone.

Having ruled out ray focusing, resonance and scattering patterns as possible explanations for the low caldera amplitudes, it now remains to determine the sensitivity of the synthetic solutions to variations in model parameters. This largely will involve perturbing one feature of the model at a time, since there are simply too many parameters to consider all possible combinations of multiple perturbations. We will see, though, that the most important parameters are those governing the LQZ and that reasonable limits may be defined for these beyond which the fit to the data begins to deteriorate significantly. Similar limits can be defined for the remaining parameters, but many of these can vary by larger amounts than those of the LQZ before the solutions deteriorate. We will begin by showing the effects of allowing

Q to vary in the LQZ and in the upper caldera fill since these are clearly the most physically important aspects of the model.

In the previous section we discussed the reliability of our solution in light of the extremely low value of $Q = 1$ used. Here we will show that increasing the value of Q in the LQZ decreases the variance reduction, but that the basic pattern remains reasonably stable until Q becomes large enough that attenuation is no longer significant. Figures 5.10, 5.11 and 5.12 show the results for $Q = 2, 5$ and 10 , respectively, in the LQZ, holding all other model parameters fixed. For $Q = 2$ the major features of the amplitude pattern are preserved but the total variance reduction has decreased from 84% to about 66%. For $Q = 5$, Figures 5.11a,b, the fit is much worse. Although there is still a trend of low amplitudes in the horizontal component at ALM, REB and RDT, this trend has all but disappeared in the vertical components. Also, we now begin to see some strong relative peaks and troughs at certain frequencies, particularly in the horizontal components. These features presumably are due to the effects of resonance and scattering mentioned above, and now these are becoming dominant because the attenuation is no longer strong enough to damp them out. In Figures 5.12a,b the results for $Q = 10$ are so bad that the homogeneous halfspace model (HHS) is preferable, as evidenced by the large negative variance reduction for the vertical component. Although the horizontal components at REB and RDT still show relative lows, those at SOS and ALM do not. Further the resonance and scattering effects are now so strong that the synthetic spectral ratios show strong relative peaks and troughs even in the vertical components. The clear trend of decreasing variance reduction with increasing Q lends strong support to the validity of using $Q = 1$. We discussed in Chapter 3

VERTICAL COMPONENT SPECTRAL RATIOS
OBSERVED: KURIL ISLANDS (4 EVENTS) recorded in VALLES CALDERA
SYNTHETIC: model= pertq302.mod $\theta_0= 20.0$ $f_{1M}= 0.0000$
 $\sigma_{MOD}^2(\log)$: Vertical= 0.625E-01 Total= 0.104E+00
Variance Reduction (HHS): Vertical= 64.9% Total= 65.8%

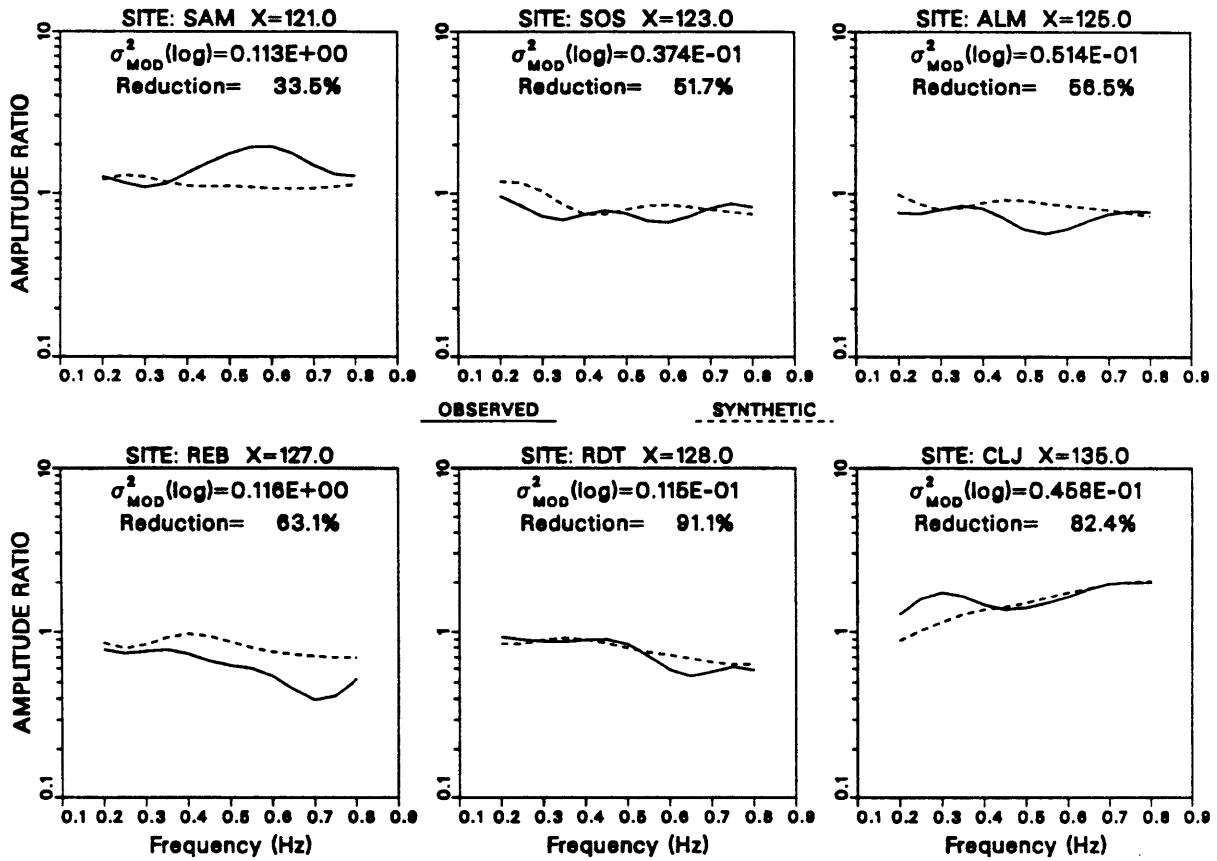


Figure 5.10a Vertical synthetic spectral ratios for best model with Q increased to 2 in the low Q zone, compared with the Kuril Islands data as shown before in Figure 5.2a.

HORIZONTAL COMPONENT SPECTRAL RATIOS
OBSERVED: KURIL ISLANDS (4 EVENTS) recorded in VALLES CALDERA
SYNTHETIC: model= pertq302.mod $\theta_0= 20.0$ $f_{IM}= 0.0000$
 $\sigma_{MOD}^2(\log)$: Horizontal= 0.145E+00 Total= 0.104E+00
Variance Reduction (HHS): Horizontal= 66.2% Total= 65.8%

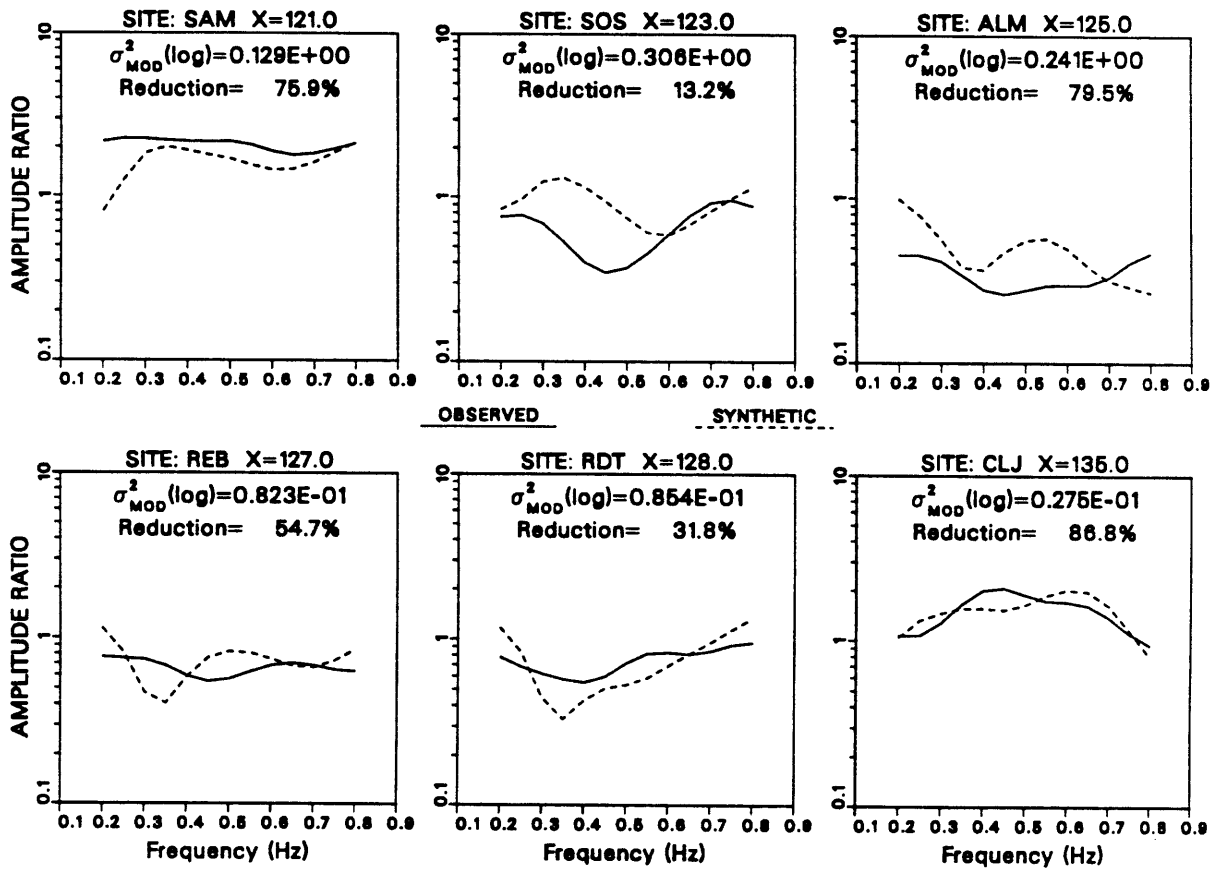


Figure 5.10b Same as Figure 5.10a except the horizontal components are shown.

VERTICAL COMPONENT SPECTRAL RATIOS
OBSERVED: KURIL ISLANDS (4 EVENTS) recorded in VALLES CALDERA
SYNTHETIC: model= pertq305.mod $\theta_0= 20.0$ $f_{IM}= 0.0000$
 $\sigma_{MOD}^2(\log)$: Vertical= 0.154E+00 Total= 0.239E+00
Variance Reduction (HHS): Vertical= 13.8% Total= 21.3%

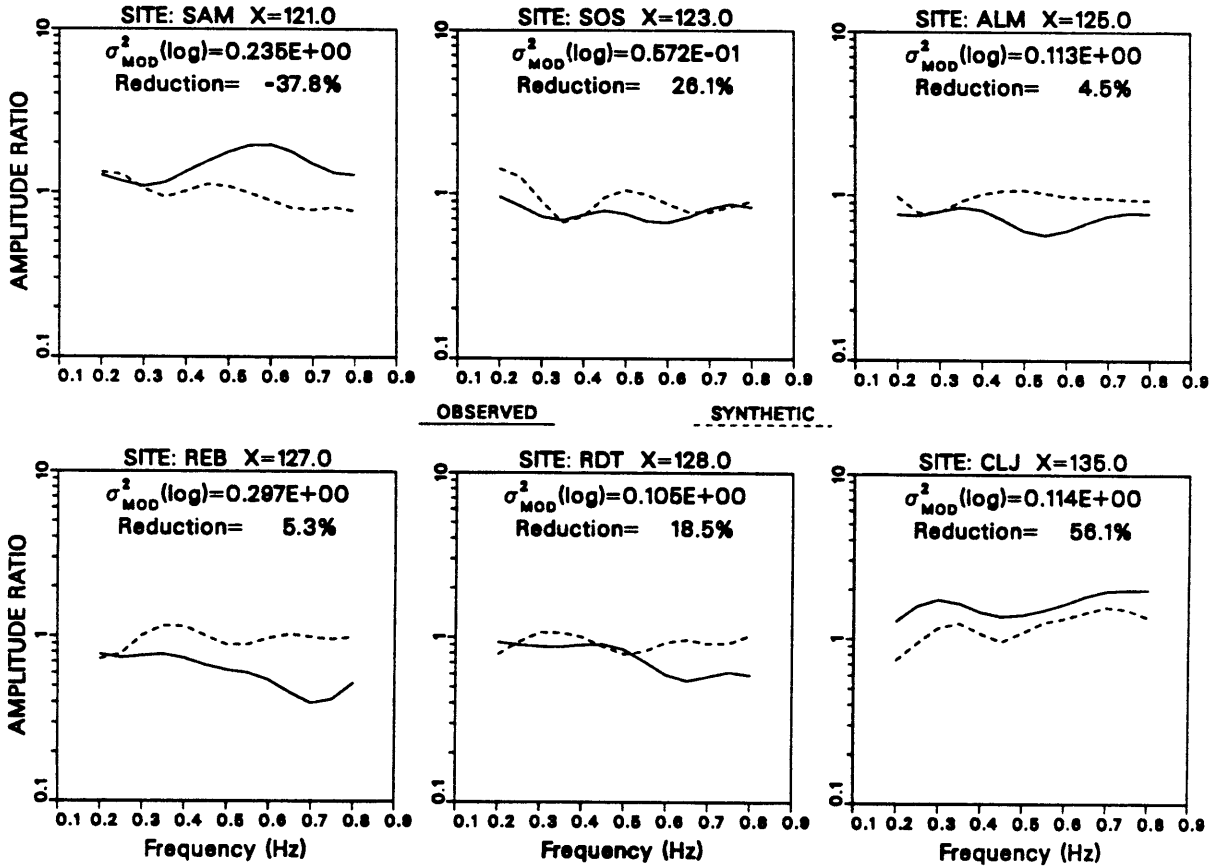


Figure 5.11a Vertical synthetic spectral ratios for best model with Q increased to 5 in the low Q zone, compared with the Kuril Islands data.

HORIZONTAL COMPONENT SPECTRAL RATIOS
OBSERVED: KURIL ISLANDS (4 EVENTS) recorded in VALLES CALDERA
SYNTHETIC: model= pertq305.mod $\theta_0 = 20.0$ $f_{IM} = 0.0000$
 $\sigma_{MOD}^2(\log)$: Horizontal= 0.325E+00 Total= 0.239E+00
Variance Reduction (HHS): Horizontal= 24.3% Total= 21.3%

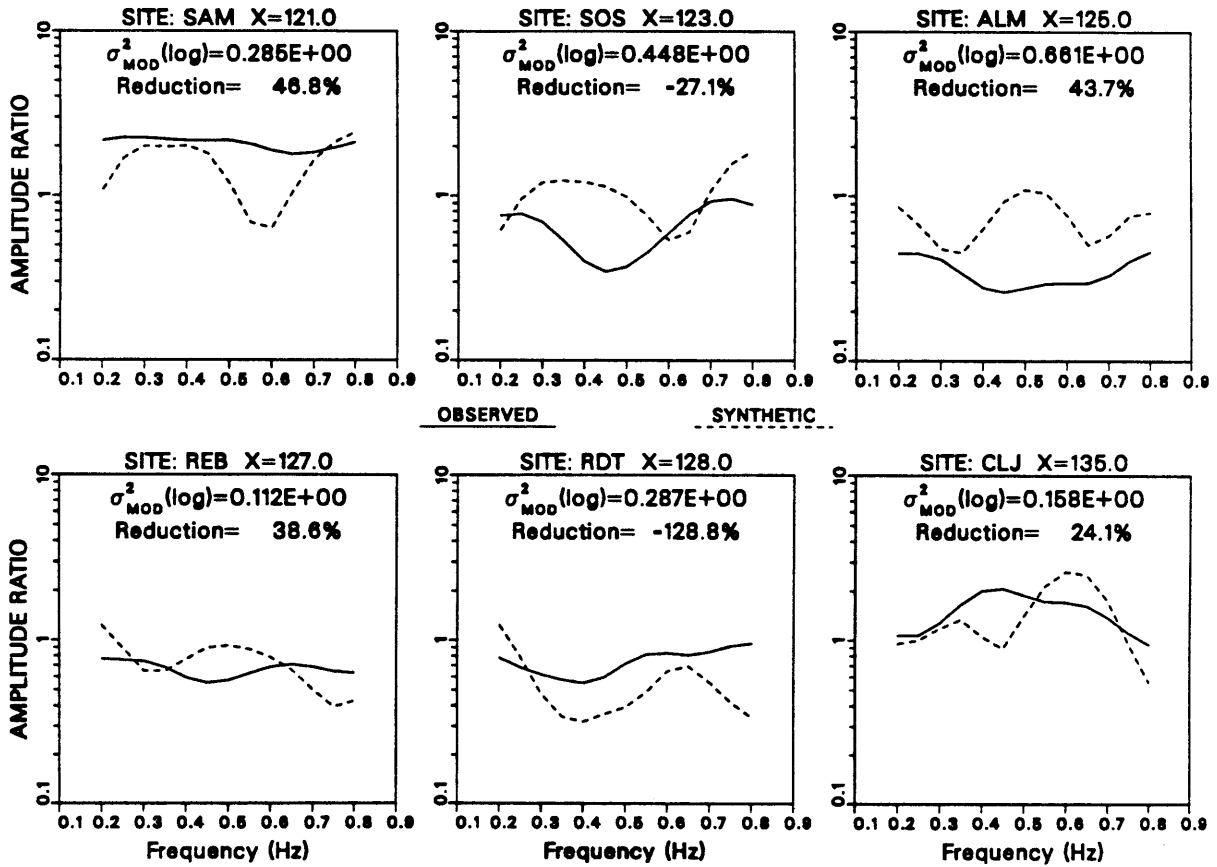


Figure 5.11b Same as Figure 5.11a except the horizontal components are shown.

HORIZONTAL COMPONENT SPECTRAL RATIOS
OBSERVED: KURIL ISLANDS (4 EVENTS) recorded in VALLES CALDERA
SYNTHETIC: model= pertq310.mod $\theta_0= 20.0$ $f_{1M}= 0.0000$
 $\sigma_{MOD}^2(\log)$: Horizontal= 0.351E+00 Total= 0.308E+00
Variance Reduction (HHS): Horizontal= 18.2% Total= -1.4%

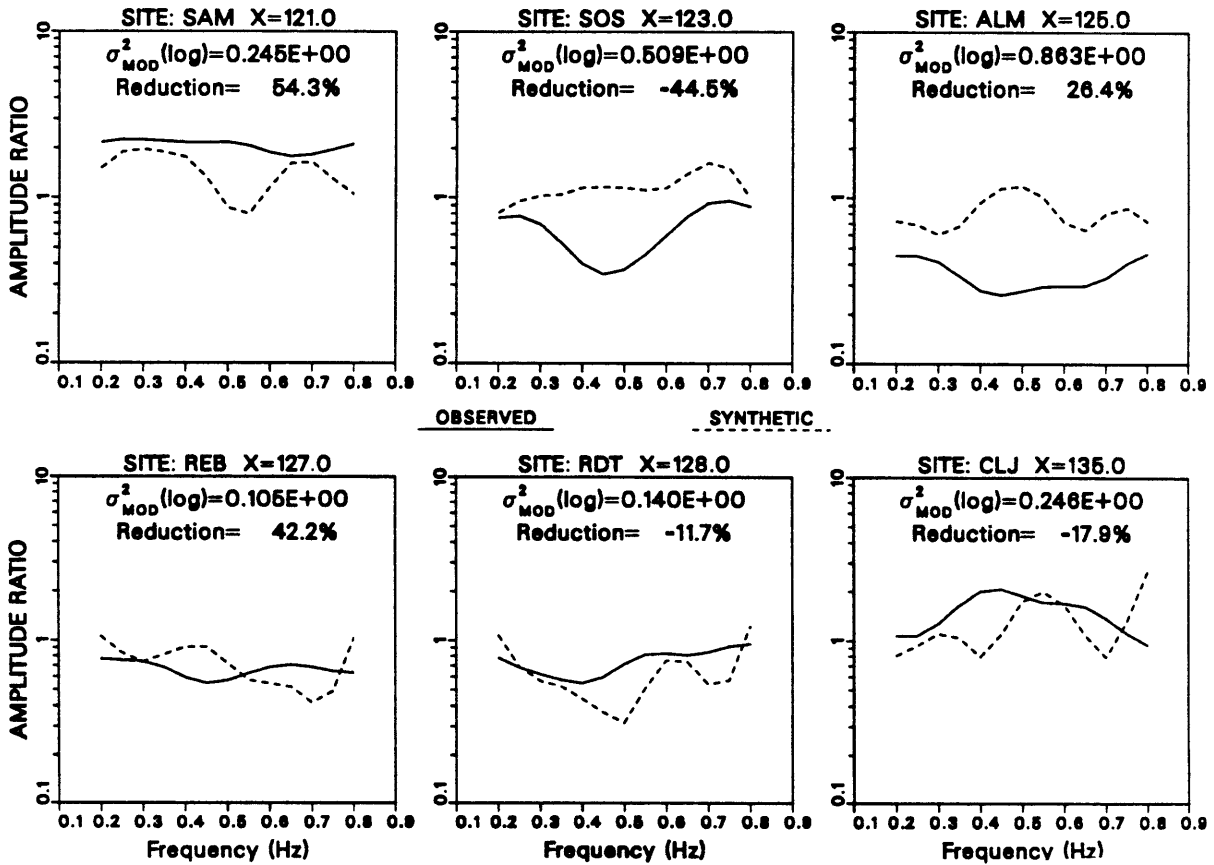


Figure 5.12b Same as Figure 5.12a except the horizontal components are shown.

that the Azimi dispersion law should hold well at least down to $Q = 5$. Since at this value of Q the attenuation is not strong enough to produce the necessary low amplitude or to damp out the resonant peaks sufficiently, it is clear that Q needs to be less than 5. We believe now that enough evidence has been given to justify the validity of our solution for $Q = 1$, and we will question it no further.

Next, we wish to examine the range of possible values for Q used in the upper caldera fill. Figures 5.13 and 5.14 show the effects of reducing the value from $Q = 100$ for the best model, to $Q = 5$ and $Q = 1$ respectively. For $Q = 5$ the variance reduction of 74.5% is significantly lower than the best model but the major features are still retained. However, for $Q = 1$ the results in Figures 5.14a,b show very serious deterioration in the fits for the horizontal components at SOS, ALM and CLJ and the total variance reduction has decreased to about 32%. This demonstrates a clear need to have a localized zone of very low Q relative to the surrounding media. Allowing the entire caldera fill (including the LQZ) to have the same low Q value does not produce strong enough attenuation for the horizontals at SOS and ALM relative to SAM. This is because now the material beneath SAM is also low Q , whereas for the best model it was not. In effect then we have also demonstrated that the LQZ can not be significantly wider than shown in Figure 5.1 without producing a pattern similar to that in Figure 5.14. Also, if the LQZ were narrower the attenuation at SOS would be too weak for the horizontal component. We also ran tests for $Q = 10, 20, 50$ and 1000 in the upper caldera fill. We found that the results for the best model are virtually unaffected by these changes. The total variance reduction remains stable between about 81% and 83%. Thus we can place no upper bound on Q in the upper caldera fill since the observed attenuation effect

VERTICAL COMPONENT SPECTRAL RATIOS
OBSERVED: KURIL ISLANDS (4 EVENTS) recorded in VALLES CALDERA
SYNTHETIC: model= pertq105.mod $\theta_0 = 20.0$ $f_{IM} = 0.0000$
 $\sigma_{MOD}^2(\log)$: Vertical= 0.385E-01 Total= 0.776E-01
Variance Reduction (HHS): Vertical= 78.4% Total= 74.5%

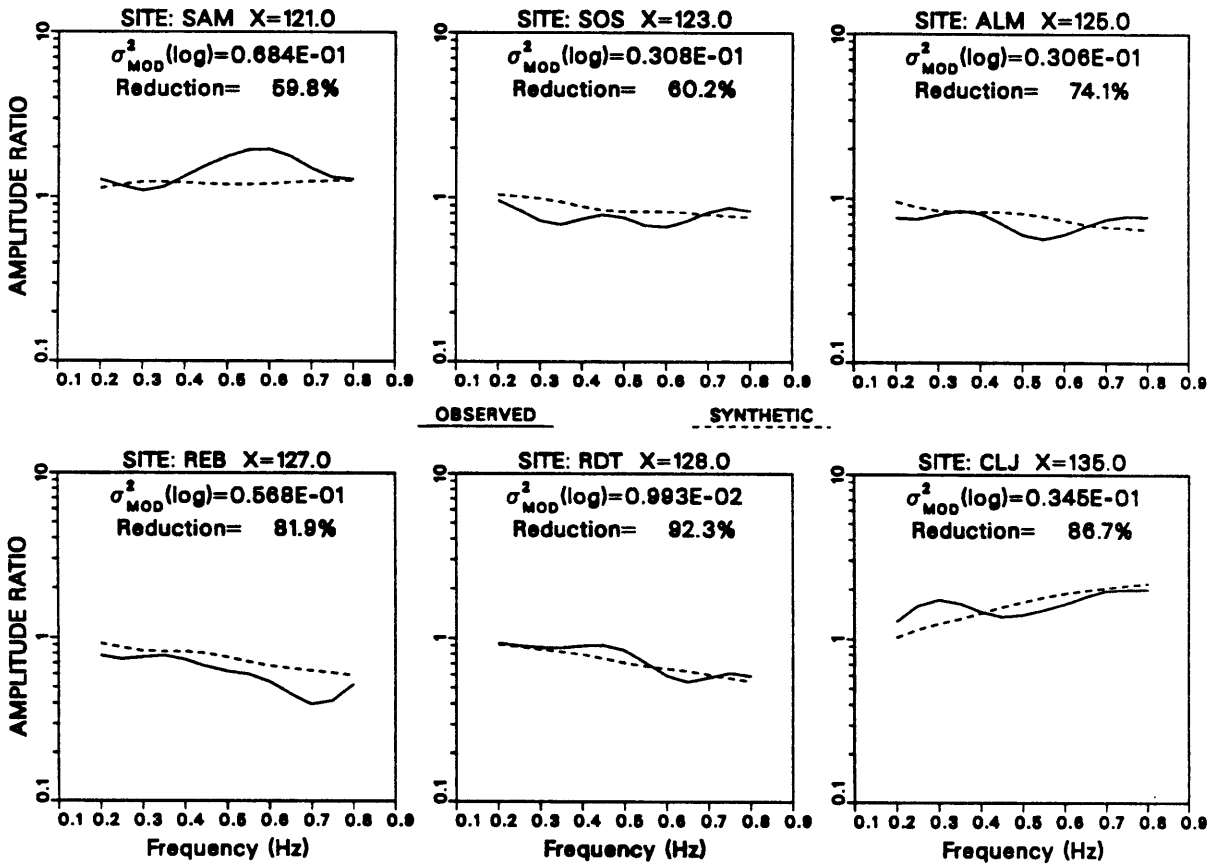


Figure 5.13a Vertical synthetic spectral ratios for best model with $Q = 5$ in the upper caldera fill, compared with the Kuril Islands data.

HORIZONTAL COMPONENT SPECTRAL RATIOS
OBSERVED: KURIL ISLANDS (4 EVENTS) recorded in VALLES CALDERA
SYNTHETIC: model= pertq105.mod $\theta_0= 20.0$ $f_{IM}= 0.0000$
 $\sigma_{MOD}^2(\log)$: Horizontal= 0.117E+00 Total= 0.778E-01
Variance Reduction (HHS): Horizontal= 72.9% Total= 74.5%

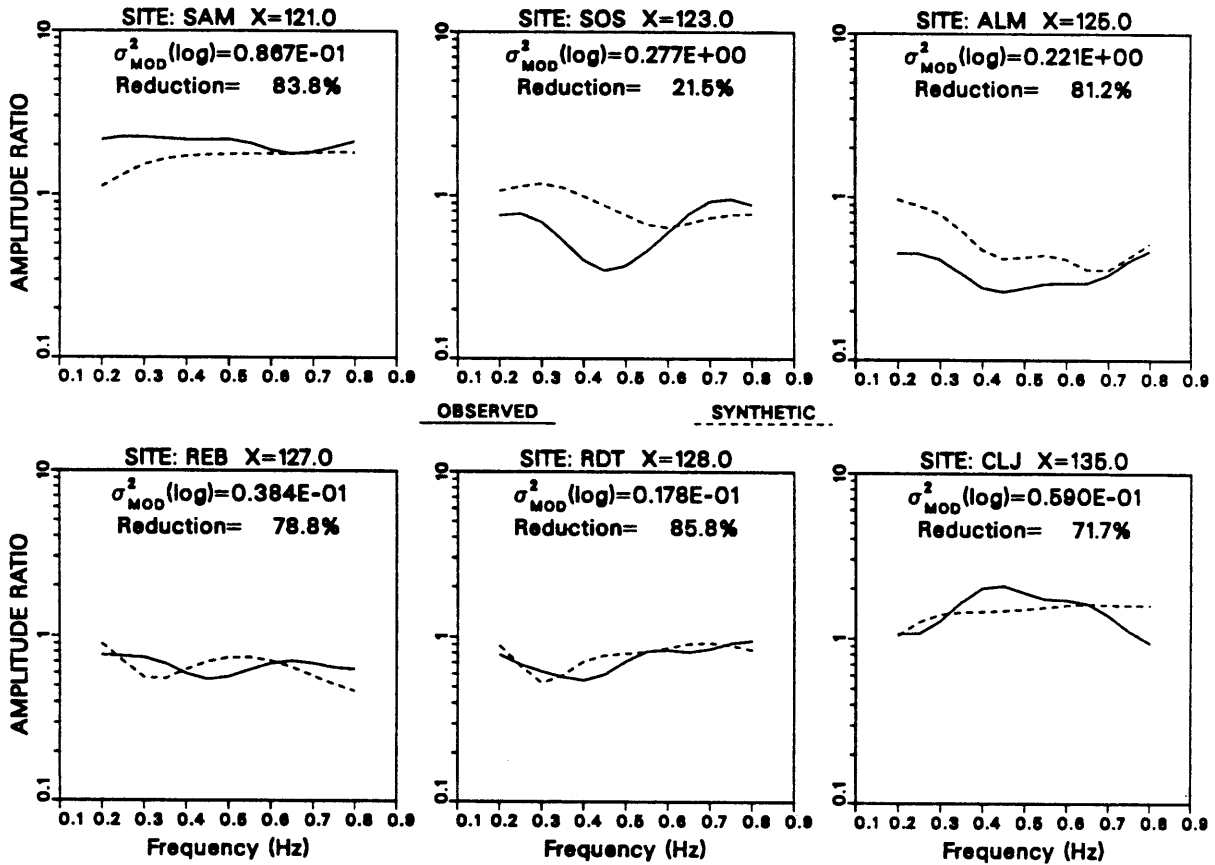


Figure 5.13b Same as Figure 5.13a except the horizontal components are shown.

VERTICAL COMPONENT SPECTRAL RATIOS
OBSERVED: KURIL ISLANDS (4 EVENTS) recorded in VALLES CALDERA
SYNTHETIC: model= pertq101.mod $\theta_0 = 20.0$ $f_{IM} = 0.0000$
 $\sigma_{MOD}^2(\log)$: Vertical= 0.584E-01 Total= 0.208E+00
Variance Reduction (HHS): Vertical= 67.2% Total= 31.6%

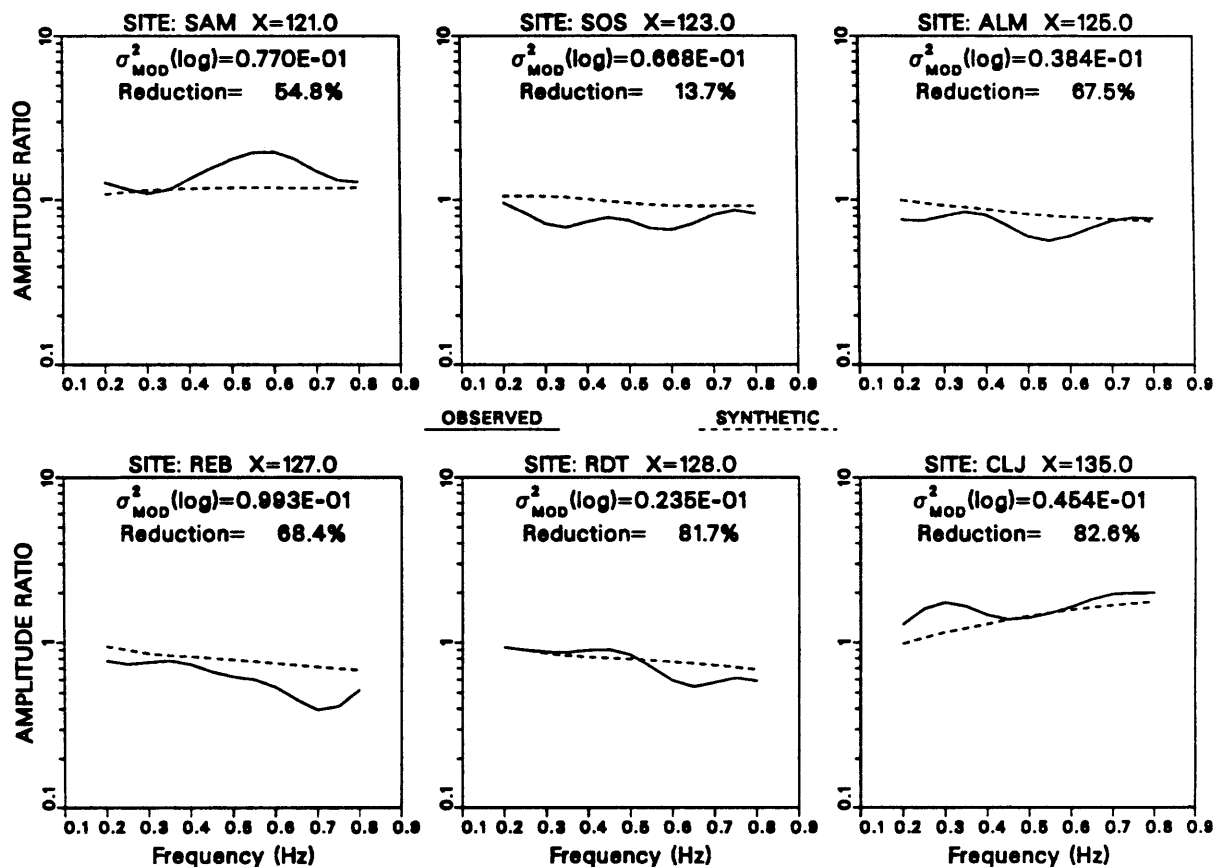


Figure 5.14a Vertical synthetic spectral ratios for best model with $Q = 1$ in the upper caldera fill, compared with the Kuril Islands data.

HORIZONTAL COMPONENT SPECTRAL RATIOS
OBSERVED: KURIL ISLANDS (4 EVENTS) recorded in VALLES CALDERA
SYNTHETIC: model= pertq101.mod $\theta_0 = 20.0$ $f_{IM} = 0.0000$
 $\sigma_{MOD}^2(\log)$: Horizontal= 0.357E+00 Total= 0.208E+00
Variance Reduction (HHS): Horizontal= 16.9% Total= 31.6%

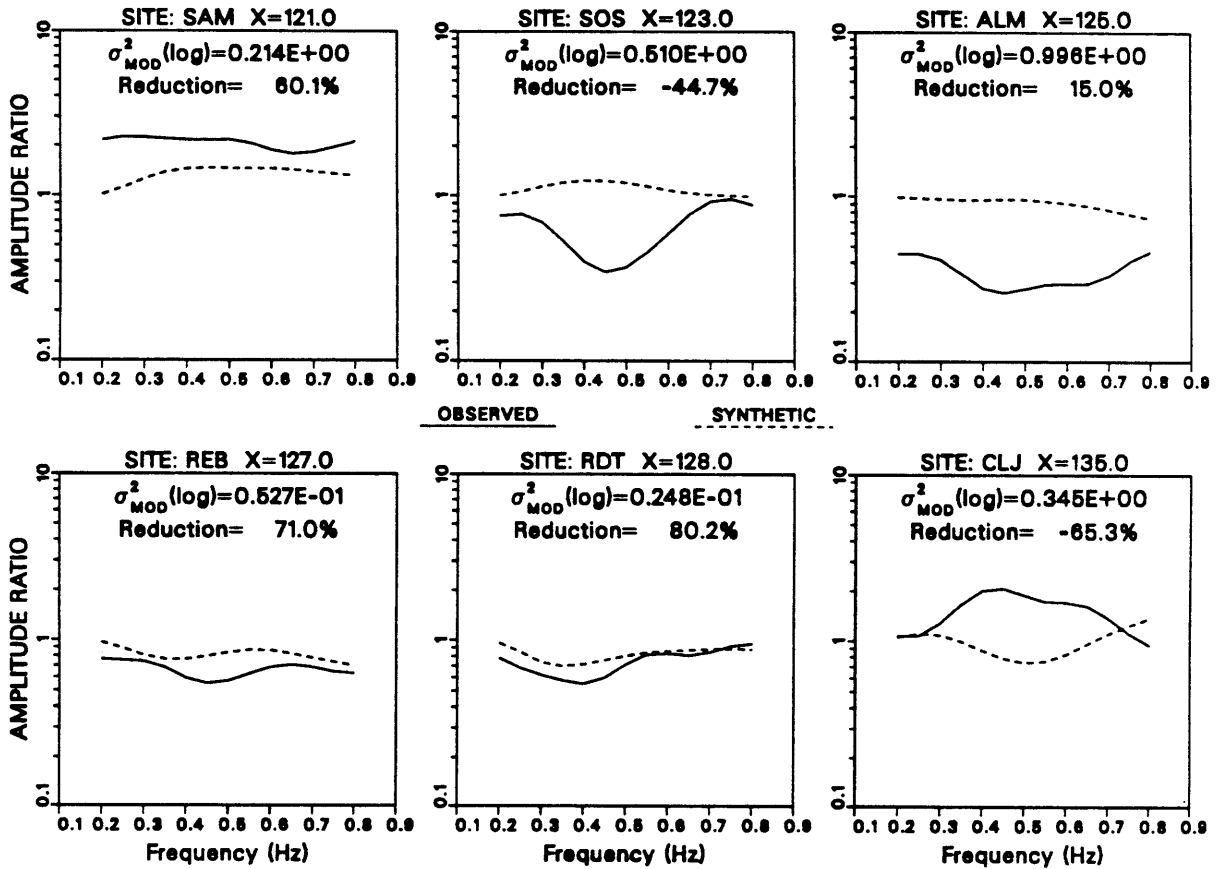


Figure 5.14b Same as Figure 5.14a except the horizontal components are shown.

is completely controlled by the LQZ. As a lower bound we can say that Q in the upper caldera fill cannot be significantly lower than 10, as evidenced by Figures 5.13 and 5.14.

One final test will help emphasize the importance of the localized low Q zone as well as the need to include the upper caldera fill as well. In Figures 5.15a,b we show the results for a model containing only the LQZ and free surface topography of Figure 5.1, with the upper caldera fill layer removed. Here we can see that the major attenuating effect of the LQZ is still dominant, with the low caldera amplitudes reasonably well represented. However, the variance reduction is considerably lower than for the best model, due to the absence of the upper surface layer. This is a very simple demonstration that the structural components shown in Figure 5.1 represent the minimum requirements for reproducing the major features of the amplitude data.

The remaining model parameters are numerous and, in general, less critical than those comprising the basic Q structure discussed above. However, the attenuation effects are dependent on wavelength, and the wavelength for a given frequency is determined by the velocity structure. The various dimensions of the structural components, particularly of the LQZ, will also influence the degree of attenuation observed. For instance, one might expect to obtain similar results with higher Q by either decreasing the velocities or increasing the size of the LQZ. An exhaustive study of all possible alternative models is clearly impossible with a forward modeling approach. Instead it should suffice for our purposes to examine the effects of perturbing model parameters one at a time. Rather than show spectral ratio plots

VERTICAL COMPONENT SPECTRAL RATIOS
OBSERVED: KURIL ISLANDS (4 EVENTS) recorded in VALLES CALDERA
SYNTHETIC: model= lqzq001.mod $\theta_0 = 20.0$ $f_{IM} = 0.0000$
 $\sigma_{MOD}^2(\log)$: Vertical= 0.472E-01 Total= 0.100E+00
Variance Reduction (HHS): Vertical= 73.5% Total= 67.0%

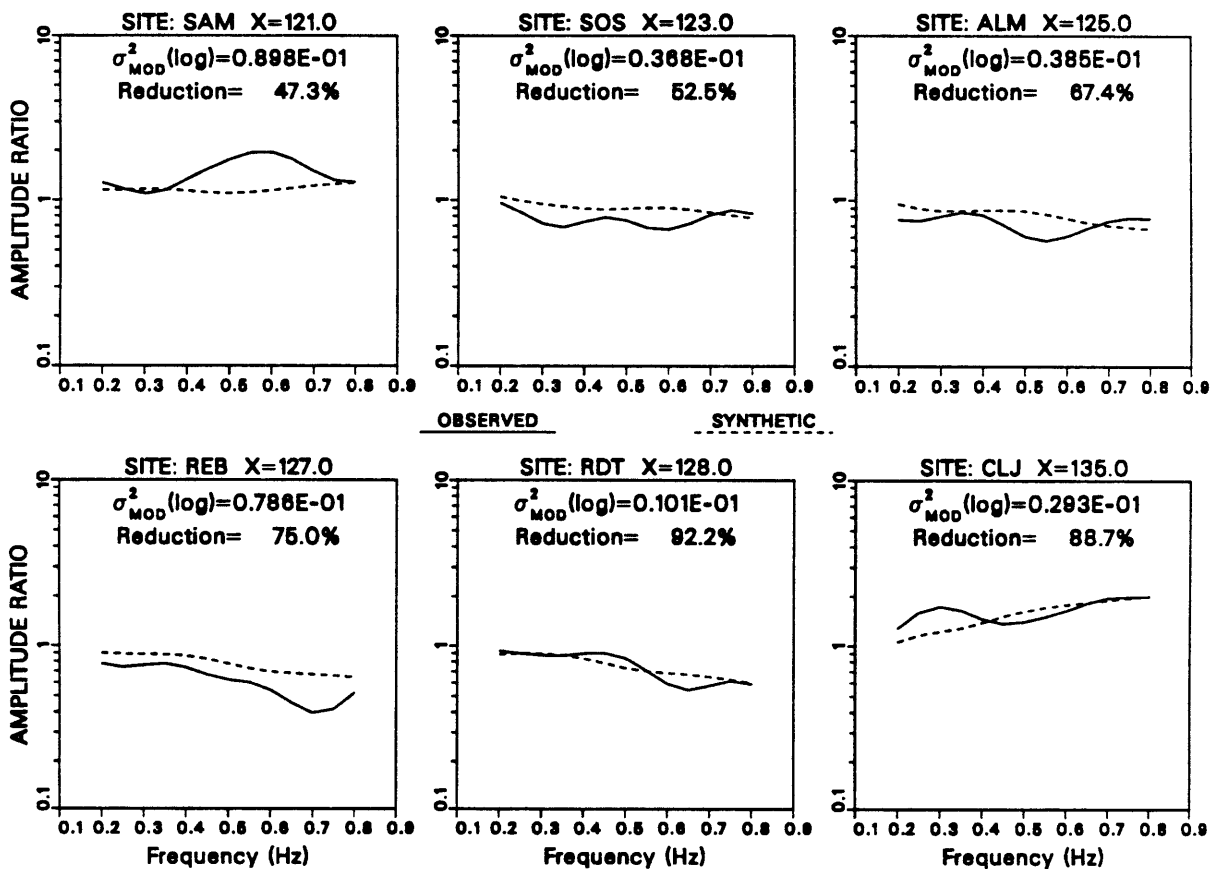


Figure 5.15a Vertical synthetic spectral ratios for the best model with the upper caldera fill removed, compared with the Kuril Islands data.

HORIZONTAL COMPONENT SPECTRAL RATIOS
OBSERVED: KURIL ISLANDS (4 EVENTS) recorded in VALLES CALDERA
SYNTHETIC: model= lqzq001.mod $\theta_0 = 20.0$ $f_{IM} = 0.0000$
 $\sigma_{MOD}^2(\log)$: Horizontal= 0.154E+00 Total= 0.100E+00
Variance Reduction (HHS): Horizontal= 64.2% Total= 67.0%

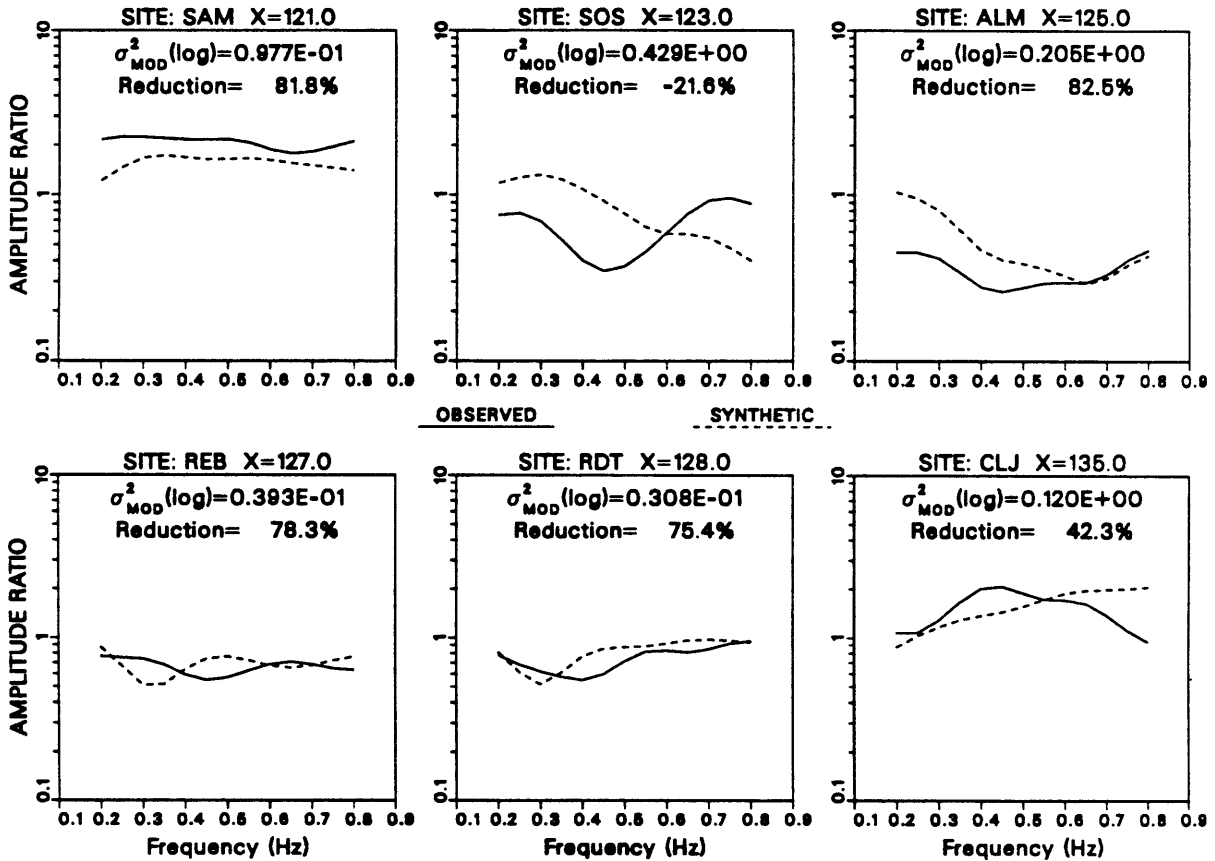


Figure 5.15b Same as Figure 5.15a except the horizontal components are shown.

for all of these tests, we have instead simply listed the variance reduction for the vertical, horizontal and combined data for each perturbed model.

The perturbations for α , β , ρ and Q are listed in Table 5.2 for a number of test models, including the Q tests presented above. The table lists identifying model name codes along with the appropriate parameters for the LQZ and the upper caldera fill perturbed in each case. We have held the elastic parameters for the granite basement (layers 2 and 4) constant in all cases because these are well determined by previous studies in the area. The best model is listed at the top of the table, and dashes shown for the test models indicate parameters which were not perturbed. The last 8 test models listed represent various perturbations to the height and depth of the LQZ and maximum depth of the upper caldera fill relative to the zero datum. These structural changes are shown in Figures 5.16a,b and the model name shown above each plot coincides with that listed in Table 5.2. In most cases the velocities and density in each medium have been perturbed by $\pm 10\%$. The changes to the structural dimensions were ± 0.5 km. We show 10% here as the minimum velocity and density perturbation in most cases because this was roughly the value at which we first started to see significant increase in the variance, based on numerous similar tests using perturbations as low as $\pm 1\%$. Similarly, the dimensional changes of ± 0.5 km correspond to perturbations below which no significant changes in the results occurred.

The vertical, horizontal and total variance reduction obtained for each of the models are listed in the three right-hand columns of Table 5.2. Notice first that all perturbed models give smaller variance reduction than the best model. For nearly all of the elastic parameter perturbations listed, the decrease in variance reduction is

TABLE 5.2
Best LQZ Model Parameter Perturbations and Resulting Variance Reduction

Model	Upper Caldera Fill					Low Q Zone						Variance Reduction(%)		
	α	β	ρ	Q	Depth	α	β	ρ	Q	Depth	Height	Vert	Horiz	Total
BEST	4.50	2.50	1.70	100	1.5	3.00	1.29	2.00	1	0.0	4.0	+80.7	+85.4	+84.0
Q302	-	-	-	-	-	-	-	-	2	-	-	+64.9	+66.2	+65.8
Q305	-	-	-	-	-	-	-	-	5	-	-	+13.8	+24.3	+21.3
Q310	-	-	-	-	-	-	-	-	10	-	-	-48.8	+18.2	-1.4
Q3100	-	-	-	-	-	-	-	-	100	-	-	-80.6	+12.9	-14.5
Q101	-	-	-	1	-	-	-	-	-	-	-	+67.2	+16.9	+31.6
Q105	-	-	-	5	-	-	-	-	-	-	-	+78.4	+72.9	+74.5
Q110	-	-	-	10	-	-	-	-	-	-	-	+79.0	+81.6	+80.8
Q120	-	-	-	20	-	-	-	-	-	-	-	+78.4	+82.0	+81.0
Q150	-	-	-	50	-	-	-	-	-	-	-	+77.0	+82.1	+80.6
Q11000	-	-	-	1000	-	-	-	-	-	-	-	+76.8	+85.3	+82.8
RO1M10	-	-	1.53	-	-	-	-	-	-	-	-	+79.0	+80.3	+79.9
RO1P10	-	-	1.87	-	-	-	-	-	-	-	-	+78.7	+79.9	+79.6
RO3M10	-	-	-	-	-	-	-	1.80	-	-	-	+78.0	+79.8	+79.3
RO3P10	-	-	-	-	-	-	-	2.20	-	-	-	+79.5	+80.3	+80.1
VP1M10	4.05	-	-	-	-	-	-	-	-	-	-	+77.9	+75.4	+76.1
VP1M20	3.60	-	-	-	-	-	-	-	-	-	-	+73.0	+43.3	+52.0
VP1P10	4.95	-	-	-	-	-	-	-	-	-	-	+78.6	+77.8	+78.1
VP3M10	-	-	-	-	-	2.70	-	-	-	-	-	+78.5	+76.8	+77.3
VP3P10	-	-	-	-	-	3.30	-	-	-	-	-	+79.3	+78.7	+78.9
VS1M10	-	2.25	-	-	-	-	-	-	-	-	-	+77.7	+78.8	+78.5
VS1P10	-	2.75	-	-	-	-	-	-	-	-	-	+78.0	+72.7	+74.3
VS3M10	-	-	-	-	-	-	1.16	-	-	-	-	+78.5	+79.1	+78.9
VS3P10	-	-	-	-	-	-	1.42	-	-	-	-	+79.5	+75.5	+76.7
NOCONT1	-	-	-	-	-	4.50	2.50	1.70	-	-	-	+79.1	+64.5	68.8
NOCONT3	3.00	1.29	2.00	-	-	-	-	-	-	-	-	+49.2	+27.2	+33.6
LOCONT3	-	-	-	-	-	3.50	2.00	-	-	-	-	+79.7	+68.2	+71.8
LOQHIV3	3.50	2.00	-	-	-	4.00	2.25	-	-	-	-	+58.6	+56.5	+57.1
SWAPALL13	3.00	1.29	2.00	-	-	4.50	2.50	1.70	-	-	-	+31.9	+15.6	+20.4
SWAPRO13	-	-	2.00	-	-	-	-	1.70	-	-	-	+76.0	+76.3	+76.2
MHM05	-	-	-	-	-	-	-	-	-	-	3.5	+77.4	+80.1	+79.3
MHP05	-	-	-	-	-	-	-	-	-	-	4.5	+73.7	+81.2	+79.0
MD05	-	-	-	-	-	-	-	-	-	0.5	-	+81.0	+73.9	+75.9
MCD05	-	-	-	-	2.0	-	-	-	-	0.5	-	+77.1	+63.2	+67.3
MD05HP05	-	-	-	-	-	-	-	-	-	0.5	4.5	+78.8	+78.1	+78.3
MD05HM05	-	-	-	-	-	-	-	-	-	0.5	3.5	+80.8	+79.3	+79.7
MCD05HP05	-	-	-	-	2.0	-	-	-	-	0.5	4.5	+73.3	+74.7	+74.3
MCD05HM05	-	-	-	-	2.0	-	-	-	-	0.5	3.5	+75.0	+72.9	+73.5

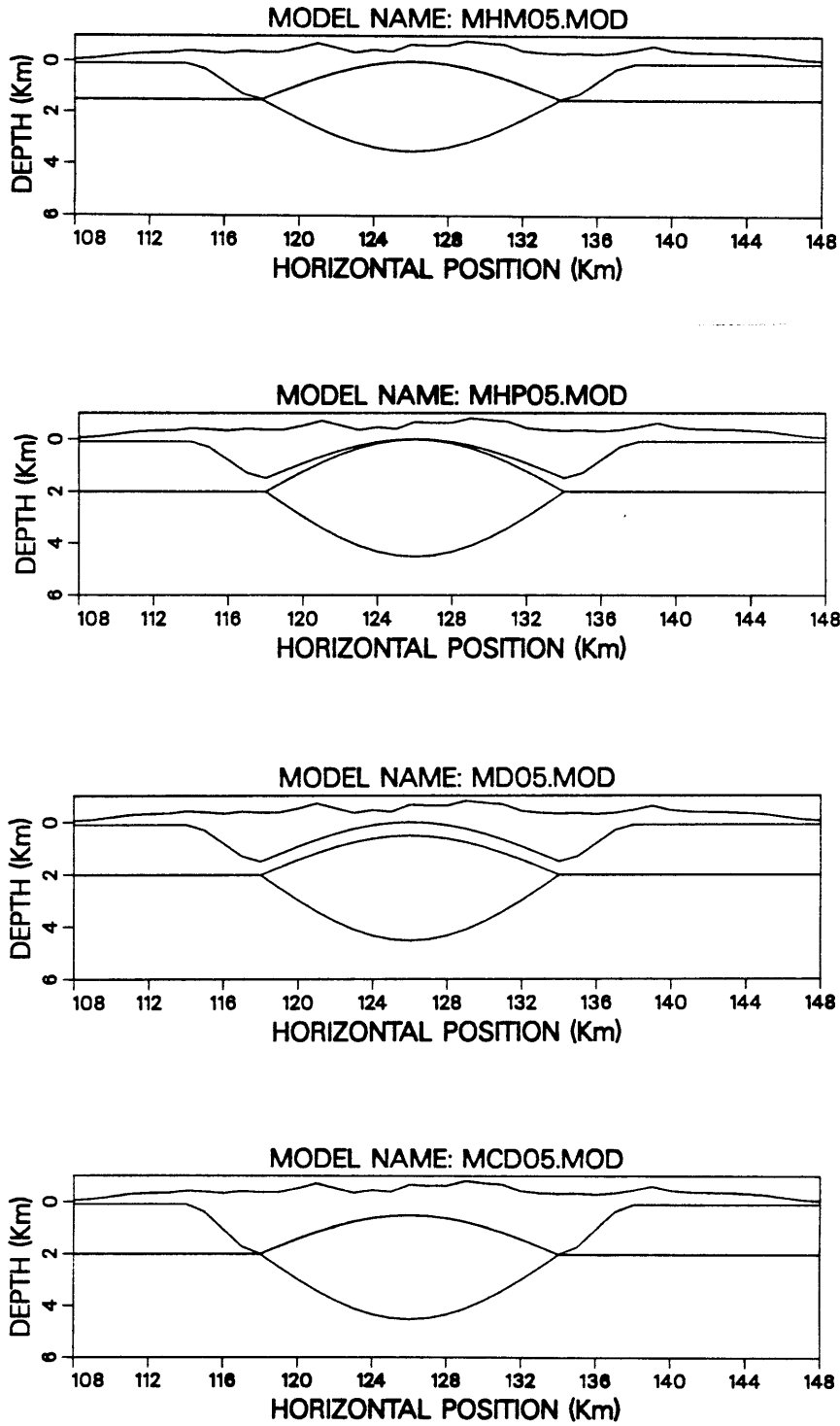


Figure 5.16a Four of the eight structural perturbations to the best model listed at the bottom of Table 5.2. The model names at the top of each plot are cross-referenced to the listings in the table.

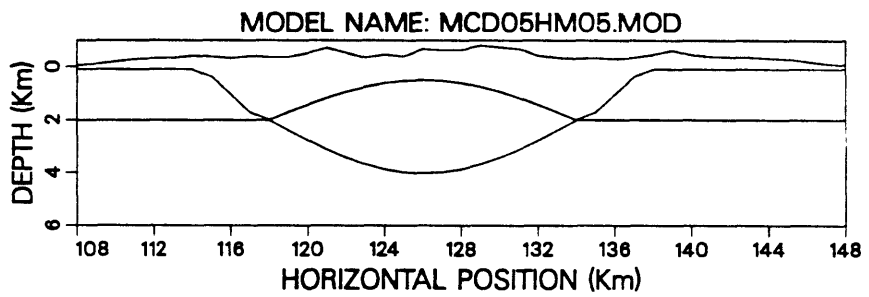
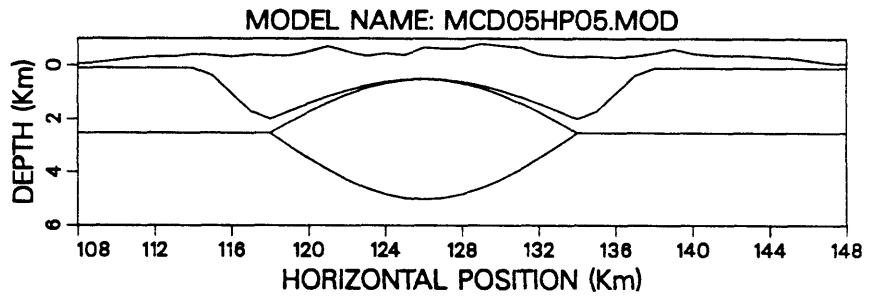
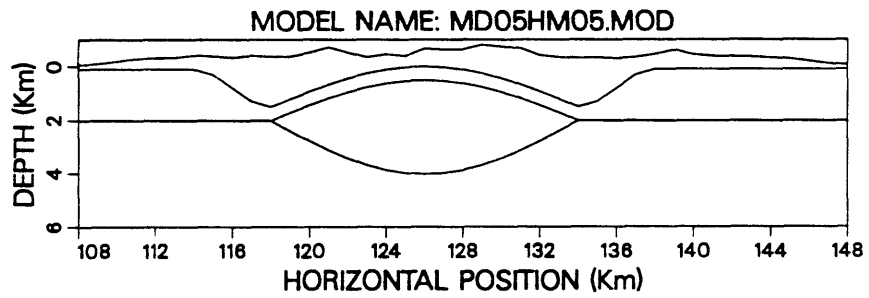
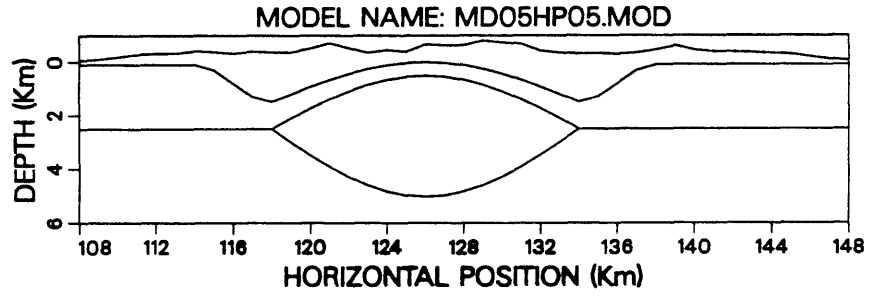


Figure 5.16b Remaining four structural perturbations tested and listed in Table 5.2.

about 5% or less. The reduction becomes worse when the parameters are perturbed by more than $\pm 10\%$. The listing for the test model "VP1M20" is a typical example of this. In this case the P-wave velocity in the upper caldera fill was decreased by 20%, and this resulted in a total variance reduction of 52%, which is much worse than for the best model or for the same parameter decreased by only 10%. This same behavior was found to hold for all α , β and ρ in both the LQZ and the upper caldera fill. Similarly for the dimensional perturbations, the depth and height of the LQZ can vary by as much as 500 meters before the total variance reduction drops below about 80%. Thus in terms of individual parameter perturbations we can only determine α , β and ρ to within about $\pm 10\%$ and structural dimensions and depth of the LQZ within ± 500 meters. The previous discussion on Q perturbations indicates that in the LQZ Q must be less than 5 and probably less than 2. We can set no upper bound on Q in the upper caldera fill but it cannot be much smaller than 10. We cannot justify quantifying the parameter limits with greater precision than discussed above, even though some parameters appear to be more stable than others. Our main purpose here is to demonstrate that the largest variance reduction is produced for models which fall within a roughly defined range of single perturbations to the model in Figure 5.1. Perturbations in all α , β and ρ by as much as 20%, or in geometry by as much as 1 km, produce significantly worse results than perturbations of 10% or 500 meters do. But within this range, only rarely does the variance reduction drop below about 75%. This stability is due mainly to the dominant attenuating effect of the LQZ. To greatly alter this effect requires a fairly large change to any particular parameter individually.

On the other hand, we can make some general statements regarding the effects of some simple multiple-parameter changes. We have listed in Table 5.2 six test models in which major changes were made to more than one elastic parameter. These include reducing the velocity and density contrast between the LQZ and upper caldera fill (“LOCONT3”), having no contrast (“NOCONT1” and “NOCONT3”), interchanging their densities (“SWAPRO13”) and allowing the LQZ to assume higher velocities than in the upper caldera fill (“LOQH1V3” and “SWAPALL13”). For all of the velocity changes the variance reduction is significantly smaller than for any of the single perturbations, and we conclude again that the LQZ must have much lower α and β relative to its surroundings. Although the interchanging of densities does not produce as drastic an effect, the decrease is significant enough that higher density appears to be favored in the LQZ than in the upper caldera fill. So, although we cannot completely quantify the uniqueness of the best model, its general characteristics are reasonably well constrained by the amplitude data.

5.4 Implications of 3-dimensional Structure

We have been concerned throughout this thesis with the validity of the 2-dimensional representation of the caldera sub-structure. In Chapter 2 we discussed how the existence at the caldera sites of large-amplitude transverse components, relative to the P wave, is a clear indication that the data contain significant effects of 3-dimensional structure. Apparently, the complexity of this structure decreases away from the caldera, as evidenced by the near absence of transverse motion at CAC. In this section we will summarize the major points of our study which lend

support to the 2-dimensional results and we will provide some additional evidence by testing the model's capability to fit the earliest portion of the vertical component seismograms for the direct P wave.

In summary then, we list the following major points in support of the validity of the 2-D modeling. 1.) The data were recorded on linear arrays, and the events used lay nearly on-azimuth to the array line and arrived with fairly steep incidence angles. 2.) The major pattern of amplitude variations across the line to first order does not depend on incidence angle or source direction and is very similar for all 3 components of motion. 3.) We are modeling only the relative variations in amplitude for one component at a time and we are not attempting to explain the differences between the vertical and horizontal component, which should be due largely to resonance and scattering, and could contain strong 3-D effects. 4.) The observed effect of low amplitudes inside the caldera can be explained by strong attenuating properties which need vary only with horizontal position along the array and can roughly be explained also by the simple 1-D calculation presented in section 5.1. 5.) We have restricted the modeling to amplitude data since the observed phase spectra were extremely complex and may be more sensitive than amplitude to 3-D irregularities.

The portion of the observed teleseismic data which should be most free of 3-D effects is the vertical component of the direct P wave. This is because, for on-azimuth events, scattered energy generated at points away from the 2-D model plane will arrive at the sites later than the strictly in-plane contributions. The first pulse of a seismogram should be nearly devoid of 3-D effects since it arrives the earliest. So to further test the validity of our best model for purely 2-dimensional data, we first chose one of the 4 Kuril Islands events from array 2 which showed the clearest

and least complicated first arrivals and the Kommandorsky Islands event from array 1. We then computed the spectral ratios as before, but for just the first full-cycle of the direct P wave for the vertical component at each site. We then computed synthetic results for the best model as before, but using a very large value for the damping factor, ω_I , so that no scattered waves would contribute to the solution. We found that using $\omega_I = \pi$ (i.e., $f_I = 0.5$) gave the best results. This large damping factor also allowed us to calculate solutions up to 1.0 Hz since the previous problems mentioned for satisfying the vanishing surface traction boundary conditions at high frequencies were significantly alleviated when higher order scattered waves were damped out. This is fortunate because the P-wave spectra used were strongly peaked between 0.8 and 1.0 Hz. Synthetic vertical spectral ratios were calculated for 5 frequencies equally spaced from 0.8 to 1.0 Hz and compared with the observed P-wave ratios.

Figures 5.17a,b show the results of this test, which are quite encouraging. Figure 5.17a is for the array 2 Kuril event. The variance reduction of 88.7% is better than the 81% that we obtained previously for the complete vertical component seismograms. This is perhaps the strongest evidence presented so far in support of the 2-D model since we have effectively removed all 3-D effects from the data in this case. However, this example should not be substituted for the results obtained with the scattered waves. The frequency band used for the P wave is too narrow to have allowed us to determine the best model with these data alone. It was only through the examination of a wide range of relatively low frequencies that we were able eventually to zero in on the best model. The present example serves primarily as a convincing test of the 2-D assumption regarding the data.

VERTICAL COMPONENT SPECTRAL RATIOS
OBSERVED: KURIL ISLANDS (EVENT C) recorded in VALLES CALDERA)ARRAY 2)
SYNTHETIC: model= w161624h40d00lh.3lqgs3 $\theta_0 = 20.0$ $f_{IM} = 0.5000$
 $\sigma_{MOD}^2(\log)$: Vertical= 0.243E-01
Variance Reduction (HHS): Vertical= 88.7%

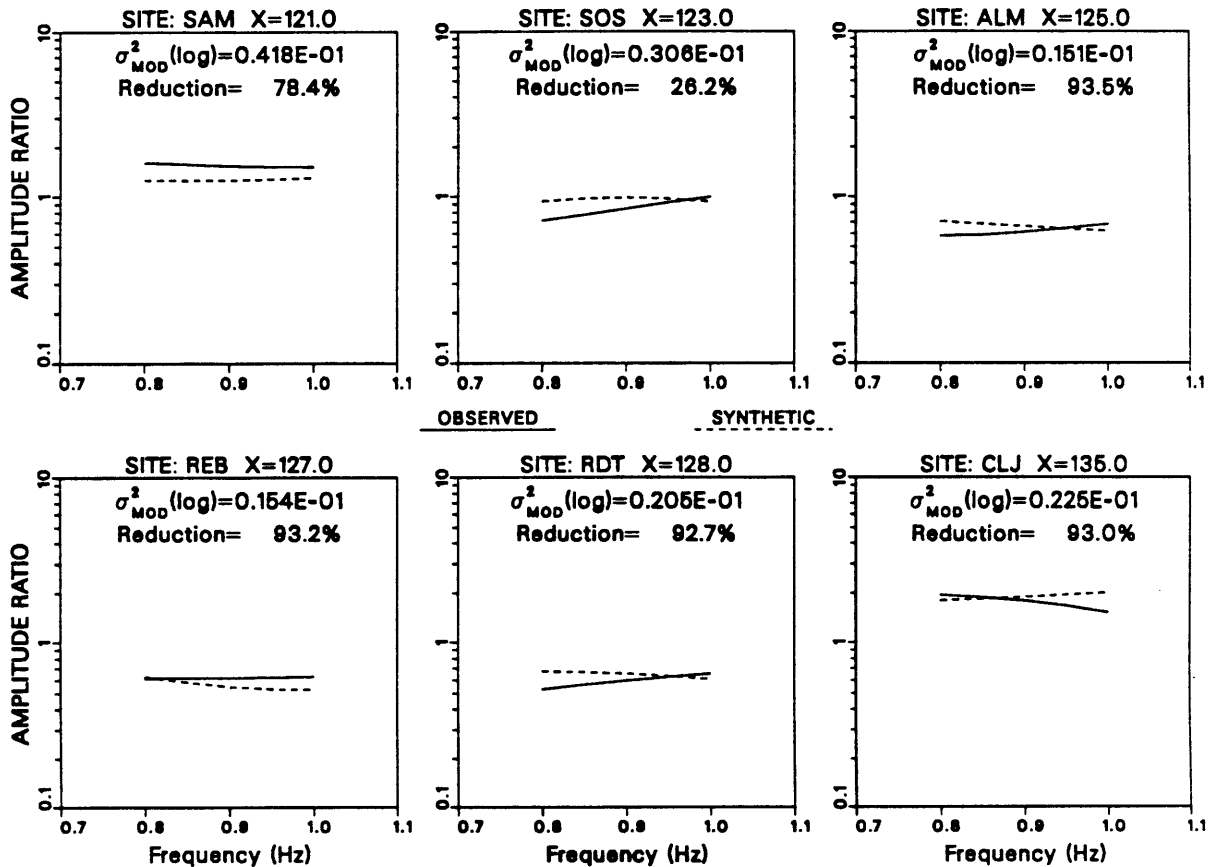


Figure 5.17a Vertical synthetic spectral ratios for the best model compared with observed ratios for the first cycle of the direct P-wave arrival from one of the Kuril Islands events recorded on array 2. The Aki-Larner results were obtained using a very large damping factor (complex frequency) in order to eliminate scattered waves from the solutions.

VERTICAL COMPONENT SPECTRAL RATIOS
OBSERVED: KOMMANDORSKY ISLANDS recorded in VALLES CALDERA (ARRAY 1)
SYNTHETIC: model= w161624h40d00lh.3lqgm3 $\theta_0 = 20.0$ $f_{IM} = 0.5000$
 $\sigma_{MOD}^2(\log)$: Vertical= 0.680E-01
Variance Reduction (HHS): Vertical= 63.0%

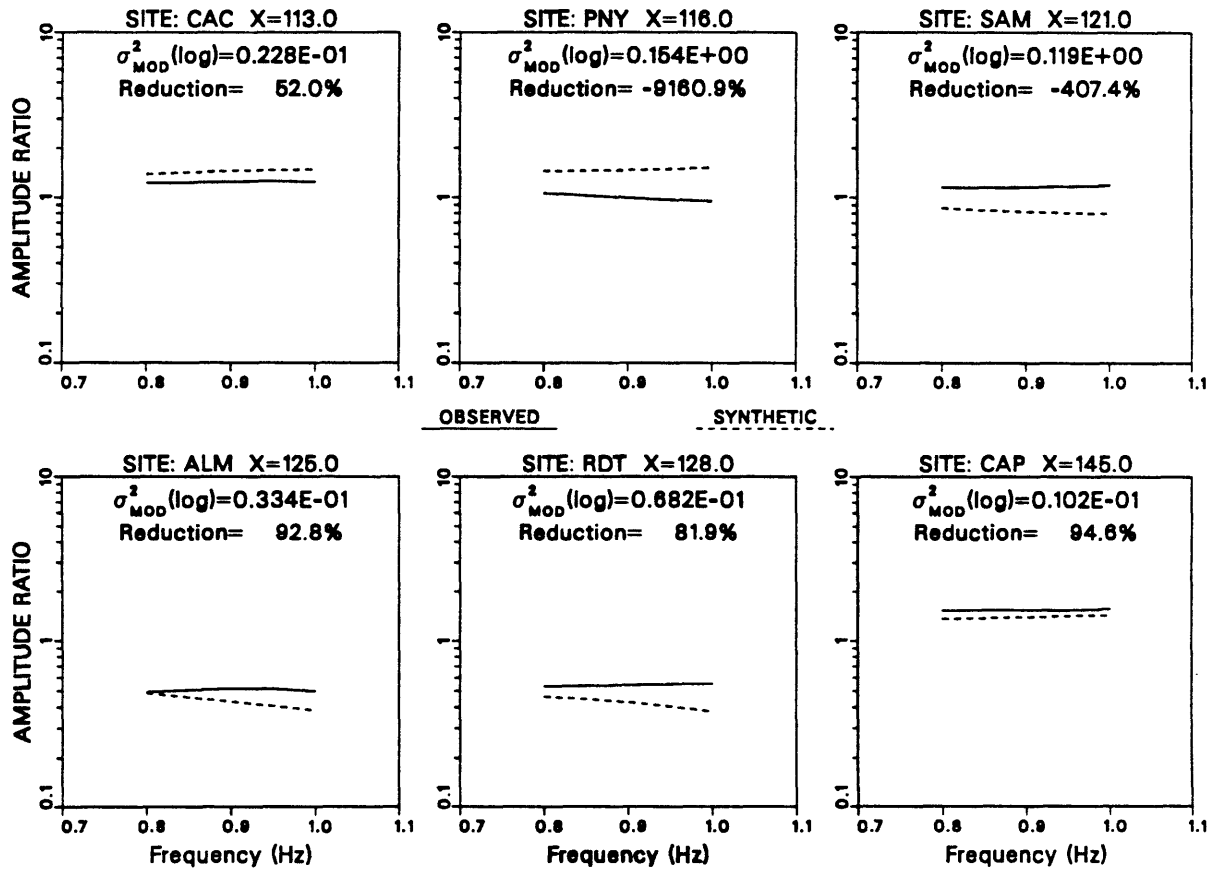


Figure 5.17b Same as Figure 5.17a, except that the synthetic solutions are compared with a Kommandorsky Islands event recorded on array 1.

Figure 5.17b shows the results for the array 1 Kommandorsky event. On this larger scale we can see that the low amplitudes of the first arrivals at ALM and RDT, relative to the those at CAC and CAP, are reproduced reasonably well by the LQZ model, with a variance reduction of 63%. The data at SAM and PNY are not reproduced well on the large scale, but the localized Q effect within the ring fracture still produces approximately the correct attenuation relative to the sites furthest from the caldera. So, although there are significant 3-D effects in our scattered-wave data, these are subsidiary to the dominant 2-D attenuation effect on the smaller scale of array 2. This also supports our assumption that the strength of scattering and resonance is similar at all array 2 sites. If this were not the case, the direct P-wave and scattered-wave amplitudes would not share the same amplitude behavior across the array. As we have seen, the array-1 data exhibit strong differences in the patterns of amplitude variation between the scattered waves and the direct P wave alone. As discussed previously, this is probably due to large-scale variations in 3-D structural complexity.

5.5 Resonance and Scattering Effects

The best fitting model presented in Figure 5.1 is the end result of almost two years of forward modeling efforts and literally thousands of CPU hours on a VAX 8650 computer. A rough estimate of the total number of individual models tested is in excess of 400. The vast majority of these initial tests were aimed at attempting to fit the Kuril Islands data by considering only resonance and scattering effects. This was a rather frustrating, albeit instructive, experience since it soon became apparent that these effects in 2-D are extremely sensitive to minor changes in model

parameters. The simplified 3-layered representation of the caldera structure requires 9 separate elastic parameters and virtually endless possibilities for the different components of the irregular structural geometry. Despite this complexity, one of our chief concerns was that the models would be too simplified to give a realistic or believable representation of the true structure, even if we did manage to fit the data eventually. We felt fortunate to have been able to find a relatively simple model which explains the data so well and which makes sense intuitively. It was not until we decided to try putting Q into our models that this became possible. The use of Q allowed us to reproduce observed amplitude patterns which exhibited a degree of stability, over a large range of frequencies and incidence angles, that could not be explained by resonance or scattering effects alone.

The reason we pursued the resonance study for so long is that this mechanism is capable of producing rather strong variations in amplitude for waves interacting with irregular structures. Resonance patterns in 2-D are significantly more complicated than for the 1-D case, and can produce very large amplification or de-amplification under certain conditions. These effects were studied in detail for a simple alluvial valley by *Bard & Bouchon* [1985]. The directionality of wavelength-dependent scattering effects is also capable of producing amplitude variations. Since the Aki-Larner method accounts for both of these effects and is particularly useful for studying sub-wavelength size structure, we felt it was an ideal choice for application to the Valles Caldera. The specific geometry and elastic parameters of the models should combine to produce resonance patterns which we had hoped could be modified to fit the observed data by adjusting the models. Guided by previous work in the caldera we began by constructing models which included free surface

topography, a low velocity inclusion and a simple bowl-shaped caldera fill layer. We wished to determine primarily whether or not the data could support the existence of a remnant magma chamber beneath the caldera.

Although we eventually did manage to obtain a model which fit the Kuril Islands data for a few frequencies, the results quickly fell apart when we attempted to use a broader frequency band and different incidence angles. In Figures 5.18a,b,c and 5.19a,b,c we have shown two very simple examples of how resonance and scattering effects can depend on frequency and incidence angle. Here we have computed synthetic spectral ratios for two models composed of free surface topography and a buried low velocity zone in a granite halfspace. The models used are plotted in Figures 5.18a and 5.19a. The only difference between these models is in the depth of the LVZ. Spectral ratios for 5 incidence angles were computed as before at six site locations relative to the average and these are shown plotted as different line styles in Figures 5.18b and 5.19b for the vertical components, and 5.18c and 5.19c for the horizontal. Incidence angles used were $\theta_0 = 0^\circ$ (vertical), $\pm 20^\circ$ and $\pm 30^\circ$ as indicated in the legend on the ratio plots.

Note the strongly peaked behavior versus frequency, particularly in the horizontal components for the shallow LVZ model, Figure 5.18c. Also note the strong dependence on incidence angle. For the vertical components there is a very clear reversal in the relative peaks and troughs at each site as the incidence angle changes from positive to negative values. For the horizontal components the primary effect of incidence angle is a change in relative amplitude of the various spectral peaks. This dominant behavior is clearly not supported by the observed data. Furthermore, none of the spectral peaks or troughs are large enough or small enough to

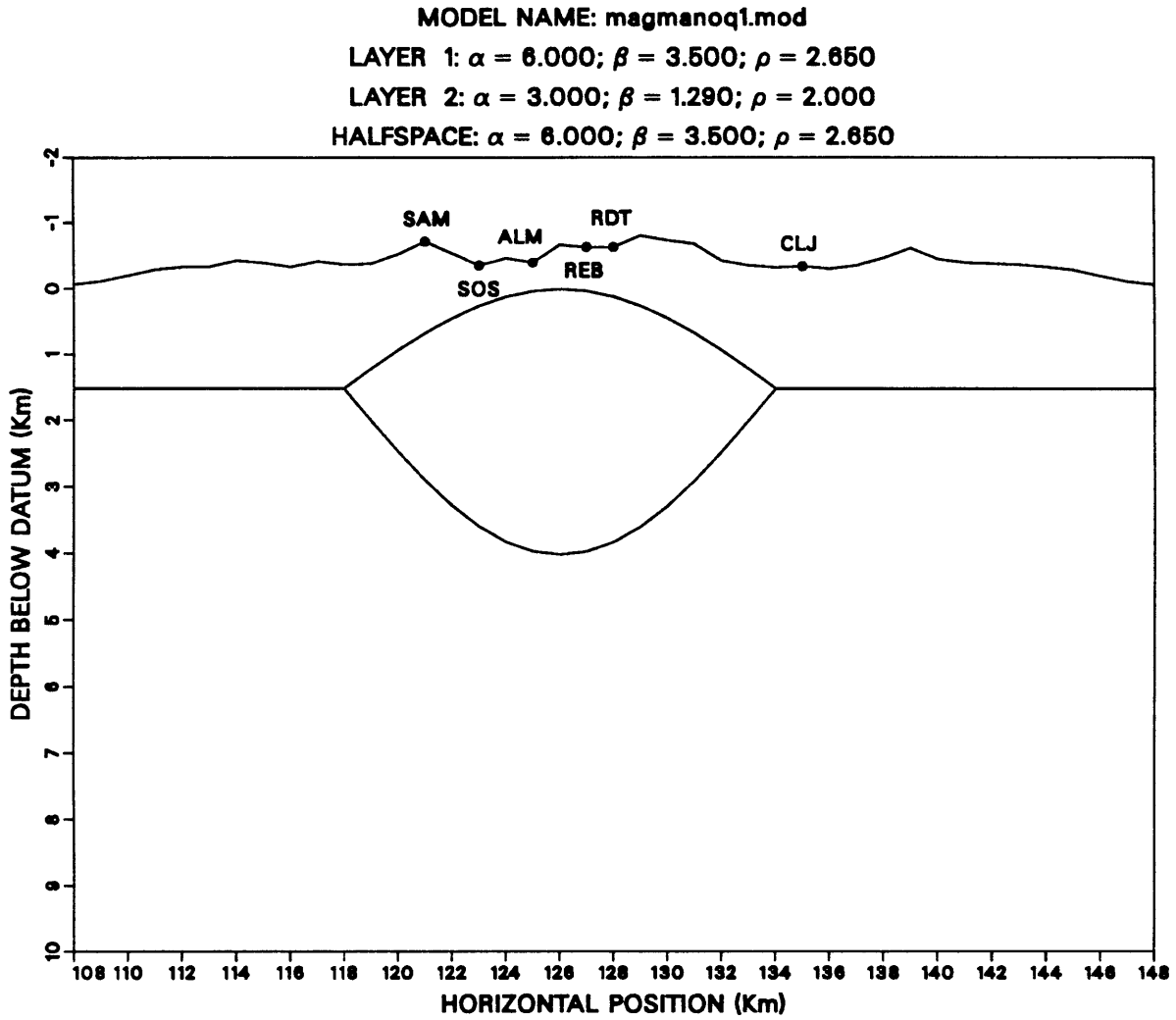


Figure 5.18a Test model for a non-attenuating low velocity inclusion used to demonstrate un-damped resonance and scattering effects.

VERTICAL COMPONENT SYNTHETIC SPECTRAL RATIOS

Model= magmanoq1.mod $f_{IM} = 0.0250$

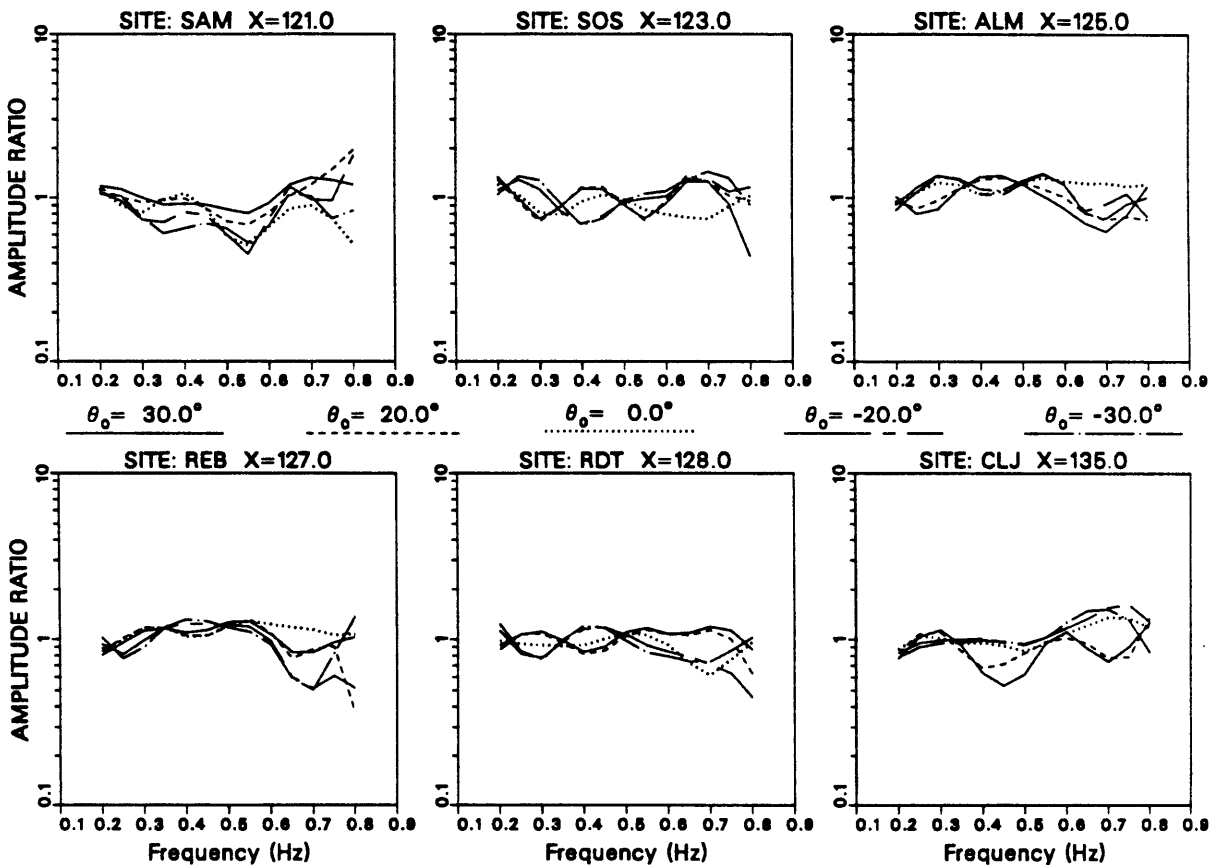


Figure 5.18b Vertical component synthetic spectral ratios for the model in Figure 5.18a. Solutions were calculated for 5 separate incidence angles and plotted in different line styles, as indicated in the legend.

HORIZONTAL COMPONENT SYNTHETIC SPECTRAL RATIOS

Model= magmanoq1.mod $f_{1M} = 0.0250$

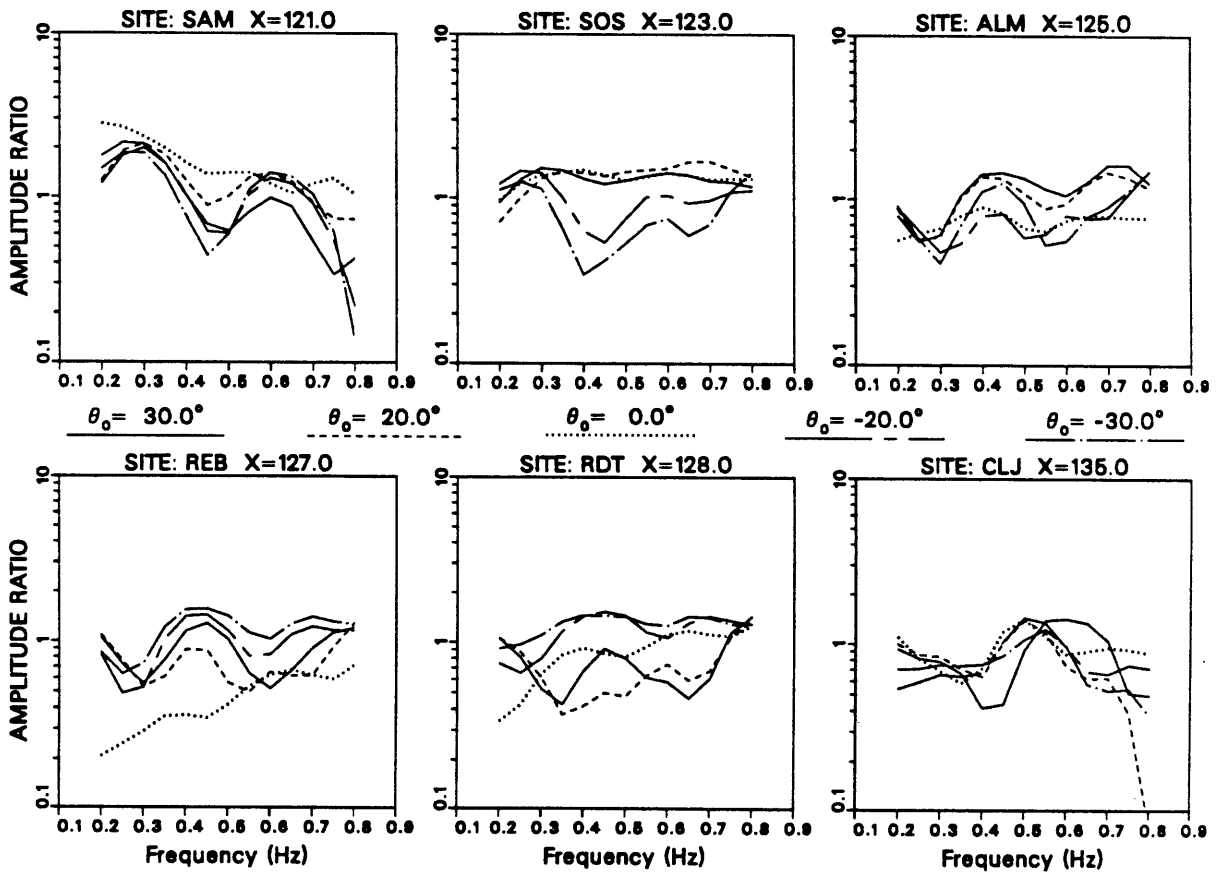


Figure 5.18c Same as Figure 5.18b except the horizontal components are shown.

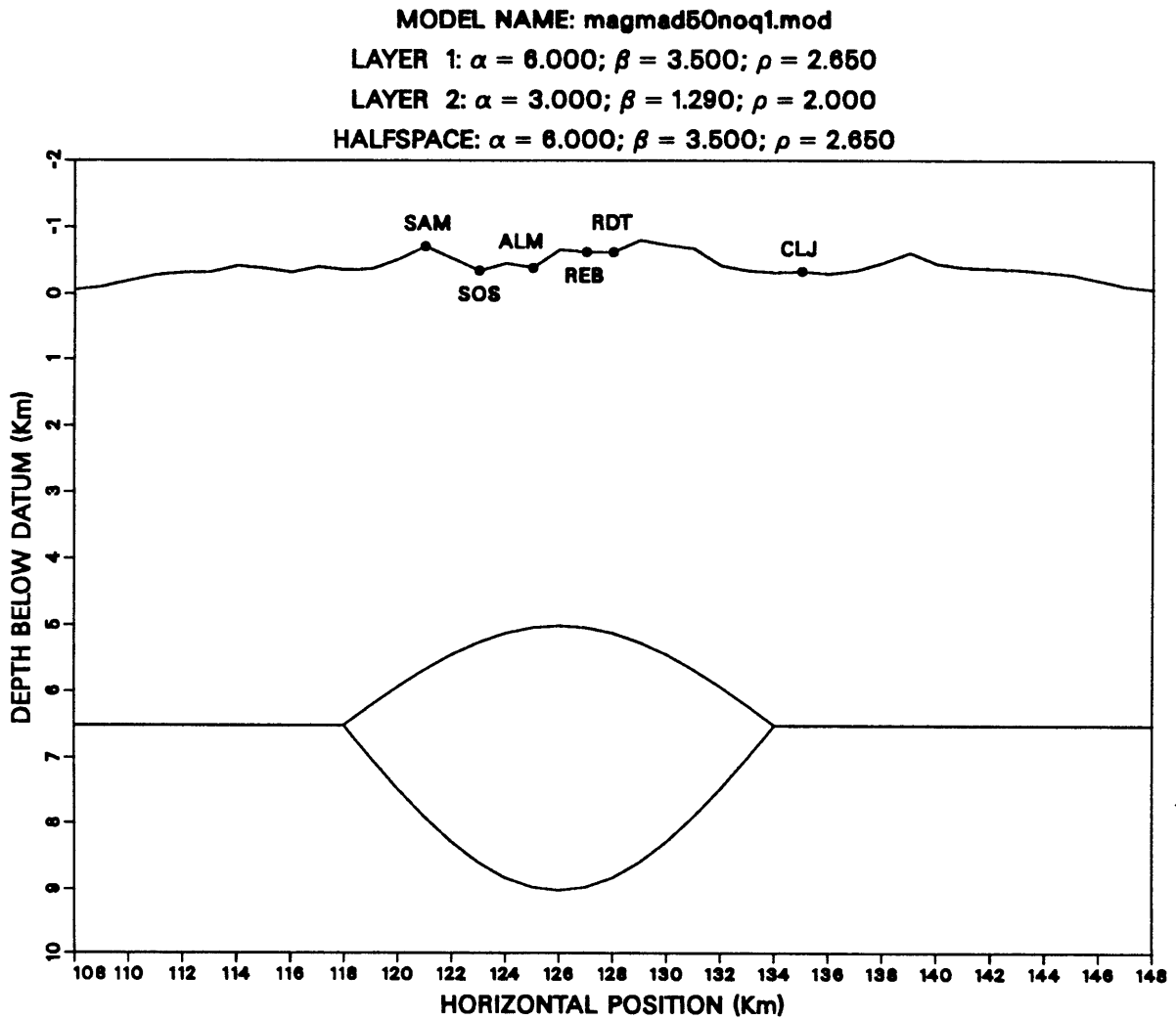


Figure 5.19a Another test model for a non-attenuating low velocity inclusion which is deeper than for the model in Figure 5.18a.

VERTICAL COMPONENT SYNTHETIC SPECTRAL RATIOS

Model= magmad50noq1.mod $f_{IM} = 0.0250$

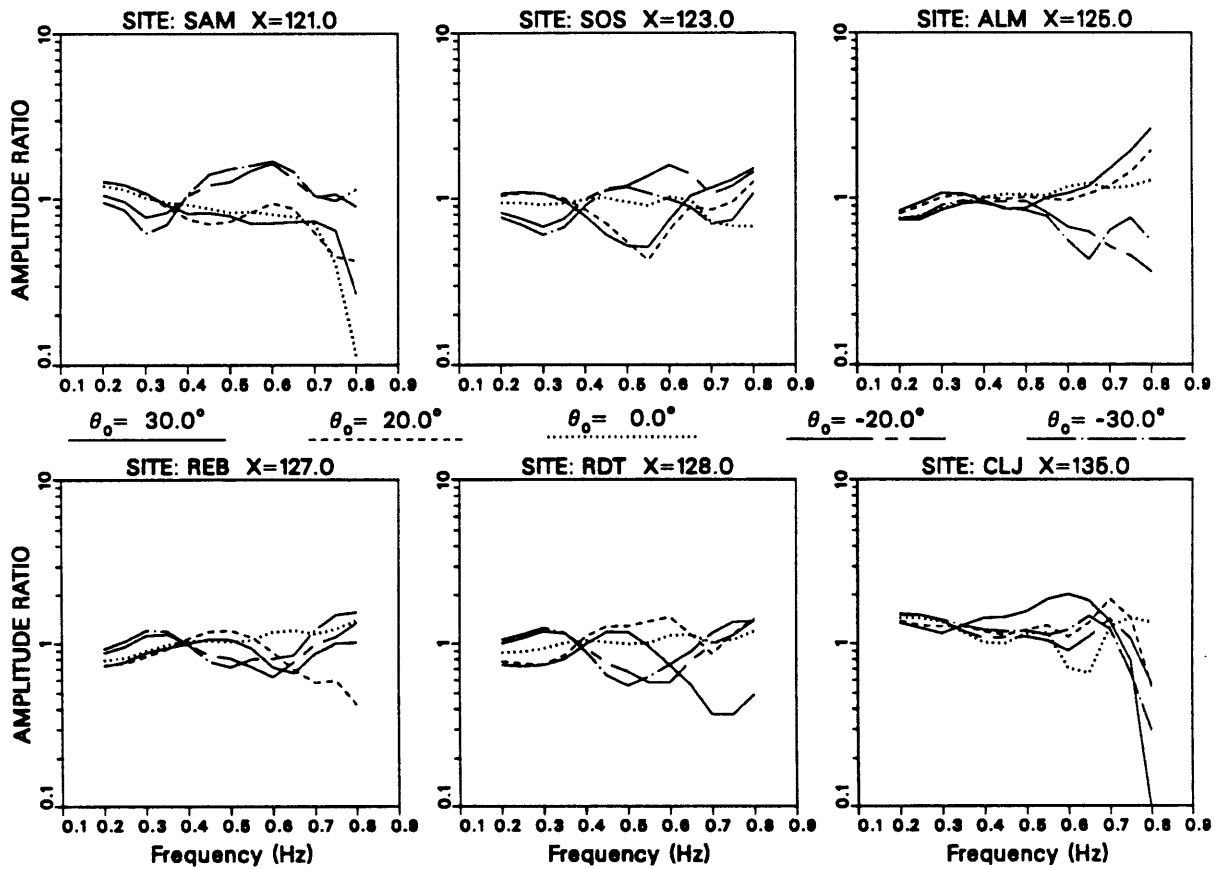


Figure 5.19b Vertical component synthetic spectral ratios for the model in Figure 5.19a. Solutions were calculated for 5 separate incidence angles and plotted in different line styles, as indicated in the legend.

HORIZONTAL COMPONENT SYNTHETIC SPECTRAL RATIOS

Model= magmad50noq1.mod $f_{IM} = 0.0250$

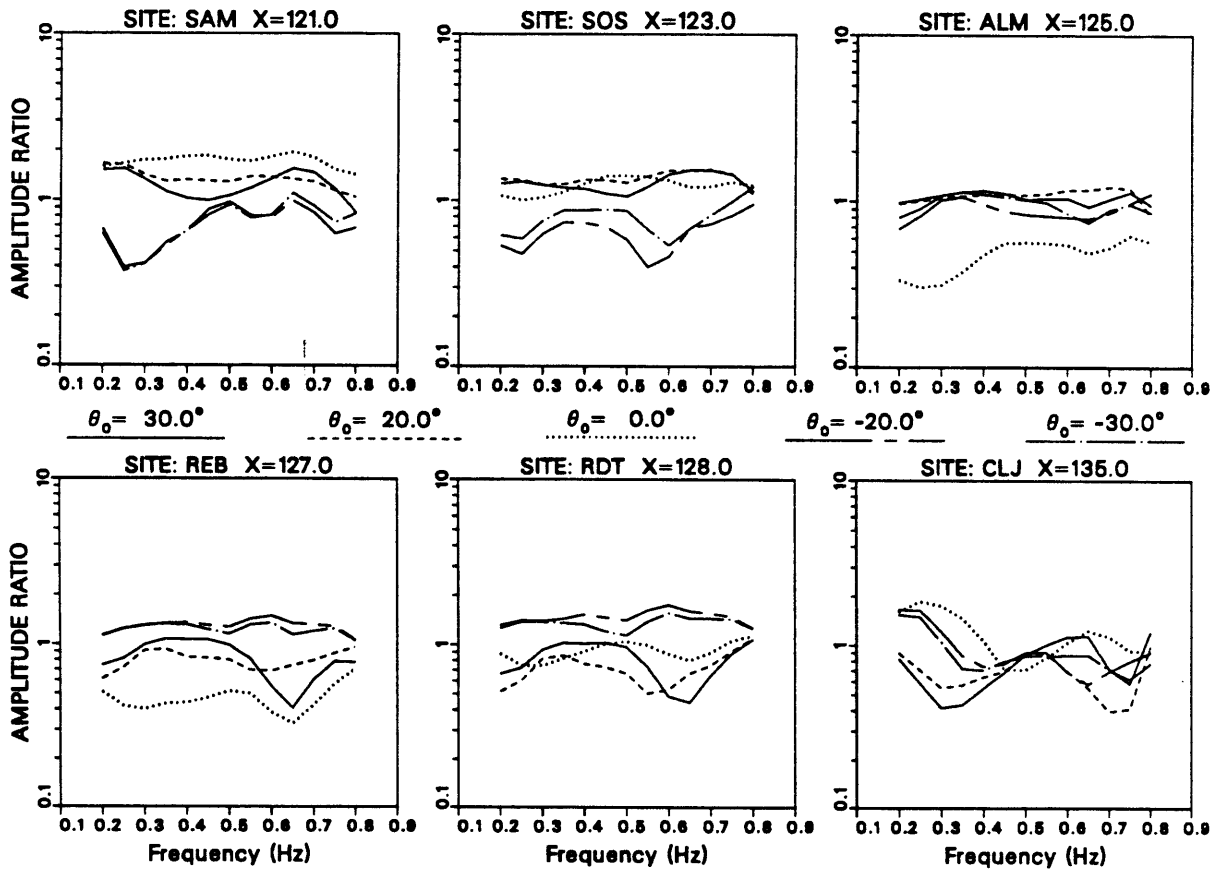


Figure 5.19c Same as Figure 5.19b except the horizontal components are shown.

match the maximum relative differences observed between some sites. Increasing the depth of the LVZ only makes matters worse because in Figures 5.19b,c we can see that this increases the variations in the vertical components.

When the upper caldera fill layer is added to the shallow LVZ model shown in Figure 5.18a, the resulting synthetics improve somewhat in that larger peaks and troughs are produced at some sites. This is how we were able to fit the Kuril Islands data for only a few frequencies. However, this addition to the models increased the complexity of the amplitude pattern so much that it became impossible to characterize any systematic relations between small changes in model parameters and the resulting changes in the spectral ratios. Changing the velocities or structural geometry by small amounts produced very unpredictable changes in the synthetics. This non-linear behavior can very easily reduce forward modeling to being little more than trial-and-error.

The shallow LVZ model shown here is nearly the same model we discussed previously for the LQZ alone with the upper caldera fill removed. The only difference is that there is no attenuation in the LVZ model. Referring back to Figure 5.15a,b for the spectral ratios of the simple LQZ model for $\theta_0 = +20^\circ$, a comparison with the plots shown here in Figure 5.18b,c shows just how important it is for the inclusion to have low Q. One of the major effects of Q on the spectral ratios is to damp out the resonant peaks, and this in turn increases the amount of control we have on predicting stable, systematic patterns in the data, as long as these observed patterns are indeed due to Q effects. This is somewhat ironic because at first we resisted putting Q in the models, in the belief that adding another parameter would only increase the complexity of the problem without providing significant benefits.

Obviously the complete opposite was true in our case. Thus, for studies of seismic amplitudes observed above complex volcanic structures, we advise that one should examine their data for Q effects first and resonance and scattering later.

CHAPTER 6

Discussion and Conclusion

6.1 Comparison of the Two Caldera Fill Models

In Chapter 4 we demonstrated that the teleseismic P-wave delays could be explained with a model that contains two relatively simple, homogeneous components. These are an irregularly shaped, low velocity caldera fill surface layer and a separate lens-shaped, low velocity inclusion at approximately 10 to 13 km true average depth beneath the resurgent dome. Although we could not constrain the depths to the top and bottom of the inclusion, we demonstrated that its minimum height is approximately 8 km and its width at the tapered section is approximately 17 km. Our solution for this inclusion was obtained only after fitting as much of the data as possible with the caldera fill layer alone. To do this we started with an initial estimate of the near-surface structure from *Self et al.* [1986] and the range of average P-wave velocities estimated by *Ankeny et al.* [1986]. We then adjusted the structure and velocity in a way which simultaneously fit most of the delay data and yielded the minimum thickness and velocity for the surface layer within the limits established by the two studies referenced above.

Thus our aim was primarily to obtain a time correction for the estimated effects of the complex surface layer so that any remaining delays could be attributed to deeper structure. In this sense the caldera fill used in our ray model should not be taken literally as an accurate representation of the true near-surface structure. The actual caldera structure above the precambrian granite basement is in fact an

extremely complex mixture of numerous sedimentary and volcanic rock types, as evidenced from lithologic logs taken directly from drill hole cutting and core samples [Nielson & Hulen, 1984; Goff *et al.*, 1986; Self *et al.*, 1986]. The surface layer we used then, is in essence a compression of the average effects due to all of these near-surface components into a single homogeneous layer. The internal inhomogeneities of the actual structure were adequately modeled by variations along the bounding interface above the granite basement. The low velocity of 3.2 km/sec used allowed us to keep these interface variations to a minimum so that large changes in slope could be avoided. This helped maintain some control over the ray-tracing. Although the caldera fill structure is over-simplified, the general trend of deepening to the southeast observed by Self *et al.* [1986] and Nielson & Hulen [1984] is represented well. This trend is very well constrained by core data and gravity profiles in the caldera which indicate a low relative Bouguer anomaly beneath the southeastern portion of the caldera.

We also demonstrated in Chapter 4 that there is an ambiguity in the overall modeled thickness of the caldera fill layer which is inherent to the relative-delay method. The caldera fill interface can be shifted arbitrarily within a wide range of depths without significantly decreasing the variance reduction. Although the known lithology can help constrain some of the general features of the near-surface structure, it cannot remove the basic ambiguity in the overall depth. The data used by Self *et al.* [1986] to obtain the structure in Figure 1.4 contained very little information about seismic velocity variations within and just below the caldera fill. It is certainly possible that the low P-wave velocities could extend down into the precambrian granite near the highly deformed center of the caldera. The core-hole

stratigraphy tells us little about the state of competence of the various rock types intersected by the drill. This is why we have emphasized here the point that the caldera fill in the best ray model should be viewed mainly as a correction layer, rather than as an accurate depiction of the complex near-surface velocity structure beneath the caldera.

Our results from Chapter 5 for the amplitude data give an alternative view of the near-surface structure. Here we showed that the one major feature required to explain the low amplitudes inside the caldera was a large zone of very low Q at the bottom of the caldera fill layer. This LQZ was constrained reasonably well to be about 16 km in width, 4 km in height and approximately 1 km deep to its top. To obtain the best fit to the data, we showed that a relatively non-attenuating upper caldera fill layer was also required, but that the effects of this feature were secondary to the dominant LQZ effect. It was also necessary that the LQZ have significantly lower P and S velocities than its surroundings, in order to produce strong enough attenuation. In this case our approach was somewhat the opposite of the ray tracing approach. We were more concerned here with obtaining the large-scale general features of the near-surface structure than with obtaining a detailed structural correction to the data. The fact that we could reproduce the data reasonably well without the upper caldera fill indicates that the details of this secondary structure could vary considerably and still maintain consistency with the data. Also, since the Q effect is clearly dominant, and since we restricted our models to include only simple symmetric shapes representing separate homogeneous bodies, it is certainly reasonable to expect the true velocity structure to be considerably more complex than the best amplitude model indicates. We would have to conclude this even

if we had no a priori information on the geology of the structure. Although we demonstrated in Chapter 5 that perturbing individual model parameters by as much as $\pm 10\%$ decreased the variance reduction, this is by no means a justification for claiming the modeled velocity structure to be accurate. These kinds of tests tell us nothing about alternative models that could be obtained by allowing velocities and Q to vary within each structural component. Furthermore, our low frequency data would not be capable of constraining such details, even if we had the capability of modeling them. The use of higher frequency data, as mentioned at the outset, would be more sensitive to structural detail, but we would need much better instrument coverage than we had in order to constrain these details.

In light of the major differences between the ray-tracing and Aki-Larner methods, and between the types of data used, it is not surprising that we obtained a different model for the shallow caldera structure in each case. The ray-tracing is very sensitive to the P-wave velocity structure only, and the amplitude data, modeled with the Aki-Larner method, were dominated by the large-scale Q structure. Thus the P-wave delay data could not detect the low Q zone and the amplitude data could not detect the deeper low velocity zone. Beyond these basic differences in the methods and the types of data, our approaches to modeling the shallow structure were also quite different, as described above. We modeled the caldera fill for the ray-tracing only with the intent of isolating the minimum effects of deeper structure, and therefore obtained only a single correction layer with minimum allowable dimensions and velocity needed to represent the average effects of the true structure. In Figure 6.1 we have superimposed the two models on the same plot. The solid lines show the best amplitude model of Figure 5.1 and the dashed lines show

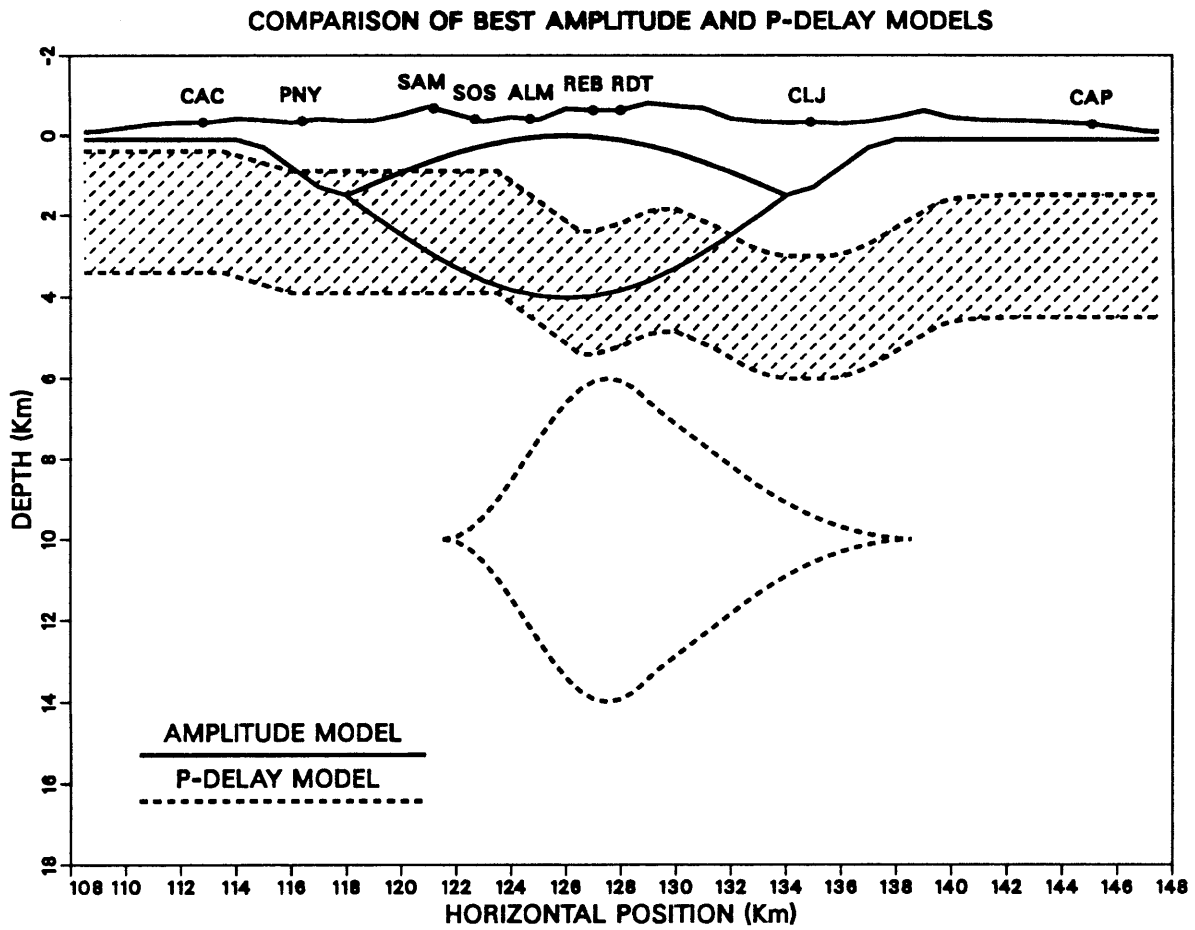


Figure 6.1 Direct comparison of the two best models obtained from the modeling efforts in Chapters 4 and 5. Solid lines show the best amplitude model and dashed lines show the best ray model. The hatched area shows the range of ambiguity in the overall depth of the caldera fill interface for the ray model.

the range of best ray models defined by Figures 4.2 and 4.9. The acceptable range of overall depths for the caldera fill interface in the ray model is indicated by the hatched area. This plot demonstrates that the maximum depths of the surface layers are similar in both models beneath the caldera. Although the amplitude model is subdivided into regions of higher and lower velocity, 4.5 km/sec at the surface and 3.0 km/sec in the LQZ, these velocities bracket that of 3.2 km/sec used in the ray model.

To obtain perfect consistency between the two models would require additional structural complexity which would be impossible to define uniquely, given the limitations in the data and in the modeling methods. As examples, the amplitude model should have a deeper caldera fill beneath the southeastern ring fracture and the ray model should have a subdivided surface layer. We should point out that the ambiguity in the delay modeling, mentioned above, implies that a low velocity zone could be placed within the existing caldera fill correction layer without changing the results, as long as it produces similar amounts of additional delay at all caldera sites. However, since we have already managed to fit both types of data well with the simpler models, we cannot justify a need for increased complexity based on model inconsistencies alone. On the other hand, we could justify the use of more complex models if they were capable of improving the residual variance without reducing the predictability of the synthetic solutions. In the present case, this condition is not satisfied and is the main reason why we restricted the model structures to relatively simple shapes. The fact that the general features of the caldera fill layer are at least similar in the two models lends support to the approach we have taken of determining the simplest possible structures which produce a high degree

of consistency between the synthetic and observed data. Increased site coverage within the caldera would be required to resolve further the secondary differences between the two models.

6.2 Interpretation and Discussion

If we combine the major features of our best ray-tracing and amplitude models, we obtain a general picture of the caldera sub-structure which is consistent with the phases of its known volcanic and thermal evolutions following the last Bandelier ash-flow eruption 1.12 Ma. The major stages in the formation of the Valles Caldera were outlined in *Smith & Bailey* [1968] as follows. 1.) Doming and swelling on a regional scale of the pre-existing Jemez volcanic field and local formation of ring-fractures above the Valles magma chamber. 2.) Eruption of the second member of the Bandelier Tuff through the established ring-fracture system. 3.) Caldera formation due to collapse of the roof of the Valles magma chamber and subsidence of the central caldera block along the ring fractures. 4.) Caldera lake formation and eruption of the early rhyolites, during which approximately 600 m of caldera fill accumulated on top of the subsided central block. 5.) Resurgence and doming of the central caldera block due to renewed magma rise, during which time the middle period rhyolites were erupted from the northwestern ring fracture zone and from the longitudinal graben at the center of the dome. 6.) Eruption of the late period rhyolites as isolated domes in the moat area between the resurgent dome and the topographic caldera rim. 7.) Hot spring activity in the western part of the caldera and erosion of the caldera fill. These seven basic stages were recognized by *Smith & Bailey* [1968] as being common to the development of all Valles-like resurgent

calderas that they examined. The Valles Caldera is currently in the final stage above, which terminates the cycle. The most recent volcanic activity in the caldera occurred about 100,000 years ago [*Heiken & Goff*, 1983].

We propose that our modeling results are consistent with the general structural features one might expect to have been formed by the processes governing stages 3.) through 7.) above. Specifically, our low Q zone is consistent with a highly fractured, partially water-saturated volume of material which could have been formed by the process of post-subsidence magma rise and caldera floor resurgence, followed by development of a large hydrothermal system. *Smith & Bailey* [1968] favored magma rise as a mechanism for resurgence in Valles-like calderas over laccolithic intrusion or forcible injection of other types of bodies into the collapsed caldera floor block. One of the reasons they gave for this preference was that they were unaware of any mapped laccolithic domes which displayed the complex fault patterns typical of domes in resurgent calderas. Thus they proposed that doming in this case involves the deformation of the entire caldera floor block, which necessarily must have a minimum diameter defined by the ring-fracture zone. In addition to this upward deformation, both surface volcanism and injection of magma into fracture systems within the floor block can also occur, as evidenced by the middle period rhyolites which erupted during formation of the Redondo dome. Adding to this the pre-resurgence alluvial and volcanic deposits of the caldera fill, the numerous post-resurgence rhyolite eruptions, and the multi-layered volcanic tuff and sedimentary structure of the original pre-collapse caldera floor block, it is clear that the near-surface structure within the ring fracture must be extremely complex and highly fractured. It would be surprising if the material directly beneath the resurgent dome

did not possess the strongly attenuating properties that we observed for seismic waves.

O'Connell & Budiansky [1977] calculated elastic moduli and seismic Q for fluid-saturated cracked solids. They found that Q decreases with increasing crack density and can reach values less than 10. Also, for a water-saturated rock, they found that if the cracks had a uniform distribution of aspect ratios then Q can be relatively frequency independent. This was attributed to a linear superposition of individual relaxation peaks [*Liu et al.*, 1976] which depend on crack geometry and thus on frequency. They also discussed two possible mechanisms for attenuation, which for a given crack geometry, produce two attenuation peaks with different characteristic frequencies. These mechanisms are 1.) induced fluid flow between cracks; and 2.) relaxation of shear stress in the fluid. It is very likely that water infiltration in the rocks beneath the caldera may contribute significantly to the high attenuation we observed at the inner four sites. As discussed in Chapter 1, the Valles Caldera possesses a highly developed hydrothermal system, as evidenced by the numerous active hot sulfur springs scattered around, near and inside of the ring-fracture zone. The major features of the hydrothermal system have been mapped by *Goff et al.* [1988] and indications are that significant water-saturation may exist to depths in excess of 2 km near the resurgent dome (see Figure 1.3). In fact, the site where we observed the strongest S-wave attenuation, ALM, was installed within 0.5 km or less of a minor hot spring. Although local variations in near-surface water concentration may account for some of the observed variations in attenuation, this view cannot replace the need for a much larger zone of nearly uniform low Q , primarily because the attenuation is so strong at such low frequencies. But it is reasonable to expect

that some large portion of the uplifted and fractured caldera floor must contain a significant amount of water, and in light of O'Connell & Budson's work, this could lend support to the extremely low value of Q that we found.

Our results for the LQZ represent a unique observation in seismology. We are aware of no other attenuation study which yielded such low values for Q at such low frequencies. Furthermore, it is rarely possible to define Q -structures as distinctly as we have because usually Q is too high to allow its effects on seismic waves to be isolated so clearly. Previous studies of volcanoes have found that Q is typically lower than in other tectonically active regions. *Fehler, Roberts & Fairbanks* [1988] determined that Q for 6 to 32 Hz coda waves at Mount St. Helens has values in the mid to lower 100's. Their results were restricted to higher frequencies because the coda-wave method requires the use of local earthquakes. *Chouet* [1976] obtained similar results for coda Q at Kilauea Volcano in Hawaii. The Valles Caldera differs considerably from these volcanoes in many ways. First, the size and complexity of its magmatic system are much greater. Secondly, the process of collapse and resurgence has imparted a particularly complex upper-crustal structure to the caldera. Finally, the large hydrothermal system in the caldera is a major feature that is absent in these other volcanoes. This last feature is perhaps the most important aspect of our interpretation of the LQZ. If in fact some major contribution to the strong observed attenuation arises from water saturation, then the search for low Q zones in known geothermal regions may prove to be an excellent target for defining the approximate volumes of existing hydrothermal systems.

An interesting comparison with another geothermal system can be made from the work of *Majer & McEvilly* [1979]. They studied the seismic properties of the

vapor-dominated reservoir at The Geysers geothermal field in northern California. Using explosions and microearthquakes as local sources, they found that the shallow, vapor-dominated portions of the reservoir had higher Q than its surroundings, whereas the deeper portions had significantly lower Q . They suggested a possible interpretation that the lower portion contains significant amounts of pore water. The major difference in the Valles Caldera is that the hydrothermal field is an entirely fluid-dominated system, and the higher Q associated with steam reservoirs is not observed there. Although Majer & McEvilly reported Q values only as low as about 10, their data and their Q analysis were considerably different from ours. They studied only P-wave attenuation for the first half-cycle, their data were restricted to frequencies above 1.0 Hz, and their Q analysis was based on differential path attenuation relative to assumed Q values at a reference site. Our amplitude modeling was for P and S scattered waves at lower frequencies and we did not have to define Q as a relative parameter in our models. Given these differences in the methods, the similarities between the results for the low Q zones are encouraging. It would be most interesting to repeat our experiment in other geothermal areas.

Previous seismic studies have also indicated that an attenuating anomaly may exist somewhere beneath the caldera. Suhr [1982] used a modified fan-shooting method to detect a large P-wave shadowing anomaly at considerable depth. Using recordings of mine blasts which had passed beneath the caldera and to the north and south of it, he delineated a low Q zone approximately 16-20 km in diameter located at approximately 20 km depth beneath the caldera. This anomaly is much deeper than our LQZ and may be related in some way to the deep low velocity zone of our ray model. However, Suhr's quantitative results are speculative at best,

as he himself states, because of the poor control he had over numerous aspects of his experiment. He clearly points out these problems in his report. In addition, *Felch* [1987] gave a very good review of *Suhr's* work, so we will not discuss the shortcomings in detail here. Qualitatively, though, there can be no doubt that *Suhr* observed anomalously low amplitudes for waves which passed beneath the caldera. He interpreted the attenuating zone as being due to a region of partial melt. *Felch* also used mine blast data to observe S-wave shadowing at the one station he had inside the caldera, which was near our site RDT. Although the amplitudes he observed for S and Lg phases were extremely low in the caldera he could not uniquely attribute this effect to either a near-surface anomaly or to deeper structure. *Felch* also used a spectral ratio technique to characterize the relative difference in P-wave attenuation between the one caldera site and a reference site well outside. This method provided results only for relative differences in $1/Q$ between the two sites. However for one of his events, the spectra at about 1.0 Hz showed a decrease in amplitude of about 50% between the outside site and the caldera site. This is remarkably similar to our observations for the vertical component teleseismic data recorded at SAM compared with the inner caldera sites on array 2, shown in Chapters 2 and 5. So there do exist a few independent observations besides our own which also indicate that attenuation is quite high inside the caldera. The speculative results of *Suhr* [1982] suggest that some part of the observed attenuation may be due to the much deeper low velocity zone, for which we could not model amplitudes. There are two reasons why we believe that such effects should not be significant in our data. First, the depth of the inclusion should cause the attenuation pattern to shift laterally along the surface as the angle of incidence changes, and we

observed no significant dependence of the amplitudes on incidence angle. Secondly, the pattern would probably not vary from site to site as strongly as we observed because the low amplitudes in the caldera were related strongly to the proximity of the recording sites to the thickest portions of the LQZ, and this effect would be smoothed out if the attenuation zone was not shallow. So we find no contradictions to our shallow LQZ in any previous studies of the region.

We now turn attention to the interpretation of the low velocity zone in the best ray model. There is certainly no doubt in any of the literature on the evolution of the Valles Caldera that a large, shallow, silicic magma chamber was responsible for at least the two major caldera forming eruptions of 1.1 and 1.4 Ma. The range of P-wave velocities of 3.5 to 4.2 km/sec that we determined for the LVZ is probably too high to consider the inclusion as completely molten. For the cooling basaltic lava lake of Kilauea Iki, Hawaii, *Aki et al.* [1978] used an active seismic refraction survey to determine that the P-wave velocities varied between 2.2 and 0.8 km/sec in the fractured upper crust and could be as low as 0.9 to 0.3 km/sec in the deeper partially molten to molten portions of the lake. With these velocities as a lower limit we cannot assume that the LVZ is completely molten. This is in agreement with the interpretation of *Suhr* [1982] that the anomalous deep zone of attenuation he found is probably due to partial melt.

Smith & Shaw [1975] estimated the initial volume of the Valles magma chamber to be approximately 1000 to 4000 km³. *Smith & Bailey* [1968] estimated the volume of magma required to account for resurgent doming to be approximately 15 cubic miles. This is simply the amount of additional magma required, after caldera collapse, to push the caldera floor block up to its present height, and the main

point here is that one possible explanation for resurgence is through replenishment of the depleted magma chamber. Based on the estimates by *Smith & Shaw* [1975] of the initial volume and heat content of the magma chamber, *Kolstad & McGetchin* [1978] performed numerical calculations for various heat conduction models in order to predict the thermal evolution of a cylindrical pluton, using a variety of initial conditions. They used a radius for the cylinder of 8 km and lengths from 15 to 25 km. For these tests the pluton was buried at a depth of 3 km. They also tested the 8 km \times 20 km pluton at a depth of 5 km. Five major assumptions were used for their modeling. 1.) heat transfer is by conduction only; 2.) no crystal settling or differentiation is allowed; 3.) the pluton is emplaced instantaneously; 4.) there is no heat transfer due to mass transfer; and 5.) the magma is not replenished after it has been emplaced. This last assumption is perhaps the most serious since the history of continued volcanism after caldera collapse implies that the magma chamber did not become static after resurgence was completed. By allowing the pluton to cool over a period of 1 million years, *Kolstad & McGetchin* found that the percent of melt remaining after a given elapsed time was proportional to the initial volume of the magma chamber and to its depth of emplacement. After 1 million years, the 8 km \times 25 km pluton still had about 25% of the original melt remaining, but the 8 \times 15 pluton had less than 10% left. The 8 \times 20 pluton at 5 km depth required approximately 15% more time than the 3 km deep pluton to reach a given percentage of remaining melt.

We can roughly estimate the volume of the LVZ in our best ray model, assuming that it is axi-symmetric in three dimensions, using either a sphere with a radius of 4 km, or a cylinder with radius 5 km and length 8 km. These two cases should

give reasonable lower and upper estimates for the volume, respectively. For the lower estimate we obtain approximately 270 km^3 for the volume, and for the upper estimate we get approximately 630 km^3 . The Kolstad & McGetchin models above for the three different initial sizes of pluton yielded, after cooling for 1 million years, a range of remnant melt volumes of approximately 150 km^3 (for the 8×15 initial pluton) to 1260 km^3 (for the 8×25 initial pluton). So our results fall well within the range of their calculations. Since their assumption of no magma replenishment is probably not correct, we cannot say much about the probable size of the initial magma chamber based on its present size. This is also true because we were not able to place an upper bound on the height of our LVZ. It is encouraging, though, that an independent calculation based on heat flow predicts generally similar results as what we obtained using P-wave delays. So we conclude here that the minimum size we obtained for the LVZ is consistent with what we might expect the approximate size to be for a zone of melt within an initially much larger magma chamber which has cooled and crystallized significantly over the last million years.

If we follow the limiting case of Kolstad & McGetchin's calculation, for which the initial volume of the magma chamber was less than about 3000 km^3 and magma replenishment did not occur, then the original Valles magma chamber would be completely cooled and crystallized by now. However, as discussed in Chapter 1, there is evidence from temperature logs taken in drill holes at Fenton Hill that significant reheating has occurred in the region as recently as 40 ka [*Harrison et al.*, 1986]. Furthermore, the very existence of high temperatures and heat flow at Fenton Hill, which is located outside of the caldera, may be an indication that the Valles magma

chamber originally extended well beyond the edges of the caldera. Also, the post-resurgence volcanic activity in the caldera has been well documented. As discussed briefly in Chapter 1, *Doell et al.* [1968] reported potassium-argon ages for the series of late rhyolite dome eruptions in the caldera which show a clear counterclockwise progression towards younger ages. The oldest of these eruptions occurred about 1.04 Ma and formed the eastern-most dome, named Cerro Del Medio. From this dome, the ages decrease steadily counterclockwise to the large western dome, San Antonio Mountain, dated at 0.5 Ma, and the southern-most, South Mountain, dated at 0.49 Ma. In between San Antonio and South Mountain, the Banco Bonito Obsidian flow represents the last volcanic episode at 0.13 Ma [*Self et al.*, 1988]. So, regardless of whether the original Valles magma chamber has completely crystallized or not, there is clear evidence from the post-resurgence volcanism that significant magmatic activity has continued up until geologically recent times. It is still not known whether this activity resulted from reheating or replenishment of the main magma chamber or whether subsidiary magma bodies have existed for brief periods of time. What is clear is that there is no reason to expect that the entire upper-crustal structure beneath the caldera is completely crystallized. So in light of this discussion, it is not unreasonable to interpret our LVZ as a zone of partial melt.

There have been few attempts in the past to determine the local velocity structure beneath the Valles Caldera. The most notable are the CARDEX time-term analysis of *Olsen et al.* [1986] and the P-wave travel-time inversions of *Ankeny et al.* [1986] and *Felch* [1987]. The major deficiency in all of these studies was the lack of station coverage inside the caldera, where at most only one station was operating. Although *Ankeny et al.* [1986] discovered a very large but weak velocity

anomaly beneath the caldera, their results are ambiguous because alternative models could also reproduce their data, due to the poor local coverage of the caldera region. Even with the good coverage that we had for our P-delay data, we could not constrain all parameters of the LVZ. Although we cannot completely rule out Ankeny et al.'s view of the velocity anomaly, it is not uniquely constrained by their data. Furthermore the size of their anomaly is much too large to be consistent with the thermal evolution calculations of Kolstad & McGetchin discussed earlier. *Felch* [1987] also concluded that the results of Ankeny et al. were ambiguous. He performed a travel-time inversion using a slightly different parameterization scheme for his models than that used by Ankeny et al. *Felch's* major conclusion was that there is no velocity anomaly associated with the deep caldera structure. Again, this result was due primarily to the lack of instrument coverage inside the caldera. So although our LVZ model is quite different than what other investigators have found, it actually represents the only conclusive evidence presented to date in support of a large deep remnant magma chamber beneath the Valles Caldera.

There have been several non-seismological investigations which yielded estimates for the depth to the top of original Valles magma chamber, prior to the eruption of the Tshirege member of the Bandelier Tuff. *Nielson & Hulen* [1984] used a structural model for dome resurgence to estimate the thickness of the overburden above the causative magma chamber. They used a formula derived by *Johnson* [1970] for the bending of a circular plate in response to a laccolithic intrusion. The formula relates the diameter of the dome to the depth and pressure of the magma chamber and the dome amplitude. To simplify his formula, Johnson had to assume that the magma pressure was constant and that all dome structures had a similar

amplitude-to-diameter ratio. This allowed him to obtain a very simple linear relation between dome diameter and overburden thickness. To justify the extension of Johnson's laccolith formula to resurgent domes, Nielson & Hulen showed that many resurgent caldera domes had approximately the same amplitude-to-diameter ratio that Johnson used. For the Redondo dome, then, they estimated the depth to the causative magma chamber to be approximately 5 km. After cooling for a million years the top of the molten zone should be significantly deeper than this. So it appears now that the depth to the top our LVZ, as shown in Figure 4.2, may be reasonable, even though we could not constrain this feature of the model with our data. If we assume that the height we obtained is correct, then we can place the present top of the melt between 6 to 9 km depth beneath the peak of Redondo Dome. The estimated overburden thickness of 5 km is also nearly identical to the maximum depth to the bottom of our low Q zone, which is very encouraging.

Evidence from two petrological studies also indicate that a depth of about 5 km is reasonable for the pre-collapse magma chamber. *Sommer* [1977] used the volatile contents in the upper Bandelier Tuff to infer a depth of burial of approximately 5 km. *Warshaw & Smith* [1988] examined chemical compositions of various components in the upper Bandelier Tuff and determined that the earliest erupted material, at the top of the magma chamber, was formed at a temperature and pressure corresponding to a depth of 5-7 km. So our interpretations here of the major features in our two models are consistent with the results of numerous non-seismological investigations in the area, as well as with the known history and evolution of the caldera from the time of its collapse to the present. Although the details of the

caldera's sub-structure have yet to be determined, we believe that the general features presented here are well-supported and can serve as good starting points for higher resolution studies.

6.3 Summary and Conclusion

We recorded a suite of high quality teleseismic events at numerous sites along a line spanning the ring fracture of Valles Caldera and at several sites outside of the caldera on the same line. We demonstrated that the variations in spectral amplitude of the scattered waves, for frequencies from 0.2 to 0.8 Hz, displayed a very clear pattern of strong relative lows at sites inside the caldera relative to sites on the ring fracture. All three components of motion displayed the same general pattern, and to first order this pattern did not vary with incidence angle or with direction of approach. By modeling the relative amplitude variations across the instrument array for the vertical and radial components, we obtained a structural model for a 2-dimensional vertical section of the caldera beneath the array line. The major feature of this best-fitting model was a large, shallow attenuating zone located at the bottom of the surface caldera fill layer. In order to reproduce the very low amplitudes in the caldera, we needed to use values of $Q = 1$, $\alpha = 3.0$ km/sec and $\beta = 1.29$ km/sec in the attenuation zone. We demonstrated the internal reliability of the synthetic solutions for this model, discussed numerous alternative models and gave reasons why these alternatives cannot reproduce the data as well as a simple low Q zone does. Although our data clearly contain effects of 3-D structure, we discussed how these effects were minimized by the design of the experiment, method of data analysis and restriction to considering each component of motion separately. We

also demonstrated that our 2-D model reproduces the amplitude variations of the first P-wave pulse extremely well, and this type of data should be nearly devoid of 3-D effects. We found that our model fit all data recorded on array 2 extremely well for events from the northwest, but less well for southeastern events. We attributed this to the symmetric interface shapes used in the model and concluded that the secondary details of the southeastern portion of the caldera structure were not well-represented in our model. We could not fit the data from array 1 because the strength of scattering was not strong enough in the caldera relative to the sites outside. We attributed this to deeper structure which we could not include in the model due to limitations of the modeling method. But since the local Q effect dominated so strongly within the caldera, the effects of deeper structure were negligible in the array-2 data. So our amplitude model is only representative of the shallow local structure directly beneath the caldera.

We also modeled observed P-wave delay times for events from the northwest and southeast. We found that the delays for southeastern events were much stronger than for northwestern events. Through ray-tracing we found that northwestern data could be reproduced by an irregularly shaped low velocity layer at the surface, representing the caldera fill. This layer was used mainly to correct the delay data so that the effects due to deep structure could be isolated. To fit the southeastern data, a deep low velocity zone was needed beneath the caldera. By adjusting its size, shape, location and P-wave velocity, we were able to fit all of our delay observations extremely well. The best fit was obtained for a lens-shaped inclusion approximately 17 km across at its widest section and 8 km in height with a P-wave velocity in the range of 3.5 to 4.2 km/sec. Although we could not constrain the maximum

height and velocity of this low velocity zone, we gave reasons why neither of these parameters could be any smaller. The width, horizontal position and average depth to the center of the inclusion, however, were constrained quite well by the width and location of the observed zone of the strongest delays at the surface and by the strength of the delays themselves.

Although the two methods yielded different views of the near-surface structure, the discrepancies were attributed mainly to the difference between the two techniques and the structural simplifications used to maintain control over the forward modeling approach in each case. The major features of each model do not pose any contradictions. We interpreted the deep low velocity zone as the residual, partially molten core of the original caldera forming magma chamber. We demonstrated that the approximate size and depth is consistent with other studies in which the properties of the original pre-collapse magma chamber were estimated by non-seismological means. The shallow low Q zone was attributed to a highly fractured and partially water-saturated region of the lower caldera fill layer. This interpretation is consistent with the extreme deformation of the caldera floor block which must have accompanied dome resurgence. The maximum depth of the low Q zone is consistent with the estimate of *Nielson & Hulen* [1984] for the presumed thickness of overburden which was uplifted by magma pressure to create Redondo Dome. The value of $Q = 1$ used in our model is surprisingly low but is reasonably consistent with the calculations of *O'Connell & Budiansky* [1971] for water-saturated cracked rocks, where they predicted values of Q smaller than 10 for certain extreme cases. This condition must certainly exist to some significant extent beneath the Valles Caldera, as evidenced by its well-developed hydrothermal system.

The combined view of a deep cooling remnant magma chamber beneath a large zone of water-saturated fractured material near the surface represents a predictable outcome of the seven stages of resurgent caldera formation outlined by *Smith & Bailey* [1968]. Not only are our results consistent with widely held theories about the evolution of the Valles Caldera, they also provide additional support to these theories in the form of direct evidence from seismic data.

6.4 Suggestions for Future Work

The two largest deficiencies in the present study were the limited instrument coverage and the limited capabilities of the Aki-Larner method. These necessitated the restriction to two dimensions and the use of very simple models. The ray-tracing also suffered from unfortunate holes in the site coverage, as well as from the use of only steeply incidence P-wave data. We deployed instruments along only one line across the caldera, and similar experiments for different azimuth lines would be highly recommended, given that the same restrictions above were still imposed. This would help resolve some of the unanswered questions concerning the 3-D structure that we encountered. In hindsight, we now realize also that it is more important to give equal coverage to the entire caldera rather than to lump most of the instruments on one side as we did. Presumably, then, we would also observe strong P-wave delays between our sites RDT and CLJ for northwestern events. By far the best suggestion we can make, though, is to blanket the entire caldera with a two-dimensional array of closely spaced instruments, all with similar response. This is a rather tall order, but is probably the only way in which the detailed 3-dimensional structure can be constrained adequately. This should also allow one to relax the restriction of using

only teleseismic data, because it may then be possible to characterize systematic variations in amplitude for higher frequencies and for shallower incidence angles. To interpret this higher frequency information, though, a modeling method will be required which is more versatile than the low-frequency smoothly varying layered-structure approximation of the Aki-Larner method. The restriction to small-slope interface irregularities will have to be eliminated completely. Waveform modeling techniques are improving steadily with continuing advances in both theory and computing capabilities. Due to its structural complexity on a fine scale, the Valles Caldera will certainly remain a likely candidate to try new modeling methods on for some time to come.

In addition to the above improvements for future studies in the Valles Caldera, it would also be most informative to carry out experiments similar to ours at other volcanic and geothermal areas. A comparison with geothermal areas that are not related to resurgent calderas, as well as with volcanic structures that do not possess a significant hydrothermal system, should help to separate the numerous component effects that are combined in the Valles Caldera.

APPENDIX 1

Detailed Formulas for Setting Up the Aki-Larner P-SV Problem

In Chapter 3 we showed the basic steps required to obtain the boundary condition integral equations (3.16) which must be solved simultaneously to obtain the unknown wave potential coefficients, $A_j(\omega, k)$. By imposing a periodicity requirement on all functions of x the integral equations were transformed to the equivalent infinite-sum equations (3.18). Finally, by truncating the wavenumber summation index and Fourier Transforming all functions of x , the square linear system of equations (3.21) was obtained which can be solved directly for discrete values of $A_n^{(j)}$. These coefficients may then be substituted into either of equations (3.7) or (3.8), depending on which medium we are considering, to obtain the k -decomposed total wave potentials, $\tilde{\Phi}$ and $\tilde{\Psi}$, at an arbitrary (x, z) location in the model. The k -decomposed displacements, u and w , are then computed using equations (3.5) and finally the integrated displacements, \hat{u} and \hat{w} , are obtained by a simple summation over k_n :

$$\hat{u}(x, z, \omega) = \sum_{n=-N1}^{N2} u(x, z, \omega, k_n),$$

$$\hat{w}(x, z, \omega) = \sum_{n=-N1}^{N2} w(x, z, \omega, k_n).$$
(A1.1)

To set up the linear system $\underline{G} \cdot \underline{A} = \underline{H}$ in equation (3.21) we need to evaluate explicitly the displacements, $u(x, z, \omega, k)$ and $w(x, z, \omega, k)$, and tractions, $T_x(x, z, \omega, k)$ and $T_z(x, z, \omega, k)$ at each interface. To keep the notation simple, all formulas will be given as functions of x and k , realizing that they must eventually be discretized

over these variables. When the medium index, p , corresponds to a layer, the displacements may be written by combining equations (3.7) and (3.5):

$$\begin{aligned}
u_p(x, z, \omega, k) &= \left[ik \Phi_p^d(\omega, k) e^{i\nu_p z} - i\nu'_p \Psi_p^d(\omega, k) e^{i\nu'_p z} \right. \\
&\quad \left. + ik \Phi_p^u(\omega, k) e^{-i\nu_p z} + i\nu'_p \Psi_p^u(\omega, k) e^{-i\nu'_p z} \right] e^{ikx}, \\
w_p(x, z, \omega, k) &= \left[i\nu_p \Phi_p^d(\omega, k) e^{i\nu_p z} + ik \Psi_p^d(\omega, k) e^{i\nu'_p z} \right. \\
&\quad \left. - i\nu_p \Phi_p^u(\omega, k) e^{-i\nu_p z} + ik \Psi_p^u(\omega, k) e^{-i\nu'_p z} \right] e^{ikx}.
\end{aligned} \tag{A1.2}$$

In the halfspace we have $p = P$ and the expressions for u_P and w_P are obtained using equations (3.8) and (3.5):

$$\begin{aligned}
u_P(x, z, \omega, k) &= \left[ik \Phi_P^d(\omega, k) e^{i\nu_P z} - i\nu'_P \Psi_P^d(\omega, k) e^{i\nu'_P z} \right] e^{ikx} + ik_0 e^{i(k_0 x - \nu_0 z)}, \\
w_P(x, z, \omega, k) &= \left[i\nu_P \Phi_P^d(\omega, k) e^{i\nu_P z} + ik \Psi_P^d(\omega, k) e^{i\nu'_P z} \right] e^{ikx} - i\nu_0 e^{i(k_0 x - \nu_0 z)}.
\end{aligned} \tag{A1.3}$$

The three required k -decomposed stress components, S_{xx} , S_{zz} and S_{xz} , for a layer can be obtained by putting equations (A1.2) into the k -decomposed versions of equations (3.13). It will be convenient first to eliminate λ explicitly from the resulting expressions for S_{xx} and S_{zz} . Terms involving both λ and μ will appear in only two forms, and these may be replaced by terms involving only μ through the following identities:

$$\begin{aligned}
\lambda K_\alpha^2 + 2\mu\nu^2 &= \mu (K_\beta^2 - 2k^2), \\
\lambda K_\alpha^2 + 2\mu k^2 &= \mu (K_\beta^2 - 2K_\alpha^2 + 2k^2).
\end{aligned} \tag{A1.4}$$

The three stress components for a layer can then be written as:

$$\begin{aligned}
S_{xz}^{(p)}(x, z, \omega, k) &= \mu_p \left[F_1^{(p)} \Phi_p^d(\omega, k) e^{i\nu_p z} + 2k\nu'_p \Psi_p^d(\omega, k) e^{i\nu'_p z} \right. \\
&\quad \left. + F_1^{(p)} \Phi_p^u(\omega, k) e^{-i\nu_p z} - 2k\nu'_p \Psi_p^u(\omega, k) e^{-i\nu'_p z} \right] e^{ikx}, \\
S_{zz}^{(p)}(x, z, \omega, k) &= \mu_p \left[F_2^{(p)} \Phi_p^d(\omega, k) e^{i\nu_p z} - 2k\nu'_p \Psi_p^d(\omega, k) e^{i\nu'_p z} \right. \\
&\quad \left. + F_2^{(p)} \Phi_p^u(\omega, k) e^{-i\nu_p z} + 2k\nu'_p \Psi_p^u(\omega, k) e^{-i\nu'_p z} \right] e^{ikx}, \\
S_{xz}^{(p)}(x, z, \omega, k) &= \mu_p \left[-2k\nu_p \Phi_p^d(\omega, k) e^{i\nu_p z} - F_2^{(p)} \Psi_p^d(\omega, k) e^{i\nu'_p z} \right. \\
&\quad \left. + 2k\nu_p \Phi_p^u(\omega, k) e^{-i\nu_p z} - F_2^{(p)} \Psi_p^u(\omega, k) e^{-i\nu'_p z} \right] e^{ikx},
\end{aligned} \tag{A1.5}$$

$$\text{where: } F_1^{(p)} = 2K_{\alpha_p}^2 - K_{\beta_p}^2 - 2k^2,$$

$$F_2^{(p)} = 2k^2 - K_{\beta_p}^2,$$

$$\mu_p = \rho_p \beta_p^2.$$

Similarly, putting equations (A1.3) into equations (3.13), we can write the stress components in the halfspace, $p = P$, as:

$$\begin{aligned}
S_{xz}^{(P)} &= \mu_P \left[\left[F_1^{(P)} \Phi_P^d(\omega, k) e^{i\nu_P z} + 2k\nu'_P \Psi_P^d(\omega, k) e^{i\nu'_P z} \right] e^{ikx} + F_1^{(0)} e^{i(k_0 x - \nu_0 z)} \right], \\
S_{zz}^{(P)} &= \mu_P \left[\left[F_2^{(P)} \Phi_P^d(\omega, k) e^{i\nu_P z} - 2k\nu'_P \Psi_P^d(\omega, k) e^{i\nu'_P z} \right] e^{ikx} + F_2^{(0)} e^{i(k_0 x - \nu_0 z)} \right], \\
S_{xz}^{(P)} &= \mu_P \left[\left[-2k\nu_P \Phi_P^d(\omega, k) e^{i\nu_P z} - F_2^{(P)} \Psi_P^d(\omega, k) e^{i\nu'_P z} \right] e^{ikx} + 2k_0 \nu_0 e^{i(k_0 x - \nu_0 z)} \right], \\
\text{where: } F_1^{(0)} &= 2K_{\alpha_P}^2 - K_{\beta_P}^2 - 2k_0^2,
\end{aligned} \tag{A1.6}$$

$$F_2^{(0)} = 2k_0^2 - K_{\beta_P}^2.$$

Using equation (3.11) for the unit normal along each interface, the tractions in each medium, evaluated at each interface, can be obtained by substituting either equations (A1.5) or (A1.6) into equations (3.12).

We are now in a position where the boundary conditions can be set up, using the integral equations (3.14) and (3.15). As discussed in Chapter 3, the first step is to move all functions of k to the left-hand sides of equations (3.14) and separate the unknown wave potentials to yield the general expression for each boundary condition given in equation (3.16). The simplest model in which all three basic forms discussed for this equation will appear contains two buried irregular interfaces in addition to the irregular free surface topography. Once we have set up the problem for this model, additional layers may be added by reproducing the expressions for boundary conditions at the layer-layer interface. The free-surface and layer-halfspace expressions occur at most only once in any given model. The motion-stress terms for transmitted and scattered waves, $g_{ij}(x, \omega, k)$, and for the source wave, $h_i(x, \omega)$, must be evaluated explicitly along each interface for the media above and below. Clearly h_i will be non-zero only in the halfspace and g_{ij} will be non-zero only for the wave potentials, $A_j(\omega, k)$, which contribute to the solutions in each medium (see Chapter 3 for discussion). In the following we give the explicit expressions for g_{ij} and h_i for setting up the 2-layered problem and will then describe how to expand the problem to 3 or more layers. For the 2-layered model, the indexing scheme presented in Chapter 3 will identify the three media by $p = 1, 2, 3$, with $p = 3$ corresponding to the halfspace. The interfaces are identified by $p = 0, 1, 2$ with $p = 0$ corresponding to the free-surface.

The index j identifies the various unknown wave potentials, and in the present case there are 10 of these (4 in each layer and 2 in the halfspace). The index i identifies the 10 boundary conditions required to solve for the potentials. The order in which the potentials and boundary conditions are assigned to j and i is arbitrary, as long as one keeps careful track of how the resulting linear system is filled with these elements. We have chosen here to order the boundary conditions beginning with the bottom-most interface, such that $i = 1, 2, 3, 4$ corresponds to the conditions on u, w, T_x, T_z , respectively, at interface $p = 2$. The same boundary conditions at interface $p = 1$ are indexed as $i = 5, 6, 7, 8$ and the two traction conditions at the free surface, $p = 0$, are $i = 9, 10$. For the wave potentials we begin the index j with the up-going potentials in the deepest layer, Φ_2^u and Ψ_2^u , and end with the down-going potentials in the surface layer, Φ_1^d and Ψ_1^d . The resulting linear system of integral equations, $\underline{g} \cdot \underline{A} = \underline{h}$, will then have the following form, where we use the subscript 0 to denote $i, j = 10$:

$$\begin{pmatrix} g_{11} & g_{12} & 0 & 0 & g_{15} & g_{16} & g_{17} & g_{18} & 0 & 0 \\ g_{21} & g_{22} & 0 & 0 & g_{25} & g_{26} & g_{27} & g_{28} & 0 & 0 \\ g_{31} & g_{32} & 0 & 0 & g_{35} & g_{36} & g_{37} & g_{38} & 0 & 0 \\ g_{41} & g_{42} & 0 & 0 & g_{45} & g_{46} & g_{47} & g_{48} & 0 & 0 \\ g_{51} & g_{52} & g_{53} & g_{54} & 0 & 0 & g_{57} & g_{58} & g_{59} & g_{50} \\ g_{61} & g_{62} & g_{63} & g_{64} & 0 & 0 & g_{67} & g_{68} & g_{69} & g_{60} \\ g_{71} & g_{72} & g_{73} & g_{74} & 0 & 0 & g_{77} & g_{78} & g_{79} & g_{70} \\ g_{81} & g_{82} & g_{83} & g_{84} & 0 & 0 & g_{87} & g_{88} & g_{89} & g_{80} \\ 0 & 0 & g_{93} & g_{94} & 0 & 0 & 0 & 0 & g_{99} & g_{90} \\ 0 & 0 & g_{03} & g_{04} & 0 & 0 & 0 & 0 & g_{09} & g_{00} \end{pmatrix} \cdot \begin{pmatrix} \Phi_2^u \\ \Psi_2^u \\ \Phi_1^u \\ \Psi_1^u \\ \Phi_3^d \\ \Psi_3^d \\ \Phi_2^d \\ \Psi_2^d \\ \Phi_1^d \\ \Psi_1^d \end{pmatrix} = \begin{pmatrix} h_1 \\ h_2 \\ h_3 \\ h_4 \\ 0 \\ 0 \\ 0 \\ 0 \\ 0 \\ 0 \end{pmatrix} \quad (A1.7)$$

In the following formulas we assume that all expressions for g_{ij} must be multiplied by $e^{i\vec{k}x}$ before being discretized and FFT'd. Also, all stress terms have been divided by $(1 + s_p^2)^{1/2}$ in order to simplify the formulas. Keep in mind that all g_{ij}

are functions of x and k , and all h_i and interface topographies and slopes, ζ_p and s_p , are functions of x . For the boundary conditions on u at interface 2 the following expressions are needed:

$$\begin{aligned}
g_{11} &= ike^{-i\nu_2\zeta_2} & g_{12} &= i\nu'_2 e^{-i\nu'_2\zeta_2} & g_{15} &= -ike^{i\nu_3\zeta_2} \\
g_{16} &= i\nu'_3 e^{i\nu'_3\zeta_2} & g_{17} &= ike^{i\nu_2\zeta_2} & g_{18} &= -i\nu'_2 e^{i\nu'_2\zeta_2} \\
h_1 &= ik_0 e^{-i\nu_0\zeta_2}.
\end{aligned} \tag{A1.8}$$

For w at interface 2:

$$\begin{aligned}
g_{21} &= -i\nu_2 e^{-i\nu_2\zeta_2} & g_{22} &= ike^{-i\nu'_2\zeta_2} & g_{25} &= -i\nu_3 e^{i\nu_3\zeta_2} \\
g_{26} &= -ike^{i\nu'_3\zeta_2} & g_{27} &= i\nu_2 e^{i\nu_2\zeta_2} & g_{28} &= ike^{i\nu'_2\zeta_2} \\
h_2 &= -i\nu_0 e^{-i\nu_0\zeta_2}.
\end{aligned} \tag{A1.9}$$

For T_x at interface 2:

$$\begin{aligned}
g_{31} &= (\mu_2/\mu_3)(F_1^{(2)}s_2 - 2k\nu_2) e^{-i\nu_2\zeta_2} & g_{32} &= -(\mu_2/\mu_3)(2k\nu'_2s_2 - F_2^{(2)}) e^{-i\nu'_2\zeta_2} \\
g_{35} &= -(F_1^{(3)}s_2 + 2k\nu_3) e^{i\nu_3\zeta_2} & g_{36} &= -(2k\nu'_3s_2 + F_2^{(3)}) e^{i\nu'_3\zeta_2} \\
g_{37} &= (\mu_2/\mu_3)(F_1^{(2)}s_2 + 2k\nu_2) e^{i\nu_2\zeta_2} & g_{38} &= (\mu_2/\mu_3)(2k\nu'_2s_2 + F_2^{(2)}) e^{i\nu'_2\zeta_2} \\
h_3 &= (F_1^{(0)}s_2 - 2k_0\nu_0) e^{-i\nu_0\zeta_2}.
\end{aligned} \tag{A1.10}$$

For T_x at interface 2:

$$\begin{aligned}
g_{41} &= (\mu_2/\mu_3)(2k\nu_2s_2 - F_2^{(2)}) e^{-i\nu_2\zeta_2} & g_{42} &= -(\mu_2/\mu_3)(F_2^{(2)}s_2 + 2k\nu'_2) e^{-i\nu'_2\zeta_2} \\
g_{45} &= (2k\nu_3s_2 + F_2^{(3)}) e^{i\nu_3\zeta_2} & g_{46} &= (F_2^{(3)}s_2 - 2k\nu'_3) e^{i\nu'_3\zeta_2} \\
g_{47} &= -(\mu_2/\mu_3)(2k\nu_2s_2 + F_2^{(2)}) e^{i\nu_2\zeta_2} & g_{48} &= -(\mu_2/\mu_3)(F_2^{(2)}s_2 - 2k\nu'_2) e^{i\nu'_2\zeta_2} \\
h_4 &= (2k_0\nu_0s_2 - F_2^{(0)}) e^{-i\nu_0\zeta_2}.
\end{aligned} \tag{A1.11}$$

The remaining h_i are all zero. So for u at interface 1 we only need the following g_{ij} :

$$\begin{aligned}
g_{51} &= -ike^{-i\nu_2\zeta_1} & g_{52} &= -i\nu'_2 e^{-i\nu'_2\zeta_1} \\
g_{53} &= ike^{-i\nu_1\zeta_1} & g_{54} &= i\nu'_1 e^{-i\nu'_1\zeta_1} \\
g_{57} &= -ike^{i\nu_2\zeta_1} & g_{58} &= i\nu'_2 e^{i\nu'_2\zeta_1} \\
g_{59} &= ike^{i\nu_1\zeta_1} & g_{50} &= -i\nu'_1 e^{i\nu'_1\zeta_1}.
\end{aligned} \tag{A1.12}$$

For w at interface 1:

$$\begin{aligned}
g_{61} &= i\nu_2 e^{-i\nu_2\zeta_1} & g_{62} &= -ike^{-i\nu'_2\zeta_1} \\
g_{63} &= -i\nu_1 e^{-i\nu_1\zeta_1} & g_{64} &= ike^{-i\nu'_1\zeta_1} \\
g_{67} &= -i\nu_2 e^{i\nu_2\zeta_1} & g_{68} &= -ike^{i\nu'_2\zeta_1} \\
g_{69} &= i\nu_1 e^{i\nu_1\zeta_1} & g_{60} &= ike^{i\nu'_1\zeta_1}.
\end{aligned} \tag{A1.13}$$

For T_z at interface 1:

$$\begin{aligned}
g_{71} &= -(F_1^{(2)} s_1 - 2k\nu_2) e^{-i\nu_2\zeta_1} & g_{72} &= (2k\nu'_2 s_1 - F_2^{(2)}) e^{-i\nu'_2\zeta_1} \\
g_{73} &= (\mu_1/\mu_2)(F_1^{(1)} s_1 - 2k\nu_1) e^{-i\nu_1\zeta_1} & g_{74} &= -(\mu_1/\mu_2)(2k\nu'_1 s_1 - F_2^{(1)}) e^{-i\nu'_1\zeta_1} \\
g_{77} &= -(F_1^{(2)} s_1 + 2k\nu_2) e^{i\nu_2\zeta_1} & g_{78} &= -(2k\nu'_2 s_1 + F_2^{(2)}) e^{i\nu'_2\zeta_1} \\
g_{79} &= (\mu_1/\mu_2)(F_1^{(1)} s_1 + 2k\nu_1) e^{i\nu_1\zeta_1} & g_{70} &= (\mu_1/\mu_2)(2k\nu'_1 s_1 + F_2^{(1)}) e^{i\nu'_1\zeta_1}.
\end{aligned} \tag{A1.14}$$

For T_z at interface 1:

$$\begin{aligned}
g_{81} &= -(2k\nu_2 s_1 - F_2^{(2)}) e^{-i\nu_2\zeta_1} & g_{82} &= (F_2^{(2)} s_1 + 2k\nu'_2) e^{-i\nu'_2\zeta_1} \\
g_{83} &= (\mu_1/\mu_2)(2k\nu_1 s_1 - F_2^{(1)}) e^{-i\nu_1\zeta_1} & g_{84} &= -(\mu_1/\mu_2)(F_2^{(1)} s_1 + 2k\nu'_1) e^{-i\nu'_1\zeta_1} \\
g_{87} &= (2k\nu_2 s_1 + F_2^{(2)}) e^{i\nu_2\zeta_1} & g_{88} &= (F_2^{(2)} s_1 - 2k\nu'_2) e^{i\nu'_2\zeta_1} \\
g_{89} &= -(\mu_1/\mu_2)(2k\nu_1 s_1 + F_2^{(1)}) e^{i\nu_1\zeta_1} & g_{80} &= -(\mu_1/\mu_2)(F_2^{(1)} s_1 - 2k\nu'_1) e^{i\nu'_1\zeta_1}.
\end{aligned} \tag{A1.15}$$

At the free surface only 4 unknown potentials are involved. For T_x we need:

$$\begin{aligned}
 g_{93} &= (F_1^{(1)} s_0 - 2k\nu_1) e^{-i\nu_1 \zeta_0} & g_{94} &= -(2k\nu_1' s_0 - F_2^{(1)}) e^{-i\nu_1' \zeta_0} \\
 g_{99} &= (F_1^{(1)} s_0 + 2k\nu_1) e^{i\nu_1 \zeta_0} & g_{90} &= (2k\nu_1' s_0 + F_2^{(1)}) e^{i\nu_1' \zeta_0}.
 \end{aligned}
 \tag{A1.16}$$

Finally, for T_z at the free surface:

$$\begin{aligned}
 g_{03} &= (2k\nu_1 s_0 - F_2^{(1)}) e^{-i\nu_1 \zeta_0} & g_{04} &= -(F_2^{(1)} s_0 + 2k\nu_1') e^{-i\nu_1' \zeta_0} \\
 g_{09} &= -(2k\nu_1 s_0 + F_2^{(1)}) e^{i\nu_1 \zeta_0} & g_{00} &= -(F_2^{(1)} s_0 - 2k\nu_1') e^{i\nu_1' \zeta_0}.
 \end{aligned}
 \tag{A1.17}$$

The expressions in equations (A1.8) through (A1.17) must now be evaluated for each value of the discrete wavenumber, k_n , and for each point x at which the topography profiles are defined, remembering that the $e^{i\bar{k}x}$ factor must be included in all g_{ij} . Next, g_{ij} and h_i must be FFT'd over the x variable for each separate k_n . Then after truncating the FFT index to match the discrete-wavenumber index, the matrix, \underline{G} , and the source vector, \underline{H} , can be filled as described in Chapter 3. After solution of the linear system for the wave potentials in \underline{A} , the displacements or tractions at any location in the model can be easily computed by first making appropriate substitutions into one of equations (A1.2) or (A1.3) for displacement, and (A1.5) or (A1.6) for the stress components. The total integrated displacements are then obtained by the summation over the discrete wavenumber as in equations (A1.1). The integrated tractions are obtained from the stress components and unit normals using equations (3.9) through (3.12), where now the integrals in (3.10) are replaced by discrete summations over k_n . We should also note that equations (A1.2), (A1.3), (A1.5) and (A1.6) allow one to calculate separately the P-wave and

S-wave contributions to the displacement and traction fields by simply substituting only the Φ or Ψ potentials individually. As we demonstrated in Chapter 5, this is often very useful for understanding the effects that dominate a particular component of motion.

Finally, to extend the above formulation to account for models with more irregular interfaces, all we need do is reproduce the expressions in equations (A1.12) through (A1.15) for each additional interface and update the indices p , i and j . Specifically, to expand the problem for the 3-layered models we used in Chapter 5, we proceed as follows:

Free-surface expressions: no changes

Interface 1 expressions: no changes

Interface 2 expressions: change index p in (A1.12)–(A1.15)

as $2 \rightarrow 3$ and $1 \rightarrow 2$

Interface 3 expressions: change index p in (A1.8)–(A1.11)

as $3 \rightarrow 4$ and $2 \rightarrow 3$

The resulting linear system will now have 14 integral equations in 14 unknowns and the new entries may be inserted by following the same pattern shown above in equation (A1.7) after increasing the maximum value for the indices i and j to 14 and noting carefully where the appropriate non-zero entries should be located. This is the largest problem that we were able to solve confidently on a VAX 8650 computer. Approximately 12 Mbytes of either physical or virtual memory are required to run the program for this problem. However, if physical memory is severely limited, the amount of page-faulting required to run in virtual memory will greatly increase the amount of real time needed to solve the large linear system. This is also dependent

on the efficiency of the subroutine used to perform the LU decomposition and Gaussian elimination. The VAX 8650 that we used at Los Alamos provided almost all of the needed memory as physical storage, and one run for a single frequency with the 3-layered models required approximately 30 minutes of CPU time. A significant improvement to these storage and CPU requirements could probably be obtained by taking advantage of the sparsity of the linear system, which increases dramatically as more interfaces are added to the problem. We attempted this for the present 3-layered case using an iterative conjugate-gradient method for solution. We found that this method, although requiring less storage, took almost four times as much CPU as used by the straight Gaussian elimination method. This was due to the large number of iterations needed before the solution would converge. There may be better methods which reduce both storage and CPU time and we highly recommend that these should be tried. In the mean time, copies of the program code used in this thesis are freely available from the author upon request.

APPENDIX 2

A Versatile Equalization Circuit for Increasing Seismometer Velocity Response Below the Natural Frequency

by Peter M. Roberts

(in press, *Bull. Seism. Soc. Am.*, 1989)

ABSTRACT

A versatile and easily implemented circuit is described which increases the velocity amplitude response of seismometers below their natural frequency in order to extend the useful bandwidth to lower frequencies. The circuit employs a simple design which counteracts the ω^2 rolloff of the seismometer by cascading two 1-pole active low-pass filters in series. The low-pass stages are each summed with the unfiltered signal to maintain a flat unity amplitude response near and above the natural frequency. The design, testing and field implementation are described for a version of the circuit used with Mark Products L4-C 1.0 Hz seismometers. The design produced a nominally flat response extending down to 0.1 Hz with tolerable stability over a wide range of ambient temperatures. Design procedures are described so that the circuit may be easily modified for any arbitrary natural frequency and range of desired equalization. The circuit can be installed very easily in nearly any recording equipment with minimal modification of existing circuitry. An example is shown of the measured and theoretical amplitude and phase responses for an existing seismic event recorder with and without the equalization circuit installed. The agreement between the measured and theoretical responses is excellent for both of these instrument configurations.

INTRODUCTION

The concept of boosting short-period seismometer signals below the natural frequency to obtain better signals at longer periods is not new. This has been accomplished before by authors such as *Daniel* [1979] and *Prothero & Schaecher* [1984]. The obvious advantages of this approach over the use of intermediate-period sensors include increased ease of field installation, better tolerance to temperature and leveling effects, and the lower cost of short-period transducers. The circuit described here provides a gain boost inversely proportional to the ω^2 rolloff of the seismometer velocity amplitude response below its natural frequency, f_{nat} . The boost is applied over the frequency range of $0.1 f_{\text{nat}}$ to f_{nat} . The circuit gain flattens out to unity above this range and to a large constant factor below this range. This is accomplished by cascading two identical stages in series, each composed of a 1-pole active low-pass filter, a unity-gain amplifier and a summing amplifier.

The circuit described by *Daniel* [1979] is similar in that it provides the ω^{-2} amplification below f_{nat} , but it does not include the summation section needed to maintain a flat response above f_{nat} . Thus its resulting response is intermediate-period rather than broadband. *Prothero & Schaecher* [1984] have described a successful broadband instrument with a useful bandwidth from 0.05 Hz to 10 Hz using 1.0 Hz seismometers. Their equalization circuit is integrated into a complete seismic amplifier section (W. Prothero, personal communication, 1987) and provides an increase in gain of approximately 100 at 0.05 Hz relative to the gain at 1.0 Hz. The alternative circuit presented here provides a gain boost of 100 at 0.1 Hz relative to 1.0 Hz, yielding the correct ω^{-2} behavior. Furthermore, it is designed to be more useful for modifying existing recording equipment since there is no need to replace

or alter the amplifier or anti-aliasing filter sections. The cost of making the design general-purpose, however, is an increase in power consumption over the Prother & Schaecher design. This increase is due to the use of 6 op-amps to accomplish the equalization as opposed to only 2 for their design. The 6 op-amps totaled consume approximately 0.03 Watts of power on both the positive and negative 5-volt power supplies. For most existing instruments this will be a small price to pay for the increased bandwidth.

The design, construction, testing and field implementation of the present circuit were all performed in preparation for a teleseismic experiment in the Jemez Mountains of New Mexico during 1987 [Roberts *et al.*, 1987]. The circuits were installed in existing portable digital event recorders, described in Fehler & Chouet [1982], which were originally designed for recording short-period local earthquakes. Figure A2.1 is a block diagram of a single recording channel, showing where the two equalization stages were inserted in the analog circuitry of the instruments. The dashed line indicates the old connection from the preamp output for the unequalized configuration. Other than some minor re-wiring, no modifications were made to any existing instrument components. The extended bandwidth greatly increased the ability of the instruments to detect and record small first arrivals for teleseisms as far away as 10,000 km ($\Delta \approx 90^\circ$) with magnitudes at this distance as small as $m_b = 5.5$. The following describes the design, testing and implementation of this circuit in sufficient detail that it may be reproduced as is, or easily modified by those with little working knowledge of electronic circuit theory.

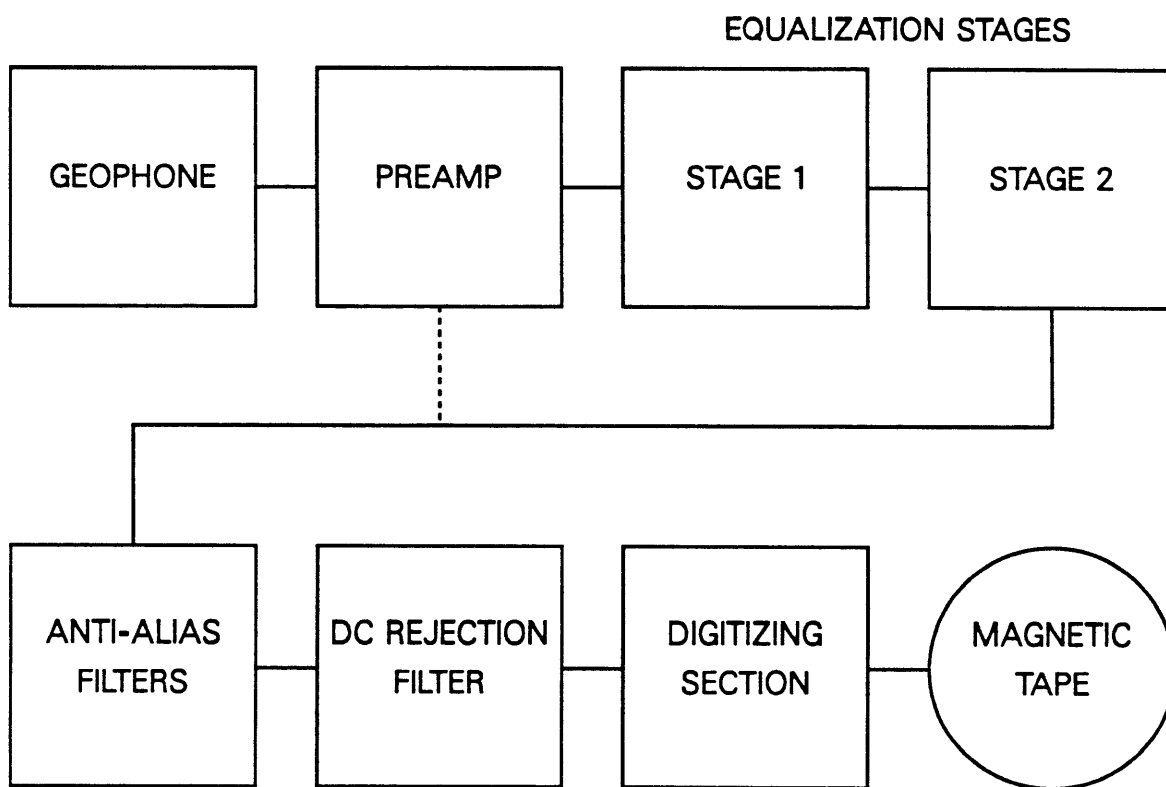


Figure A2.1 Schematic block diagram of circuit components for a single recording channel in the instruments used in the Jemez Mountains. The locations of the two equalization stages are shown in the middle of the analog signal path. The dashed line indicates the old connection for the unequalized configuration.

CIRCUIT DESIGN

The circuit presented here was specifically designed to equalize the velocity amplitude response down to 0.1 Hz for Mark Products L4-C seismometers with $f_{nat} = 1.0$ Hz. The theoretical seismometer velocity response function may be written as [e.g., *Aki & Richards*, 1980]:

$$V(\omega) = \frac{-G\omega^2}{(\Omega^2 - \omega^2) + 2i\omega\zeta\Omega} \quad (\text{V/cm/sec}), \quad (\text{A2.1})$$

where G = transducer sensitivity (V/cm/sec), ω = angular frequency ($2\pi f$), $\Omega = 2\pi f_{nat}$ and ζ = damping constant. The output voltage amplitude response for a constant input ground velocity is flat and proportional to G for frequencies above Ω and decays as ω^{-2} below Ω . In order to extend the flat portion to lower frequencies, a boost in gain must be applied which varies as ω^{-2} over the desired range of equalization, defined from f_{nat} down to the chosen low frequency cutoff of the applied gain boost, f_{eq} . For the present application a factor of 100 boost is required at $f_{eq} = 0.1$ Hz and the gain must flatten out to unity near and above $f_{nat} = 1.0$ Hz.

The simplest way to accomplish this is to sum an active 2-pole low-pass filter with a unity-gain amplifier, requiring only 3 op-amps. However, this design suffers from partial amplitude cancellation for signals near 1.0 Hz. This problem occurs over a narrow band of frequencies around $f = f_{nat}$ where the 2-pole filter gain is near unity and its signal polarity is inverted due to a -180° phase shift (-90° for each filter pole). Summation of the 2-pole filter with a zero-shift unity-gain amplifier will produce a net output gain less than unity for these frequencies, resulting in a narrow trough around $f = f_{nat}$ in the combined amplitude response. To avoid this problem

and maintain simplicity of design procedures it was necessary to split the 2-pole filter stage into two separate 1-pole filters and sum each of these independently with its own unity-gain amplifier. Since the maximum phase shift of a 1-pole filter is -90° (near and above f_{nat}) its signal polarity is never inverted and the net gain after summation will never be less than unity. More details on this are given below. The complete 2-pole equalization is then achieved by cascading two identical 1-pole summation stages in series, requiring 6 op-amps.

Proceeding with the design, the transfer function for a 1-pole active low-pass filter is [e.g., *Anderson & Beeman, 1973*]:

$$L(\omega) = \frac{A}{1 + i\omega RC} \quad (\text{V/V}), \quad (\text{A2.2})$$

where A = signal gain at $\omega = 0$ (DC) and RC = time constant (secs) corresponding to the desired low-pass corner frequency. Summation of this circuit with a unity-gain stage forces the net gain back to unity for frequencies at which the low-pass amplitude response is much less than unity. The total response of one summation stage is then given by:

$$T(\omega) = 1 + \frac{A}{1 + i\omega RC} \quad (\text{V/V}), \quad (\text{A2.3})$$

Finally, the response function for the 2-stage cascaded circuit is simply the square of equation (A2.3) and its DC gain is $(1 + A)^2$.

The specific design of the cascaded circuit for a particular application amounts to simply choosing appropriate values for A and RC as follows. The corner frequency of the low-pass filter, given by $f_c = 1/(2\pi RC)$, corresponds to the so-called 3db point

on the 1-pole amplitude response curve. Since the response does not have a sharp corner at f_c it is necessary to choose the 3db point at a frequency sufficiently lower than the desired equalization cutoff frequency, f_{eq} , to obtain the proper gain. A practical rule-of-thumb is to choose $f_c \leq 0.5 f_{eq}$, which is low enough to place f_{eq} well within the strictly ω^{-2} portion of the response. Then by setting $RC = 1/(2\pi f_c)$ and $\omega_{eq} = 2\pi f_{eq}$, we can solve for the correct 1-pole filter DC gain, A, by first equating the two-stage cascaded circuit amplitude response with the inverse seismometer amplitude response, both evaluated at ω_{eq} :

$$|T(\omega_{eq})|^2 = |V(\omega_{eq})|^{-1}. \quad (A2.4)$$

By putting ω_{eq} and RC, determined as above, into the squared modulus of equation (A2.3) and putting ω_{eq} , $\Omega = 2\pi f_{nat}$, ζ and $G = 1.0$ into the inverse modulus of equation (A2.1) and equating the two results, a quadratic equation results which can be solved to determine A:

$$\begin{aligned} aA^2 + bA + c &= 0, \\ \text{where : } a &= \frac{1}{1 + (\omega_{eq}RC)^2}, \quad b = 2a, \\ \text{and : } c &= 1 - \frac{[(\Omega^2 - \omega_{eq}^2)^2 + 4(\omega_{eq}\zeta\Omega)^2]^{1/2}}{\omega_{eq}^2}. \end{aligned} \quad (A2.5)$$

All that remains now is to choose the proper circuit components to approximate the theoretical values for A and RC determined above.

Figure A2.2 shows the theoretical amplitude and phase response curves for a 1.0 Hz seismometer, the two-stage cascaded equalization circuit and the combined

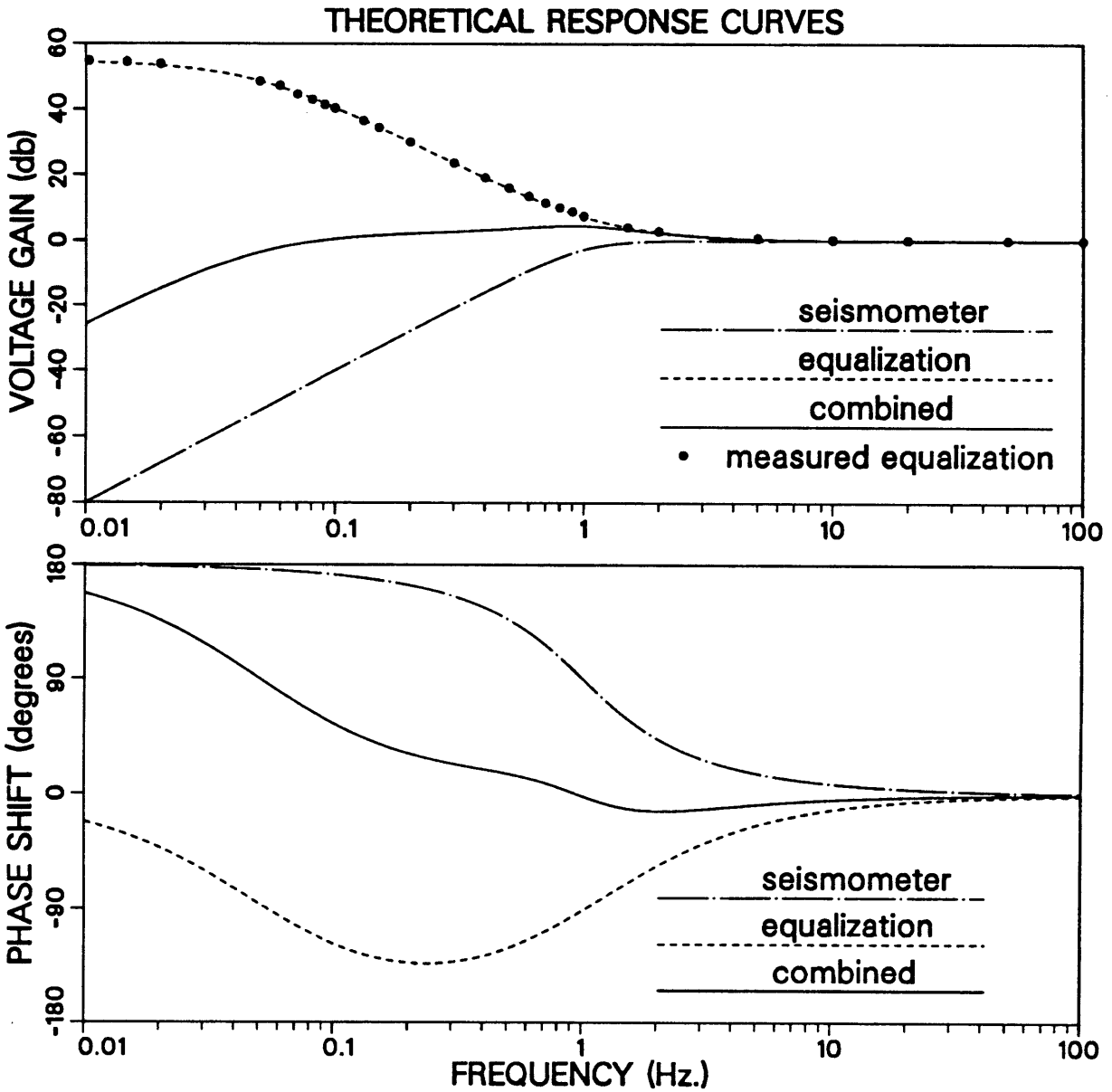


Figure A2.2 Theoretical amplitude (top) and phase (bottom) response curves for a 1.0 Hz seismometer (dash-dot), 0.1 Hz cascaded equalization circuit (dash) and the combination of these two components (solid). Dots on the amplitude plot are laboratory measurements of gain at selected frequencies for the prototype equalization circuit.

results for an equalized amplitude response down to $f_{eq} = 0.1$ Hz. The seismometer response curves were calculated using equation (A2.1) with the constants $\Omega = 2\pi$, $\zeta = 0.7$ and $G = 1.0$ so that the amplitude plot represents voltage output gain (in db) for a constant input ground velocity of 1.0 cm/sec. The two-stage equalization curves were calculated using the square of equation (A2.3) with design parameters $RC = 3.234$ secs ($f_c = 0.0492$ Hz) and $A = 22.1$, which were limited by available resistor and capacitor values. The actual solution to equation (A2.5) above yields $A = 21.6$. The dots on the amplitude plot are laboratory measurements of the voltage gain at selected frequencies for a prototype 2-stage circuit. The agreement with the theoretical curve is quite good. Unfortunately, laboratory measurements of the circuit's phase response could not be made accurately with the test equipment available to the author. However, the measured total phase response of an equalized instrument, shown later in this paper, agrees well with the theoretical instrument response. The maximum phase shift of the 2-stage cascaded circuit is approximately -135° near $f = 0.2$ Hz and partially counteracts the positive phase shift of the seismometer over the frequency range of interest. The phase characteristics of the combined response are certainly tolerable and easily corrected for. The combined amplitude response has a slight peak near 1.0 Hz due to the rounded corners of the seismometer and equalization curves as their gains approach unity. This is a minor departure from the ideal flat behavior and again is easily corrected for.

The amplitude cancellation problem mentioned previously for the 2-pole non-cascaded circuit may be clarified at this point. The total response function of the cascaded equalization circuit may be written simply as:

$$E_1(\omega) = T(\omega)^2 = [1 + L(\omega)]^2, \quad (A2.6)$$

whereas the response of the non-cascaded circuit would be:

$$E_2(\omega) = 1 + L(\omega)^2. \quad (A2.7)$$

If one evaluates the modulus of each of these two functions at $\omega \approx 20/RC$ (corresponding to $f \approx f_{nat} \approx 20 f_c$ for the present choice of $f_{eq} = 0.1 f_{nat}$), and using $A = 22.1$ determined previously, it can be confirmed that the gain for $E_1(\omega)$ is greater than unity (≈ 2.3) and the gain for $E_2(\omega)$ is less than unity (≈ 0.24). This is the primary reason for using the cascaded circuit.

Figure A2.3 shows the schematic circuit diagram for a single 1-pole summation stage. The complete 2-pole circuit is obtained by cascading two of these identical 1-pole stages in series. The component values listed in Table A2.1 produce the response shown in Figure A2.2.

TABLE A2.1
Circuit Component Values for
0.1 to 1.0 Hz Equalization Range

Component	Value
R_1, R_3	66.5 K Ω
R_2	1.47 M Ω
R_4 (pot)	100 K Ω
R_5, R_6	100 K Ω
R_7, R_{11}	49.9 K Ω
R_8, R_9, R_{10}	150 K Ω
C_1	2.2 μ F
OP-AMP	LM-312

Design parameters A and RC are controlled by the components R_1, R_2 and C_1 as:

$$A = R_2/R_1, \quad \text{and} \quad RC = R_2 C_1. \quad (A2.8)$$

For stability reasons each op-amp circuit uses the inverting configuration but the polarity is correct at the output of each stage since there are an even number of

1-POLE SUMMATION CIRCUIT SCHEMATIC DIAGRAM

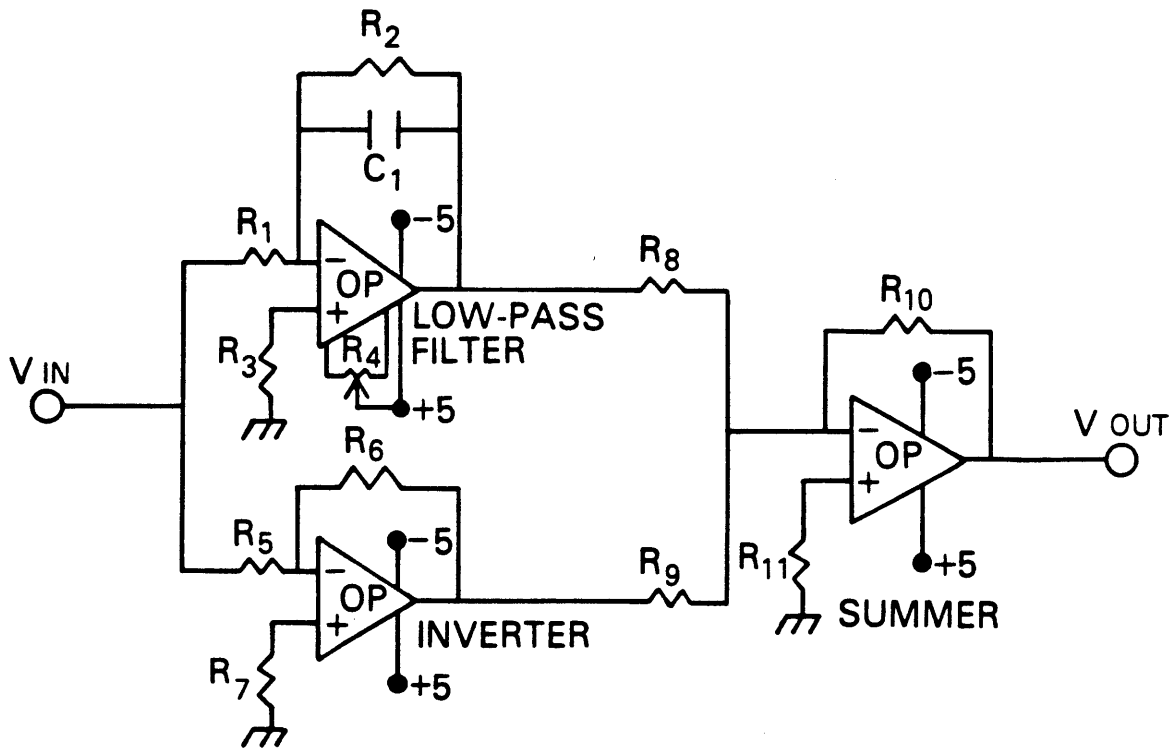


Figure A2.3 Schematic diagram for the prototype 1-pole summation circuit described in the text. Two of these circuits in series will yield the correct equalization. Component values listed in Table A2.1 for this circuit will produce the cascaded response shown in Figure A2.2.

inversions in series. Modifications for different natural frequencies require changes only in the components R_1 , R_2 , R_3 and C_1 . R_3 should approximately equal the equivalent parallel resistance combination of R_1 and R_2 . The trimming potentiometer, R_4 , is required to remove DC offset at the output of each summation stage. This adjustment can be very critical due to the high gain present for DC inputs. An advantage of the cascaded design is that offset adjustments can be made separately for each 1-pole filter. It is much easier to fine tune this adjustment when the DC gain is A (as for a 1-pole filter) rather than A^2 (as for a 2-pole filter). Also, ambient temperature changes can cause changes in the op-amp input offset currents, which in turn are greatly amplified by the low-pass filters. Therefore it is necessary to include an additional high-pass filter in the signal path after the second summation stage to remove large variable DC offsets which could saturate the pre-existing analog circuitry of the recording instruments being used. The high-pass can be a simple 1-pole RC filter with corner frequency significantly lower than f_c of the low-pass equalization filters. Most existing instruments will already have an adequate DC rejection stage incorporated into their analog circuitry, so this additional filter might be optional and is not shown here. The DC drift can be minimized by using op-amps with a sufficiently broad temperature stability range and low input offset current. LM312 op-amps were found to be adequate.

IMPLEMENTATION AND TESTING

The 2-stage equalization circuit was installed in six existing portable digital event recorders in preparation for a teleseismic earthquake field experiment in the Jemez Mountains of New Mexico during 1987 [Roberts *et al.*, 1987]. The circuit

was inserted between the seismometer preamp and the instrument anti-aliasing filters, as shown previously in Figure A2.1. Note that the DC rejection filter was located immediately after the anti-aliasing filters. The same instruments were used previously for local earthquake and volcanic tremor studies at Mount St. Helens and are described in *Fehler & Chouet* [1982]. They were also used by the present author in 1986, prior to installing the equalization, to try to obtain teleseismic data in the Jemez Mountains. During 3 months of field operation only 2 teleseisms were recorded at all six sites and the records at several sites were missing the first arrival because the system did not trigger soon enough. The experiment was repeated in 1987 after installing the equalization and modifying the response of the event detection circuitry for compatibility with the extended frequency band. This time, during a 3 month period, approximately 30 teleseismic events were recorded at all six sites, nearly all of which contained clear and often small first arrivals. The furthest events recorded originated in Japan and the Tonga and Mariana Trenches, with epicentral distances of about 10,000 km ($\Delta \approx 90^\circ$). At these distances the smallest events recorded were magnitude $m_b = 5.5$.

Figure A2.4 shows a typical vertical component seismogram for a teleseismic event recorded during the 1987 experiment. Superimposed on the teleseismic signal is a large noise component with a period of about 10–20 secs. This noise component may have been produced either by wind noise or by microseismic oceanic tremor. This type of low-frequency signal would not be visible in a normal short-period recording. This demonstrates that the equalization circuit succeeds in boosting previously unseen intermediate-period signals to an observable level. Low-frequency

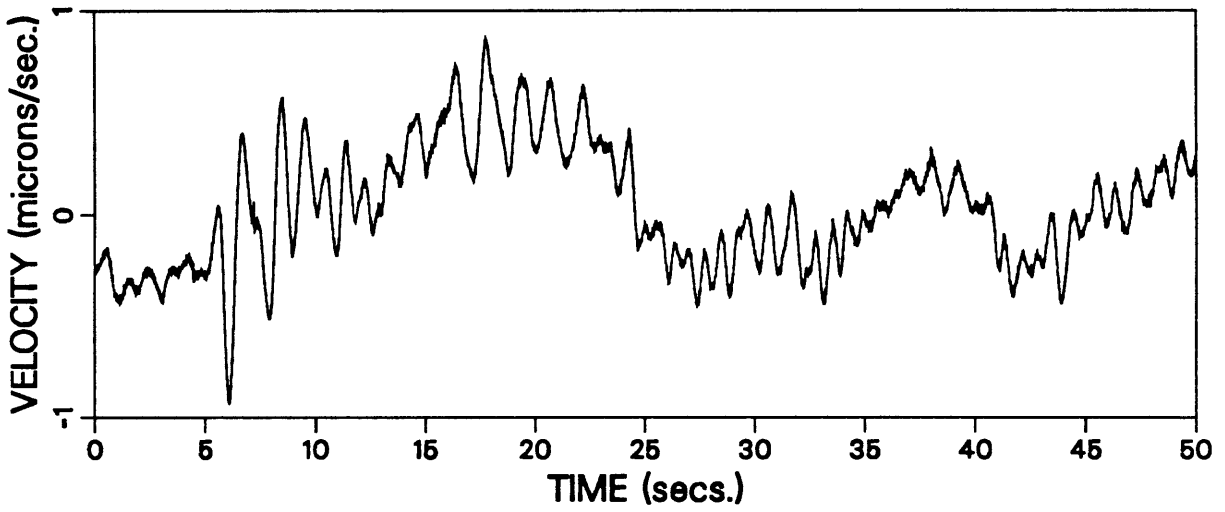


Figure A2.4 Typical vertical component P-Wave seismogram for a teleseismic event recorded in the Jemez Mountains in 1987 on an equalized instrument.

noise contamination can be easily removed through subsequent data processing techniques, if desired.

When using any extended-bandwidth instrument one must be aware of the corresponding increase in dynamic range of possible signal amplitudes which could be recorded. Ideally it is desirable to have the capability to record small micro-earthquakes with high resolution as well as large teleseisms or surface waves without the signals clipping. These extremes can easily cover an amplitude range at least six orders of magnitude wide (120 db). Depending on the dynamic range of the recorder being used, there may be a tradeoff involved in choosing the best overall system gain. Gains typically used to record small short-period earthquakes ($m_b \approx 2.0$ or less) may cause large recorded teleseisms ($m_b \approx 5.0$ or greater) to be clipped. Reducing the gain enough to eliminate clipping may result in poor resolution for micro-earthquakes. So with limited dynamic recording range (perhaps < 60 db) it may be necessary to sacrifice either the highest or lowest portions of the instrument bandwidth. During the 1987 Jemez experiment, using the equalized instruments with a dynamic recording range of 72 db, the overall system gain was reduced from the previous (unequalized) setting by a factor of approximately 1/4 (from ~ 2000 in 1986 to ~ 500 in 1987 using the L4-C seismometers). Only two events recorded in 1987 were clipped using the reduced gain setting. These were a magnitude 7.7 earthquake from the Gulf of Alaska ($\Delta \approx 33^\circ$) and a 6.2 from California ($\Delta \approx 8^\circ$).

To test the actual response of an entire instrument both with and without the equalization installed, an input step in acceleration was applied to the seismometer's calibration coil and the resulting velocity signals were recorded for both the equalized and unequalized instrument configurations. The high-pass DC rejection

filter mentioned earlier was included in both of these configurations. The resulting time series, with peak amplitudes normalized to unity, are plotted in Figure A2.5 and their Fourier amplitude and phase spectra up to ~ 5.0 Hz are shown in Figures A2.6 and A2.7 respectively. The unequalized time series was padded with zeros at the end to obtain a 68 sec width Fourier Transform window identical to that used for the equalized signal. The transform windows were started as close as possible to the first motion of the pulses in order to remove the phase components associated with a non-zero arrival time. The spectra have been converted to the equivalent velocity impulse response by multiplying the step acceleration response by $-\omega^2$.

The amplitude response plots (Figure A2.6) were corrected for differences in instrument gain by normalizing them to unity gain (0 db) at 2.0 Hz for the unequalized spectrum and at 0.2 Hz for the equalized spectrum. The theoretical amplitude and phase response curves for each case are also plotted in Figures A2.6 and A2.7 for comparison. The theoretical curves were calculated using equations (A2.1) and (A2.3) and the transfer function for the DC rejection filter. These plots confirm that the equalization circuit succeeds in shifting the instrument's low-end cutoff frequency from 1.0 Hz down to 0.1 Hz and that the actual measured response below 2.0 Hz approximates the theoretical curves quite well for both amplitude and phase. Differences between these plots and the combined response curves shown in Figure A2.2 are due to the DC rejection filter.

The background noise level above 1.0 Hz was very high when the equalized calibration signal was recorded, and this noise dominates the amplitude and phase spectra above ~ 2.0 Hz. This is because the actual velocity amplitude response to an input step in acceleration decays as ω^{-2} (ω^{-1} for the spectral behavior of a step

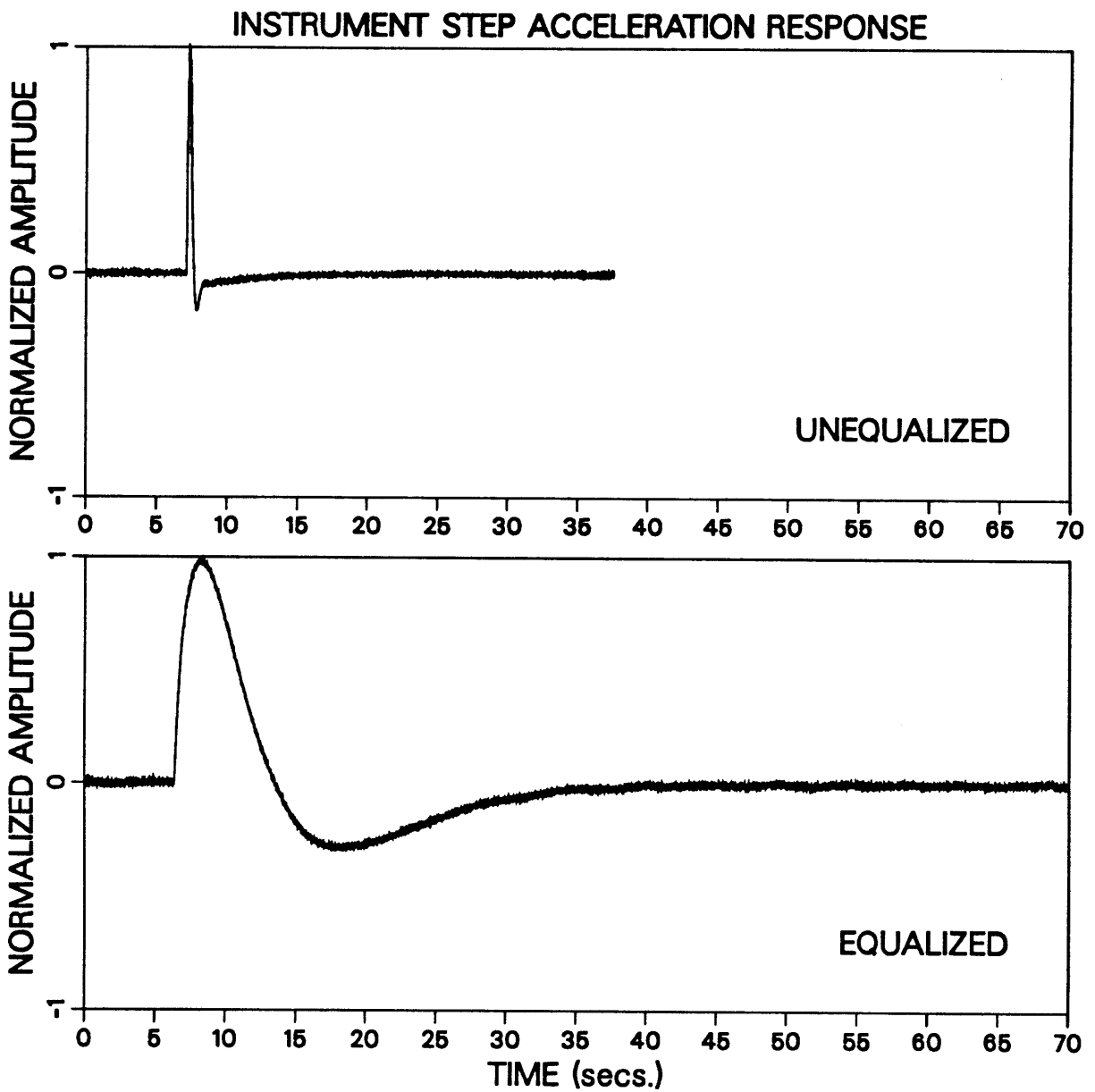


Figure A2.5 Equalized (bottom) and unequalized (top) velocity signals generated by an input step acceleration to the seismometer calibration coil and recorded on one of the instruments used in the Jemez Mts. Plots are normalized to unity peak amplitude.

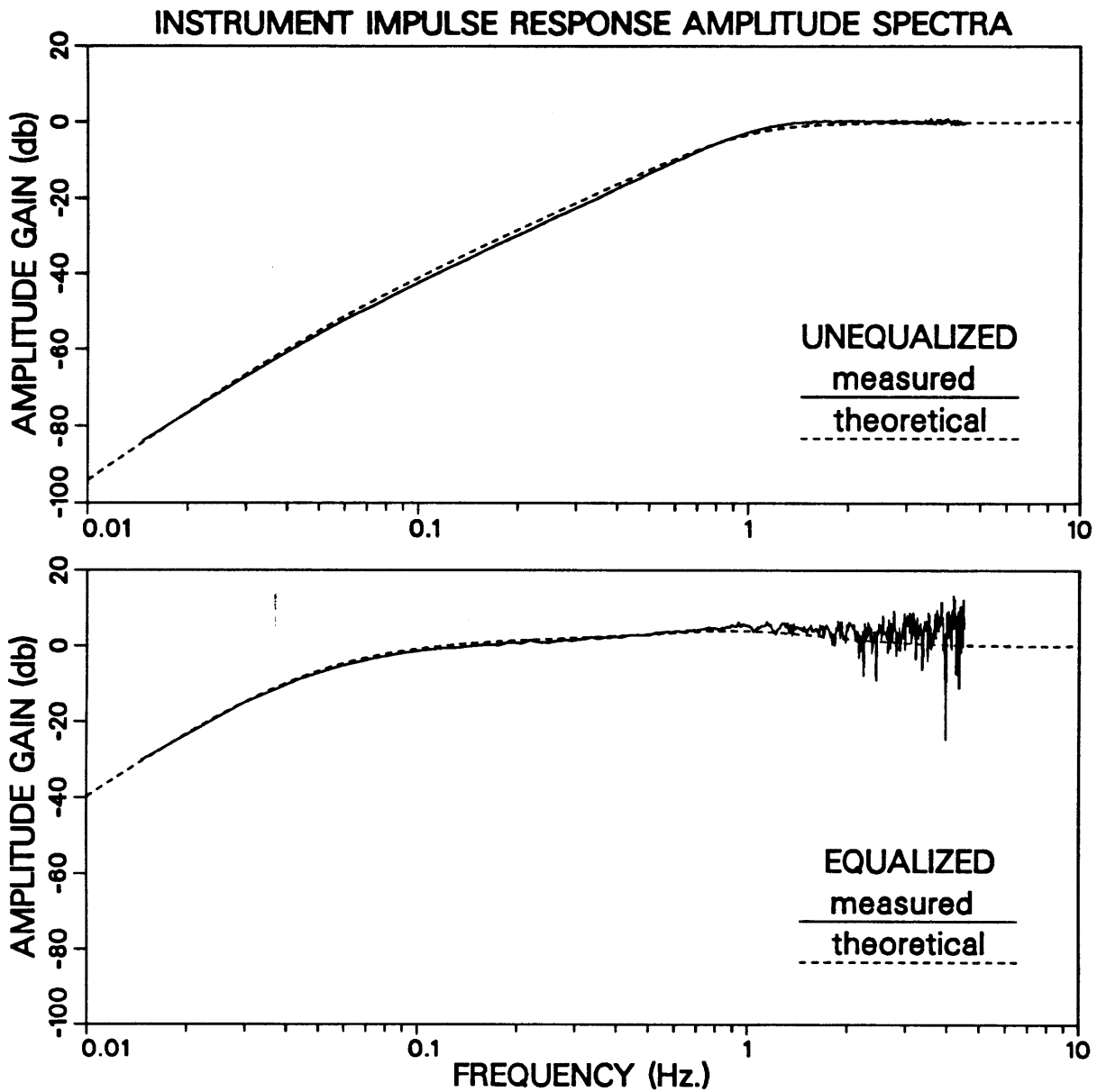


Figure A2.6 Measured (solid) and theoretical (dash) velocity impulse amplitude response curves for unequalized (top) and equalized (bottom) instrument configurations. Measured curves were obtained by multiplying the Fourier Transforms of the signals in Figure A2.5 by $-\omega^2$ and computing the modulus. Data windowing and normalization for the measured plots are described in the text. Theoretical curves were computed using equations (A2.1) and (A2.3) and the DC rejection filter response function.

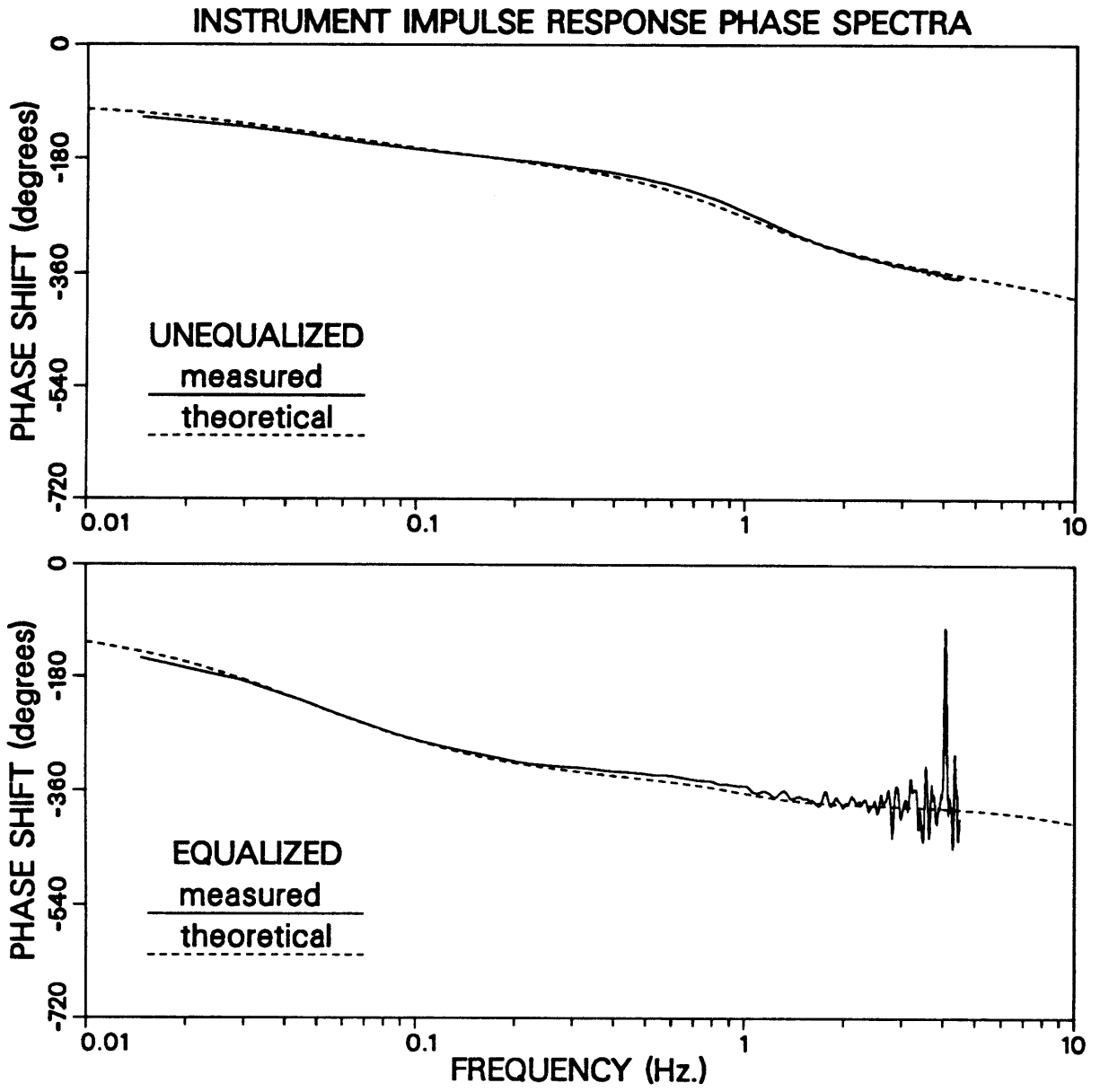


Figure A2.7 Measured (solid) and theoretical (dash) phase response curves for unequaled (top) and equalized (bottom) instruments. Phase angles were computed from the same Fourier Transforms and response functions used in Figure A2.6.

function and another ω^{-1} for the conversion of acceleration to velocity). So the signal-to-noise ratio above a certain frequency can become very low for this type of input in the presence of moderate noise. Unless performed in an extremely quiet environment, the step acceleration test is rarely sufficient for measuring instrument response much above 5-10 Hz. However, as shown in Figures A2.6 and A2.7, it is often quite good for determining the lower frequency portion of the response. It is certainly adequate here for demonstrating the effect of the equalization over the 0.1 to 1.0 Hz band. More rigorous methods [e.g., *Sauter & Dorman*, 1986] should be employed to measure the response and system-related noise over the entire extended bandwidth of the equipment before being used in the field. Further discussions of total instrument response and noise tests, however, are beyond the scope of this paper. It is advisable, though, to test at least the low-frequency system noise for any instrument containing the equalization circuit. This can be done by recording a test signal with either the geophone mass clamped or with a resistor replacing the geophone input. Any slow variations from zero volts at the output will be attributable to the electronics noise in the equalization circuit.

As mentioned previously, the extreme sensitivity of the equalization circuit to small DC signals at the input and changes in op-amp input offset currents with temperature create the potential of saturating subsequent analog stages in the instrument. This is especially true if the DC rejection filter is far-removed from the output of the equalization circuit. For this reason it should become a matter of routine during field servicing of the instruments to monitor and null out any DC offset at the output of each 1-pole stage with the trimming pots. However, the

author's experience with this circuit in the field has been that the DC stability increases with time and offset adjustments become unnecessary after several weeks of continuous operation. Typical measured offsets after this initial time period rarely exceeded 100 mV at the second-stage output and usually were less than 50 mV. Typical ambient temperatures encountered during the experiment reached as high as approximately $+38^{\circ}$ C at midday in the summer and as low as -5° C at night in mid-autumn. The DC drift under these severe conditions never became large enough to cause saturation and data loss.

CONCLUSION

A versatile circuit has been described which can increase seismometer signal levels for frequencies below the natural frequency of the sensors, thereby allowing increased bandwidths for existing short-period recorder systems. The simplicity of design procedures makes it readily understandable and easily modified and implemented without extensive knowledge of electronics. The circuit has been tested in the laboratory and in the field and has been proven to perform reliably under severe climatic conditions. The ability to detect and record teleseismic events is greatly increased through the use of this circuit.

ACKNOWLEDGMENTS

This work was partially funded by DOE contract number DE-FG03-87ER-13807 to Professor Keiiti Aki of the University of Southern California. Additional support was provided by the Earth and Space Sciences Division of the Los Alamos National Laboratory. Walter Cook of M.I.T. suggested the basic single-stage circuit

used here as the building block for the eventual working design. Bill Prothero of U.C. Santa Barbara provided valuable suggestions and precautions based on his field experience with the *Prothero & Schaecher* [1984] design. He also kindly provided the author with detailed schematic diagrams for their circuit which were very useful for comparisons with the present design. Special thanks go to Mike Fehler and Jim Albright of the Hot Dry Rock Geothermal Energy Group (ESS-4) at LANL for their encouragement in undertaking this work and for providing valuable laboratory facilities.

REFERENCES

- Aki, K. and K. L. Larner, 1970. Surface Motion of a Layered Medium Having an Irregular Interface Due to Incident Plane SH Waves, *J. Geophys. Res.*: **75**, 933-954.
- Aki, K. and P. G. Richards, 1980. *Quantitative Seismology, vols. 1 & 2*, W. H. Freeman and Company, San Francisco, 932 pp.
- Aki, K., A. Christofferson and E. S. Husebye, 1976. Determination of the 3-Dimensional Seismic Structures of the Lithosphere, *J. Geophys. Res.*: **82**, 277-296.
- Aki, K., B. Chouet, M. Fehler, G. Zandt, R. Koyanagi, J. Colp and R. G. Hay, 1978. Seismic Properties of a Shallow Magma Reservoir in Kilauea Iki by Active and Passive Experiments, *J. Geophys. Res.*: **83**, 2273-2282.
- Aldrich, M. J., 1986. Tectonics of the Jemez Lineament in the Jemez Mountains and Rio Grande Rift, *J. Geophys. Res.*: **91**, 1753-1762.
- Aldrich, M. J. and A. W. Laughlin, 1984. A model for the Tectonic Development of the Southeastern Colorado Plateau Boundary, *J. Geophys. Res.*: **89**, 10207-10218.
- Anderson, L. W. and W. W. Beeman, 1973. *Electric Circuits and Modern Electronics*, Holt, Rinehart and Winston, New York, pp. 137-142.
- Ankeny, L. A., L. W. Braile and K. H. Olsen, 1986. Upper Crustal Structure Beneath the Jemez Mountains Volcanic Field, New Mexico, Determined by Three-Dimensional Simultaneous Inversion of Seismic Refraction and Earthquake Data, *J. Geophys. Res.*: **91**, 6188-6198.
- Azimi, Sh. A., A. Y. Kalinin, V. B. Kalinin and B. L. Pivovarov, 1968. Impulse and Transient Characteristics of Media with Linear and Quadratic Absorption Laws, *Izv. Earth Phys.*: **2**, 42-54.
- Baldrige, W. S., K. H. Olsen and J. C. Callender, 1984. Rio Grande Rift: Problems and Perspectives, in *Rio Grande Rift: Northern New Mexico*, New Mexico Geological Society Guidebook, 35th Field Conference, pp. 1-11.
- Bard, P.-Y. and M. Bouchon, 1980a. The Seismic Response of Sediment-Filled Valleys. Part 1. The Case of Incident SH Waves, *Bull. Seism. Soc. Am.*: **70**, 1263-1286.

- Bard, P.-Y. and M. Bouchon, 1980b. The Seismic Response of Sediment-Filled Valleys. Part 2. The Case of Incident P and SV Waves, *Bull. Seism. Soc. Am.*: **70**, 1921-1941.
- Bard, P.-Y. and M. Bouchon, 1985. The Two-Dimensional Resonance of Sediment-Filled Valleys, *Bull. Seism. Soc. Am.*: **75**, 519-541.
- Bard, P.-Y. and B. E. Tucker, 1985. Underground and Ridge Site Effects: A Comparison of Observation and Theory, *Bull. Seism. Soc. Am.*: **75**, 905-922.
- Bard, P.-Y. and J.-C. Gariel, 1986. The Seismic Response of Two-Dimensional Sedimentary Deposits with Large Vertical Velocity Gradients, *Bull. Seism. Soc. Am.*: **76**, 343-346.
- Boore, D. M., K. L. Lerner and K. Aki, 1971. Comparison of Two Independent Methods for the Solution of Wave-Scattering Problems: Response of a Sedimentary Basin to Vertically Incident SH Waves, *J. Geophys. Res.*: **76**, 558-569.
- Borcherdt, R. D., 1973. Energy and Plane Waves in Linear Viscoelastic Media, *J. Geophys. Res.*: **78**, 2442-2453.
- Borcherdt, R. D., 1977. Reflection and Refraction of Type-II S Waves in Elastic and Anelastic Media, *Bull. Seism. Soc. Am.*: **67**, 43-67.
- Bouchon, M., 1973. Effect of Topography on Surface Motion, *Bull. Seism. Soc. Am.*: **63**, 615-632.
- Bouchon, M., 1976. Discrete Wavenumber Representation of Seismic Wave Fields with Application to Various Scattering Problems, Ph.D. thesis, Mass. Inst. of Technol., Cambridge.
- Bouchon, M., 1979. Discrete Wavenumber Representation of Elastic Wave Fields in Three Space Dimensions, *J. Geophys. Res.*: **84**, 3609-3614.
- Bouchon, M. and K. Aki, 1977. Discrete Wavenumber Representation of Seismic-Source Wave Fields, *Bull. Seism. Soc. Am.*: **67**, 259-277.
- Bridwell, R. L., 1976. Lithospheric Thinning and the Late Cenozoic Thermal and Tectonic Regime of the Northern Rio Grande Rift, in *Vermejo Park*, New Mexico Geological Society Guidebook, 27th Field Conference, pp. 283-292.
- Brigham, E. O., 1974. *The Fast Fourier Transform*, Prentice-Hall, Inc., Englewood Cliffs, N.J., 252 pp.
- Buchen, P. W., 1971. Plane Waves in Linear Viscoelastic Media, *Geophys. J. R. Astr. Soc.*: **23**, 531-542.

- Chouet, B., 1976. Source Scattering and Attenuation Effects on High Frequency Seismic Waves, Ph.D. thesis, Mass. Inst. of Technol., Cambridge.
- Clayton, R. W. and R. A. Wiggins, 1976. Source Shape Estimation and Deconvolution of Teleseismic Bodywaves, *Geophys. J. R. Astr. Soc.*: **47**, 151-177.
- Cooper, H. F. and E. L. Reiss, 1966. Reflection of Plane Viscoelastic Waves from Plane Boundaries, *J. Acoust. Soc. Am.*: **39**, 1133-1138.
- Daniel, R. G., 1979. An Intermediate-Period Field System Using A Short-Period Seismometer, *Bull. Seism. Soc. Am.*: **69**, 1623-1626.
- Davis, P. M., E. C. Parker, J. R. Evans, H. M. Iyer and K. H. Olsen, 1984. Teleseismic Deep Sounding of the Velocity Structure Beneath the Rio Grande Rift, in *Rio Grande Rift: Northern New Mexico*, New Mexico Geological Society Guidebook, 35th Field Conference, pp. 29-38.
- Doell, R. R., G. B. Dalrymple, R. L. Smith and R. A. Bailey, 1968. Paleomagnetism, Potassium-Argon Ages, and Geology of Rhyolites and Associated Rocks of the Valles Caldera, New Mexico, *Mem. Geol. Soc. Am.*: **116**, 211-248.
- Dondanville, R. F., 1971. The Hydrothermal Geology of the Valles Caldera, Jemez Mountains, New Mexico, open file report, Union Oil Co., Santa Rosa, Calif., 36 pp.
- Dondanville, R. F., 1978. Geologic Characteristics of the Valles Caldera Geothermal System, New Mexico, *Trans. Geotherm. Resour. Council*: **2**, 157-160.
- Evans, J. R., 1981. Fortran Computer Programs for Running Median Filters and a General Despiker, *U. S. Geol. Survey open file report*: **81-1091**, 17 pp.
- Fehler, M. and B. Chouet, 1982. Operation of a Digital Seismic Network on Mt. St. Helens Volcano and Observations of Long Period Seismic Events that Originate under the Volcano, *Geophys. Res. Lett.*: **9**, 1017-1020.
- Fehler, M., P. Roberts and T. Fairbanks, 1988. A Temporal Change in Coda Wave Attenuation Observed During an Eruption of Mount St. Helens, *J. Geophys. Res.*: **93**, 4367-4373.
- Felch, R. N., 1987. A Study of the Seismic Structure in the Valles Caldera Region of Northern New Mexico, Ph.D. thesis, Penn. State Univ., State College, 251 pp.
- Gardner, J. N., F. Goff, S. Garcia and R. C. Hagan, 1986. Stratigraphic Relations and Lithologic Variations in the Jemez Volcanic Field, New Mexico, *J. Geophys. Res.*: **91**, 1763-1778.

- Goff, F. and C. O. Grigsby, 1982. Valles Caldera Geothermal Systems, New Mexico, U.S.A., *J. Hydrol.*: **56**, 119-136.
- Goff, F. and J. N. Gardner, 1988. Valles Caldera Region, New Mexico, and the Emerging Continental Scientific Drilling Program, *J. Geophys. Res.*: **93**, 5997-5999.
- Goff, F., J. Rowley, J. N. Gardner, W. Hawkins, S. Goff, R. Charles, L. Pisto, A. White, J. Eichelberger and L. Younker, 1984. Valles Caldera no. 1, a 856 m. Corehole in the Southwestern Ring-Fracture Zone of the Valles Caldera, New Mexico, *EOS, Trans. Am. Geophys. Un.*: **65**, 1096.
- Goff, F., J. Rowley, J. N. Gardner, W. Hawkins, S. Goff, R. Charles, D. Wachs, L. Massen and G. Heiken, 1986. Initial Results from VC-1: First Continental Scientific Drilling Program Core Hole in the Valles Caldera, New Mexico, *J. Geophys. Res.*: **91**, 1742-1752.
- Goff, F., J. N. Gardner, W. S. Baldrige, J. B. Hulen, D. L. Nielson, D. Vaniman, G. Heiken, M. A. Dungan and D. Broxton, 1989. Volcanic and Hydrothermal Evolution of the Valles Caldera and Jemez Volcanic Field: Field Excursion 17B, submitted to *IAVCEI Field Trip Guides*, New Mexico Bureau of Mines and Mineral Resources, Socorro, New Mexico.
- Harrison, T. M., Morgan P. and D. D. Blackwell, 1986. Constraints on the Age of Heating at the Fenton Hill Site, Valles Caldera, New Mexico, *J. Geophys. Res.*: **91**, 1899-1908.
- Haskell, N. A., 1953. The Dispersion of Surface Waves in Multilayered Media, *Bull. Seism. Soc. Am.*: **43**, 17-34.
- Haskell, N. A., 1960. Crustal Reflection of Plane SH Waves, *J. Geophys. Res.*: **65**, 4147-4150.
- Haskell, N. A., 1962. Crustal Reflection of Plane P and SV Waves, *J. Geophys. Res.*: **67**, 4751-4767.
- Heiken, G. and F. Goff, 1983. Hot Dry Rock Geothermal Energy in the Jemez Volcanic Field, New Mexico, *J. Volcanol. Geotherm. Res.*: **15**, 223-246.
- Heiken, G., H. Murphy, G. Nunz, R. Potter and C. Grigsby, 1981. Hot Dry Rock Geothermal Energy, *Am. Sci.*: **69**, 400-407.
- Hulen, J. B. and D. L. Nielson, 1986. Hydrothermal Alteration in the Baca Geothermal System, Redondo Dome, Valles Caldera, New Mexico, *J. Geophys. Res.*: **91**, 1867-1886.

- Johnson, A. M., 1970. *Physical Processes in Geology*, Freeman, Cooper, San Francisco.
- Knopoff, L., 1964. Q, *Rev. Geophys.*: **2**, 625-660.
- Kohketsu, K., 1987. 2-D Reflectivity Method and Synthetic Seismograms for Irregularly Layered Structures—I. SH-wave Generation, *Geophys. J. R. Astr. Soc.*: **89**, 821-838.
- Kolstad, C. D. and T. R. McGetchin, 1978. Thermal Evolution Models for the Valles Caldera with Reference to a Hot-Dry-Rock Geothermal Experiment, *J. Volc. and Geotherm. Res.*: **3**, 197-218.
- Lapwood, E. R., 1949. The Disturbance Due to a Line Source in a Semi-Infinite Elastic Medium, *Phil. Trans. Roy. Soc. London, A*: **242**, 63-100.
- Larner, K. L., 1970. Near-Receiver Scattering of Teleseismic Body Waves in Layered Crust-Mantle Models having Irregular Interfaces, Ph.D. thesis, Mass. Inst. of Technol., Cambridge, 274 pp.
- Lee, W. H. K. and S. W. Stewart, 1981. *Principles and Applications of Microearthquake Networks*, Academic Press, New York.
- Liu, H.-P., D. L. Anderson and H. Kanamori, 1976. Velocity Dispersion due Anelasticity; Implications for Seismology and Mantle Composition, *Geophys. J. R. Astr. Soc.*: **47**, 41-58.
- Lockett, F. J., 1962. The Reflection and Refraction of Waves at an Interface Between Viscoelastic Materials, *J. Mech. Phys. Solids*: **10**, 53-64.
- Lokshtanov, D. E., 1987. Method of Taking into Consideration Absorption in Calculations of Theoretical Seismograms in a Stratified Medium, *Comp. Seism.*: **20**, 192-196.
- Majer, E. L. and T. V. McEvilly, 1979. Seismological Investigations at The Geysers geothermal field, *Geophysics*: **44**, 246-269.
- Nielson, D. N. and J. B. Hulen, 1984. Internal Geology and Evolution of the Redondo Dome, Valles Caldera, New Mexico, *J. Geophys. Res.*: **89**, 8695-8711.
- O'Connell, R. J., and B. Budiansky, 1977. Viscoelastic Properties of Fluid Saturated Cracked Solids, *J. Geophys. Res.*: **82**, 5719-5735.
- Olsen, K. H., L. W. Braile, J. N. Stewart, C. R. Daudt, G. R. Keller, L. A. Ankeny and J. J. Wolff, 1986. Jemez Mountains Volcanic Field, New Mexico: Time Term Interpretation of the CARDEX Seismic Experiment and Comparison with Bouguer Gravity, *J. Geophys. Res.*: **91**, 6175-6187.

- Owens, T. J., G. Zandt and S. R. Taylor, 1984. Seismic Evidence for an Ancient Rift Beneath the Cumberland Plateau, Tennessee: A Detailed Analysis of Broadband Teleseismic P Waveforms, *J. Geophys. Res.*: **89**, 7783-7795.
- Prothero, W. A. and Schaefer, 1984. First Noise and Teleseismic Recordings on a New Ocean Bottom Seismometer Capsule, *Bull. Seism. Soc. Am.*: **74**, 1043-1058.
- Rayleigh, Lord (J. W. Strutt), 1907. On the Dynamical Theory of Gratings, *Proc. Roy. Soc. London, A*: **79**, 399-416.
- Richter, C. F., 1958. *Elementary Seismology*, W. H. Freeman and Company, San Francisco, 768 pp.
- Roberts, P. M., 1989. A Versatile Equalization Circuit for Increasing Seismometer Velocity Response Below the Natural Frequency, *Bull. Seism. Soc. Am.*: (in press).
- Roberts, P. M., K. Aki and M. Fehler, 1987. A Study of the 2-D Seismic Structure of the Valles Caldera, New Mexico Using Discrete Wavenumber Modeling of Teleseismic P-Waves, *EOS, Trans. Am. Geophys. Un.*: **68**, 1347.
- Ross, C. S., 1938. The Valles Volcano, New Mexico, *Wash. Acad. Sci. J.*: **28**, 417.
- Sanchez-Sesma, F. J. and J. A. Esquivel, 1979. Ground Motion on Alluvial Valleys Under Incident Plane SH Waves, *Bull. Seism. Soc. Am.*: **69**, 1107-1120.
- Sauter, A. M. and L. M. Dorman, 1986. Instrument Calibration of Ocean Bottom Seismographs, *Marine Geophys. Researches*: **8**, 265-275.
- Self, S., F. Goff, J. N. Gardner, J. V. Wright and W. M. Kite, 1986. Explosive Rhyolite Volcanism in the Jemez Mountains: Vent Locations, Caldera Development and Relation to Regional Structure, *J. Geophys. Res.*: **91**, 1779-1798.
- Self, S., D. E. Kircher and J. A. Wolff, 1988. The El Cajete Series, Valles Caldera, New Mexico, *J. Geophys. Res.*: **93**, 6113-6128.
- Shaw, R. P. and P. Bugl, 1969. Transmission of Plane Waves through Layered Linear Viscoelastic Media, *J. Acoust. Soc. Am.*: **46**, 649-654.
- Smith, R. L. and R. A. Bailey, 1966. The Bandelier Tuff—A Study of Ash-flow Eruption Cycles from Zoned Magma Chambers, *Bull. Volcanol.*: **29**, 83-104.
- Smith, R. L. and R. A. Bailey, 1968. Resurgent Cauldrons, *Mem. Geol. Soc. Am.*: **116**, 613-662.

- Smith, R. L. and H. R. Shaw, 1975. Igneous-Related Geothermal Systems. in Assessment of Geothermal Resources of the United States-1975 (D. E. White and D. L. Williams, eds.) *U.S. Geol. Surv. Circ.:* **726**, 58-83.
- Smith, R. L., R. A. Bailey and C. S. Ross, 1961. Structural Evolution of the Valles Caldera, New Mexico and its Bearing on the Emplacement of Ring Dikes, *U.S. Geol. Surv. Prof. Pap.:* **424-D**, D145-D149.
- Sommer, M. A., 1977. Volatiles H₂O, CO₂, and CO in Silicate Melt Inclusions in Quartz Phenocrysts from the Rhyolitic Bandelier Air-fall and Ash-flow tuff, New Mexico, *J. Geol.:* **85**, 423-432.
- Stacey, F. D., M. T. Gladwin, B. McKavanagh, A. T. Lindh and L. M. Hastie, 1975. Anelastic Damping of Acoustic and Seismic Pulses, *Geophys. Surveys:* **2**, 133-151.
- Steeple, D. W. and H. M. Iyer, 1976. Low-Velocity Zone Under Long Valley as Determined from Teleseismic Events, *J. Geophys. Res.:* **81**, 849-860.
- Suhr, G., 1982. Seismic Crust Anomaly under the Valles Caldera in New Mexico, USA, *Prakla-Seismos GMBH report:* **ET 4327 A**, 56 pp.
- Thomson, W. T., 1950. Transmission of Elastic Waves Through a Stratified Solid Medium, *J. Appl. Phys.:* **21**, 89-93.
- Tribolet, J. M., 1977. A New Phase Unwrapping Algorithm, *IEEE Trans. Acoust., Speech, and Signal Proc.:* **ASSP-25**, 170-177.
- Truesdell, A. H. and C. J. Janik, 1986. Reservoir Processes and Fluid Origins in the Baca Geothermal System, Valles Caldera, New Mexico, *J. Geophys. Res.:* **91**, 1817-1833.
- Warshaw, C. M. and R. L. Smith, 1988. Pyroxenes and Fayalites in the Bandelier Tuff, New Mexico: Temperatures and Comparison with other Rhyolites, *Am. Mineralogist:* **73**, 1025-1037.